# **THÈSE**

# UNIVERSITE DE PAU ET DES PAYS DE L'ADOUR

École doctorale de sciences exactes

Présentée et soutenue le 30 octobre 2014

par Marfa NAZAROVA CHERRIERE

pour obtenir le grade de docteur de l'Université de Pau et des Pays de l'Adour **Spécialité : génie pétrolier** 

WETTABILITY STUDY THROUGH X-RAY MICRO-CT PORE SPACE IMAGING IN EOR APPLIED TO LSB RECOVERY PROCESS

ETUDE DE LA MOUILLABILITE PAR IMAGERIE MICRO-CT DE L'ESPACE INTER PORAL APPLIQUEE AU PROCEDE DE RECUPERATION D'INJECTION D'EAU DOUCE

## **MEMBRES DU JURY**

### **RAPPORTEURS**

Anthony R. KOVSCEK
 Henri BERTIN
 Professeur / Chairman of the ERE Department / Stanford University
 Directeur de Recherche CNRS / Laboratoire I2M / Université de Bordeaux

#### **EXAMINATEUR**

• Gérald DEBENEST Professeur / Institut de Mécanique des Fluides de Toulouse

#### **DIRECTEURS**

Patrice CREUX
 Maître de Conférences HDR / Université de Pau et des Pays de l'Adour
 Gérald HAMON
 Docteur / TOTAL EP



## **RESUME**

La thèse a pour but d'étudier les effets de changements de mouillabilité de roches dans des conditions d'injections d'eau douce en tant que méthode de récupération d'hydrocarbures. Afin d'identifier le ou les mécanismes à l'origine du gain additionnel de récupération nous avons utilisé un microtomographe RX. Nous avons ainsi imagé les états de saturations finales d'un milieu poreux rempli de saumures et d'huiles. Une fois le drainage primaire réalisé nous avons effectué deux phases d'imbibitions : avec une saumure (récupération secondaire) puis une imbibition d'eau douce (récupération tertiaire). L'analyse de la mouillabilité à l'échelle du pore a permis de mettre en évidence l'effet de la température et de la salinité sur la mouillabilité. Nous avons montré que les changements de mouillages des roches n'étaient pas occasionnées par la seule expansion de la couche électrique en revanche des changements de mouillabilité ont été montrés. Ces changements s'expliquant par des transitions de mouillages de second ordre observées non seulement pour des gouttes d'huiles sur de l'eau mais également sur un substrat en verre. Au final, la mouillabilité en milieux poreux doit être mise en évidence à une échelle sousmicrométrique ce qui est relativement nouveau dans le domaine pétrolier.

# **ABSTRACT**

The aim of the thesis is to study rock wettability change effects caused by Low Salinity brine injection as tertiary recovery method. To identify the underlying mechanism or mechanisms of additional oil recovery X-ray imaging technology was applied. We have also imaged the end-point saturations of filled by brine and water core samples. Once the primary drainage is realized we carried out two phases imbibitions: with high salinity brine (waterflooding) and with low salinity brine (tertiary recovery mode). The wettability analysis at pore scale permitted to put in evidence the thermal and saline effects playing a decisive role in rock wettability. We have showed wettability changes are not caused by only electrical double layer expansion, however wettability changes was shown. These changes are explained by wettability transition of second order and observed not only for oil droplet on brine, but also for oil deposited on glass substrate. Finally, the pore space wettability needs to be evidenced at sub-micrometric scale that is new for the petroleum domain.

# **ACKNOWLEDGMENTS**

This PhD would have not been possible without the support of many persons: my family, my mentors and friends.

This thesis was sponsored by TOTAL and I would like to express my gratitude to Gérald Hamon, my industrial advisor, petrophysical expert at TOTAL for his supervision and for the beneficial discussions we had during the past 4 years. I also want to express my gratitude to Richard Rivenq, project leader at TOTAL, for his interest and his support that he provided to me.

I thank the Scientific Division of TOTAL, Philippe-Franck Girard and Philippe Ricoux who facilitated numerous scientific exchanges.

I want to thank Hélène Berthet, Igor Bondino, Mathilde Didier and Abbas Zerkoune, engineers in the petrophysical lab in the CSTJF TOTAL, for their involvement and their precious advices.

I express my gratitude to Patrice Creux, Associate Professeur at the University of Pau, which holds a special place in my heart. I would like to thank him for all the support that he gave me, whatever scientifically or spiritually, for the words of encouragements. I am extremely fortunate to have him as my scientific supervisor for this work.

I sincerely appreciated the honor I had Henri Bertin, Research Director at CNRS in the University of Bordeaux in I2M laboratory, and Antony R. Kovscek, Professor and Chairman of the ERE Department in the Stanford University, agreed to judge this work and to participate to PhD defense jury.

I would like also thank Gérald Debenest, Professor in the Institute of Mechanics of Fluids of Toulouse (IMFT) to me honoring by his presence in the PhD defense jury, but also for all discussions we had during this work. It was a great pleasure to work with the IMFT team; Romain Guibert and Pierre Horgue find my recognition here.

I would like also express my gratitude to all members of the Laboratoire des Fluides Complexes et de leurs Réservoirs of the University of Pau, and especially Christophe Dicharry to host me in the team; Fabrice Guerton to help me in the experimental part of work; and Patrick Bouriat for scientific exchanges and the numerous discussions we had.

I cannot forget to thank other students and my friends: Lourdes, Leticia, Romuald and Vanessa, you helped me a lot during the working time but also outside of work.

I am especially grateful to my family: my mother, my father, my grand-ma Ludmila and my brother Timofey, I hope I had made you proud. I would like also thank my family-in-law: Sylvie, Alain, Audrey, Geoffrey and Rose-Marie, thanks a lot for your support! And the biggest thanking I address to the person which was here every day to support me, and who knew to encourage me in difficult moments during this thesis: here, I would like render thanks to my husband Cédric and to my son Alexandre for their love, kindness, patience, encouragements and understandings. With all my love I dedicate this work to you.

# **CONTENTS**

1.	INTRODU	RODUCTION			
1.1	Low Sa	Low Salinity Brine injection study			
2.	MICRO-0	COMPUTED TOMOGRAPHY AS 3D VIZUALIZATION TECHNIQUE	27		
2.1	Image	acquisition	29		
	2.1.1	Micro-CT principles and main biases	29		
	2.1.1.1	X-Ray emitter	29		
	2.1.1.2	X-Ray microtomography	33		
	2.1.1.2.1	Principles	33		
	2.1.2	Image generation	35		
	2.1.2.1	Fiber Optic System	35		
	2.1.2.2	Charges-Coupled Device (CCD)	36		
	2.1.2.2.1	SkyScan detector system	37		
	2.1.2.2.2	CCD artifacts linked to radiaographies acquisition	37		
	2.1.2.2.2	.1 Temporal artifacts	38		
	2.1.2.2.2	.2 Temporal stability	38		
	2.1.2.2.2	.3 Dynamic range	38		
	2.1.2.2.2	.4 Scintillator	39		
	2.1.2.3	Noise and Signal-to-Noise ratio	39		
	2.1.2.4	Acquisition sequence	40		
	2.1.2.5	X-Ray adsorption and tomography reconstruction principles	42		
	2.1.2.5.1	Beer Lambert's law	42		
	2.1.2.5.2	Filtered Back Projection reconstruction	43		
	2.1.3	Conclusions	49		
	2.1.4	References	50		
2.2	Image	post-processing	53		
	2.2.1	Numerical filters	54		
	2.2.1.1	Median Filter	56		
	2.2.1.2	Bilateral Filter	57		
	2.2.1.3	Non-Local Means Filter	59		

2.2.1.4	Edge	e-Preserving Smoothing Filter (Avizo)	60	
2.2.1.5	Anis	otropic Diffusion Filter	62	
2.2.1.6	Unsl	harp Masking Filter	63	
2.2.2	Sign	al/Noise ratio for numerical filtering	63	
2.2.3	Ann	ex A: Some examples of Filters applying	64	
2.2.3.1	Med	lian Filter	64	
2.2.3.2	Bilat	teral Filter	65	
2.2.3.3	Non	-Local Means Filter	67	
2.2.4	Imag	ge Segmentation	69	
2.2.4.1	Segr	mentation by thresholding	69	
2.2.4.2	Regi	on Growing	71	
2.2.4.3	Conv	verging Active Contours Algorithm	72	
2.2.4.4	Cond	clusions	73	
2.2.5	Calc	ulation in image	74	
2.2.5.1	Prob	plematic of the resolution sensitivity on static properties	74	
2.2.5.1.1	Thre	ee resolutions sandstone sample	74	
2.2.5.1.2	Lack	of resolution on limestone	78	
2.2.5.1.3	Synt	hetic sample	83	
2.2.5.2	Com	puted petrophysics : mesh and method sensitivities (paper form)	89	
2.2.5.2.1	Intro	oduction	89	
2.2.5.2.2	Mat	erials and methods	91	
2.2.5.2.2.	1	Experimental imaging and processing	91	
2.2.5.2.2.	1.1	Pore-space imaging protocol	91	
2.2.5.2.2.	1.2	Image processing	92	
2.2.5.2.2.	2	Numerical work-flow	94	
2.2.5.2.2.	2.1	Configurations	95	
2.2.5.2.2.	2.2	Meshes	95	
2.2.5.2.2.	2.3	Mathematical models	97	
2.2.5.2.2.	2.4	Numerical methods	97	
2.2.5.2.3 Results and discussion				
2.2.5.2.3.	1	Representativity of the sample	99	

	2.2.5.2.3.	2 Mesh sensitivities	100
	2.2.5.2.3.	3 Comparison between experimental and numerical permeability evaluation	ons101
	2.2.5.2.3.	4 Comparison of numerical methods	101
	2.2.5.2.3.	5 Parallel efficiency	103
	2.2.5.2.4 Conclusions		104
	2.2.6	Wettability determination	106
	2.2.7	References	108
2.3	Experi	mental protocol	111
	2.3.1	Used materials	111
	2.3.1.1	X-ray microtomograph (summary)	111
	2.3.1.2	Rock type	112
	2.3.1.3	Fluid phases	112
	2.3.1.4	Experimental processes	114
	2.3.1.4.1	Initial water saturation	114
	2.3.1.4.2	Initial oil saturation	115
	2.3.1.4.3	High Salinity Brine Waterflooding	115
	2.3.1.4.4	Low Salinity Brine Injection (Tertiary mode)	115
	2.3.2	Experiment representativity	115
	2.3.2.1	Representative Elementary Volume	115
	2.3.2.2	Saturation profiles	116
	2.3.3	Wettability	118
	2.3.3.1	Mineral wettability and pore morphology	118
	2.3.3.2	Homogeneity of rock wettability at end points	119
	2.3.4	References	121
3.	TWO PH	ASE DISTRIBUTION IMAGING IN POROUS MEDIUM	123
3.1	Introdu	uction	123
3.2	Case o	f the responsible to LSB injection effect system	124
	3.2.1 Case of the responsible to LSB injection effect system with applied therma conditions		
	3.2.1.1	Initial Oil Saturation	124
	3.2.1.2	High Salinity Brine Waterflooding	127
	3.2.1.3	Low Salinity Brine Injection (Tertiary mode)	128

	3.2.1.4	Analysis and discussion	. 130
	3.2.2	Case of the responsible to LSB injection effect system without thermal aging conditions	133
	3.2.2.1	Initial Oil Saturation	. 133
	3.2.2.2	High Salinity brine injection	. 136
	3.2.2.3	Low Salinity brine Waterflooding	. 137
	3.2.3	Analysis and comparison	. 139
	3.2.3.1	Initial Oil Saturation	. 139
	3.2.3.2	Residual Oil Saturation	. 141
	3.2.3.3	Low Salinity Brine Injection (Tertiary mode)	. 143
	3.2.4	Conclusions	. 145
3.3	Effect	of crude oil on LSB injection effect	. 146
	3.3.1	Representative Elementary Volume	. 146
	3.3.1	Initial Oil Saturation	. 147
	3.3.2	High Salinity Brine Waterflooding	. 149
	3.3.3	Low Salinity Brine Injection (Tertiary mode)	. 150
	3.3.4	Analysis and conclusions	. 151
3.4	Conclu	usions	. 152
3.5	Refere	ences	. 155
4.		MOGRAPHIC METHODS TO STUDY OIL-ROCK-BRINE SYSTEM	
4.1 solu		c double layer expansion impact on the oil-quartz adhesion for high and low salinity ber form)	
	4.1.1	Introduction	. 157
	4.1.2	Experimental section	. 158
	4.1.2.1	Fluid phases	. 158
	4.1.2.2	Minerals	. 159
	4.1.2.3	Methods	. 159
	4.1.2.4	Set-ups	. 160
	4.1.3	Results	. 161
	4.1.3.1	Minerals	. 161
	4.1.3.2	Oil	. 164
	4.1.4	Discussion	. 165
	4.1.5	Conclusions	. 169

# WETTABILITY STUDY THROUGH X-RAY MICRO-CT PORE SPACE IMAGING IN EOR APPLIED TO LSB RECOVERY PROCESS

5.	CONCLUS	SIONS and PERSPECTIVES	187
	4.2.4	References	185
	4.2.3	Conclusions	183
	4.2.2	Evidence of Temperature Transition of Crude Oil Spreading on substrate	179
	4.2.1.5.2	Ja crude oil behavior on high salinity brine	178
	4.2.1.5.1	Ac crude oil behavior on high salinity brine	175
	4.2.1.5	Ellipsometry experiments	175
	4.2.1.4	Experimental Results	174
	4.2.1.3	Methods	173
	4.2.1.2	Materials	173
	4.2.1.1	Introduction	172
	4.2.1	Evidence of Temperature Transition of Crude Oils Spread on Brines (paper form)	172
4.2	Eviden	ce of Temperature Transition of Crude Oils Spreading	172
	4.1.6	References	170

#### 1. INTRODUCTION

The waterflooding as an oil recovery process was accidently discovered in Pennsylvania in 1865 when water from overlying aquifers penetrated the oil reservoir. The good results in terms of oil recovery were quite seducing. Consequently, waterflooding became a common process since the 1880's. Nowadays this is the most popular recovery method and about 70% of all oil fields are exploited through water injection. It might be explained by several reasons such as water accessibility, simplicity of water injection by pumps, the water ability to propagate and high displacement properties of water (Craig 1971). Water flooding has two main goals: maintain reservoir pressure and push hydrocarbons towards the production well.

The first academic study of waterflooding process was performed in Oklahoma University in 1949. The aim was to understand fluid distribution in porous media and its evolution during the waterflooding process (Meldrum 1949). The study was carried out on synthetic material represented by glass beads between two transparent pellicles. Since those first experiments the observation methods are evaluated. Nevertheless, it showed the importance of wettability studies of reservoir rock regarding the difference in water-oil displacement in different systems.

In the subject of wettability it is important to introduce terms like interfacial surface tension and contact angle (figure 1-1). Interfacial surface tension appears when two non-miscible phases are in contact. In the bulk of each fluid its molecules are mutually attracted in all directions. At the fluid boundary, the molecular attraction points only inwards, since there are no fluid molecules in the other side. Therefore on the fluid surface there is a film-like layer of molecules. To minimize its energy the system seeks to minimize its surface, therefore to form a sphere.

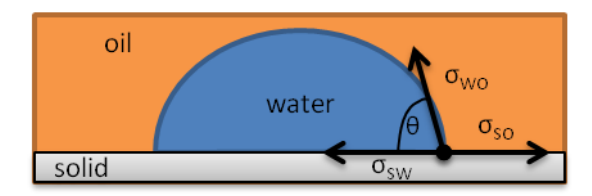


Figure 1-1 Interfacial tensions and contact angle for water-wet solid in presence of oil

The wettability of the solid surface is characterized by a contact angle between the fluid and the solid surface in the presence of other fluid or gas. The contact angle  $\theta$  depends on the adhesion forces balance and is described by Young's equation (Israelachvili 2011):

$$\cos\theta = \frac{\sigma_{so} - \sigma_{sw}}{\sigma_{wo}}$$

Where:  $\sigma_{so}$  – interfacial tension between solid and oil,  $\sigma_{sw}$  – interfacial tension between solid and water,  $\sigma_{wo}$  – interfacial tension between water and oil.

When there are two immiscible fluids in a porous medium each of these fluids has an internal pressure, therefore the difference in these two pressures across the separation interface is called capillary pressure. The capillary pressure depends on the surface tension and the curvature of the surface separating two fluids. This relation was described by Laplace law in 1805. For capillary equilibrium state (no flow condition) one may define capillary pressure dependence on contact angle separating two immiscible fluids through the Young-Laplace equation:

$$p_c = \frac{2\sigma\cos\theta}{r}$$

Where r is the pore radius and  $p_c$  is the capillary pressure.

From this equation it is evident that for smaller pores the capillary pressure is greater and therefore the wetting fluids fill smaller pores leaving greater pores for non-wetting fluid.

Based on the Laplace equation one may estimate the rock wettability importance in view of fluid displacement into pore space. Capillary pressure curves represent fluid displacement in porous medium during drainage (non-wetting phase is pushed into the pore, non-wetting phase saturation increasing) and imbibition (wetting phase saturation increasing). Measuring the phases pressure differences (capillary pressure) during each displacement (drainage or imbibition) Amott (Amott 1959) elaborated an index allowing to quantify the rock sample wettability in laboratory conditions (Amott wettability index). The principle of Amott wettability index calculation is shown in figure 1-2.

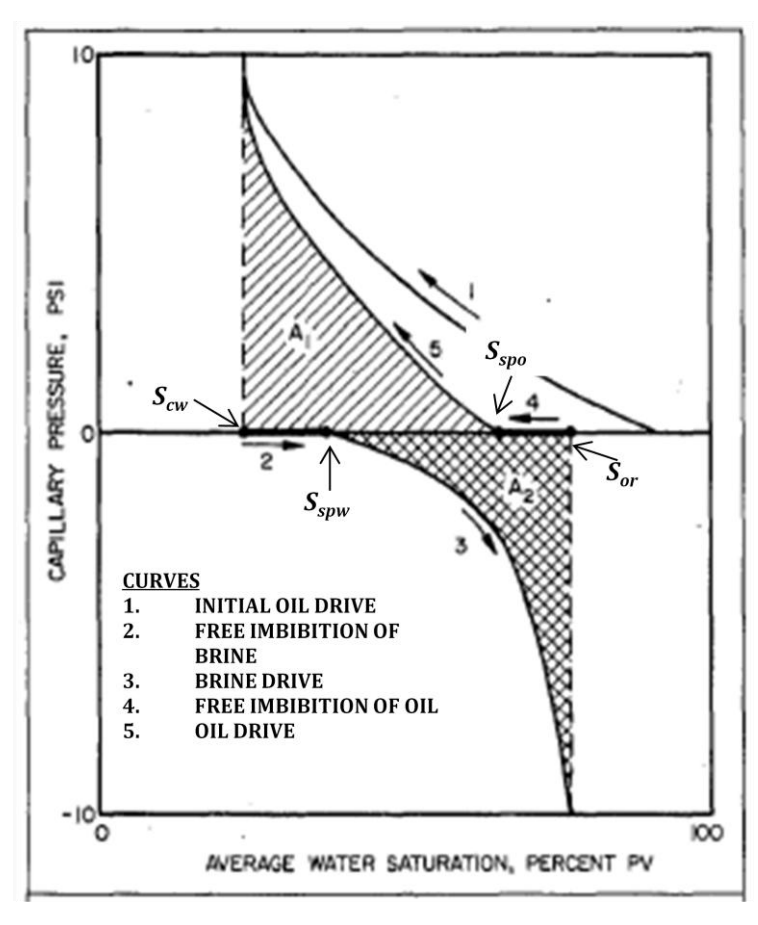


Figure 1-2 Combined Amott and USBM method (Anderson 1986; Sharma & Wunderlich 1985).

Primary drainage consists of the oil penetration in porous medium fully saturated in water ( $S_w$ =100) and the initial pressure needed to permit oil filling. The primary drainage occurs until the minimal water saturation is reaching ( $S_{cw}$  – connate water saturation). When oil pressure decreases water imbibes spontaneously the porous medium to balance capillary pressure ( $P_c$ =0) and spontaneous water saturation is reached ( $S_{spw}$ ). After this point spontaneous oil displacement is impossible, oil may be displaced only by forced imbibition. Thereby to displace oil from this point on and decrease oil saturation water pressure must be higher than oil pressure, therefore the capillary pressure becomes negative by definition. Once the oil saturation is irreducible ( $S_{or}$ =1- $S_w$ ) oil might penetrate the core sample reaching null capillary pressure ( $S_{spo}$ ). Water displacement by oil from this point on is possible only by forced drainage up to connate water saturation.

Amott wettability index consists in a ratio characterization between spontaneous and full imbibition recoveries for both fluids.

$$I_{w-o} = I_{w} - I_{o}$$

$$I_{w} = \frac{S_{pw} - S_{cw}}{1 - S_{cw} - S_{or}}$$

$$I_{o} = \frac{S_{or} - S_{spo}}{1 - S_{cw} - S_{or}}$$

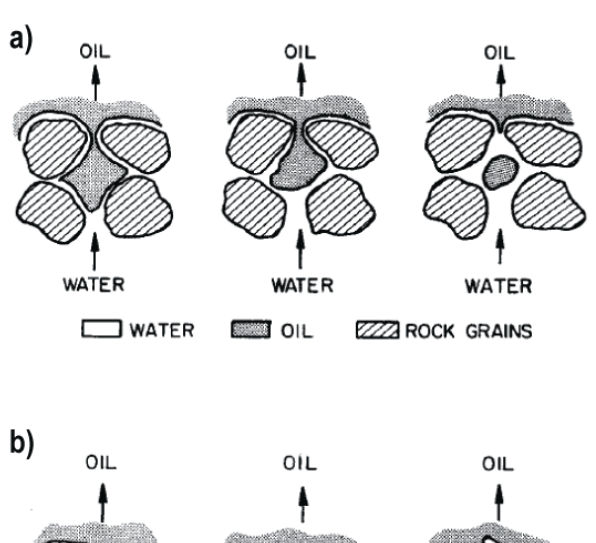
For extremely water-wet system,  $I_o$  will be zero and  $I_w$  will be 1, therefore  $I_{wo}$  will be zero, contrariwise for extremely oil-wet system,  $I_o$  will be 1 and  $I_w$  will be zero, therefore Amott wettability index will be -1.

The Amott wettability index does not take into account the shape of capillary pressure curves. That is why the US Bureau of Mines proposed another wettability index (Donaldson et al. 1969) based also on curves shape. This method is based on a correlation between the degree of wettability and the integrals of capillary pressure curves of successive first imbibition and second drainage flows, as suggested by Gatenby and Marsden (Gatenby & Marsden 1957):

$$I_{USBM} = log \frac{A_1}{A_2}$$

Where  $A_w$  and  $A_o$  are integrals of drainage and imbibition curves respectively (from figure 1-2).

Wettability determination of reservoir rocks is a crucial experiment in reservoir engineering due to its link with final oil production. Relative initial oil-water distribution in the reservoir depends on the wettability of the enclosing rock. Wettability characterizes the interaction between fluids and solid phases. In porous media wettability is the property of the solid-liquid systems and means the preferential adhesion (spreading) of one of the liquids on the solid (Donaldson & Tiab 2004). In real systems the rock wettability might vary from strongly hydrophilic to strongly hydrophobic. If the rock does not interact preferentially with either fluid, it is said to have a neutral wettability. In hydrophilic rocks water covers the rock surface like a film and fills smaller pores and its throats, leaving the oil in the center of larger pores. Thereby oil has no contact with mineral surfaces and both saturations are continuous. Oil displacement in this case is achieved by water imbibitions a in porous medium (Figure 1-3a) (Craig, 1971; Surguchev, 1985). In the long-term oil exposed to high temperatures might come in contact with large pores walls rendering it more hydrophobic. Therefore in general reservoir rocks present mixed wettability. Oil displacement in purely hydrophobic systems is achieved by water flow leading oil. (Figure 1-3b)



WATER WATER WATER

WATER OIL ROCK GRAIN

Figure 1-3 Water displacing oil from a pore in (a) a strongly water—wet rock, and (b) a strongly oil-wet rock (Raza et al. 1968)

And from the beginning of wettability studies new terms have appeared. If the rock is partially water-wet and partially oil-wet Brown and Fatt have named it "Dalmatian wettability" (Brown & Fatt 1956). In this case some discrete parts of the rock's surface are hydrophobic and rest of it is hydrophilic. It is important to note that "Dalmatian wettability" is not the same as neutral wettability. Neutral wettability means the same adhesion preference for both fluids throughout the entire rock's surface.

A "mixed wettability" was described by Alba in 1958 (Donaldson & Tiab 2004) and means, for example, small pores occupation by water and therefore the presence of a hydrophilic surface, and in larger pores the minerals surface is covered by oil. This type of wettability may occur when oil penetrates a hydrophilic medium. In this case oil will occupy larger pores and polar surfactants present in it will react with the mineral surface displacing the water film which covers the hydrophilic surface. The water film is displaced as oil arrives leading to an oil-matrix direct interaction as water film fractures (Melrose 2013). In fact, the mechanism of wettability alteration depends on numerous factors as crude oil composition, rock and mineral nature, connate water (brine) composition and also displacement brine composition ((Buckley et al. 2003), (Agbalaka et al. 2008))

The wettability study is very important, due to its influence on the majority of reservoir characteristics like fluid displacement, capillary pressure, relative permeability, and therefore the final reservoir production ((Donaldson et al. 1969), (Emery et al. 1970), (Kyte et al. 1961), (Masalmeh 2002)) First studies on wettability mainly pointed out the importance of maintaining water-wet conditions for better oil recovery (Coley et al. 1956), (Newcombe et al. 1955) (figure 1-3a).

Jadhunandan and Morrow (Jadhunandan & Morrow 1995) showed that the maximal oil recovery by waterflooding is reached for lightly water-wet core with Amott index between 0.1 and 0.2 and for intermediate wettability (Morrow 1990). More recent many authors have shown differences on oil recovery a dependence on rock sample wettability (Morrow & Mason 2001); (Kumar et al. 2012); (Skauge

et al. 2007). In fact, rock wettability determination is not a simple parameter especially in the case of mixed wettability (Kumar et al. 2012).

# 1.1 Low Salinity Brine injection study

Low Salinity brine effect and "smart water" general effect are most discussed problems on wettability concepts. Indeed, the first "smart water" injection was carried out accidently in Wyoming University in 1990's (Tang et al. 1997). Tang and Morrow have showed oil recovery enhancement with low salinity brine injection instead of classically used high salinity brine. High salinity brine is classically injected because of it is widely available (from aquifers or sea) and to avoid a number of problems such as clays swelling that reduces reservoir permeability and therefore reduces hydrocarbon recovery ((Hower 1974),(Donaldson & Tiab 2004), (Mohan et al. 1993)).

After the first experiment in Wyoming University many authors have observed oil recovery enhancement in sandstones by "smart water" injection in laboratory studies (Tang et al. 1997; Morrow et al. 1998; Zhang et al. 2006; Sharma & Filoco 2013; Morrow & Buckley 2013) and reservoir scale experiments (Mcguire et al. 2005) Initially, "smart water" effect was reported only in sandstone core plugs and the presence of clay in rock cores was noted as a necessary condition (Morrow et al. 1998). Nevertheless some researchers showed additional oil recovery on carbonates (Webb et al. 2005; Austad & Standnes 2003; Al-Attar et al. 2013; Pu et al. 2010; Loahardjo et al. 2010). The challenge is more important considering not permanent response of crude oil, brine, rock system to Low Salinity Brine injection (Cissokho 2010; Winoto et al. 2014)

Firstly, the necessary initial conditions of the sandstone rock was discussed by Tang and Morrow in Tang's PhD thesis (Morrow et al. 1998). They established the indispensability of the presence of fine particles in coating in pore space. The fine particles must be smaller than the pore's throat allowing their migration. The presence of polar crude oil components, connate water and the mixed wettability of rocks are necessary conditions as well. Tang and Morrow noted also clay presence in the studied Berea sandstone however they did not specify the type of clay needed for "smart water" additional oil recovery. Later, Jerauld (Jerauld et al. 2006) reported the proportionality of oil recovery increasing with the initial kaolinite content in used rock.

In all these studies of "smart water" effects authors tried to explain the oil recovery improvement with numerous hypotheses. Tang and Morrow proposed fines migration (1999) mechanism. It is one of the most popular mechanisms in literature to explain the "smart water" effect and later some authors supported this hypothesis (Loahardjo et al. 2010; Li 2011; Pu et al. 2010; Lebedeva & Fogden 2011; Hamouda et al. 2014). According to them, potentially mobile fine particles are strongly adhered on mineral surface and being filled by connate water make their not to react on high salinity brine injection similar to connate water. In high salinity brine condition fines particles retain their oil-wet nature that permits oil to adsorb on their surfaces. Change in brine salinity permits to proceed to oil-wet clays particles detachment leading to additional oil recovery. The phenomenon of fines migration is widely referenced in the literature and is explained by DLVO theory. Fines migration mechanism is associated with permeability reduction and pressure increase caused by pore occluding. Nevertheless, in 2009 Boussour et al. (Boussour et al. 2009) have shown contradictory results with fine production but without any additional oil recovery and with pressure drop increase also not leading to additional recovery. These results disprove the idea that the fines migration might be the key mechanism of low salinity brine injection.

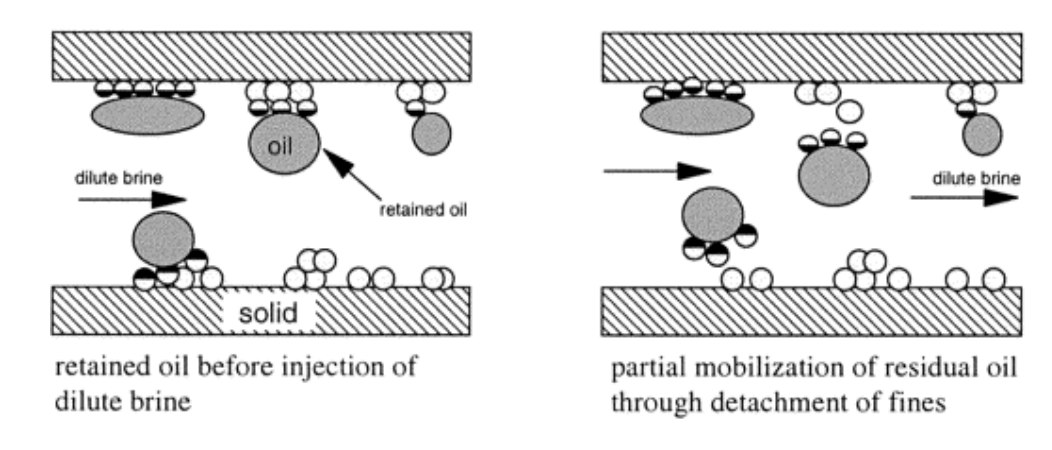


Figure 1.1-1 Trapped oil mobilization by fine migration (Tang, Morrow 1999)

Surfactant generation as a possible mechanism of smart water effect was proposed by McGuire(Mcguire et al. 2005). According to his study the "smart water" injection reacts like an alkaline solution injection and it generates surfactants from crude oil. Surfactant generation reduces the IFT and permits to produce more oil. The hypothesis of in-situ surfactant generation originates from widely observed pH increasing during smart water injection. The pH increase was previously explained by carbonate mineral dissolution (Mcguire et al. 2005) and is at origin of the cation exchange with mineral surfaces consequently to low salinity brine injection. This possible explanation was refuted by Lager et al. (Lager et al. 2006). In fact, they showed the additional oil recovery with pH less than 7 that is in contradiction with the necessary condition established by McGuire which is pH over 9 and an important presence of acidic compounds in crude oil. In reality, McGuire's conditions might cause buffering process at reservoir scale that confirms theirs inconsistency. Otherwise, there are some experimental evidences of additional oil recovery absence despite the important pH rise (Cissokho et al. 2009).

Multi-component ionic exchanges were evidenced by Lager et al. in 2006 (Lager et al. 2006). In fact, they showed an important difference of Mg<sup>2+</sup> and Ca<sup>2+</sup> concentrations between the incoming and the outgoing solutions after low salinity brine injection. Cation adsorption was proposed as underlying mechanism of low salinity brine phenomenon. Considering the widely referenced adsorption mechanisms in Soil science (Sposito 1989) Lager (Lager et al. 2006) proposed some of these to explain low salinity brine effect. For these authors polar components of crude oil might adsorb onto clay surfaces by multivalent cation bridge formed between clay surface and an organo-metal complex of crude oil, or by a direct adsorption of oil polar component on clay by clay ions displacing.

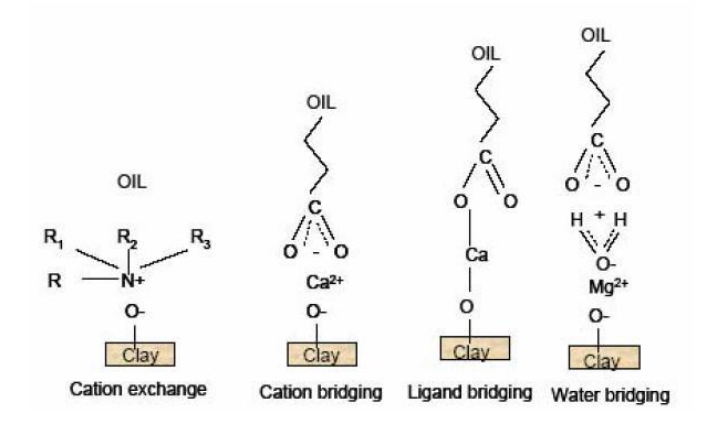


Figure 1.1-2 Attraction between clay surface and crude oil by divalent cations (Lager et al. 2008).

The Lager's theory was confirmed by additional experiments with atomic force microscopy (AFM) by Mugele et al. (Mugele et al. 2014). They proposed for an idealized system that wettability alteration might occur in two ways: inversion of surface charges due to ion adsorption from brine and desorption of hydrophobic layers from rock surface.

Buckley (Buckley et al. 1998) and later Seccombe (Seccombe et al. 2008) concluded on "bridge construction" by multivalent cations between negatively charged clay surfaces and negatively charged oil surface in high salinity brine presence. Recently other authors supported this proposition (Fjelde et al. 2014). After low salinity brine injection clays became more water-wet and cation bridges broke releasing the adsorbed oil, thereby increasing the final oil production. In contradiction with the proposed theory there are many articles in literature showing the additional oil recovery in case of low salinity brine injection containing only monovalent ions (Ligthelm et al. 2009; Zhang et al. 2007; Cissokho et al. 2009).

In addition to proposed cation exchange mechanism Lightelm et al. (Lightelm et al. 2009) and more recently RezaeiDoust (RezaeiDoust et al. 2011) supposed the electrical double layer (EDL) expansion of clays favoring oil detachment. In theory in high salinity conditions mineral (and/or clay) negative surfaces are screened by availability of cations thereby the double electrical layer inexistence in high salinity brine condition permits oil to adhere on mineral and/or clay surface during the first drainage step. The availability of cations decreases with low salinity brine injection, therefore electrical double layer grows and the repulsive forces between minerals and oil increases permitting additional oil recovery. The theory of the EDL expansion more recently was supported by other authors who explain EDL expansion caused by pH changes and therefore it results in surface charges changes (Al-shalabi et al. 2014). Authors applied EDL expansion theory to carbonate rocks.

Recently, Nasralla et al. (Nasralla & Bataweel 2013; Nasralla et al. 2012) published similar results with zeta-potential measurements on rock-brine interfaces and oil-brine interfaces. They showed a quasi-inexistence of surface charge in high salinity brine conditions and important negative charges for the both types of measurements in low salinity conditions. They observed additional oil recovery with LSB injection in secondary mode, but they did not observe any improvement in tertiary mode. We will discuss their results and electrical double layer repulsive forces sufficiency to additional oil production in the last chapter.

The latest works on subject showed the existence of micro-dispersions on oil-water surface in case of LS brine and theirs coalescence if HS brine is injected (Emadi & Sohrabi 2013; Mahzari & Sohrabi 2014). Authors used micromodels for direct visualization of micro-dispersions.

Despite the availability of numerous propositions in literature trying to explain low salinity brine effect and absence of the key underlying mechanisms the scientific community agrees with rock wettability change during low salinity brine injection. It was reported by many authors that rocks with initial neutral wettability or lightly oil-wet are more responsive to low salinity brine injection (Shaker Shiran & Skauge 2012).

In 1997, Buckley (Buckley et al. 1997) showed the importance of water film stability on rock wettability state, since water film presence in porous medium might separate two charged surfaces as oil and mineral. She elaborated wettability maps of oil adhesion on glass surface in dependence on temperature, solvent, pH and brine salinity. Recently, Lebedeva et al. (Fogden & Lebedeva 2011) showed the residual oil adhesion on mineral surface with Field Emission Scanning Electron Microscopy after a waterflooding. Recently, the surface changes after Low Salinity Brine injection in the system was visualized by other authors (Mahani et al. 2014). Authors used a glass substrate with deposited Na-montmorillonites and covered by oil droplet (Fig1.1-3) to visualize oil droplet receding under low salinity brine conditions with following oil detachment. They also proposed the EDL expansion as a possible mechanism to explain Low Salinity Brine effect responsible to additional oil recovery (Figure 1.1-4).

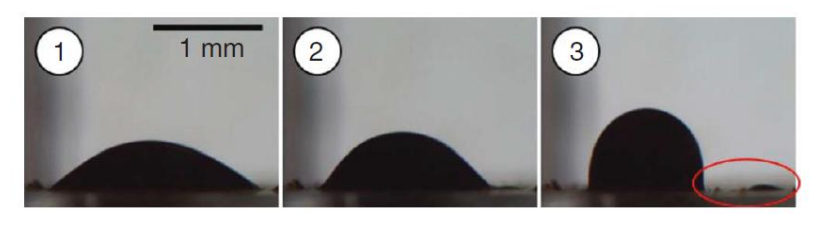
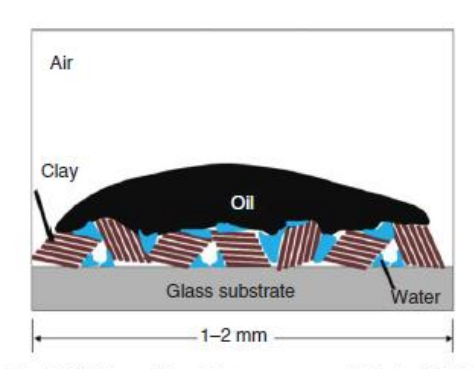
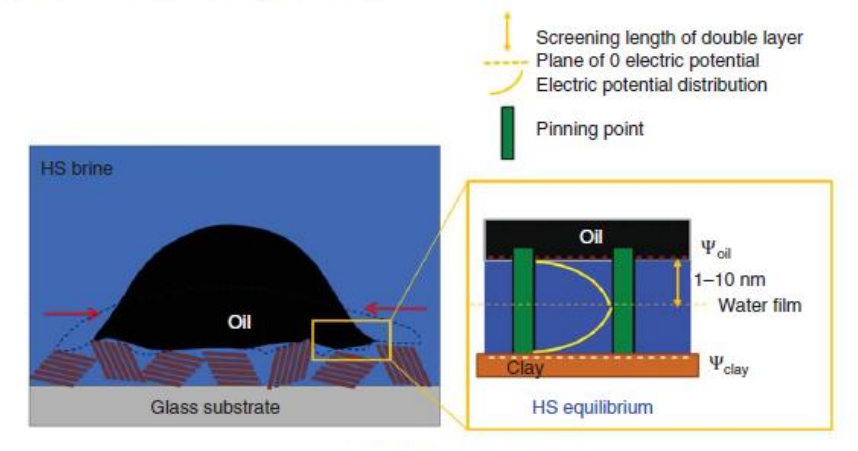


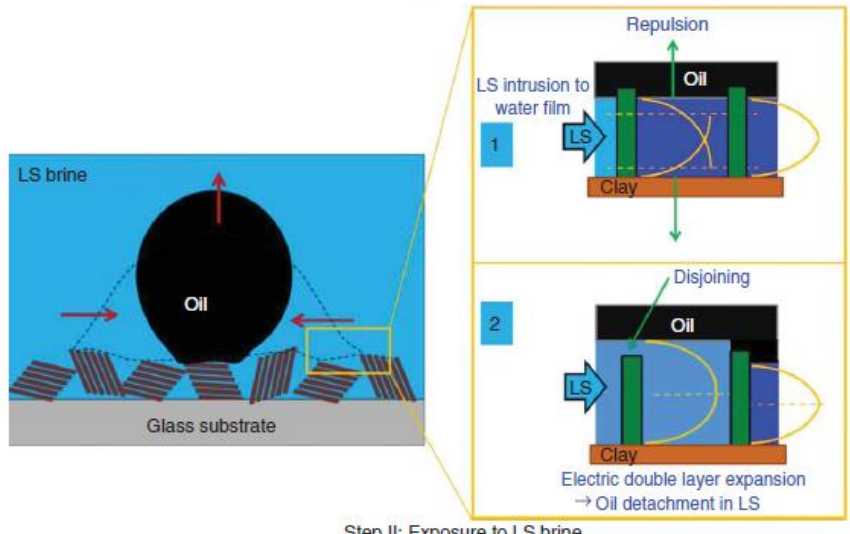
Figure 1.1-3 High resolution imaging of oil droplet at HS (1), after 7 hours (2), after 2 days exposed to LS brine, residual oil is circled when oil recedes (Mahani et al. 2013)



Step 0: Initial condition before exposure of clay to HS brine.



Step I: Exposure to HS brine



Step II: Exposure to LS brine

1.1-4 Potential mechanism of oil detachment proposed by Mahani et al. (Mahani et al. 2014)

In this thesis we will discuss about such wettability changes and their possible mechanisms. The mainly used instrument in the thesis was X-ray micro-computed tomography which allowed observing in-situ the wetting changes and fluids redistributions with a resolution of a few microns.

X-rays were first discovered by Wilhelm Conrad Röntgen in 1895. From this date many researchers have thrived to make this discovery useful for the world especially the medical world. Radon proposed in 1917 a method of integral conversion to reconstitute the initial function from its projection (Helgason 1980).

X-ray computed tomography was born officially in 1971. Godfrey Hounsfield and Allan McLeod Cormack proposed a method of stratified study of the internal structure of the object based on measurement and computer treatment of X-Ray attenuation differences caused by different material densities. They are known as the CT inventors for which they were awarded a Nobel Prize. The first patient brain-scan was carried out in October 1971 in Atkinson Morley Hospital in Wimbledon, England (Beckmann 2006).

The first micro-CT scanner was built in the beginning of 1980's by J. Elliott (Elliott & Dover 1982) and it was extended in 1990's for the petroleum industry (Dunsmuir et al. 1991).

The micro-CT principals, advantages, errors sources and their eliminations are described in the following part.

#### References

- Agbalaka, C.C. et al., 2008. The Effect Of Wettability On Oil Recovery: A Review. In *SPE Asia Pacific Oil and Gas Conference and Exhibition*. Society of Petroleum Engineers.
- Al-Attar, H.H. et al., 2013. Low-salinity flooding in a selected carbonate reservoir: experimental approach. *Journal of Petroleum Exploration and Production Technology*, 3(2), pp.139–149.
- Al-shalabi, E.W., Sepehrnoori, K. & Pope, G., 2014. Geochemical Interpretation of Low Salinity Water Injection in Carbonate Oil Reservoirs. In *SPE Improved Oil Recovery Symposium*. Society of Petroleum Engineers.
- Amott, E., 1959. Observations Relating to the Wettability of Porous Rock.
- Anderson, W., 1986. Wettability Literature Survey- Part 2: Wettability Measurement. *Journal of Petroleum Technology*, 38(11), p.1 246–1 262.
- Austad, T. & Standnes, D.C., 2003. Spontaneous imbibition of water into oil-wet carbonates. *Journal of Petroleum Science and Engineering*, 39(3-4), pp.363–376.
- Beckmann, E.C., 2006. CT scanning the early days. The British journal of radiology, 79(937), pp.5-8.
- Boussour, S. et al., 2009. SPE 124277 Oil Recovery by Low Salinity Brine Injection: Laboratory Results on Outcrop and Reservoir Cores., (2005).
- Brown, R.J.S. & Fatt, I., 2013. Measurements Of Fractional Wettability Of Oil Fields' Rocks By The Nuclear Magnetic Relaxation Method. In *Fall Meeting of the Petroleum Branch of AIME*. Society of Petroleum Engineers.
- Buckley, J.S. et al., 1997. Asphaltenes and Crude Oil Wetting The Effect of Oil Composition. *SPE Journal*, 2(02), pp.107–119.
- Buckley, J.S., Liu, Y. & Monsterleet, S., 1998. Mechanisms of Wetting Alteration by Crude Oils. *SPE Journal*, 3(01), pp.54–61.
- Cissokho, M., 2010. Etude expérimentale des interactions Huile brute/Saumure/Roche sur la récupération d'hydrocarbures par injection d'eau de faible salinité.
- Cissokho, M. et al., 2009. LOW SALINITY OIL RECOVERY ON CLAYEY SANDSTONE: EXPERIMENTAL STUDY., pp.1–12.
- Coley, F., Marsden, S. & Calhoun, J., 1956. A study of the effect of wettability on the behavior of fluids in synthetic porous media. *Producers Monthly*.
- Craig, F., 1971. The reservoir engineering aspects of waterflooding, New York: H.L. Doherty Memorial Fund of AIME.
- Donaldson, E.C., Thomas, R.D. & Lorenz, P.B., 1969. Wettability Determination and Its Effect on Recovery Efficiency. *Society of Petroleum Engineers Journal*, 9(01), pp.13–20.
- Donaldson, E.C. & Tiab, D., 2004. *Petrophysics: Theory and Practice of Measuring Reservoir Rock and Fluid Transport Properties*.
- Dunsmuir, J.H. et al., 1991. X-Ray Microtomography: A New Tool for the Characterization of Porous Media. In *SPE Annual Technical Conference and Exhibition*. Society of Petroleum Engineers.

- Elliott, J.C. & Dover, S.D., 1982. X-ray microtomography. *Journal of Microscopy*, 126(2), pp.211–213. Available at: http://doi.wiley.com/10.1111/j.1365-2818.1982.tb00376.x [Accessed August 11, 2014].
- Emadi, A. & Sohrabi, M., 2013. SPE 166435 Visual Investigation of Oil Recovery by Low Salinity Water Injection: Formation of Water Micro-Dispersions and Wettability Alteration., (1999), pp.1–15.
- Emery, L.W., Mungan, N. & Nicholson, R.W., 1970. Caustic Slug Injection in the Singleton Field. *Journal of Petroleum Technology*, 22(12), pp.1569–1576..
- Fjelde, I., Omekeh, A.V. & Sokama-Neuyam, Y.A., 2014. Low Salinity Water Flooding: Effect Of Crude Oil Composition. In SPE Improved Oil Recovery Symposium. Society of Petroleum Engineers.
- Fogden, A. & Lebedeva, E. V, 2011. CHANGES IN WETTABILITY STATE DUE TO WATERFLOODING., pp.1–12.
- Gatenby, W. & Marsden, S., 1957. Some Wettability Characteristics of Synthetic Porous Media. *Producers Monthly*, 22, pp.5–12.
- Hamouda, A.A. et al., 2014. Possible Mechanisms for Oil Recovery from Chalk and Sandstone Rocks by Low Salinity Water (LSW). In SPE Improved Oil Recovery Symposium. Society of Petroleum Engineers.
- Helgason, S., 1980. The Radon Transform. Progress in Mathematics 5. Boston-Basel-Stuttgart, Birkhäuser Verlag 1980. VII, 192 S., sFr. 15.—. ISBN 3-7643-3006-6. ZAMM Zeitschrift für Angewandte Mathematik und Mechanik, 61(8), pp.411–411.
- Hower, W.F., 1974. Influence of Clays on the Production of Hydrocarbons. In *SPE Symposium on Formation Damage Control*. Society of Petroleum Engineers.
- Israelachvili, J.N., 2011. Intermolecular and Surface Forces: Revised Third Edition.
- Jadhunandan, P.P. & Morrow, N.R., 1995. Effect of Wettability on Waterflood Recovery for Crude-Oil/Brine/Rock Systems. *SPE Reservoir Engineering*, 10(01), pp.40–46.
- Jerauld, G.R. et al., 2006. SPE 102239 Modeling Low-Salinity Waterflooding.
- Kumar, M. et al., 2012. Investigation of Pore-Scale Mixed Wettability. SPE Journal, 17(01), pp.20-30.
- Kyte, J.R., Naumann, V.O. & Mattax, C.C., 1961. Effect of Reservoir Environment on Water-Oil Displacements. *Journal of Petroleum Technology*, 13(06), pp.579–582.
- $Lager, A.\ et\ al.,\ 2006.\ LOW\ SALINITY\ OIL\ RECOVERY\ -\ AN\ EXPERIMENTAL\ INVESTIGATION.\ ,\ pp.1-12.$
- Lager, A., Limits, P.R. & Webb, K.J., 2008. SPE 113976 LoSal TM Enhanced Oil Recovery: Evidence of Enhanced Oil Recovery at the Reservoir Scale.
- Lebedeva, E. V. & Fogden, A., 2011. Micro-CT and wettability analysis of oil recovery from sand packs and the effect of waterflood salinity and kaolinite. *Energy and Fuels*, 25(12), pp.5683–5694.
- Li, Y., 2011. Oil Recovery by Low Salinity Water Injection into a Reservoir: A New Study of Tertiary Oil Recovery Mechanism. *Transport in Porous Media*, 90(2), pp.333–362.
- Ligthelm, D.J. et al., 2009. Novel Waterflooding Strategy By Manipulation Of Injection Brine Composition. In *EUROPEC/EAGE Conference and Exhibition*. Society of Petroleum Engineers.

- Loahardjo, N., Xie, X. & Morrow, N.R., 2010. Oil recovery by sequential waterflooding of mixed-wet sandstone and limestone. *Energy and Fuels*, 24(9), pp.5073–5080.
- Mahani, H. et al., 2014. Kinetics of Low-Salinity-Flooding Effect. SPE Journal, Preprint(Preprint).
- Mahani, H. et al., 2013. SPE 165255 Kinetics of the Low Salinity Waterflooding Effect Studied in a Model System.
- Mahzari, P. & Sohrabi, M., 2014. Crude Oil/Brine Interactions and Spontaneous Formation of Micro-Dispersions in Low Salinity Water Injection. In *SPE Improved Oil Recovery Symposium*. Society of Petroleum Engineers.
- Masalmeh, S.K., 2002. Studying the effect of wettability heterogeneity on the capillary pressure curves using the centrifuge technique. *Journal of petroleum science & engineering*, 33(1-3), pp.29–38.
- Mcguire, P.L.L. et al., 2005. Low Salinity Oil Recovery: An Exciting New EOR Opportunity for Alaska's North Slope. In *SPE Western Regional Meeting*. Society of Petroleum Engineers, pp. 1–15.
- Meldrum, A.H., 1949. The Efficiency of Displacement of Oil from Unconsolidated Sand by Water Drive.
- Melrose, J.C., 2013. Interpretation Of Mixed Wettability States In Reservoir Rocks. In *SPE Annual Technical Conference and Exhibition*. Society of Petroleum Engineers.
- Mohan, K.K. et al., 1993. Water sensitivity of sandstones containing swelling and non-swelling clays. *Colloids and Surfaces A: Physicochemical and Engineering Aspects*, 73, pp.237–254.
- Morrow, N. & Buckley, J., 2013. Improved Oil Recovery by Low-Salinity Waterflooding. *Journal of Petroleum Technology*, 63(05), pp.106–112.
- Morrow, N.R., 1990. *Interfacial Phenomena in Petroleum Recovery*, CRC Press.
- Morrow, N.R. et al., 1998. Prospects of improved oil recovery related to wettability and brine composition. *Journal of Petroleum Science and Engineering*, 20(3-4), pp.267–276.
- Morrow, N.R. & Mason, G., 2001. Recovery of oil by spontaneous imbibition. *Current Opinion in Colloid & Interface Science*, 6(4), pp.321–337.
- Mugele, F. et al., 2014. Charge Control And Wettability Alteration At Solid-liquid Interfaces. In SPE Improved Oil Recovery Symposium. Society of Petroleum Engineers.
- Nasralla, R.A. & Bataweel, M.A., 2013. Investigation of Wettability Alteration and Oil-Recovery Improvement by Low-Salinity Water in Sandstone Rock. , (January), pp.6–8.
- Nasralla, R.A., Nasr-el-din, H.A. & Texas, A., 2012. SPE 154334 Double-Layer Expansion: Is It A Primary Mechanism of Improved Oil Recovery by Low-Salinity Waterflooding?, (2008).
- Newcombe, J., McGhee, J. & Rzasa, M.J., 1955. Wettability Versus Displacement in Water Flooding in Unconsolidated Sand Columns.
- Pu, H. et al., 2010. SPE 134042 Low Salinity Waterflooding and Mineral Dissolution., (September), pp.19-22.
- Raza, S.H., Treiber, L.E. & Archer, D.L., 1968. Wettability of reservoir rocks and its evaluation. *Prod. Mon.; (United States)*, 32:4.

- RezaeiDoust, A., Puntervold, T. & Austad, T., 2011. Chemical Verification of the EOR Mechanism by Using Low Saline/Smart Water in Sandstone. *Energy & Fuels*, 25(5), pp.2151–2162.
- Seccombe, J.C. et al., 2008. SPE 113480 Improving Wateflood Recovery: LoSal TM EOR Field Evaluation Ad Re c =. , pp.1–19.
- Shaker Shiran, B. & Skauge, A., 2012. Wettability and Oil Recovery by Low Salinity Injection. In *SPE EOR Conference* at Oil and Gas West Asia. Society of Petroleum Engineers.
- Sharma, M.M. & Filoco, P.R., 2013. Effect of Brine Salinity and Crude-Oil Properties on Oil Recovery and Residual Saturations. *SPE Journal*, 5(03), pp.293–300.
- Sharma, M.M. & Wunderlich, R.W., 1985. The Alteration of Rock Properties Due to Interactions With Drilling Fluid Components. In SPE Annual Technical Conference and Exhibition. Society of Petroleum Engineers.
- Skauge, A. et al., 2007. Theoretical and experimental evidence of different wettability classes. *Journal of Petroleum Science and Engineering*, 57(3-4), pp.321–333..
- Sposito, G., 1989. The Chemistry of Soils.
- Surguchev, M. & Сургучев, M., 1985. Secondary and tertiary methods of enhanced oil recovery. Вторичные и третичные методы увеличения нефтеотдачи пластов, Available at:
- Tang, G.Q., Morrow, N.R. & Wyoming, U., 1997. Salinity, Temperature, Oil Composition, and Oil Recovery by Waterflooding., (November), pp.269–276.
- Webb, K.J. et al., 2005. IPTC 10506 A Laboratory Study Investigating Methods for Improving Oil Recovery in Carbonates 70 Cross-Section of GASM Apparatus., pp.1–7.
- Winoto, W., Loahardjo, N. & Morrow, N.R., 2014. Assessment of Oil Recovery by Low Salinity Waterflooding from Laboratory Tests. In *SPE Improved Oil Recovery Symposium*. Society of Petroleum Engineers..
- Zhang, P., Tweheyo, M.T. & Austad, T., 2007. Wettability alteration and improved oil recovery by spontaneous imbibition of seawater into chalk: Impact of the potential determining ions Ca2+, Mg2+, and SO42–. *Colloids and Surfaces A: Physicochemical and Engineering Aspects*, 301(1-3), pp.199–208.
- Zhang, Y., Morrow, N.R. & Wyoming, U., 2006. SPE 99757 Comparison of Secondary and Tertiary Recovery With Change in Injection Brine Composition for Crude Oil / Sandstone Combinations.

# 2. MICRO-COMPUTED TOMOGRAPHY AS 3D VIZUALIZATION TECHNIQUE

Petrophysical laboratory measurements are cumbersome but permit to estimate accurately macroscopic rock properties. Since the late 1980's X-ray computed microtomography has been a tool for the non-destructive investigation of 3D porous materials (Flannery, Deckman, Roberge, & D'Amico, 1987). The 3D geometric structure information contributed to improve petrophysical characterization such pore space extraction to model fluid flow in porous medium, or wave propagation. Since the late 1990's, simultaneously with the first calculation in images algorithms, the introduction of contrast agents allowed to discern between dense fluids by an increase of X-ray absorption of one of the fluids (Mossoti & Castanier, 1989; R.S. Seright, Liang, Lindquist, & Dunsmuir, 2003; Vinegar, 1986). Nowadays the technique of contrast agent introduction is also widely used to selectively "dope" fluids and to enhance the contrast of the different phases, commonly authors use iodine solution to boost organic phase and diiodomethane to facilitate pore space separation from other materials (Dodd, Marathe, Middleton, Fogden, & Carnerup, 2014; Fogden, McKay, Turner, Marathe, & Senden, 2014; Fogden, Middleton, et al., 2014).

Digital rock physics studies permits to access to rock properties from the image of the rock. Digital rock physics predict multiphase flow simulations in real porous medium extracted from micro-CT images (Piri & Blunt, 2005) or its properties (Øren & Bakke, 2002). Micro-CT imaging gives access to pore-to-plug calibration in view to upscale to field scale characterization (Lopez et al., 2012). The X-ray techniques permit to validate or enhance the numerical codes by comparison of representative imaged experiments. The residual oil saturation distribution (Randall S. Seright, Prodanovic, & Lindquist, 2006) or more recently characterization of very low permeability rocks (Saraji & Piri, 2014; Shah, Yang, Crawshaw, Gharbi, & Boek, 2013) are very interesting experiments for who is interested in physical simulation.

To identify fluids and to perform petrophysical properties calculation from image it is necessary to be able to detect oil blobs, menisci and contact angles at high resolution (Iglauer, Favretto, Spinelli, Schena, & Blunt, 2010; Iglauer, Paluszny, Pentland, & Blunt, 2011; Karpyn, Piri, & Singh, 2010; Prodanović, Lindquist, & Seright, 2007). The recent progress in micro-CT visualization have permitted to access to rapid 3D visualization of fluids in porous medium and thereby theirs dynamics. Multiphase flow imaging with high detectability at short time was performed at the Paul Scherrer Institute using the Swiss Light Source (SLS). This type of works permits to identify new mechanisms in multiphase flow in the understanding of physical mechanisms in porous medium. However synchrotrons radiations access may only be envisaged for exceptional experiments (Steffen Berg et al., 2013). In 2014 Yousseff et al. (Youssef, Rosenberg, Deschamps, Oughanem, & Institut, 2014) have imaged with TOMCAT beam line of SLS (Swiss Light Source) oil ganglions dynamics in porous sandstones at different capillary numbers. A similar work was performed by Berg et al. (S Berg et al., 2014), using fast synchrotron-based X-ray computed micro tomography they observed oil mobilization and more precisely Haines jump in imbibition conditions in a sandstone sample. They showed in real time that imbibitions process in porous sample is more complex than a sample percolation, when non-wetting fluid once broken becomes immobile and static as it was previously assumed. They observed oil clusters breaking off by snap-off, which occurs when the capillary pressure exceeds the threshold pressure of non-wetting fluid phase.

Recently, micro-CT X-ray imaging was used for a new challenge to visualize very tight rocks such a carbonate. Two different teams imaged carbonate dissolution by acidizing (Agbogun et al., 2014; Qajar, Francois, & Arns, 2013). Other scientific groups studied multiphase flow in a carbonate rock:

- a two phase flow inside dolomite rock visualization (Pak et al., 2013),

- a shale rock imbibitions at nano-scale (Akbarabadi & Piri, 2014). They showed brine immobilizes oil phase in larger pores but does not penetrate in smaller, therefore smaller pores of shale remain oil-wet.

The industrial position and the advent of the digital rock physics science was mainly motivated by recent technological breakthroughs:

- High Performance Computer to access large-scale calculations or to work on very large samples sizes;
- Computing methods to work on always larger datasets from image reconstruction up to physical simulation;
  - 3D imaging set-ups mainly thanks to X-ray CT scan and FIB-SEM developed techniques.

The main consequence was a progressive interest of the industry for such techniques which now allows representing in-situ mechanisms in reservoir rocks of industrial interest. These recent evolutions lead to the emergence of digital rock physics as a real potential source of valuable petrophysical predictabilities such as porosity, absolute permeability (Adler, Jacquin, & Quiblier, 1990) capillary pressure, relative permeability, electric resistivity (Øren & Bakke, 2003) or elastic modulus (Blunt, Jackson, Piri, & Valvatne, 2002; Boek & Venturoli, 2010; Keehm, Mukerji, & Nur, 2001; Knackstedt et al., 2009; Shabro, Arns, Bryant, Torres-verdin, & Knackstedt, 2010).

The Digital Rock Physics workflow associated to a micro-CT consists of four steps: image acquisition and reconstruction (i), image treatment (ii), segmentation (iii) and calculation in images (iv). In this chapter we have focused primarily our attention on the three first steps to understand better the impact of the micro CT imaging acquisition and the consequence on the final uncertainty to estimate the Digital Rock Physics performances. This chapter has the aim to review X-ray microtomography principles and estimate the confidence level we may have in reconstructed images and in the precision of the material distribution, and therefore in boundary conditions relevant for simulation on interfaces.

# 2.1 Image acquisition

# 2.1.1 Micro-CT principles and main biases

A laboratory microscopic tomograph is constituted in general of X-ray source, thick physical filter permitting to filter low energies, sample holder, scintillator, fiber optic plate and register plate (CCD in our case) (Figure 2.1-1). X-ray source emits a conical beam (in case of the used in this thesis tomograph SkyScan 1172) of X-ray, and before they passed through the sample they are filtered by thick physical filter which might be constituted of different metals by most commonly Aluminum and Copper are used. Once X-ray passed through the sample they arrived to a scintillator when they are converted to visible light photons, which passing by Fiber Optic Plate for canalization are recovered by a detector.

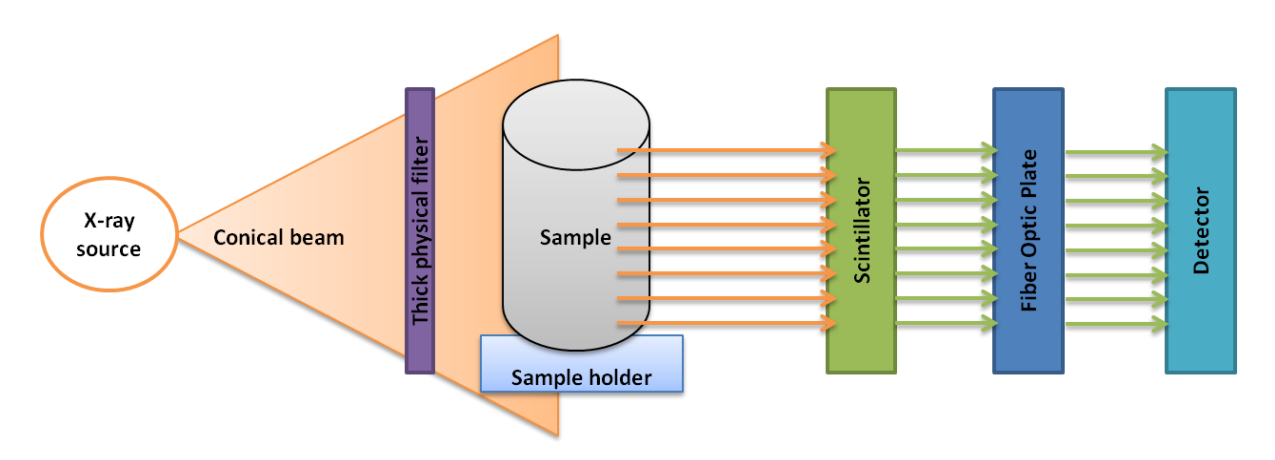


Figure 2.1-1 Global schema of an X-ray tomography

In this chapter we will look on main components constituting a lab tomograph and their work principles at details.

# 2.1.1.1 X-Ray emitter

X-ray emitting sources in laboratory are similar to electron generators. Made from a vacuum tube, an inner cathode emits electron beams into the vacuum towards a collector anode. A high power voltage generator accelerates electrons between the cathode and the anode. Electrons from the cathode collide with the anode material and usually accelerate other electrons, or ionized particles within the anode material. One part of the generated energy is emitted/radiated usually perpendicular to the path of the electron beam, as X-rays. The rest of the energy is released as heat. The emitted X-ray spectrum depends on the atomic properties of the anode and the accelerating voltage.

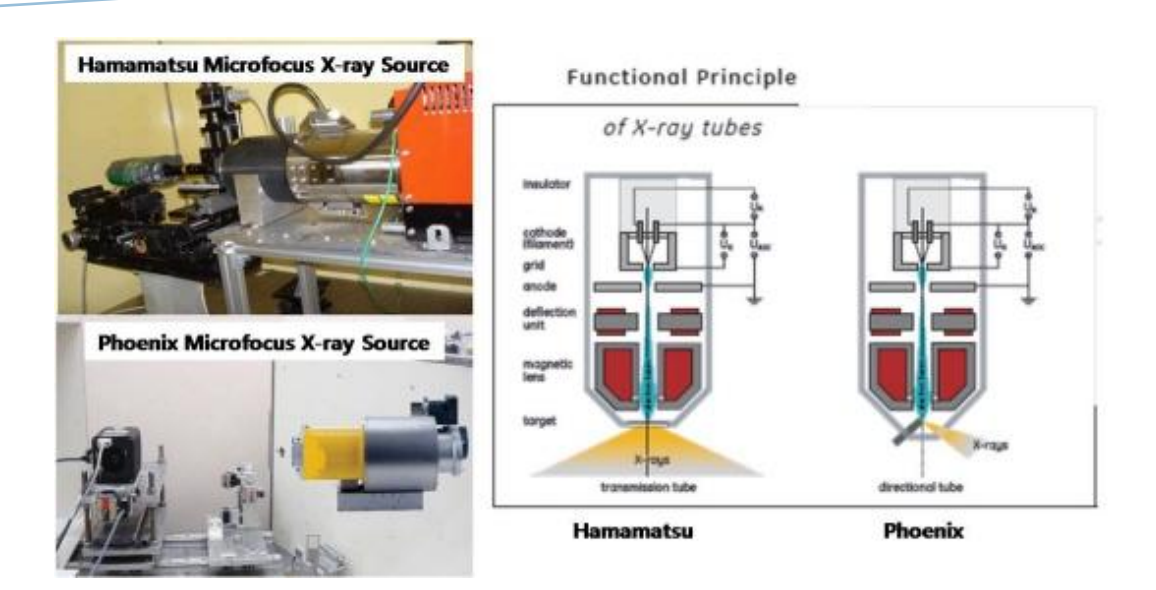


Figure 2.1-2 Two main X-ray microfocus technologies: Hamamatsu and Phoenix system

From a metallic heated filament electrons are less cohesive with the cathode and may be expulsed and accelerated when a high voltage is applied towards the anode. Through the anode the electron beam is focused by a magnetic lens to a small spot on the target. Considering the focal spot size it may be necessary to specify than whatever the setup, the electromagnetic system can focus the electrons to a zero diameter. However once inside the material (tungsten for example) the electrons spread out, and this volume of electrons determines the general diameter of the focal spot size. The only parameter to enhance this property is to limit the thickness of the tungsten or aluminum deposit but thermal heating is so high the damages caused are destructive for targets. This geometrical parameter is determining for most of actual micro—CTs based on geometrical magnification.

Around 1% of the energy appears as X-rays; the remainder becomes mostly heat. For this reason the tungsten is mostly used but it may possible to use durable material in high temperature such copper, molybdenum.

The target is usually made of a thin tungsten layer deposited on a beryllium or aluminum plate which also is the exit window for the X-radiation (transmission tube) or a massive tungsten cylinder (directional tube). To the atomic scale, the electrons are decelerated by electrostatic forces due to charged particles. Loss in kinetic energy modifies kinetics energy level of electrons and produces photons. This loss in kinetic energy translates into radiation energy is called Bremsstrahlung effect from the German: Bremsung – deceleration and Strahlung – radiation (Figure 2.1-3).

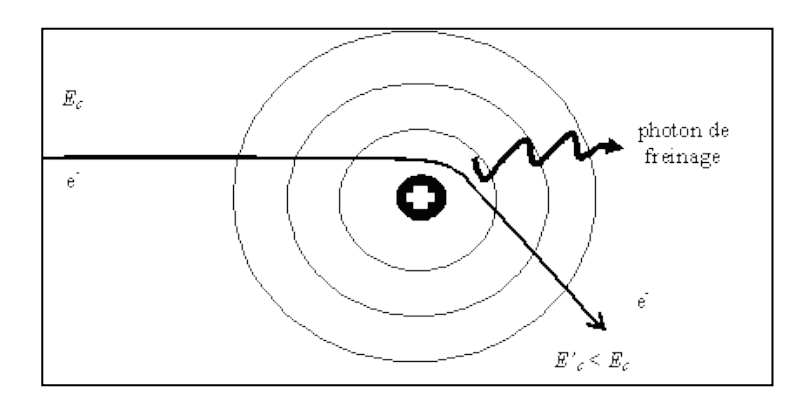


Figure 2.1-3 Bremsstrahlung effect

A second emitted radiation type occurs from the electron beam or X-ray interactions with the inner shell atomic layers due to electronic transitions. These electronic transitions are characteristic from fluorescent peaks of a material. When materials are exposed to short-wavelength X-rays or to gamma rays, ionization of their component atoms may take place. Ionization consists of the ejection of one or more electrons from the atom, and may occur if the atom is exposed to radiation with energy greater than its ionization potential. X-rays and gamma rays can be energetically enough to expel tightly held electrons from the inner orbitals of the atom. The removal of an electron in this way renders the electronic structure of the atom unstable, and electrons in higher orbitals "fall" into the lower orbital to fill the hole left behind. In falling, energy is released in the form of a photon, the energy of which is equal to the energy difference of the two orbitals involved. Thus, the material emits radiation, which has energy characteristic of the atoms present. The term fluorescence is applied to phenomena in which the absorption of radiation of a specific energy results in the re-emission of radiation of a different energy (generally lower). The whole distance between the nucleus and accelerated electrons are possible therefore energy transfer between collided and collider particles may be quite different. Thereby, the emitted energy radiations are numerous and for one applied voltage the whole X-ray wavelengths are produced from zero to a maximum energy determined by the highest energetic transfer between collider electron and emitted X photon (highest energy corresponding to shortest wavelengths). This mechanism leads to the continuity of spectra in the whole range of energy up to the maximum energy. Considering the voltage applied is U and the whole kinetic energy of the incident electron is transferred to the photon.

$$\lambda_{min}(nm) = \frac{hc}{eU}$$

h: Planck constant; c: light speed; e: electron charge; U: applied voltage

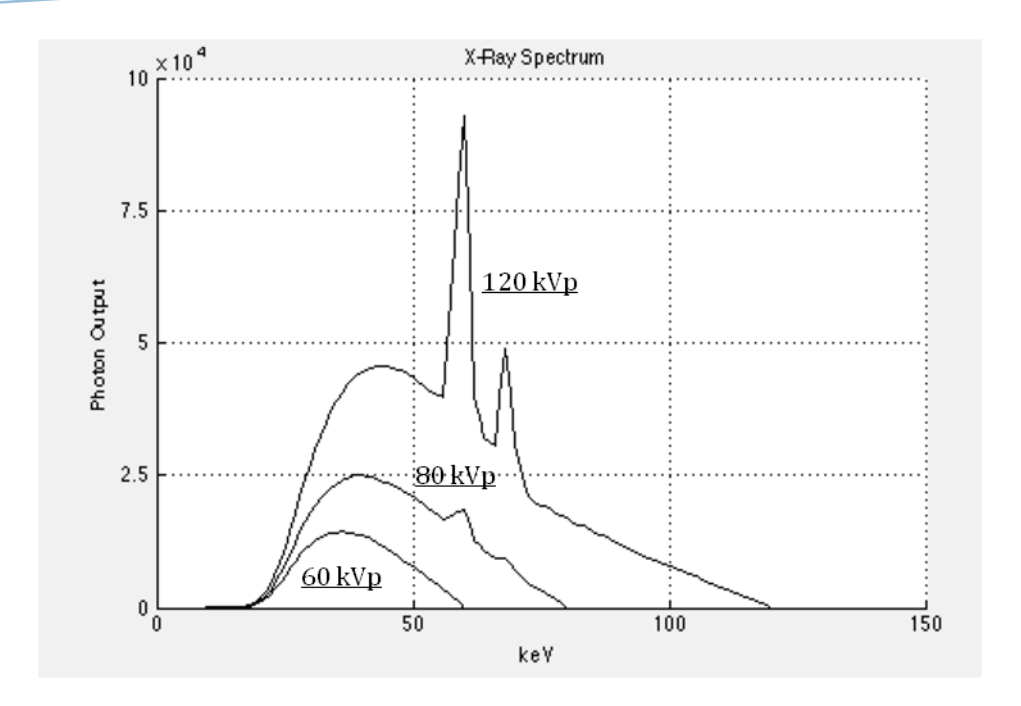


Figure 2.1-4 Impact of the applied voltage on the X-ray emitted spectrum tungsten (intern modeling).

The overlap of X-ray emission types is shown in figure 2.1-4; X-ray fluorescence represented by the very visible peaks especially for 120 kVp is shown on figure 3. This second mechanism occurs to the collision of an incident electron collides the electron form layer. Considering collider is sufficiently energetic to reach the ionization energy level of an electron layer the collided is expulsed from the atomic structure. The missing electron causes instability of the atom and electron coming from another layer will replace it emitting radiation.

Considering an electron is sufficiently energetic to reach the first electron layer (called K-layer) the second layer will compensate (L-layer).

Emitted radiation is perfectly defined by quantum physics:

$$h\nu_{K_\alpha}=E_L{-}E_k$$

Considering the electron is substituted from the third layer (M-layer):

$$h\nu_{K_{\beta}} = E_M - E_k$$

K is the layer of the missing electron and indexes  $\alpha$ ,  $\beta$  are the provenances of the electron.

The consequence is emitted radiations are very singular from the target material. This mechanism called X-ray fluorescent is also used to analyze the material thanks to these characteristic rays (Figure 2.1-5).

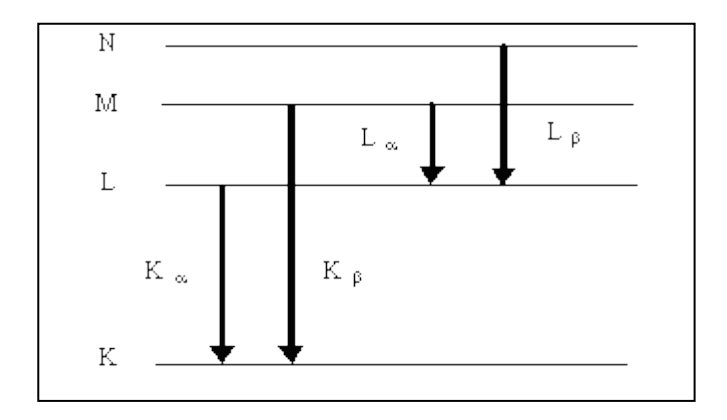


Figure 2.1-5 Electronic transitions, X-ray fluorescence principle

Fluorescence intensity is much higher than bremsstrahlung and contributes to add to the continuous spectrum discrete peaks. The polychromaticity of lab sources is at the origin of very singular spectra shapes when applied voltage is tuned. The consequence is the applied voltage choice may not be selected only to the sample size and density regards. This parameter must be optimized especially to increase the gray level dynamics especially when contrast is required for fluids with similar densities.

# 2.1.1.2 X-Ray microtomography

## 2.1.1.2.1 Principles

As is was noted previously, the microtomographs are made of X-Ray sources, a micropositioning multi axis stage and the optical system to record the radiographies. The main differences concerning the imager system are linked to the detector technology (CCD and Flat panel technology) and magnification: geometrical or optical system.

The geometrical magnification uses the relative position of source-object-detector. The cone beam effect permits to project a magnified radiograph onto the screen (Figure 2.1-6). The magnified image is reconstructed.

$$r_{\rm S} = S\left(\frac{b}{a}\right)$$

**S** is the spot size of the X-Ray spot, **a** the source to object distance and **b** is the object to detector distance. The resolution in the object plane may be calculated by dividing by the geometric magnification **M**, given by

$$M = \frac{a+b}{a}$$

The blurring caused by the size of the X-ray source is commonly referred to as geometric unsharpness or penumbra.

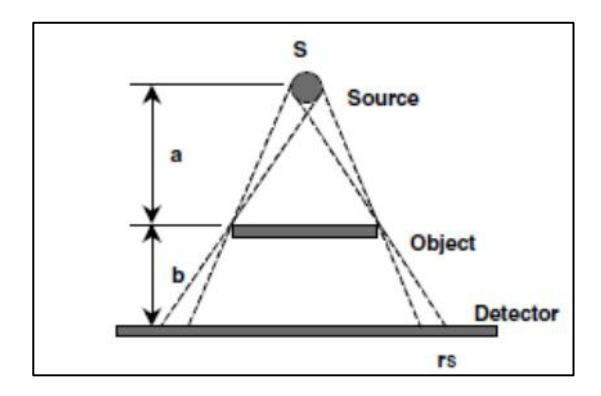


Figure 2.1-6 Geometrical magnification system

The effective resolution is linked to the two resolutions due to non-punctual X-Ray source and resolution of the detector  $r_D$ .

The relationship permitting to calculate the effective resolution is given by :

$$r_{eff} = \frac{\sqrt{r_D^2 + r_S^2}}{M}$$

The more limiting parameter in the magnification is mainly supported by the X-ray spot size.

In this work we used a Skyscan 1172 with an X-ray spot size of 5 micrometers and a resolution of the detector of 13 micrometers. The effective resolution you may reach as a function of the object size is described in the graph below.

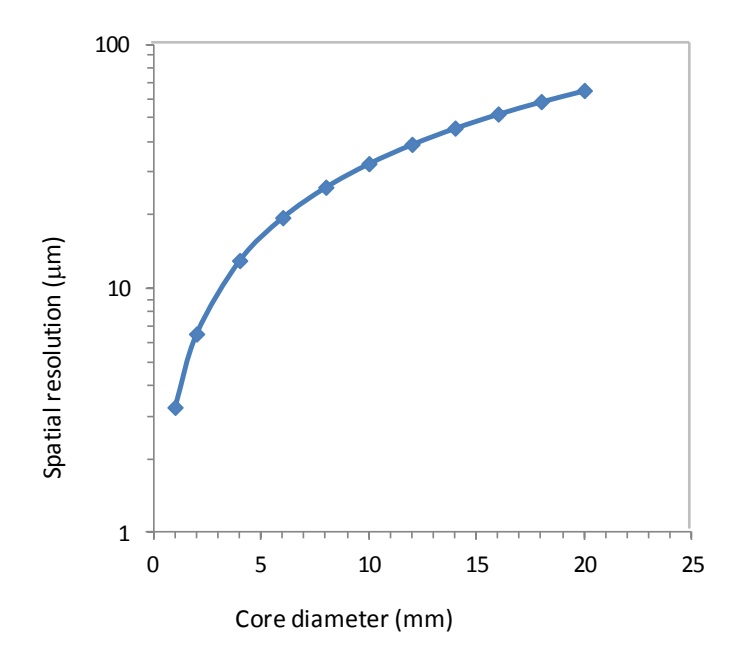


Figure 2.1-7 The effective resolution for Skyscan 1172

This curve shows the best resolution which is reasonable to reach.

We have used another tomograph based on optical magnification, this tomograph is the Versa 500 XRM manufactured by XRadia (Zeiss). This machine is based on an optical microscope (Figure 2.1-8) installed just behind the scintillator, which convert X-rays to visible lights. Therefore, the optical microscope magnify the converted visible light and he main limit here is due to Rayleigh's diffraction criterion limiting the reachable detail d to

$$d = \frac{1.22\lambda}{N.A.}$$

Where,  $\lambda$  is the wavelength of the reemitted light by scintillator and N.A. the numerical aperture. It permits to reasonably obtain the voxel size better than 700nm.

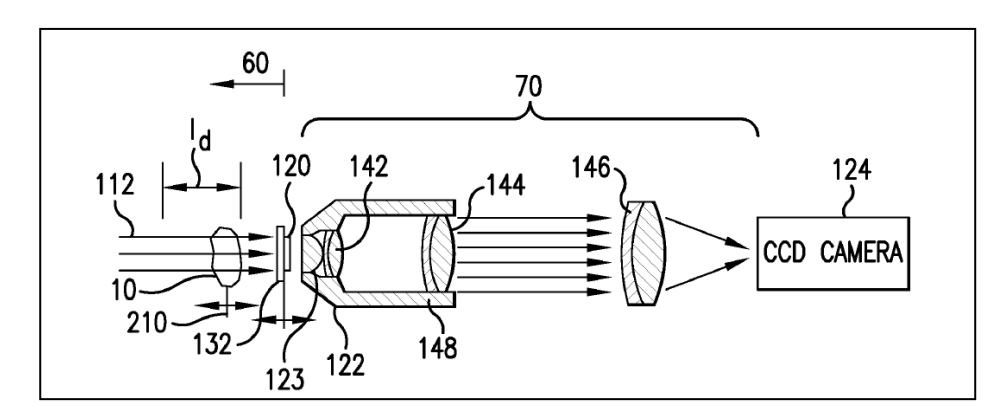


Figure 2.1-8 Schematic representation of XRadia Versa 500 mechanism (From US 7130375 B1 patent)

## 2.1.2 Image generation

Intrinsic properties of the optical system (optics or detector) may generate severe artifacts. The imaging process to be efficient requires studying carefully the detector system principle and performances. In this part we review briefly the common detectors used for micro-CT image registration.

# 2.1.2.1 Fiber Optic System

The Fiber Optic Plate (FOP) is an optical device consisting of millions of glass fibers of 6 micrometers in diameter, bundled parallel to one another. The X-rays get absorbed in the scintillator, for emitting visible light. These light photons are guided through an optical coupling, such as fiber optic, to the photocathode of an image intensifier. The role of this intensifier is to amplify the light coming from the initial phosphor. Special resins optimize optical coupling. Resolution is also enhanced due to the limited angle of visible photon transfer (Rayleigh criterion).

The photocathode converts the light photons into electrons, which are multiplied by passing through multiple stages of a photomultiplier tube. These electrons are then converted into light photons by another layer of phosphor or scintillator. These light photons are made to pass through a fiber optic guide before entering into the CCD (or CMOS) depletion region to produce electron-hole pairs. Such a multistage process ensures that the X-rays do not reach the sensitive CCD (or CMOS) sensors, prolonging the life of the detector. Also such a device can be used for a broad range of X-ray energies as compared to the

direct imaging systems, which become essentially insensitive, even at moderate energies. These Optical Fiber set-ups are used in the SkyScan 1172 and for Versa 500 limited to the (0.4x) objective.

# 2.1.2.2 Charges-Coupled Device (CCD)

In petrophysics the aim is to observe the inner morphology of the porous media and fluid configurations in the pores. The resolutions and volume of interests may be covered by CCD detectors which are the most used. Volume of interest may be long but diameter size of cores may from the specifications require vary from a few millimeters up to 10 cm diameter.

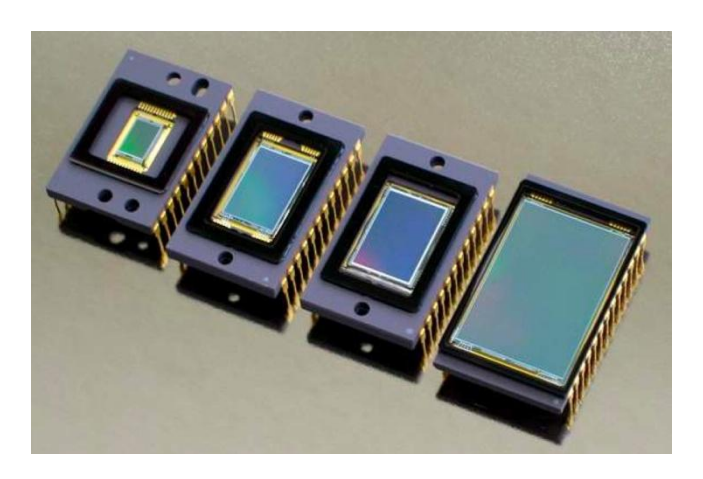


Figure 2.1-9 CCD Kodak (768x512 to 3072x2048)

Detectors used in most of low energy systems (<160keV) whatever for industrial or synchrotronic X-ray tomography are Charge Coupled Device systems. These detectors are declined in a very high number of subsystems: Interline CCD, front illuminated CCD, back illuminated CCD, EM-CCD ...

The principle of CCD detector might be described as below: each photosensitive element (pixel) works like storage of electrons. Electrons appear in pixels due to their elimination by the light source. For a given time period each photosensitive element is filled by electrons proportionally to its illumination. After each time step electric charges accumulated by pixels are transferred to "output" and measured.

CCD photosensitive area varies from a few millimeters to centimeters square. For X-ray visualization CCD are very specific to minimize the damages caused by X-ray photons. The damages are coming from:

- Increasing dark charge with accumulated X-ray exposure;
- Oxides become charged causing a shift in the ideal operating biases (voltage shift);
- CTE (Clocking Transfer Efficiency) degradation for large signals;
- The formation of traps.

# 2.1.2.2.1 SkyScan detector system

Skyscan 1172 is equipped with a camera mounted with a head which includes a scintillator and a Fiber Optic System (FOS). The FOS is used as a magnifying glass. The implant specs on the scintillator and at the outlet to illuminate the CCD (or CMOS) fits the image made by the scintillator to an optimization of the beam projection onto the CCD detector. FOS permits to increase the field of view or magnifies the projected image. CCD detector is protected against X-ray but produces a strong readout noise: 20 electrons per second.

The real resolution is 4000X2000 in interlace mode but also may work in binning mode in 2000X1000 or 1000 X 1000. Properties of such detector are given in the table below.

Imaging device Interlace readout interline CCD Effective number of pixels (H X V) 4000 X 2624 Interlace readout: 1.7 Hz Frame rate Outline readout: 8.9 Hz 2X2 binning read out: 3.4 Hz Readout noise (RMS) 20 electrons A/D converter 12 bit Cooling method Natural air cooling / Peltier Amp gain conversion factor 3.2 electrons /AD counts (13300 electrons)

Table 2.1-1 Digital CCD camera of Skyscan 1172: Hamamatsu C4742-55-12 HRF

# 2.1.2.2.2 CCD artifacts linked to radiaographies acquisition

All detectors are sensitive to pixel dropouts or pixel defects caused by nonlinear or defective elements. Numerical methods of pixel-averaging are used to effectively reduce these artifacts if the locations of the defects are identified in a pre-processing method and of course considering the defects are within a limited range.

Spatial artifacts may also be observed in CCD or flat panel detectors that are comprised of multiple tiled sensitive areas. Methods have been devised to eliminate these artifacts: pixel averaging, and gain and offset corrections, the artifacts may still appear under at high exposures. Because detector spatial artifacts are highly dependent on the technology, the assessment method is quite difficult to simulate. It

is usually considered as an intrinsic property of the detection system requiring to be experimentally tested. This artifact impacts the segmentation process and reduced the gray level contrast between the materials therefore the dynamic range of the detector but also the image matching which might be useful to compare two states of references.

# 2.1.2.2.1 Temporal artifacts

Some digital radiographic detectors exhibit lag artifacts in the form of residual signals from previous acquisitions that appear in subsequent images. Lag artifacts might be due to incomplete erasure of the image detector (in the case of computed radiography) or residual memory effects in amorphous silicon or the capture element (in the case of flat-panel detectors and CCD- or CMOS-based detectors). In the flat-panel and the CCD- or CMOS-based detectors, the residual signal fades with a finite time constant. The amount of residual signal at a given time depends on the time lapse from the prior exposure. Thus, in applications in which image acquisition is rapid (e.g., fluoroscopy or multiple-view acquisitions), strategies have been devised to reduce the effect. Two common strategies are subtracting a fraction of the prior image from the subsequent image or performing an offset correction between two image acquisitions (if there is sufficient time between the two acquisitions). The magnitude of lag artifact and the effectiveness of its reduction methods can be characterized by measuring the time constant of the fading of the signal after acquisition of a high-exposure image of a high-contrast object.

### 2.1.2.2.2 Temporal stability

Even though a detector may behave perfectly at the time of testing, its performance may vary over time due to scintillator normal deteriorations due to susceptibility to environmental conditions mainly the temperature or humidity. The thermoregulation of a micro CT system is decisive whatever for lifetime of detector electronic components. Thus, there is a vital point to ensure that the performance of a detector is stable over time.

Many detector manufacturers offer quality control tools with their products that may be used for this purpose. To establish benchmark performance levels for tracking over time the only experimental tests are appropriate.

A very performing system in the theoretical specifications may be completely inefficient due to the instabilities in emitted X-ray beam or in its recording process.

### 2.1.2.2.3 Dynamic range

The gain of a CCD is determined by the output electronics signal and determines how the amount of charge collected in each pixel will be assigned to a digital number in the output image. Gain values are usually given in terms of the number of electrons needed to produce one Analog-Digital Units step within the Analogic Digital converter.

Electrons by Analogic to Digital Unit (e-/ADU) common gain values range from one to tens or more in link with the detector technology.

The CCD technology is very linear in its response over a large range of data values. The linear accuracy means a simple linear relation between the input value (charge stored in the pixel semiconductor) and the digital output value. It considerably facilitates material identification due to the ability to associate a specific X-ray attenuation to a physical density.

The largest output number that a CCD can produce is set by the number of bits in the A/D converter. For example a 16-bit Analogic/Digital converter would be able to handle numbers as large as 65 535 ADU. A large dynamic must be coupled to a very specific scintillator to optimize imaging.

### 2.1.2.2.2.4 Scintillator

The detector must be optimized in X-ray to be efficient with the scintillator properties. The Quantum Efficiency and scintillation wavelength in the coupling with the re-emitted lights require being compatible with the CCD. Thick scintillating materials are X-ray absorbing therefore the depth of the X-ray photons conversion in visible light is a function of the X-ray energy. Large polychromatic spectra require a very strong filtering to avoid a multilayer scintillation, which might induce a kind of "blurring" on the images.

## 2.1.2.3 Noise and Signal-to-Noise ratio

The term signal-to-noise ratio, as the name suggests, is the ratio of the signal to the total noise. It plays a very important role in determining the usefulness of a particular detection system for a certain application. It should however be noted that it is not always necessary to maximize this ratio. For example in systems where resolution is not of much concern, other factors, such sampling frequency, may be more relevant than S/N.

To characterize a CCD detector and subsequently identify and correct artifacts, one needs to determine the contributions of all noise components, the effective gain, conversion factor, linearity of response, modulation transfer function (MTF) and detective quantum efficiency (DQE). Temporal noise randomly changes from frame to frame. It includes stochastic contributions such as dark-current noise, readout noise, photon noise, beam flicker, burst noise and shutter noise. There is also a source of fixed-pattern noise, especially in fiber-optic coupled digital cameras. This spatial noise does not vary from frame to frame and is caused by spatial variation in the thickness of the scintillator, fiber-optic coupling, CCD bias pattern and other artifacts that produce variations in the pixel-to-pixel sensitivity and/or distortions in the optical path to the CCD or in the CCD chip itself. Almost, source aging and anisotropy of X-rays naturally inherent to the lab sources require a flat-field correction to suppress fixed-pattern noise and to homogenize X-ray flux but also compensate failing pixels of the detector. A fiber-optic taper or lens system makes the conversion from raw images to corrected images more cumbersome, since the distortion of the demagnifying system needs to be accounted for.

Furthermore, it is not trivial to obtain the stable large uniform X-ray beam which is needed for collection the data. Stochastic distribution of noise may not be limited otherwise than by statistics analysis obtained from numerous image acquisitions. An averaged image is statistically generated to reduce the produced noise. It may be necessary to collect ten to twenty images per angle increasing the acquisition time of the same multiple.

The white reference images described above were also used to check the linearity of the pixel response. A linear least-squares fit of intensity versus exposure time was computed for each pixel to yield the average white image:

$$I_{white}(x,y) = I_{background}(x,y) + \Delta t_{exposure} \cdot \frac{dI_{exposure}}{dt}$$

The linearity response as a function of the exposure time was checked by computing.

The first step corrects dark current (measured in absence of X-rays) and white field (an image taken with X-rays in absence of sample). Non-uniformities in the white field due to non-uniformities in the X-ray beam, the scintillator detector response and the CCD detector response are removed by each image normalizing to the white field image. A low pass is used to remove ring artifacts (drifts or nonlinear responses of detectors) from the tomogram.

### 2.1.2.4 Acquisition sequence

Acquisition sequence consists to record a complete images data set of radiographies to feed the reconstructor of sufficient information for reconstruction.

First element is the brightness of radiography. A video mode permits to visualize and estimate the gray levels in images. The ideal conditions are with a minimum absorption between 30% and 40% and a maximum around the object of interest between 80% or 90% to stay in the linear zone of the used detector. These values are relatively dependent on reconstruction software intrinsic properties but in polychromatic light and strong diverging angle it is quite important to stay in the full linearity of the detector to permit to reconstruct slices with a sufficient gray level dynamic. The percentage is the amount of charge that can be accumulated in an individual pixel is defined by its full well capacity, and depends primarily on the pixel dimensions and detector technologies.

The example below is obtained with a carbonate plug with 8mm of diameter and an applied tension of 100 kVp an intensity of  $10\mu\text{A}$ . Frame rate is 0.7 second.

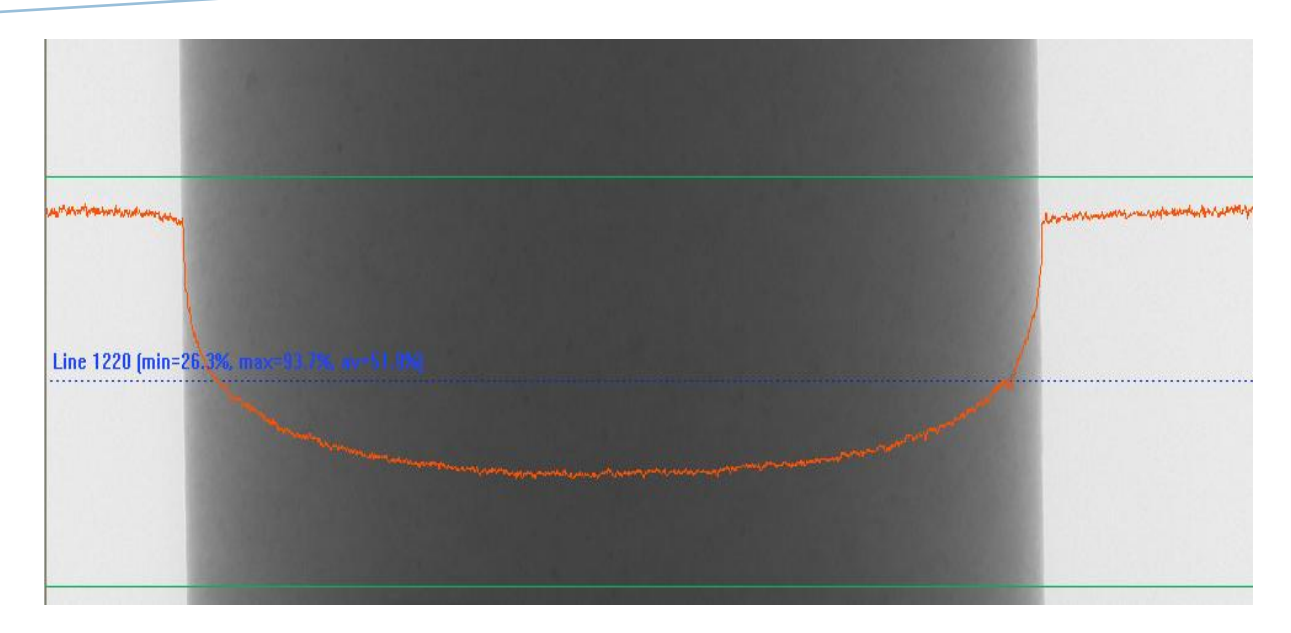


Figure 2.1-10 Radiography of a carbonate plug

In flood conditions of course the plug is more attenuating due to additional induced opacity by fluids in porosities of the rock.

There are two main solutions to work on filled sample. Considering anti-blooming set-up on the detector frame rate must be reduced to keep the same delivered number of photons per second in the whole experiments permitting to reconstruct the whole fluid conditions with the same parameters. The risk here is to work in condition of non-linearity of the detector. It means that contrast between two fluids is lower than the signal noise ratio.

The other way consists to match the frame rate to ideal tomography conditions. This way was the selected way. It permits to post-treat the data in full detector linearity zone. Therefore, during the segmentation process the attenuations coefficient may be controlled in its ratios from histogram data.

The number of radiographies is the second parameter limiting the acquisition speed. Theoretically, algorithms require an infinite number of radiographies. In practice cone beam sources require about 1800 radiographies and parallel beam geometry about 1000. The difference is linked to algorithm sensitivity in conical beam geometry to the cylindrical to Cartesian coordinates change during the reconstruction process.

The rotating step must be adjusted in link with the material scanned. Considering used in the work sandstone we applied a rotating step of 0.05° per image.

Due to random noise appearing in a few pixels for the whole radiographies the Skyscan 1172 requires to record the average of at least 3 images to regularize the aberrations due to noise.

The last required operation for acquisition is a physical filtering applying or not. It consists to install just in front of the photosensitive detector area an aluminum sheet or aluminum and copper sheets, or other materials are used to cut off the lowest energies of the spectrum to obtain a less dispersed spectrum. The

aim is to stop by absorption the low X-ray energy at the origin of the most disturbing artifact in petrophysical operations call beam hardening: changes in image gray levels caused by preferential attenuation of low-energy X-rays. Considering a cylindrical geometry low energy photons penetrate and emerge thinner part of the sample (left and right side of the cylinder) and are detected and taken into account by the detector. In the center of the cylinder the low energy X-rays are stopped and may not emerge therefore material in thicker parts attenuates the whole low X-ray energies.

Detector counts the photons in the whole pixels but it may be impossible to have information by energy level. The periphery of cylinder in reconstruction process appears overexposed in comparison of the center of object. No post treatment may correct this. The material densities are strongly impacted and the reconstructed images clearly exhibit a gradient of density in homogeneous plugs. The filtering set up requires increasing the exposure time therefore the frame rate.

2.1.2.5 X-Ray adsorption and tomography reconstruction principles

2.1.2.5.1 Beer Lambert's law

X-ray attenuation for a monochromatic X-ray beam through a homogeneous material is: given by Beer - Lambert's law:

$$I = I_0 exp(-\mu x)$$

Where  $I_0$  and I are the initial and final X-ray intensity,  $\mu$  is the material's linear attenuation coefficient (unit's 1/length) and x is the length of the X-ray path. If there are multiple materials, the equation becomes:

$$I = I_0 exp \left[ \sum_i (-\mu_i x_i) \right]$$

Index i is a material characterized by an attenuation coefficient  $\mu_i$  with linear extent  $x_i$ . This is true for well-calibrated systems using a monochromatic X-ray. X-ray sources used in lab are polychromatic therefore, to take into account the fact that the attenuation coefficient is a strong function of X-ray energy, the complete equation of the X-ray energy (E) spectrum is:

$$I = \int I_0(E) \exp \left[ \sum_i (-\mu_i(E)x_i) \right] dE$$

However, such calculation is not rigorous, moreover, reconstruction algorithms solve for uniqueness  $\mu$  value at each elementary pixel (called voxel) corresponding to the exact spatial position.  $\mu$  is an effective linear attenuation coefficient, unlike an absolute for synchrotrons. This complicates absolute calibration, as effective attenuation is a function of both the X-ray spectrum and the properties of the scan object.

# 2.1.2.5.2 Filtered Back Projection reconstruction

The radiographs (projections of the object on the detector) may be considered for parallel beam tomography corresponding to the Radon transform of the scanned object. The coordinate system is represented below by a two function f(x,y) to describe line integrals and projections. In the example below the object is represented by a two dimensional function f(x,y) and each line integral by the  $(u, \Theta)$  coordinates.

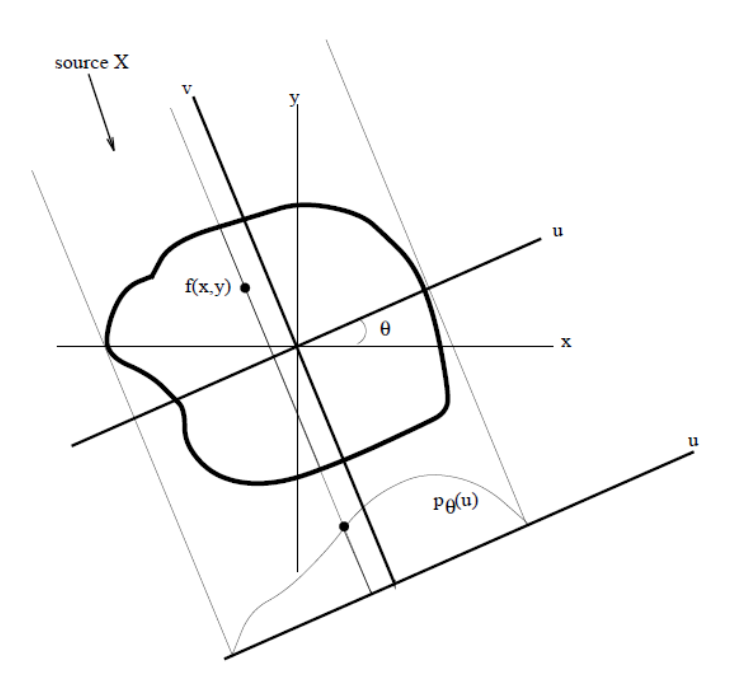


Figure 2.1-11 Example of X-ray projection construction

The function  $P_{\Theta}(u)$  is defined by the lines integrals depending on f(x,y).

$$R[f](u,\theta) = p_{\theta}(u)$$

$$R[f](u,\theta) = \int_{D_{\theta}} f(u \cos\theta - v \sin\theta, u \sin\theta + v \cos\theta) dv$$

A slice image and its Radon transform are shown below:

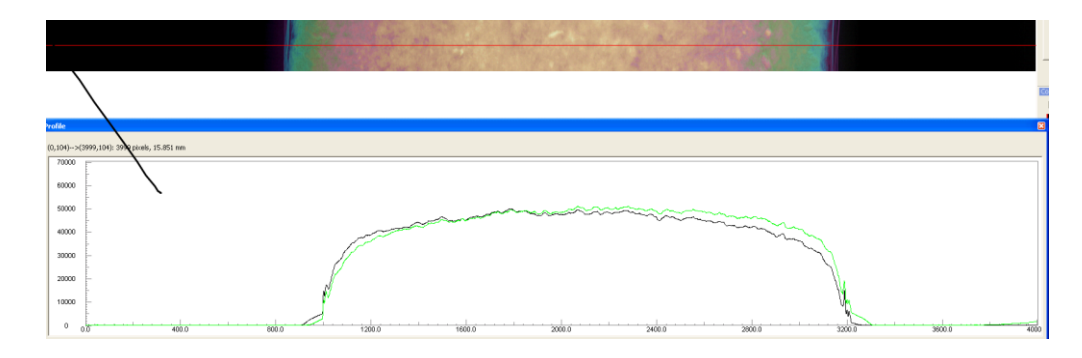


Figure 2.1-12 A slice image and its Radon transform

The function  $P_{\Theta}$  is known as the Radon transform of the function f(x,y) and it corresponds to the direct problem (from an object to the projected images). The function is often referred as a sinogram because the Radon transform of an off-centered point source is a sinusoid.

$$P_{\theta}(u) = P_{\theta+\pi}(-u)$$

A projection is formed by combining a set of line integrals for a constant  $\theta$ . Here the simplest projection, a collection of parallel ray integrals i.e. constant  $\theta$ , is shown.

The Fourier theorem considers the one dimensional Fourier transform of a parallel projection is equal to a slice of the two dimensional transform of the original object.

The object should be estimated by performing a two dimensional inverse Fourier transform. Inverse Fourier Transform permits to calculate f(x,y) in a continuous function type.

This method is not commonly used due to the polar grid coordinates required for Fourier Space interpolation. The discretization in the spatial domain has the consequent to cause inexistency of f in several parts of the space.

In a practical way this methodology is not used and only the Fourier theorem, also called projection theorem, is applied. From the Fourier transform (1D) of a projected angle  $\Theta$  to the point U we determine the 2D Fourier transform of the function f(x,y)

$$TF[f] = F(u, v) = \int_{-\infty}^{+\infty} \int_{-\infty}^{+\infty} f(x, y) e^{-j2\pi(ux + vy)} dx dy$$
$$TF[p_{\theta}] = S_{\theta}(w) = \int_{-\infty}^{+\infty} P_{\theta}(t) e^{-2\pi wt} dt$$
$$F(u, v) = S_{\theta}(w)$$

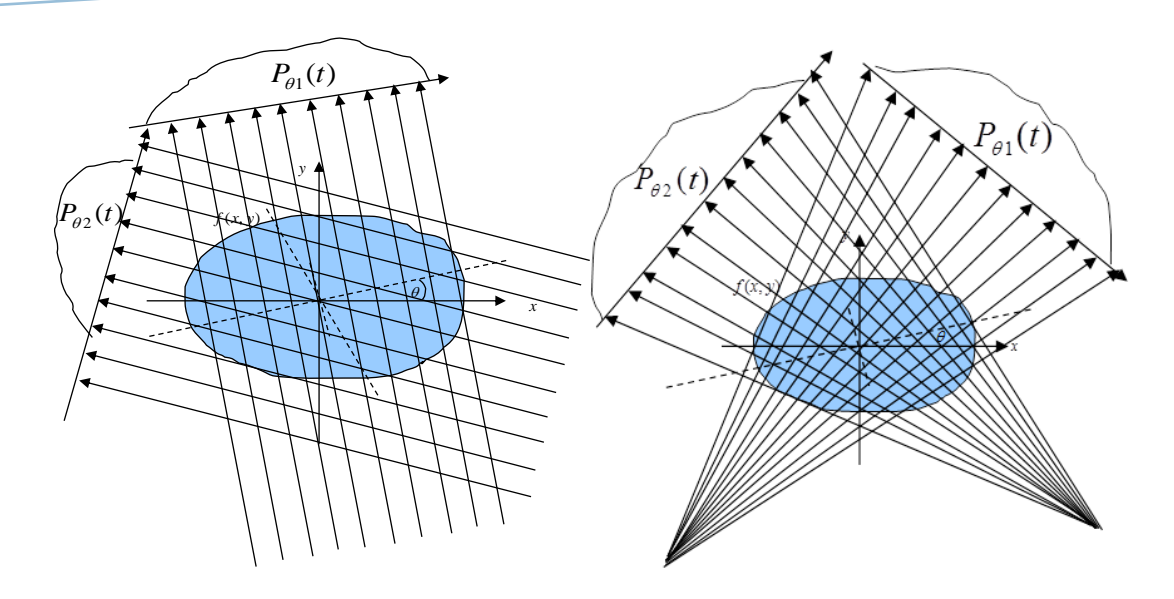


Figure 2.1-13 Schematic parallel and cone beam projections

The most used algorithm for this inverse problem consists to determine from the integral lines the object image.

Several mathematical methods may be used to reconstruct the images whatever for parallel or conical beams. The back projection algorithm is the main method used for reconstruction.

For parallel beam projection, it may necessary to express the rectangular coordinate in the frequency domain (u,v), for a polar coordinate system  $(w, \Theta)$ , by making the substitutions

$$u = w \cos \theta$$

$$v = w \sin \theta$$

And then changing the differentials by using

$$du dv = w dw d\theta$$

For a polar function

$$f(x,y) = \int_0^{2\pi} \int_0^{\infty} F(w,\theta) e^{j2\pi w (x\cos\theta + y\sin\theta)} w dw d\theta$$

$$F(w, \theta + 180^{\circ}) = F(-w, \theta)$$

Considering  $t = x \cos \theta + y \sin \theta$ 

Substituting the  $S_{\Theta}(t)$  Fourier Transform at angle  $\Theta$  for the 2D Fourier Transform  $F(w, \Theta)$ 

$$f(x,y) = \int_0^{2\pi} \left[ \int_0^\infty S_{\theta}(w) |w| e^{j2\pi w t} dw \right] d\theta$$

$$f(x,y) = \int_0^{\pi} Q_{\theta}(x\cos\theta + y\sin\theta) \ d\theta$$

With 
$$Q_{\theta}(t) = \int_{-\infty}^{\infty} S_{\theta}(w) |w| e^{j2\pi w t} dw$$

The backprojection image is a blurred version of the original image (Figure 2.1-14).

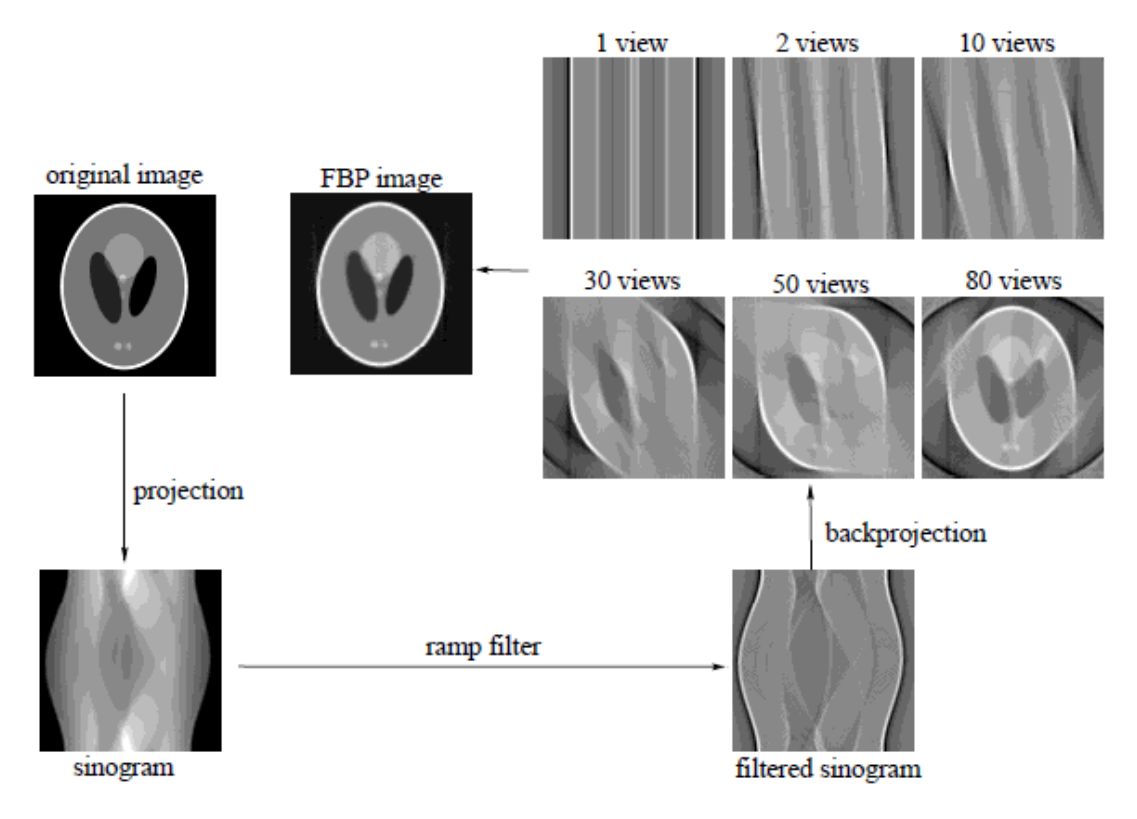


Figure 2.1-14 Schema of FBP image construction principle

During the reconstruction there are several artifacts that might appear. The dishing artifact linked to the reconstruction seems quite similar to physical artifact called beam hardening and causes a radial gradient of attenuation. The DC shifts are more linked to instabilities to the sudden changes of attenuations especially to the surrounding of the scanned object. The dishing and DC shifts artifacts caused by interperiod interference may be reduced using the zero padding interpolation to the Discrete Fourier Transform.

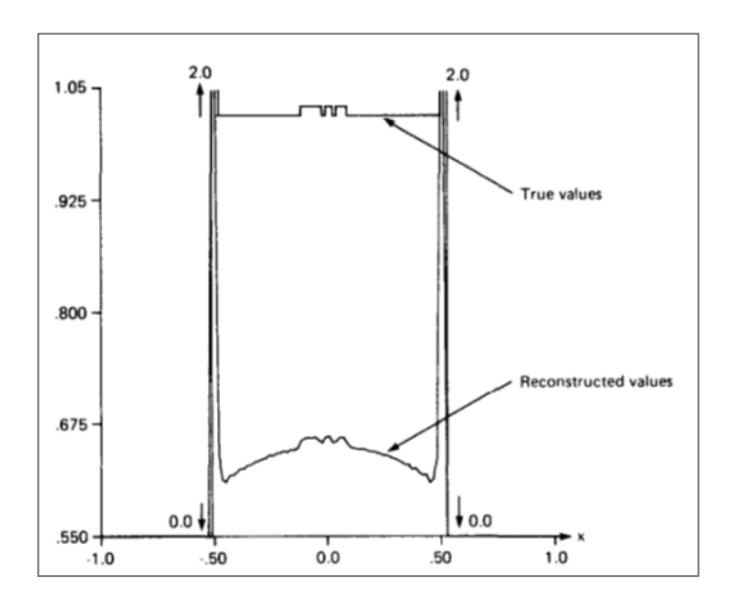


Figure 2.1-15 The dishing artifact impact

To reduce more the DC shift it is necessary to add a ramp filter. From the projection data transform  $S_{\theta}(w)$  it permits to determine the f(x,y) function. Numerical results exhibit with this algorithm a blurred version of the original image. The filtered back projection proposes applies a ramp filter which is mathematically integrated with a convolution product

With 
$$Q_{\theta}(t) = \int_{-\infty}^{\infty} S_{\theta}(w) H(w) e^{j2\pi w t} dw$$
 
$$H(w) = |w| b_{w}(w)$$
 
$$b_{w}(w) = \begin{cases} 1 & |w| < W \\ 0 & \end{cases}$$

The ramp filters efficiency and discretization is key points of the reconstruction process. A blurring or noisy imaging may clearly be obtained. For usual nondestructive control the impact is limited due to a clear frontier between material and air. For our application we work to the limit of resolution and use the gradients to identify the mineral morphology and fluids configurations at the pore scale therefore this step is very critical.

Cone beam geometry reconstruction requires fitting the parameters to the new geometry (angles of projections, distances...).

These algorithms called Feldkamp algorithms are based upon a similar formulation to 2D Filtered Back Projected algorithms. The detectors in micro-tomography are planar contrarily to the medical CT scan or several industrial nondestructive tomographs. Almost the photodetectors are arranged with equal detector spacing. The geometric parameters corresponding to an equally spaced collinear detector with a cone beam source must be introduced in the algorithms.

These algorithms convolve each projection weighted by the geometrical parameter to a filter to generate the corresponding filtered projection and a smoothing filter such a "Hamming Window". The "Hamming

window" is optimized to minimize the maximum (nearest) side lobe it is a very classical filter of signal treatment using Fourier Transform.

### 2.1.3 Conclusions

Image acquisition techniques and principles are reviewed in this part. We focus the reader attention on the importance of image acquisition and generation comprehension. It is reported often the importance and complexity of image treatment after its acquisition; we would like to note that the best image obtaining facilitates the post-treatment task, therefore any interference in material distribution presentation.

From the micro-CT invention the progress permits to obtain always more perfect images and to minimize induced interferences. Despite such progress the reconstruction is a discretization of continuum function which is the object of interest, thereby, image post-processing stays useful to separate the material of interest from noises on image.

### 2.1.4 References

- Adler, P. M., Jacquin, C. G., & Quiblier, J. A. (1990). Flow in simulated porous media. *International Journal of Multiphase Flow*, *16*(4), 691–712. doi:10.1016/0301-9322(90)90025-E
- Agbogun, H., Giurea-Bica, G., Ndatuwong, L., Glover, K., Nassichuk, B., & Henderson, G. (2014). THREE DIMENSIONAL CHARACTERIZATION OF MATRIX ACIDIZING BY X-RAY COMPUTED TOMOGRAPHY, 1–6.
- Akbarabadi, M., & Piri, M. (2014). Nanotomography of Spontaneous Imbibition in Shale. In *Proceedings of the 2nd Unconventional Resources Technology Conference*. Tulsa, OK, USA: American Association of Petroleum Geologists. doi:10.15530/urtec-2014-1922555
- Berg, S., Armstrong, R. T., Georgiadis, A., Ott, H., Schwing, A., Neiteler, R., ... Enzmann, F. (2014). ONSET OF OIL MOBILIZATION AND NON-WETTING PHASE CLUSTER SIZE DISTRIBUTION, 1–12.
- Berg, S., Ott, H., Klapp, S. A., Schwing, A., Neiteler, R., Brussee, N., ... Stampanoni, M. (2013). Real-time 3D imaging of Haines jumps in porous media flow. *Proceedings of the National Academy of Sciences of the United States of America*, 110(10), 3755–9. doi:10.1073/pnas.1221373110
- Blunt, M. J., Jackson, M. D., Piri, M., & Valvatne, P. H. (2002). Detailed physics, predictive capabilities and macroscopic consequences for pore-network models of multiphase flow. *Advances in Water Resources*, 25(8-12), 1069–1089. doi:10.1016/S0309-1708(02)00049-0
- Boek, E. S., & Venturoli, M. (2010). Lattice-Boltzmann studies of fluid flow in porous media with realistic rock geometries. *Computers & Mathematics with Applications*, *59*(7), 2305–2314. doi:10.1016/j.camwa.2009.08.063
- Dodd, N., Marathe, R., Middleton, J., Fogden, A., & Carnerup, A. (2014). Pore-Scale Imaging of Oil and Wettability in Native-State, Mixed-Wet Reservoir Carbonates.
- Flannery, B. P., Deckman, H. W., Roberge, W. G., & D'Amico, K. L. (1987). Three-Dimensional X-ray Microtomography. *Science (New York, N.Y.)*, 237(4821), 1439–44. doi:10.1126/science.237.4821.1439
- Fogden, A., McKay, T., Turner, M., Marathe, R., & Senden, T. (2014). Micro-CT Analysis of Pores and Organics in Unconventionals Using Novel Contrast Strategies. In *Proceedings of the 2nd Unconventional Resources Technology Conference*. Tulsa, OK, USA: American Association of Petroleum Geologists. doi:10.15530/urtec-2014-1922195
- Fogden, A., Middleton, J., Mckay, T., Latham, S., Marathe, R., Turner, M., ... Lane, F. D. (2014). 3D MAPPING OF PORE AND ORGANIC MATTER DISTRIBUTIONS IN UNCONVENTIONAL RESERVOIRS UTILIZING A DIGITAL ROCKS APPROACH, 1–12.
- Iglauer, S., Favretto, S., Spinelli, G., Schena, G., & Blunt, M. J. (2010). X-ray tomography measurements of power-law cluster size distributions for the nonwetting phase in sandstones. *Physical Review E*, 82(5), 056315. doi:10.1103/PhysRevE.82.056315

- Iglauer, S., Paluszny, A., Pentland, C. H., & Blunt, M. J. (2011). Residual CO 2 imaged with X-ray micro-tomography. *Geophysical Research Letters*, 38(21), n/a–n/a. doi:10.1029/2011GL049680
- Karpyn, Z. T., Piri, M., & Singh, G. (2010). Experimental investigation of trapped oil clusters in a water-wet bead pack using X-ray microtomography. *Water Resources Research*, 46(4), W04510. doi:10.1029/2008WR007539
- Keehm, Y., Mukerji, T., & Nur, A. (2001). Computational rock physics at the pore scale: Transport properties and diagenesis in realistic pore geometries. *The Leading Edge*, *20*(2), 180–183. doi:10.1190/1.1438904
- Knackstedt, M. A., Latham, S., Madadi, M., Sheppard, A., Varslot, T., & Arns, C. (2009). Digital rock physics: 3D imaging of core material and correlations to acoustic and flow properties. *The Leading Edge*, 28(1), 28–33. doi:10.1190/1.3064143
- Lopez, O., Mock, A., Long, H., Kalam, Z., Vahrenkamp, V., Gibrata, M., ... Vizamora, A. (2012). Validation of fundamental carbonate reservoir core properties using digital rock, 1–12.
- Mossoti, V. G., & Castanier, L. M. (1989). Water transport in limestone by X-ray CAT scanning, 226–235.
- ØREN, P.-E., & Bakke, S. (2002). Process Based Reconstruction of Sandstones and Prediction of Transport Properties. *Transport in Porous Media*, 46(2-3), 311–343. doi:10.1023/A:1015031122338
- Øren, P.-E., & Bakke, S. (2003). Reconstruction of Berea sandstone and pore-scale modelling of wettability effects. *Journal of Petroleum Science and Engineering*, *39*(3-4), 177–199. doi:10.1016/S0920-4105(03)00062-7
- Pak, T., Geiger, S., Jiang, Z., Sorbie, K. S., Elphick, S., van Dijke, M. I. J., & Butler, I. (2013). Pore-Scale Visualisation of Two-Phase Fluid Displacement Processes in a Carbonate Rock using X-ray micro-TomographyTechnique. In *SPE Reservoir Characterization and Simulation Conference and Exhibition*. Society of Petroleum Engineers. doi:10.2118/165997-MS
- Piri, M., & Blunt, M. (2005). Three-dimensional mixed-wet random pore-scale network modeling of twoand three-phase flow in porous media. I. Model description. *Physical Review E, 71*(2), 026301. doi:10.1103/PhysRevE.71.026301
- Prodanović, M., Lindquist, W. B., & Seright, R. S. (2007). 3D image-based characterization of fluid displacement in a Berea core. *Advances in Water Resources*, 30(2), 214–226. doi:10.1016/j.advwatres.2005.05.015
- Qajar, J., Francois, N., & Arns, C. H. (2013). Microtomographic Characterization of Dissolution-Induced Local Porosity Changes Including Fines Migration in Carbonate Rock. *SPE Journal*, *18*(03), 545–562. doi:10.2118/153216-PA
- Saraji, S., & Piri, M. (2014). High-Resolution Three-Dimensional Characterization of Pore Networks in Shale Reservoir Rocks. In *Proceedings of the 2nd Unconventional Resources Technology Conference*. Tulsa, OK, USA: American Association of Petroleum Geologists. doi:10.15530/urtec-2014-1870621

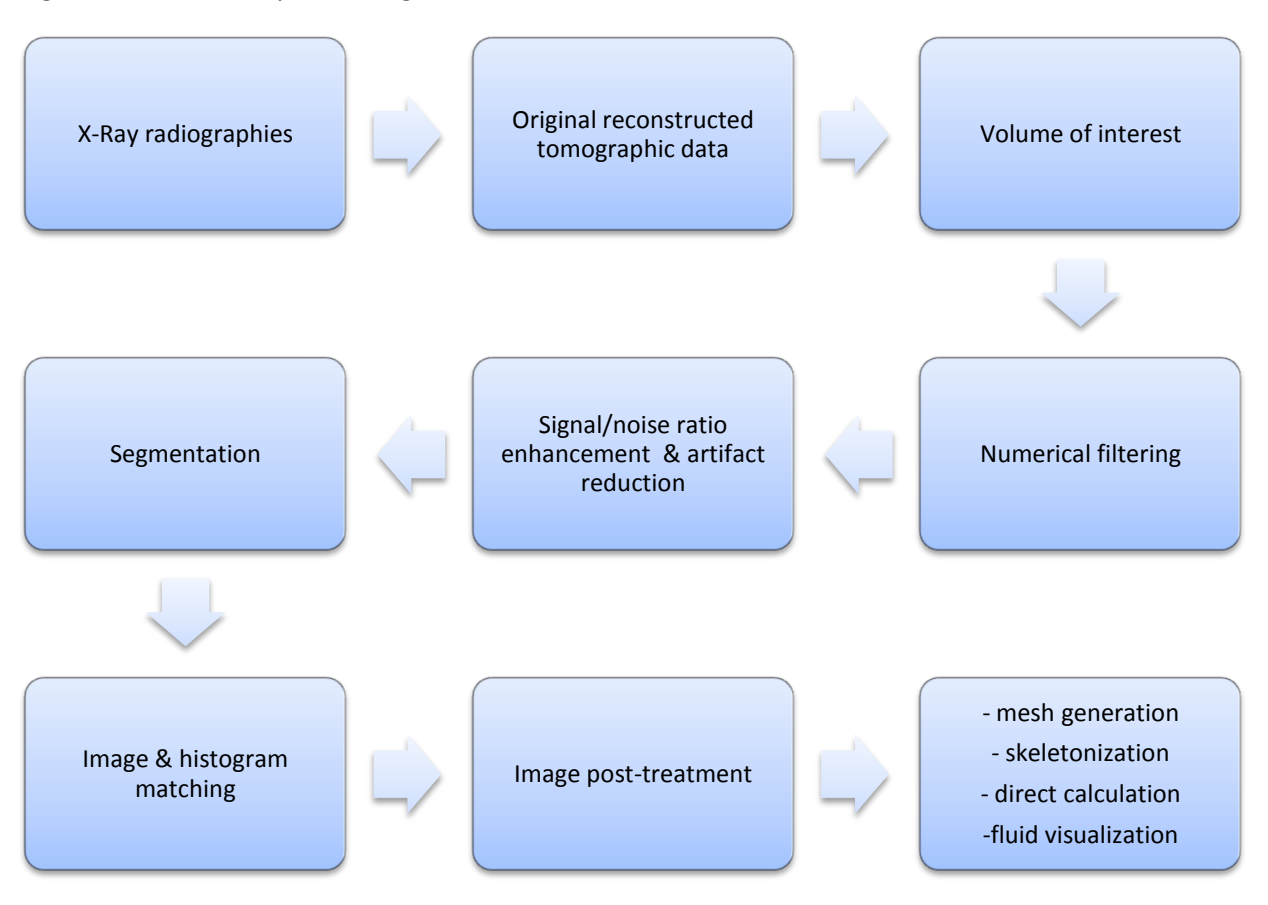
- Seright, R. S., Liang, J., Lindquist, W. B., & Dunsmuir, J. H. (2003). Use of X-ray computed microtomography to understand why gels reduce relative permeability to water more than that to oil. *Journal of Petroleum Science and Engineering*, 39(3-4), 217–230. doi:10.1016/S0920-4105(03)00064-0
- Seright, R. S., Prodanovic, M., & Lindquist, W. B. (2006). X-Ray Computed Microtomography Studies of Fluid Partitioning in Drainage and Imbibition Before and After Gel Placement: Disproportionate Permeability Reduction. *SPE Journal*, *11*(02), 159–170. doi:10.2118/89393-PA
- Shabro, V., Arns, C. H., Bryant, S. L., Torres-verdin, C., & Knackstedt, M. A. (2010). PORE SCALE MODELING OF TWO-PHASE FLOW, 1–8.
- Shah, S. M., Yang, J., Crawshaw, J. P., Gharbi, O., & Boek, E. S. (2013). Predicting Porosity and Permeability of Carbonate Rocks From Core-Scale to Pore-Scale Using Medical CT, Confocal Laser Scanning Microscopy and Micro CT. In *SPE Annual Technical Conference and Exhibition*. Society of Petroleum Engineers. doi:10.2118/166252-MS
- Vinegar, H. J. (1986). X-Ray CT and NMR Imaging of Rocks. *Journal of Petroleum Technology*, 38(03), 257–259. doi:10.2118/15277-PA
- Youssef, S., Rosenberg, E., Deschamps, H., Oughanem, R., & Institut, P. S. (2014). Oil ganglia dynamics in natural porous media during surfactant flooding captured by ultra-fast x-ray microtomography, 1–12.

# 2.2 Image post-processing

The gray level distributions in images are considered as representative of materials densities. However the interfaces between minerals or between mineral and air or fluids are very important. Therefore intermediate gray levels appear especially for low resolution. Because of this particularity, image processing becomes laborious and sensitive. In general we might formulate the main goal of image processing as material differentiation from the obtained on the micro-CT image. This goal will be reached by image filtering to enhance the contrast of different materials and remove the noise therefore to facilitate the voxel classification.

For image treatment we use 2 softwares: Avizo and Mango associated to Morphy these softwares are distributed by FEI and Mango – Morphy was initially developed by Australian National University.

In general case of X-ray data image treatments workflow is as follows:



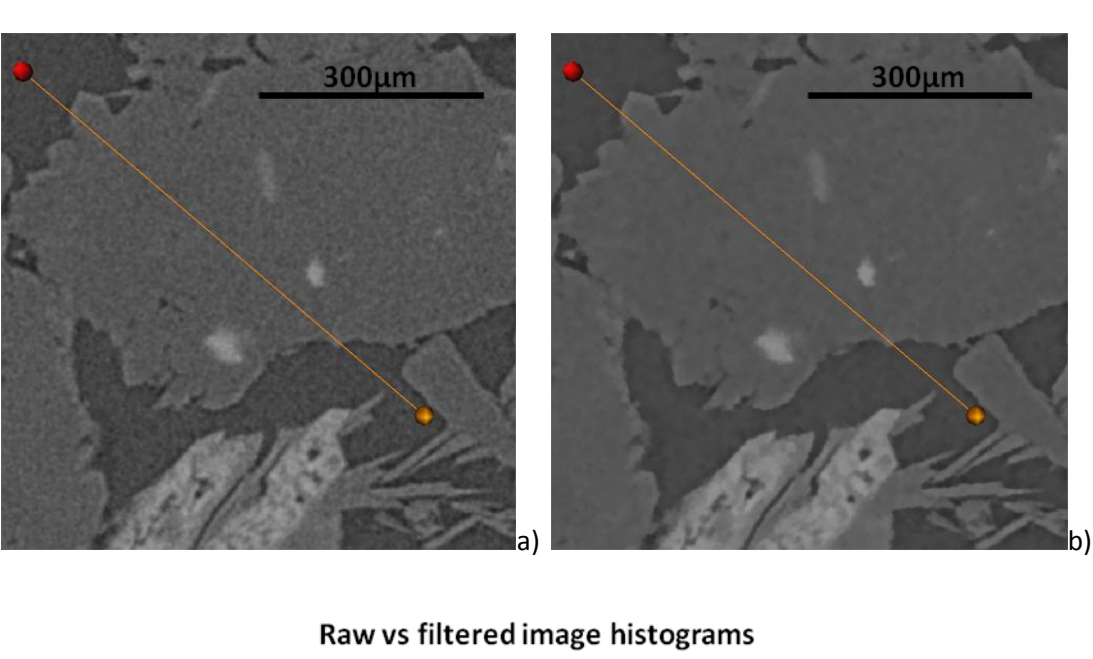
2.2-1 Image treatment workflow

The main difference between the used softwares is that Mango is dedicated to petrophysics application therefore the segmentation process and the calculation in image are more efficient and pertinent in Mango. Avizo offers large choice of filters and arithmetic operations in image. However these tools are more basic and more general in use than Mango-Morphy.

We have to pre-treat received raw images from micro-CT to facilitate successive image segmentation. Image segmentation consists to label every voxel in an image such that voxels with the same label share similar characteristics whatever the refraction index or the similitude of texture. The predominant supervised segmentation phase typically requires some form of subjective selections concerning the threshold-values. Almost, noise in images, blurring and more generally the artifacts and biases induced by the micro-CT techniques require a pre-processing phase of filtering to limit the misclassification of voxels. The main difficulty is to limit the induced biases by the image treatments. For quantitative segmented image analysis, the deficiency of this approach lies in user subjectivity and errors propagation in a quantification process.

### 2.2.1 Numerical filters

Raw image requires to be enhanced to avoid misclassification caused by segmentation thresholding application. The image filter permits smooth the gray level irregularity of each material signal with the edge preservation (Figure 2.2-2). In this way adequate filter application facilitates segmentation process. That is the main goal of image filtering. The contribution of such filtering must be moderate and controlled to avoid an alteration of the image. We present here the different filters we have found in the different articles or patents, enabling the reader to have an idea of the biases and artifacts caused by the different filters. Among these algorithms the more popular are: Median filter, Edge-preserving smooth filter, Anisotropic Diffusion filter, Bilateral filter, Non-local Means filter and Unsharp Mask filter. All filters have advantages and drawbacks and are more or less suited to detect or enhance specific information.



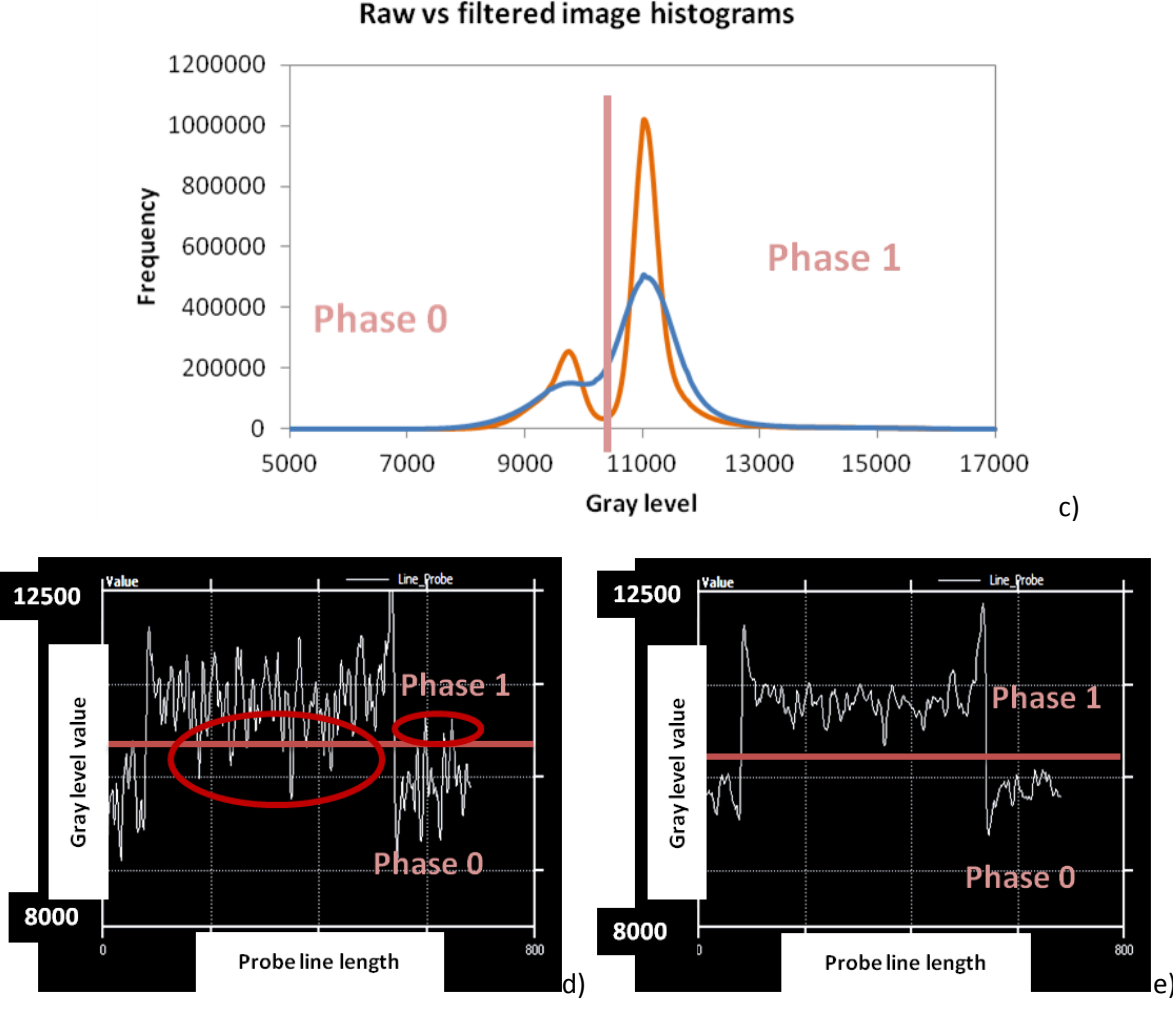


Figure 2.2-2 Filtration goal: a) raw image, b) filtered image, c) gray-level distribution of material density on the raw image (blue line) and on filtered image (orange line) with proposed thresholding level (pink line), d) misclassified voxels caused by erroneous segmentation with chosen thresholding on raw image and e) absence of voxels misclassification in case of filtered image

Before filtering micro-CT images it is necessary to note that each treatment will change the image, thereby, the essential moment at this step is to preserve physical sense in each transformation.

### 2.2.1.1 Median Filter

The Median Filter is a more common filter in post processing image treatment. This filter is used in the case of "impulse noise" as "salt and pepper". The filter based on the principal "entry by entry"; it means that each entered gray-scale value is replaced by the median value in the specified window of nearest cells. This filter permits to despeckle the image without calculation and introducing new gray value into the scale as it is shown in the figure below. Because of the quite simple algorithm formulation this filter is relatively fast.

The Median filter is one of kind of smoothing filters alike a linear Gaussian filter, but in the case of moderated noise and significant gray level difference of materials it erodes the edges (i.e. if gray level difference from both sides of edges is great, despite equalizing of Median Filter, the edge will be preserved). The usage of this filter is useless in the case of very noisy image (with blurred borders of species), because it will smooth the edges in the case of large window choice, or it will change nothing in case of a little window.

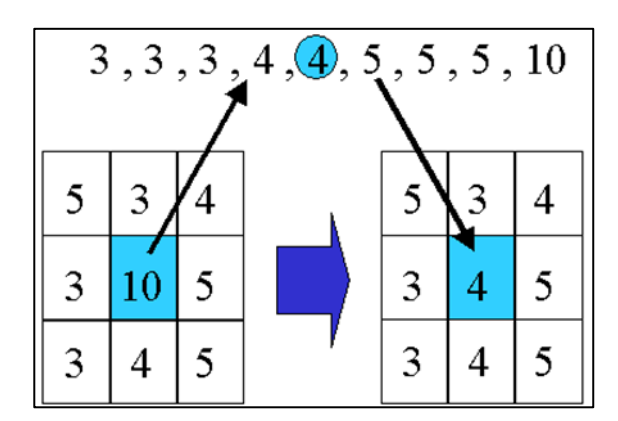


Figure 2.2-3 The principle of Median Filter

At the present time another group of filters have obtained a widely popularity, it is so-called adaptive filters. All of these filters have as a goal to preserve the maximum of edges and to smooth other regions. The main principal of this type of filter is based on research of similarity between neighboring voxels. The pioneer filter in this group is bilateral filter. It is the more simple and rapid filter in the group. All other filters are based on the principal of bilateral filter.

Examples of median filter application are founded in the annex:

- a. In the case of accumulated "impulse" noise on the homogeneous zone median filter decreases the amplitude of grey level dispersion and smooth into this zone.
- b. Filtering efficiency requires a preservation of edges, because the changes in gray level distribution on edges might erode or dilate the mineral zone and therefore increase the incertitude in petrophysical properties calculation.

c. back phase propagation caused by optically finite size of the source is at the origin of a ghost effect around the interfaces. In this particular case the median filter minimizes this artifact's errors. It may be applied just in the case of dry sample, because in the case of multiphase filling of pore medium, the wetting phase (the nearest to pore/matrix contact) might be taken for artifact error and smoothed.

#### 2.2.1.2 Bilateral Filter

Bilateral filter designed by FEI® is a nonlinear filter which permits to preserve discontinuities and to smooth similar zones at the same time. Bilateral Filter is one of nonlinear Gaussian filers. Bilateral filter has some strong points which explain its widespread occurrence. The first one is the definition simplicity: each point is replaced by an average of its neighbors. Other advantage is the fact that it depends only on two parameters that makes it understandable more intuitively. The idea is very simple; to preserve edges it takes into account not only the distance between pixels but the variations of pixel intensities. That is the pixel will be close to an analyzed, i.e. will have a weight in the filter, not only if it occupies nearby spatial position but also if it has some similarity in the photometric range.

As shown on the image the filter replaces the bright pixel at the center by an average of the bright pixels in its vicinity. Dark pixels are essentially ignored. In the case of a dark pixel at the center of the filter, bright pixels have no weight on results value of the centered pixel. (Tomasi & Manduchi 1998)

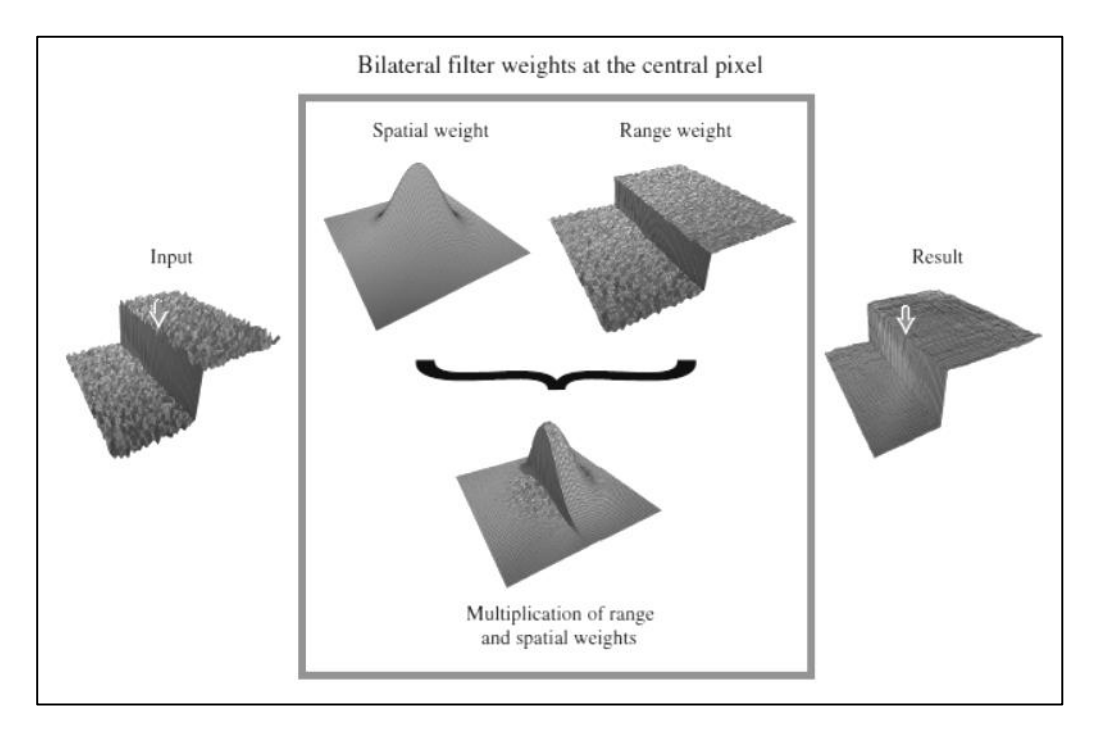


Figure 2.2-4 the principle of Bilateral Filter

To enhance the underlying mechanism of the bilateral filter let begin with Gaussian Blur. This filter is close to the Bilateral but it does not preserve the edges. Gaussian Blur is the result of convolution by a positive kernel; it is a basic operation in linear image filtering. Gaussian Blur is defined by:

$$GB[I]_p = \sum_{q \in S} G_{\sigma}(|p-q|)I_q,$$

Were G is a two-dimensional Gaussian kernel:

$$G_{\sigma}(x) = \frac{1}{2\pi\sigma^2} exp\left(-\frac{x^2}{2\sigma^2}\right).$$

As can be seen from these equations Gaussian Blur averages the pixel intensity value from its neighbor with weights depending on the spatial distance between them. Parameter "sigma" defines the extension of neighborhood. The result of this filter is the image with more or less blurred edges that depends on filter kernel.

Similar to the Gaussian Blur, the Bilateral Filter is defined as a weighted average filter. The principal difference is that the Bilateral Filter takes into account the intensity values of pixels. That permits to better preserve the edges.

$$BF[I]_{p} = \frac{1}{W_{p}} \sum_{q \in S} G_{\sigma_{S}}(|p-q|) G_{\sigma_{r}}(I_{p} - I_{q}) I_{q},$$

Here  $W_p$  is a normalization factor:

$$W_{\mathbf{p}} = \sum_{\mathbf{q} \in S} G_{\sigma_{S}}(|\mathbf{p} - \mathbf{q}|)G_{\sigma_{r}}(I_{\mathbf{p}} - I_{\mathbf{q}}).$$

As can be seen from previous equations, the principal difference between Gaussian Blur and Bilateral Filter is that the Bilateral Filter depends now not only on spatial distance between examined pixels but also on their intensity similarity. This additional factor permits to better preserve the edges.

To control Bilateral Filter there are two parameters: "sigma\_s" and "sigma\_r" which correspond to the spatial component and to the range component. If the range component increases that bilateral filter becomes closer to Gaussian blur, because the intensity value has the same weight everywhere. If the spatial component increases that edges will be more smoothed. (Paris et al. 2008)

In annex there are some examples of Bilateral Filter application.

- a. Even if on the image there are artifact of reconstruction described early, bilateral filter will smooth homogeneous zones up to its contact border, but it will preserve the slope of gradient in the transition zone between two phases.
- b. Too large analyzing windows results on value mixing between two neighboring zones around the border. This effect is due to the fact that the window is larger than pore size, so in pore zone analysis there are some values from matrix zone and conversely. This effect is more noticeable around edges.
- c. Too great value of parameter responsible for intensity will make Bilateral Filter like Gaussian Blur, because the spatial component has not any weight.

#### 2.2.1.3 Non-Local Means Filter

Classical Bilateral Filter was enhanced by Buades (Buades et al. 2005) to the Non-Local Means Filter presented in Avizo®.

Non-Local Means algorithm proposed by A. Buades et al. in 2005 (Buades et al. 2005) is based on a non-local averaging of all pixels in the image. The new value of the voxel will be given depending on the voxel comparison with its neighborhoods. This comparison takes into account the similarity of the neighborhoods. The similarity between two neighborhoods determines the weight with which the value of a voxel in a search window will influence the new value of the current voxel. The more similar neighborhoods will have more weight in the resulting mean value. This principle favors using the NLM algorithms on textured or repeatable images. The principal difference between the bilateral filter and Non-Local means algorithm is that in Bilateral Filtering the weight of neighbor pixels is taken into account, but Non-Local means algorithm the weights are depended on the similarities of neighbor blocks and not pixels.

This idea permits to take into account only blocks which have the similar nature, thereby in comparison with Bilateral Filter NL-means permits to better preserve similar structures. This algorithm has one major drawback, the filter is very time consuming due to its non-trivial formulation for block comparison and pixels averaging.



Figure 2.2-5 NL-Means algorithm principle: similar pixels in similar blocks will have a larger weight in the final filtering

To show the result of NLM applying there are image in annex:

- a. Accurate setting in NLM filter permits to smooth in homogeneous zones, to preserve borders and complex structures like fine porosity.
- b. An unjustified local neighborhood value will enhance borders between phases up to overestimate high values and underestimate low values in edges near zones.
- c. An unreasonably small windows search links to in artifact creation. It reflects on creation on image multiple square textures.
- d. Too large similarity value smooth on all differences between phases and enlarges gradient between them.

# 2.2.1.4 Edge-Preserving Smoothing Filter (Avizo)

Edge-preserving filter (available in Avizo) smoothes the gray-level differences between neighboring voxels. This is a non-linear diffusion algorithm and unlike the Gaussian filter, it preserves the edge because the algorithm is stopped (or lowered) if a boundary is approached. Boundaries are detected by high variation of gradient.

Firstly this filter was proposed by Perona and Malik at 1990 (Perona & Malik 1990). The idea was to encourage smoothing within a region and stop it at the boundaries. The question was how to estimate boundaries position on the image. It was proposed to estimate edge positions with the gradient of brightness function.

Perona and Malik showed how to choose diffusion coefficient c in the anisotropic diffusion equation:

$$I_t = div(c(x, y, t)\nabla I) = c(x, y, t)\Delta I + \nabla c \cdot \nabla I$$

Assuming that we know the edge positions at the time t, we want to smooth in the regions and not at the boundaries. It means that diffusion coefficient at the boundaries will be 0, and it will be 1 in the interior of each region. The problem is unknowing the position of the boundaries. Let E(x,y,t) be a vector-valued function (defined on the image) which has ideally following properties:

- 1. E(x,y,t) := 0, in the interior of regions
- 2. E(x,y,t):=K e(x,y,t), at the boundaries, where e is normal vector to the boundary point, K is the local contrast of edge (gray level difference on opposite sides).

The simplest estimation of this function is the gradient of brightness function, i.e.  $E(x,y,t) = \nabla I(x,y,t)$ . And if this estimation is available, the diffusion coefficient can be chosen as a function of the magnitude of  $\mathbf{\it E}$ , i.e. c=g(|E|). Thereby,  $c(x,y,t)=g(\left||\nabla I(x,y,t)|\right|)$  is a diffusion coefficient. So, the equation will transform to  $u_t=div(g|\nabla u|)\nabla u)$ ,  $(0)=u_0$ . Diffusion function in this equation may be presented as  $\nabla I=\frac{1}{1+\frac{|\nabla I|^2}{k^2}}$  were k is hand-chosen parameter.

However, this model has some difficulties which Catté et al. tried to solve (Catté et al. 1992). The first proposed method is not stable if the level of noise is very high, i.e. image in which the brightness gradient of the noise is greater than that of edges gradients. A second drawback: for some permitted functions the solution is not unique. In order to reduce smoothing on the border and solved the above-mentioned problems, Catté et al. proposed to modify the gradient function by its estimation  $\nabla u_{\sigma} = \nabla (K_{\sigma} * u)$ .

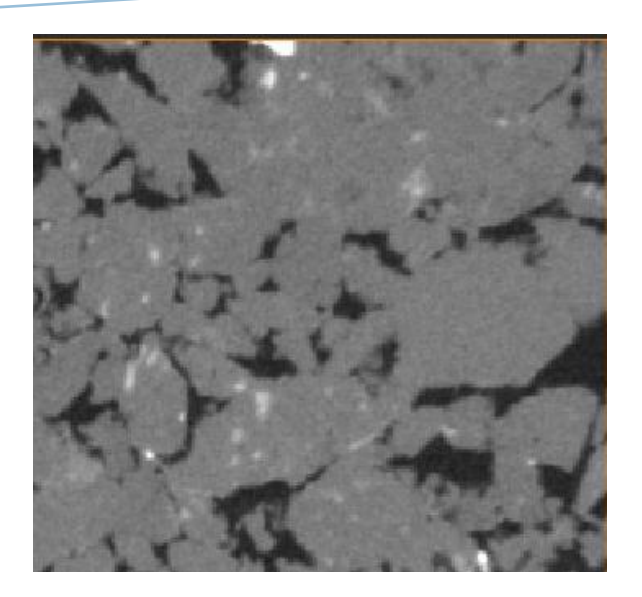
In 1998 Weickert et al. (Weickert et al. 1998) presented absolutely stable additive operator splitting schemes for non-linear diffusion filter of Catté et al. They applied Catté et al. algorithm to the higher-

dimensional case and showed that this scheme is efficient, stable and reliable. The Edge preserving smoothing in Avizo is based on the last paper.

**Table 2.2-1 Summary table of Edge-Preserving Filters** 

Method	Advantage	Disadvantage	Principal difference
Perona & Malik, 1990	Firstly proposed "conditional smoothing":  If the gradient of image increase, so diffusion will be low,  If the gradient of image is small, so it will be more smoothed	<ul> <li>Only the magnitude of the diffusion flux is controlled, not the direction</li> <li>Not working in the case of very noisy image</li> <li>Borders are not denoised</li> </ul>	
Catté et al.	<ul> <li>Has a stable solution in the presence of big noise</li> <li>Have a unique solution</li> </ul>	<ul> <li>Requires large time computation</li> <li>Restrictive stability in higher-dimension case</li> </ul>	Uses gradient estimation unlike gradient function
Weickert et al.	<ul><li>Spatial regularization</li><li>Reduced time of computation</li></ul>		<ul> <li>Novel schemes use an additive operator splitting</li> <li>Uses semi-implicit discretization</li> </ul>

The result of Edge-Preserving Filter realized in Avizo is presented on the figure below.



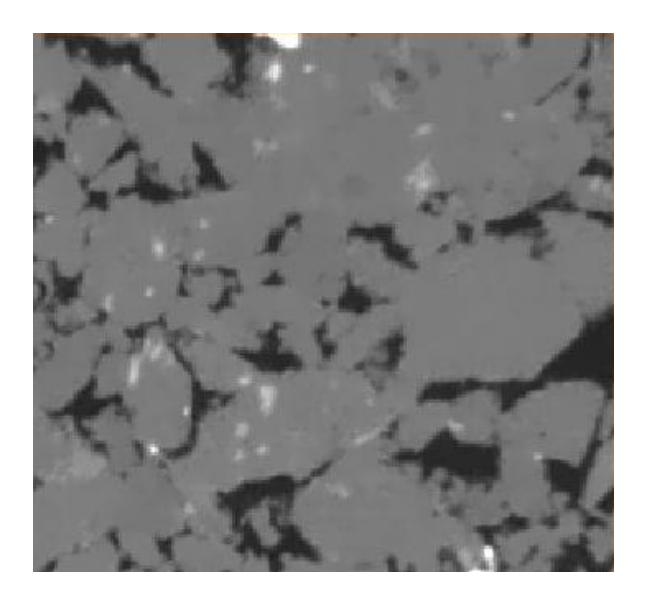


Figure 2.2-6 An example of the raw image (at left) and the result of edge-preserving filtering on it (at right).

### 2.2.1.5 Anisotropic Diffusion Filter

Anisotropic Diffusion filter used in Mango is based on the principle described in the paper of Frangakis and Hegerl (Frangakis & Hegerl 2001) in which they propose to use a hybrid approach of 2 diffusion denoising methods.

The method proposed by Malik and Perona (Perona & Malik 1990) is called Edge Enhancing Diffusion (EED). Another algorithm was proposed by Weickert in 1998 (Weickert 1998) to improve flow-like structures and to render the diffusion flux steered. The principal difference in the algorithm proposed by Weickert in 1998 is to use a semi-local analysis by means of the structure tensor combined with 1-D diffusion along one of its eigenvectors. The aim of proposed by Weickert algorithm is to enhance line-like structures based on the measure of direction coherence (Coherence –Enhancing Diffusion Filter, CED).

Frangakis and Hegerl (Frangakis & Hegerl 2001) proposed to use these two algorithms together (in turn). In this case the coherence in directions may be used as a "switch": if the difference of intensity in 2 directions is not significant, the EED algorithm will be used, else CED. It means, during the first iteration, all edges will be enhanced, homogeneous species smoothed; and subsequently, by second step, lines will be connected and flow-like structures enhanced.

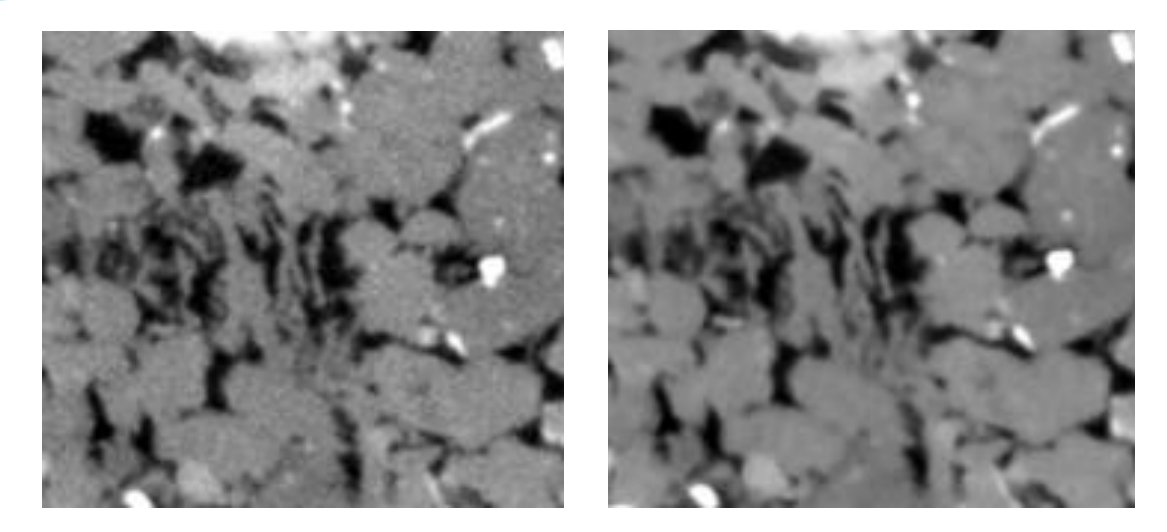


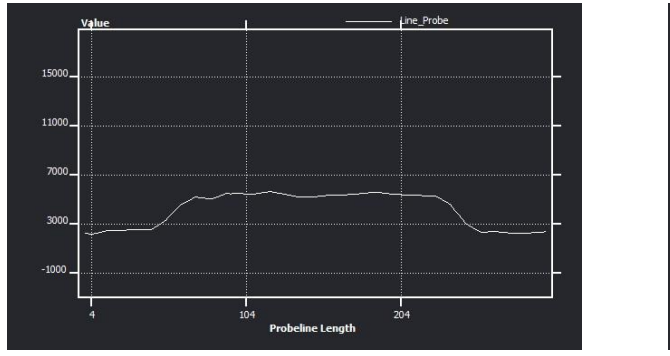
Figure 2.2-7 An example of the raw image (at left) and the result of Anisotropic Diffusion filtering on it (at right).

# 2.2.1.6 Unsharp Masking Filter

Quite frequently after image filtering it is not out of place to use Unsharp Masking Filter to enhance phase differences. This filter is also based on Gaussian Blur. From the name of the filter it is evident that an unsharp mask is used. The idea is to increase the contrast of semitones. An unsharp mask of the original image based on Gaussian Blur with chosen kernel is subtracted from the original image. Thereby, the resulting image will have only high contrast zones. It is important to note that the Unsharp Masking does not enhance the sharp of the image, because it does not restore the lost information. But it increases the local contrast on the image zones where the high changes was presented initially.

# 2.2.2 Signal/Noise ratio for numerical filtering

It is logical to assume that image enhancing by filtration may continue indefinitely. So in softwares there are the tools to verify Signal/Noise ratio amelioration. For example, the Signal-Noise ratio might be validated by applying "line-probe". This technique permits to evaluate the smoothness of the signal on matrix/pore medium in the chosen region. As it shown on the figure below, the line on raw image might be compared with the same line on the filtered image. Or it may be useful to compare the result of two different filters in the same zone.



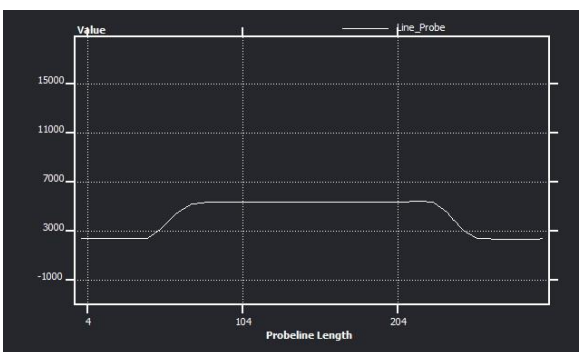


Figure 2.2-8 Line Probe of grain on the raw image (at left) and after NL-Means Filter applying (at right)

- 2.2.3 Annex A: Some examples of Filters applying
- 2.2.3.1 Median Filter

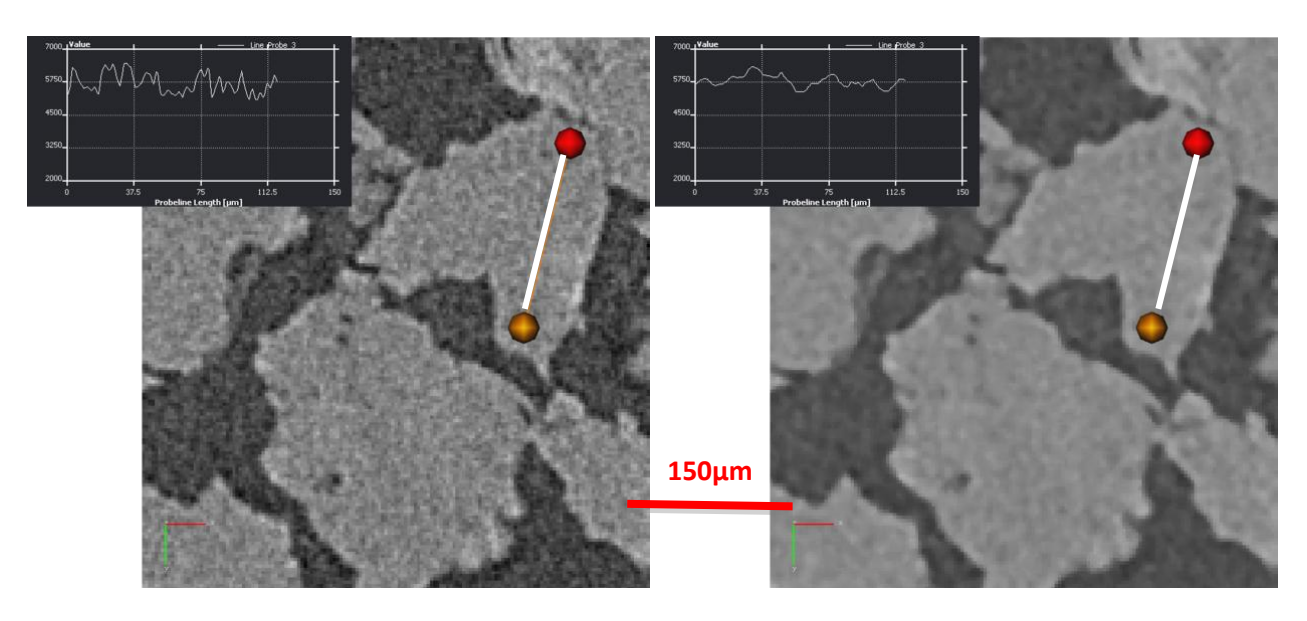


Figure 2.2-9 Median filter (right) applied on image decreases "salt and pepper" noise accumulated on raw (left) image

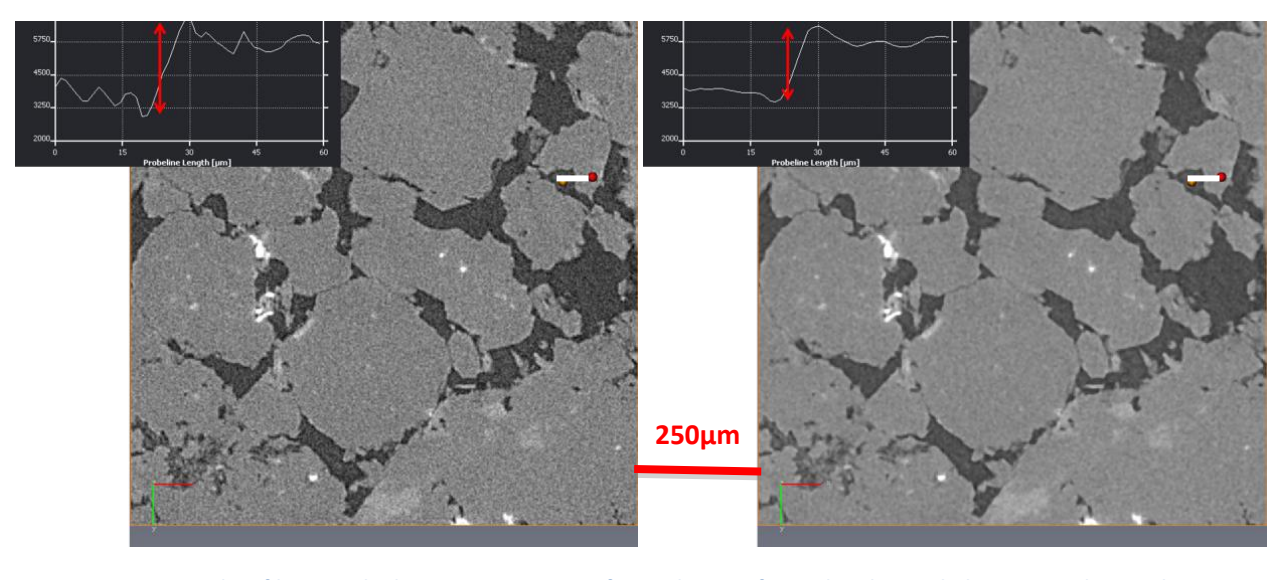


Figure 2.2-10 Median filters applied to RAW image, significant change of grey distribution behavior on edges. Values on borders are significant decreased in comparison with RAW image.

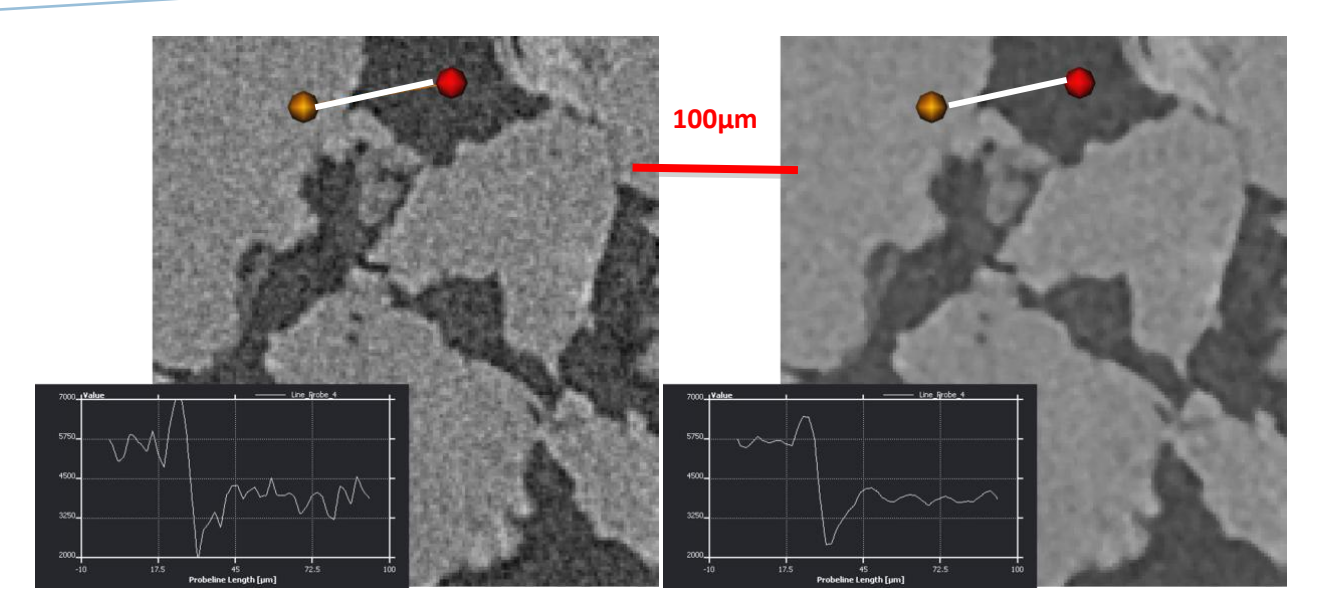


Figure 2.2-11 In particular cases Median filter permits to remove reconstructed artifact of overestimated values on borders

# 2.2.3.2 Bilateral Filter

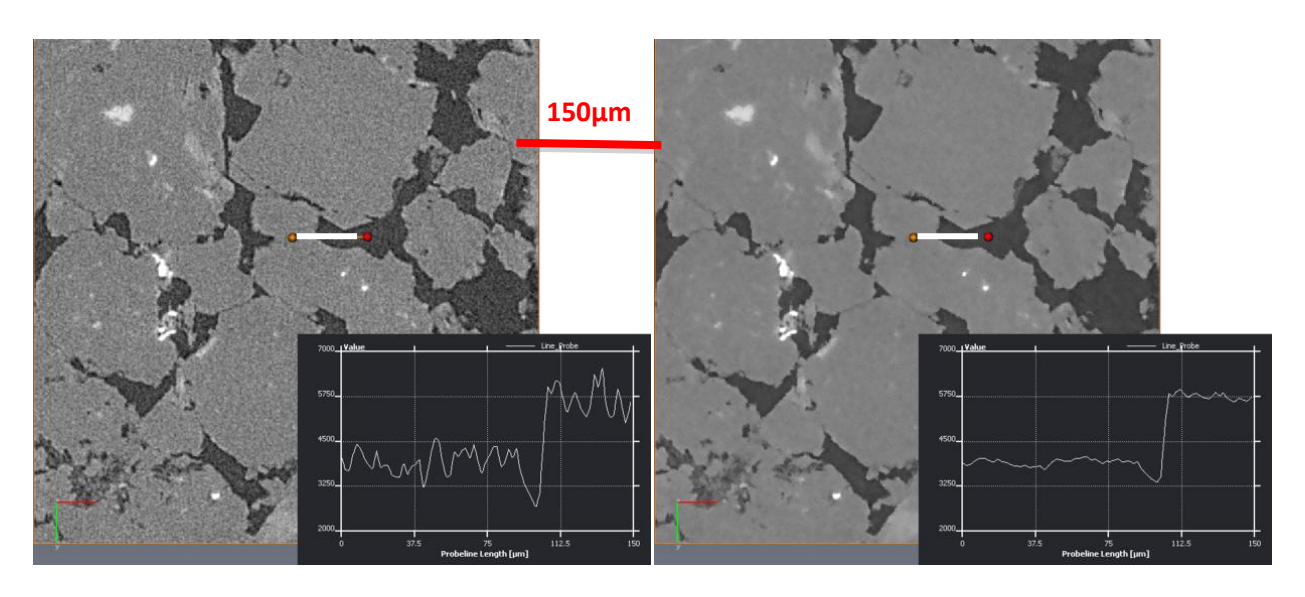


Figure 2.2-12 Bilateral filter (right) applied to RAW data (left) permits to smooth in homogeneous zones and to save gradient between phases

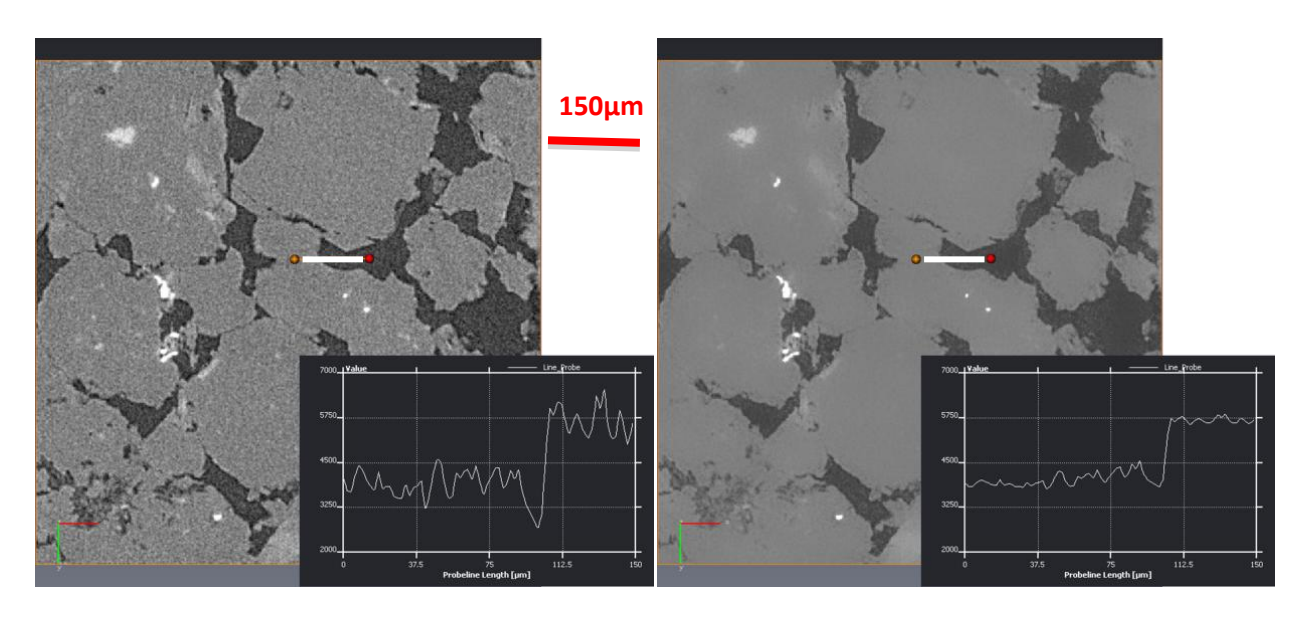


Figure 2.2-13 Applying of too large analyzing windows in Bilateral filter (right) produces unwanted effect of values mixing in neighboring zones.

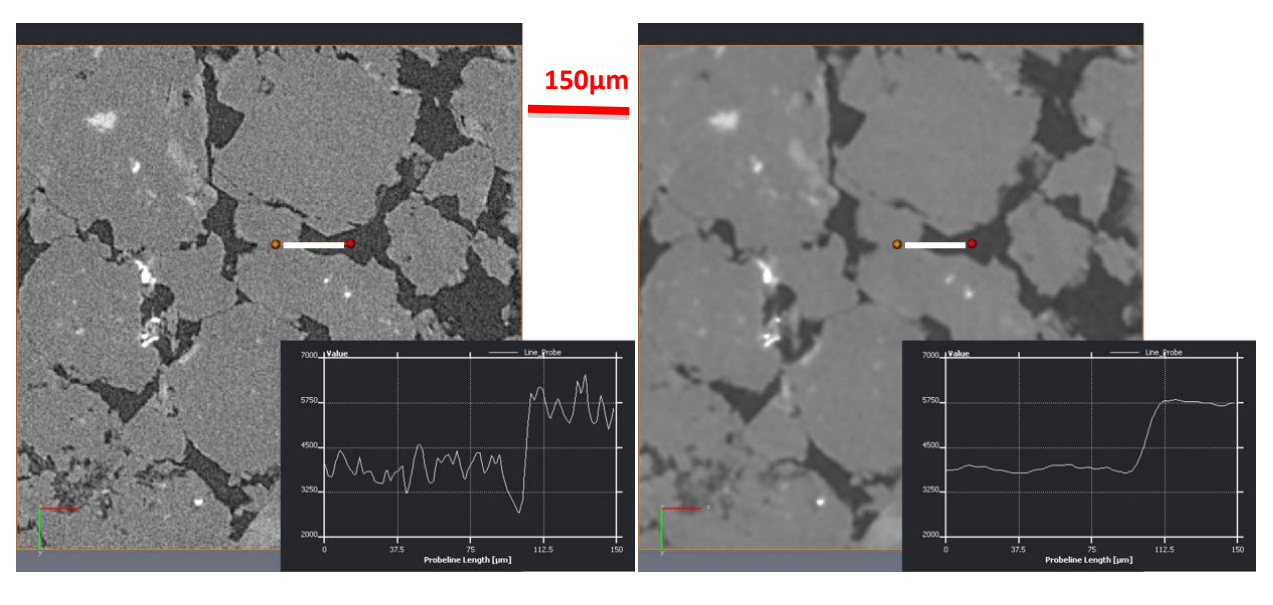


Figure 2.2-14 Applying of great values responsible of intensity approximates Bilateral filter (right) to Gaussian Blur.

# 2.2.3.3 Non-Local Means Filter

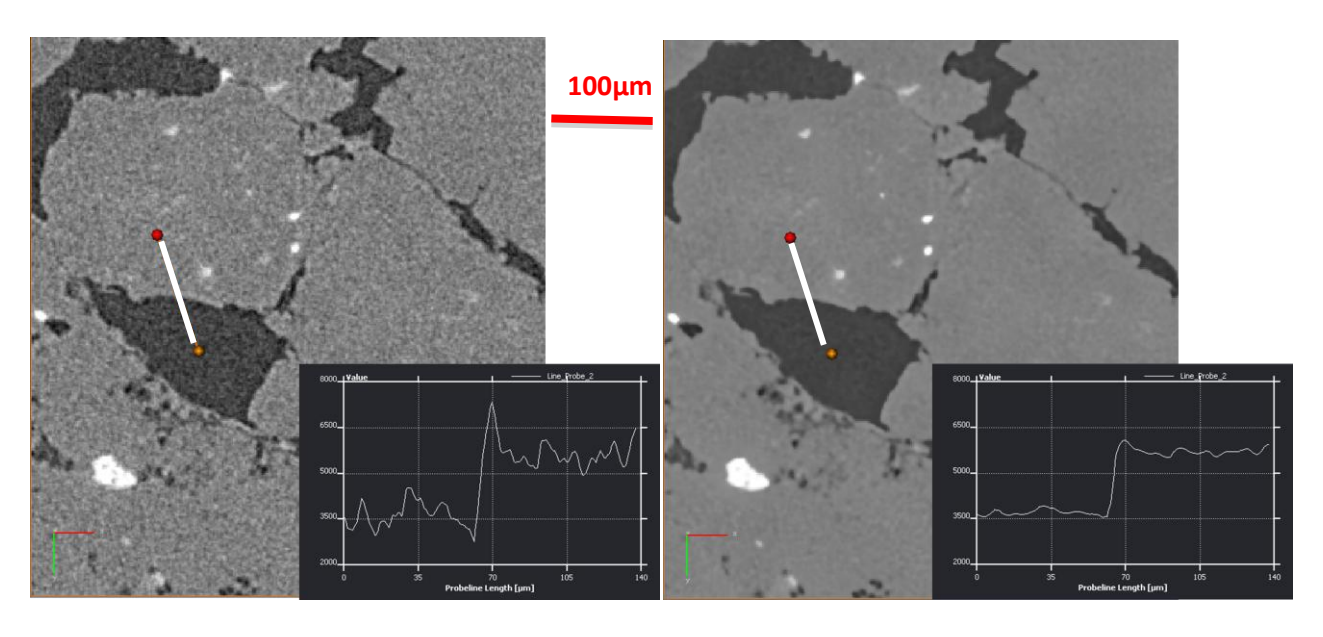


Figure 2.2-15 Applying of Non-Local Means filter (right) to raw data (left).

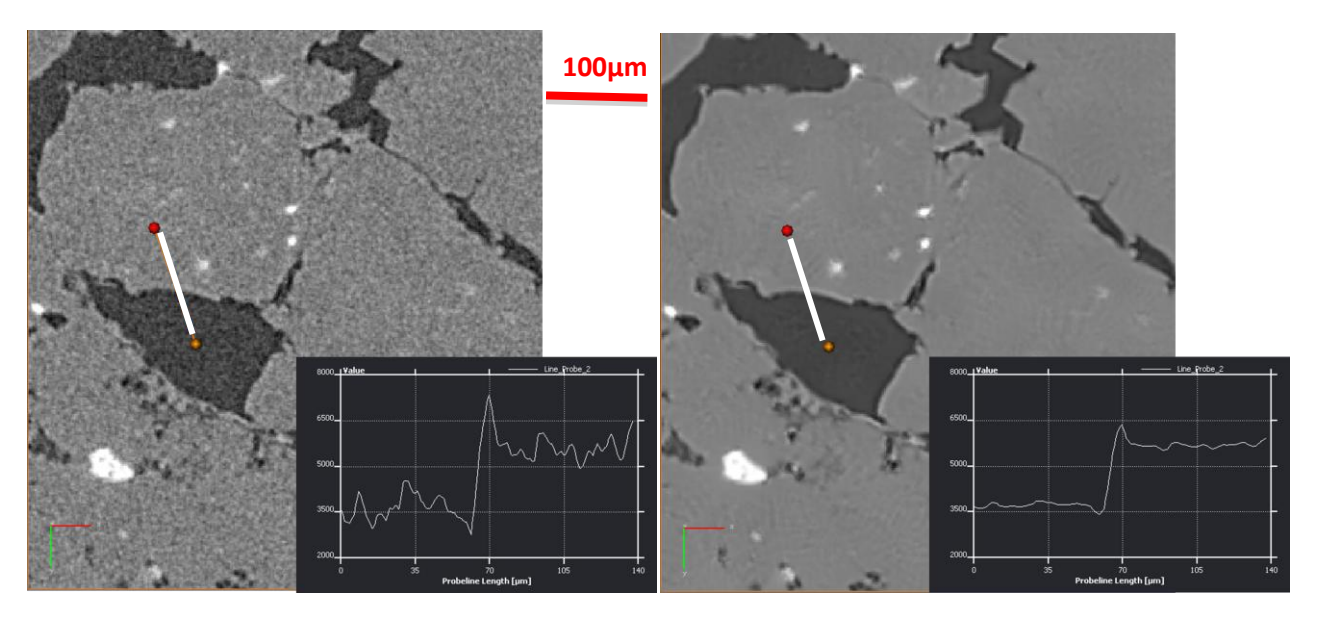


Figure 2.2-16 Applying large local neighborhood setting in NLM filter (right) provokes wrong phase distribution in edge zones.

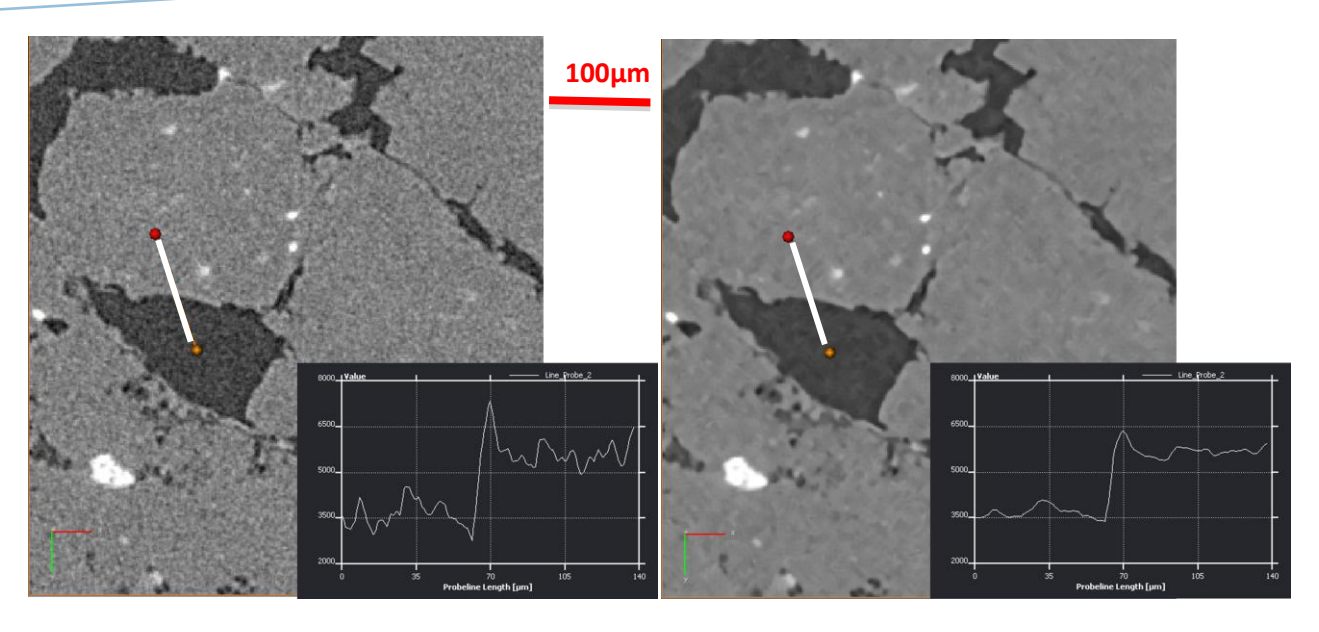


Figure 2.2-17 Small analyzing windows in NLM setting provokes square artifacts (right)

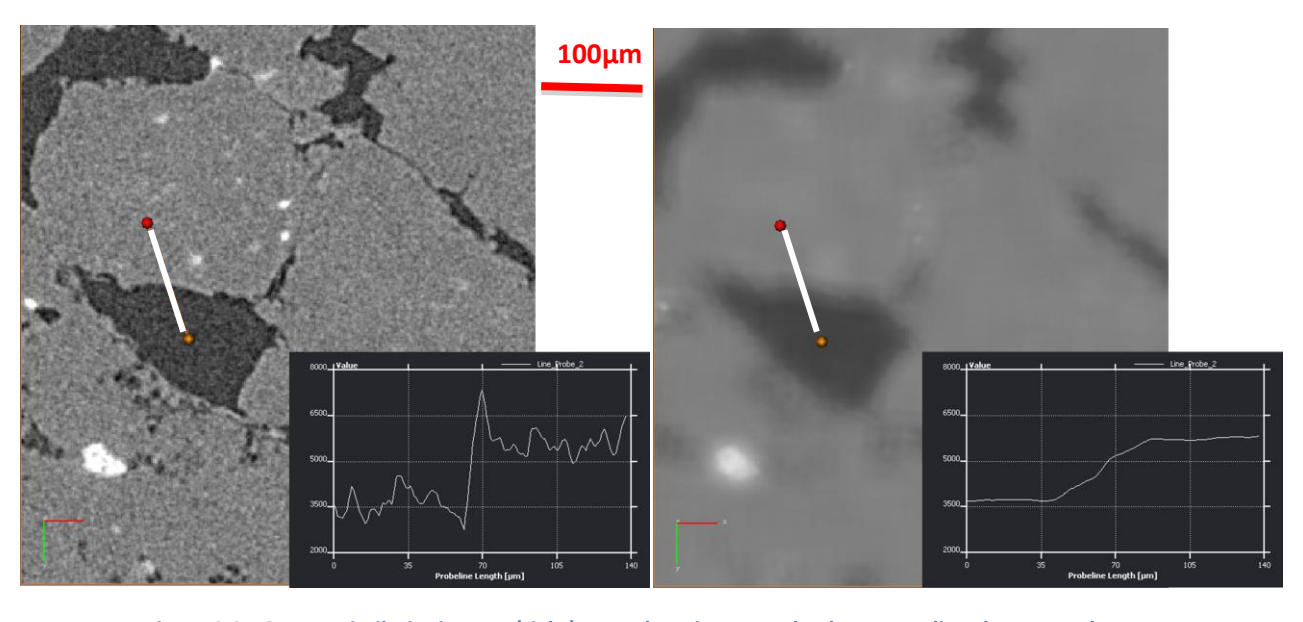


Figure 2.2-18 Large similarity in NLM (right) smooth on image and enlarges gradient between phases.

# 2.2.4 Image Segmentation

Segmentation is the second main step in image treatment and certainly the most critical. Segmentation plays a crucial role between filtered image step and quantitative estimation of physical calculation properties into image.

In one of the most fundamental paper of image segmentation techniques R. M. Haralick and L. G. Shapiro define good image segmentation (Haralick & Shapiro 1985) as:

"Regions of image segmentation should be uniform and homogeneous with respect to some characteristic such as gray tone or texture. Region interiors should be simple and without many small holes. Adjacent regions of segmentation should have significantly different values with respect to the characteristic on which they are uniform. Boundaries of each segment should be simple, not ragged, and must be spatially accurate."

Evidently it is very difficult to achieve this goal.

It is important to note that in comparison with filtering, image segmentation does not change the image and its characteristics. Robert M. Haralick defines the image segmentation as the partitioning of an image into non-overlapping, constituent regions which are homogeneous with respect to some characteristic as intensity (Haralick & Shapiro 1985). In other words, segmentation of filtered image is a kind of image labelization. The result of image segmentation is a new labeled image (mask of image) in which each separated label corresponds to its gray level region, i.e. material density distribution. The segmentation goal is therefore the choice of these gray level region distribution partitions. It is also important to note, that the labeling and the segmentation is not exactly the same thing, a segmented image may be labeled inside its regions.

An ideal segmentation method finds these labels or gray levels correspond to distinct regions of interest on the image. Thereby, image pixels will be separated into classes. Normally, the number of classes is known in advance (for example 0 - void, 1 - oil, 2 - water, 3 - clays, 4 - grains of quartz, 5 - high density material etc.).

Segmentation process consists of simultaneous operations on the image and its histogram. Thereby, to distinguish classes in the image it corresponds to separate peaks in the histogram. At this moment the work becomes very delicate. There are some classical methods to distinguish classes from the total histogram. When using the softwares Avizo and Mango it is possible to distinguish two global groups:

- Sample thresholding (Otsu's method),
- Region growing (Watershed segmentation, Converging Active Contours Algorithm)

### 2.2.4.1 Segmentation by thresholding

Thresholding algorithm is based on Otsu's method phase separation by histogram threshold. Otsu's method is based on the supposition about only two types of pixels existence on the image, and it looks for the better separation by histogram thresholding (Otsu 1979). On an ideal histogram there are two peaks representative of two materials, therefore the lowest point between these two peaks is chosen for

thresholding. Otsu's method attributes all gray level before the chosen thresholding to the first class of pixels and after the chosen thresholding to the second class corresponding to the second material. Image segmentation by thresholding is a good method in a case of quasi binarized image where the difference in X-ray attenuations of two physical materials is very important and there is not any overlap.

Otsu's method principle is based on inter-classes variance minimization for the chosen thresholding and is described by the equation below:

$$\sigma_{\omega}^2(t) = \omega_1(t)\sigma_1^2(t) + \omega_2(t)\sigma_2^2(t)$$

Where, the weights  $\omega_i$  are the probabilities of the two classes separated by a threshold t and  $\sigma_i^2(t)$  variances of these classes. (Otsu 1979)

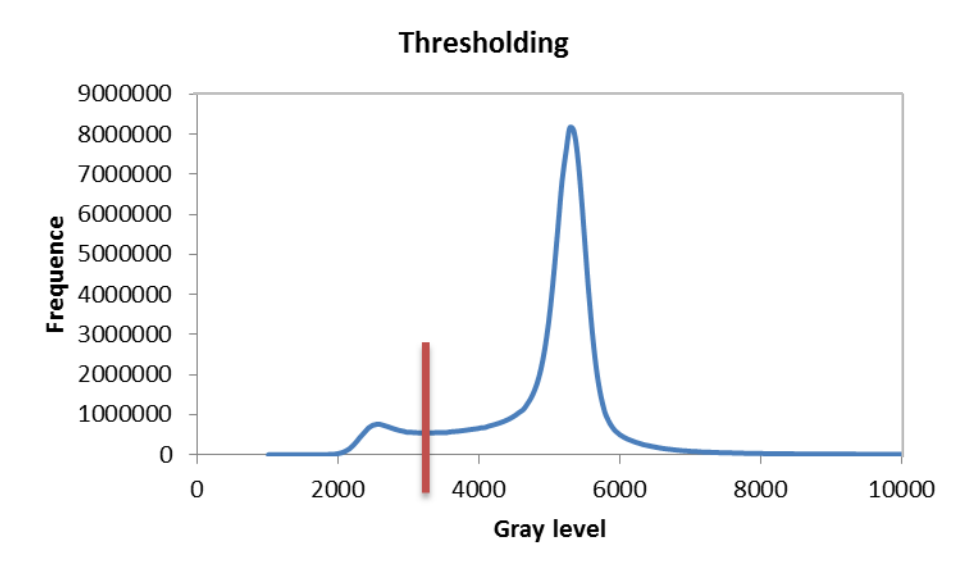


Figure 2.2-19 Histogram thresholding based on the bottom of valley search

If we use thresholding for three phase image, we will use "phase by phase" thresholding anyway, i.e. each phase is separated binary.

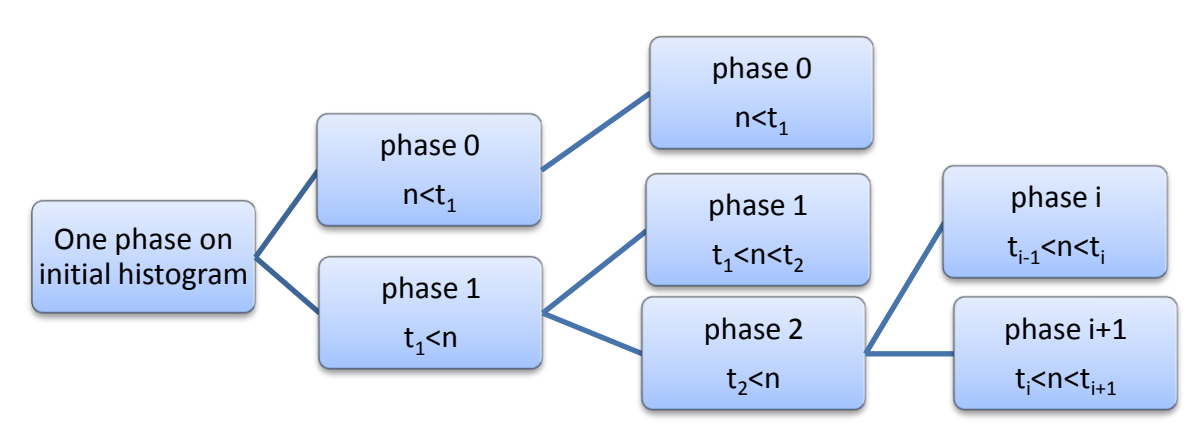


Figure 2.2-20 Principle of sequential multi thresholding

There is one major drawback in this thresholding method. In the case of multiple phase data there is a situation when the same gray level from one side corresponds to the phase "i" and from other side it corresponds to the gradient (transition) between two other phases. As follows from figure 3 in this case a sample thresholding segmentation methods are less useful and not recommended. If thresholding methods are used the final segmentation will not correspond to the real system. In this case the middle is enlarged by gradient addition, or on the contrary it is reduced and divided between two others phases. Anyway it is not possible to separate the gradient and the middle phase by thresholding methods. There is just one exception in the ideal case the edges between phases are clearly marked and very thin. Thereby there is not pixel to distribute to gradient or to middle phase.

# 2.2.4.2 Region Growing

In all other cases to have a more accurate segmentation on multiphase image Watershed Segmentation algorithm is used. The Watershed Segmentation algorithm is based on the gradient calculation, the peaks of which are used as a watershed. In other words, the gradient of the original image may be presented as a topographic relief, where the gradient intensity value of each pixel (in term of gradient) is interpreted as altitude of this relief. Thereby, it is evident if a drop of water drips on the relief it will flow in the direction of relief falling to reach a local minimum. It is logical to assume that with this problem formulation, the peaks of gradient will be watersheds. That is from where the name of algorithm comes.

The first watershed algorithm has been proposed in 1979 (Beucher & Lantuéjoul 1979). The idea was to place a source of water in each local minimum and to flood the relief from the source. The line where water of different source meets it separates the regions.

Later it was proposed to use a topographic distance as the criteria. That is in topographic terms the drop will reach the "nearest" minimum. "Nearest" that is to say the minimum where which the path if the descent is more quick. Thereby, this criterion verifies that the initial place of the drop is linked with the minimum. In 1997 another additional criteria was introduced (Couprie & Bertrand 1997), it was proposed to evaluate the minimal altitude of the neighborhood minima, and i.e. the watershed becomes smoother.

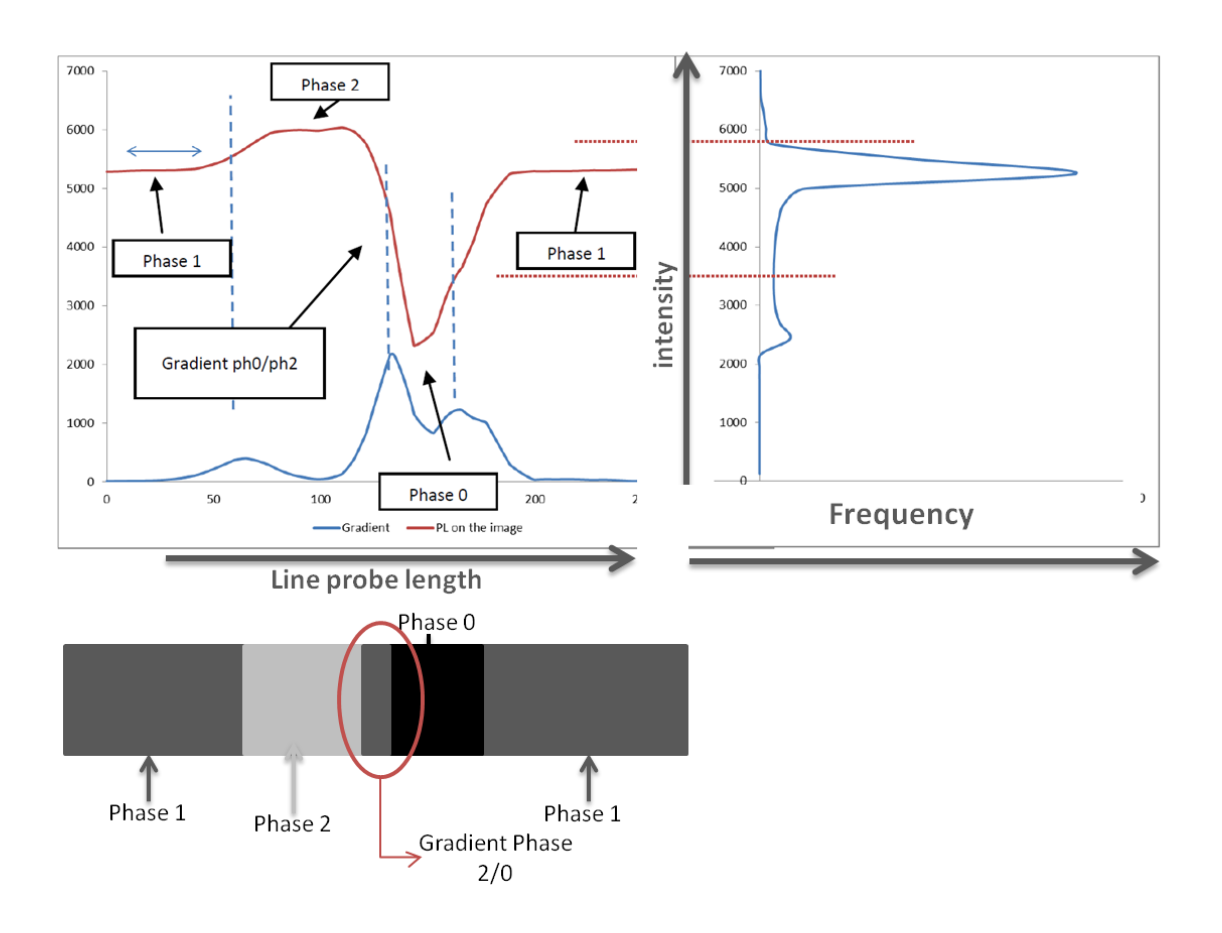


Figure 2.2-21 Watershed segmentation principle. The red line at left corresponds to the intensity value on gray level image, the blue one to the gradient. Watershed application permits to quantify the gradient between phases 2 and 0 and to not treat it as the phase 1 like with thresholding segmentation method.

# 2.2.4.3 Converging Active Contours Algorithm

Another used algorithm in phase segmentation process is the Converging Active Contours Algorithm proposed by Mango.

This algorithm proposed by Sheppard et al. (Sheppard et al. 2004) combines two common methods used in segmentation: Watershed and Active Contours.

The Active Contours Algorithm was firstly proposed by Kass et al. (Kass et al. 1988). They proposed the algorithm of deformed parameterized curves. The process of the curve adaptation is based on the vector-parameters search, which corresponds to the local minimum. If the board curve is a system of board points, it may be presented as:

$$V = [v_1, \dots, v_n],$$

where  $v_i = (x_i, y_i)$  and d i = [1; n];

So, the idea of Active Contours Algorithm is to minimize:

$$E_i = a \cdot E_{int}(v_i) + b \cdot E_{ext}(v_i)$$

The principal is to know the "optimum" between external and internal "forces" which squeezes the curve from one side and fills it from other. Internal forces depend on the form of curve; external forces depend on the image properties (intensity, gradient etc.). Internal forces combine a smoothing component, which controls the board point non-detachment, and a pushing component, which deforms the curve in the same direction. External forces are based on image intensity and image gradient variation. The method proposed by Kass et al. (Kass et al. 1988) is not optimal in the case of unsharp edges on the image. In this case the algorithm risks having some merged points, and this can generate completely "filled" image. This is why a new method of image segmentation was proposed by Sheppard et al. (Sheppard et al. 2004).

The new method, as it was noted previously, is based on Watershed Segmentation and Active Contours combination and similar to the method of video segmentation (Sifakis, Grinias, and Tziritas 379-88). Sheppard proposes to use bottom-up watershed segmentation to more accurate edge detection. This method requires the started markers, which limit the sure i-specie zone; algorithm will work at "unsure" image zone. To evaluate watershed "basins" the speed function of basin board formation is taken from Active Contours Algorithm. After edge line detection, fast marching algorithm is used to track it.

### 2.2.4.4 Conclusions

The thresholding method is widely used for simple systems, i.e. for systems with histograms characterized by non- or moderate peaks overlap. In this non-critical condition the thresholding method might permit to obtain rapidly a good segmented image. Nevertheless, in the case of indiscriminate phase identification threshold method might lead to severe misclassification. Region growing methods are more accurate in this case as it facilitates the segmentation process when the overlap between peaks occurs. These methods are more time consuming however the material and edges identification is a crucial element in Digital Rock Physics because of its direct link and influence on calculation in images, and therefore on final definition of petrophysical properties of rock samples.

# 2.2.5 Calculation in image

# 2.2.5.1 Problematic of the resolution sensitivity on static properties

A real microtomography needs to integrate filtering process to enhance the signal preserving as possible information. These filters are numerous and we described the commonly used in X-ray microtomography. But in this part we show the importance of choosing an adequate resolution and its influence on the stability of final calculated petrophysical properties. To gauge the efficiency on realistic porous media we first scanned sandstones.

# 2.2.5.1.1 Three resolutions sandstone sample

To evaluate the influence of resolution on calculated petrophysical properties of the sample we have studied the same sample of sandstone under three different resolutions. We have imaged a global sample (8mm of diameter and 10mm of height) with a resolution of 9.6 $\mu$ m per voxel and two of its subsamples with resolutions of 2.0 $\mu$ m per voxel and 0.96 $\mu$ m per voxel. For three-resolution experiment we used Versa 500XRM tomograph manufactured by XRadia (Zeiss). We imaged 380.53 mm<sup>3</sup> of the sample at 9.6 $\mu$ m per voxel resolution, but to simplify petrophysical properties calculation the image volume was reduced to 110.59mm<sup>3</sup>. For two other subsamples we carried out our research on 1mm<sup>3</sup> and 0.11mm<sup>3</sup> respectively. Sample was imaged with 60kVp for 9.6 $\mu$ m and 2 $\mu$ m resolutions and with 80kVp for 0.96 $\mu$ m resolution. The gray scales contrast changes from one resolution to the other due to local tomography reconstruction using different photons fluxes and energy levels.

From obtained micro-CT images we have calculated two global petrophysical properties: porosity and permeability. The uncertainty estimation is given for porosity putting in evidence the importance of the good thresholding choice. Permeability is calculated with commercial software Avizo ® from FEI group for each corresponding binarized image.

For the optimal threshold obtained at  $9.6\mu\text{m/vxl}$  image we found 13% of porosity and 1.2D for permeability. We showed porosity might vary from 8% to 21% depending on the chosen threshold value. It results in a 600% error for porosity. We showed permeability variation from 0.3D to 5.8D depending on corresponding threshold. Such variation results in a 300% error for permeability calculation.

Zooming with a voxel size of 2 micrometers the size occurring variations are between 0.3 and 1.2 D for permeability and 15 to 20% porosity. The most objective values are respectively 0.8 D for permeability and 17% for porosity. To the highest resolutions tested of 0.96 micrometers per voxel the most convincing values are 1.7 D for permeability and 22 % for porosity. The variations occurring from one peak to the other are a change of permeability from between 1.35 to 1.95 D and the porosity increases from 21.5 to 24.5 %.

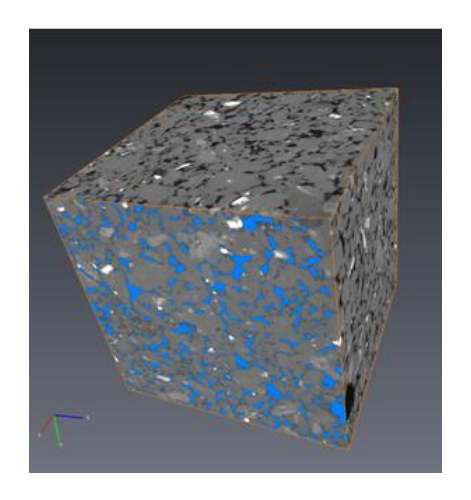


Figure 2.2-22 Spatial resolution 9.6 micrometers per voxel at 60 kVp (500 X 500 X 500 voxels<sup>3</sup>)

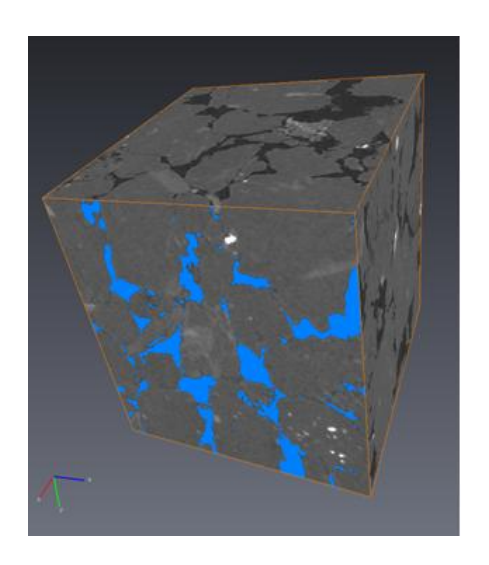


Figure 2.2-23 Spatial resolution 2 micrometers per voxel 60 kVp (500 X 500 X 500 voxels<sup>3</sup>)

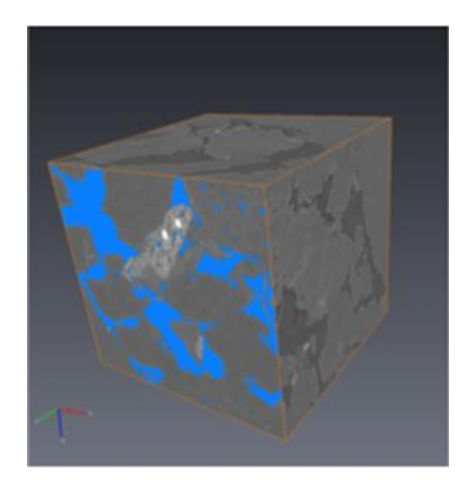


Figure 2.2-24 Spatial resolution 0.96 micrometers per voxel at 80 kVp (500 X 500 X 500 voxels<sup>3</sup>)

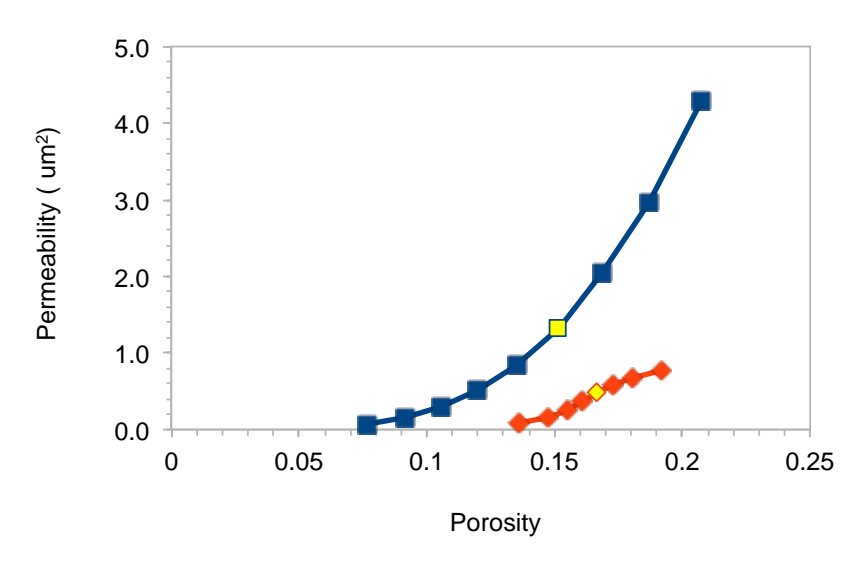
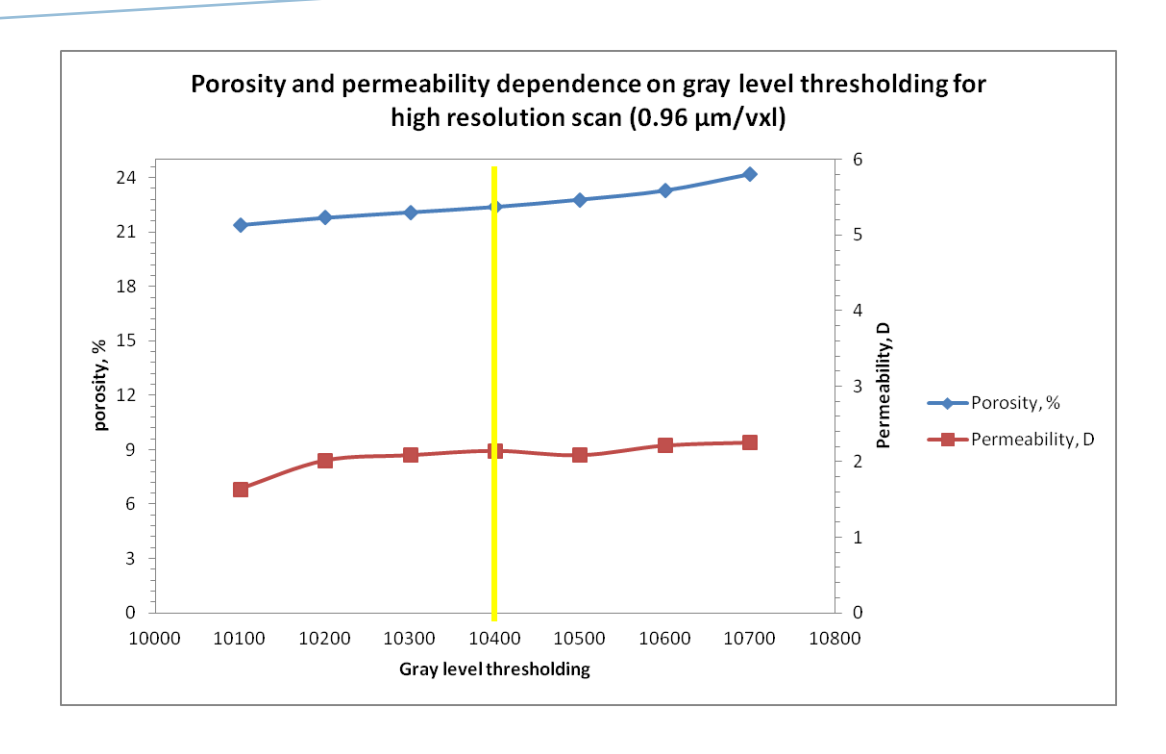
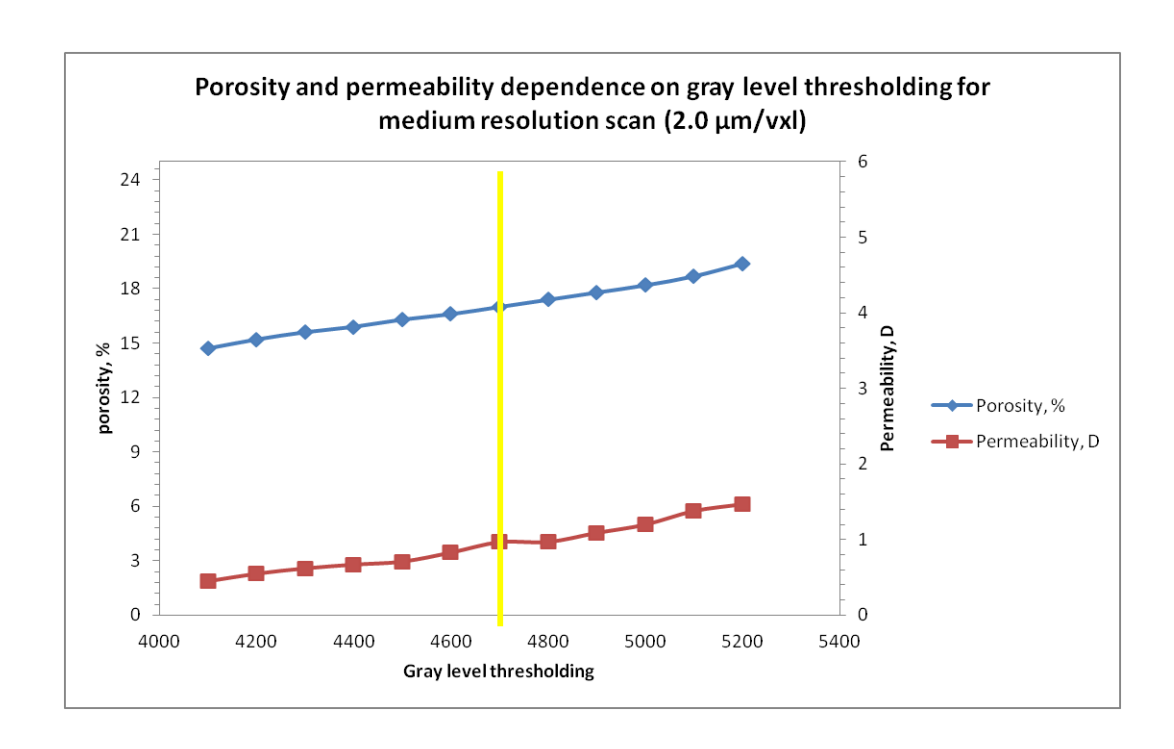


Figure 2.2-25 Scattering of k-φ plots obtained for 9.6 micrometers of voxel size (blue square) and 2 micrometers of voxel size (red diamond) for different selected thresholds between void and grains peaks. Yellow markers are the most convincing performed thresholds





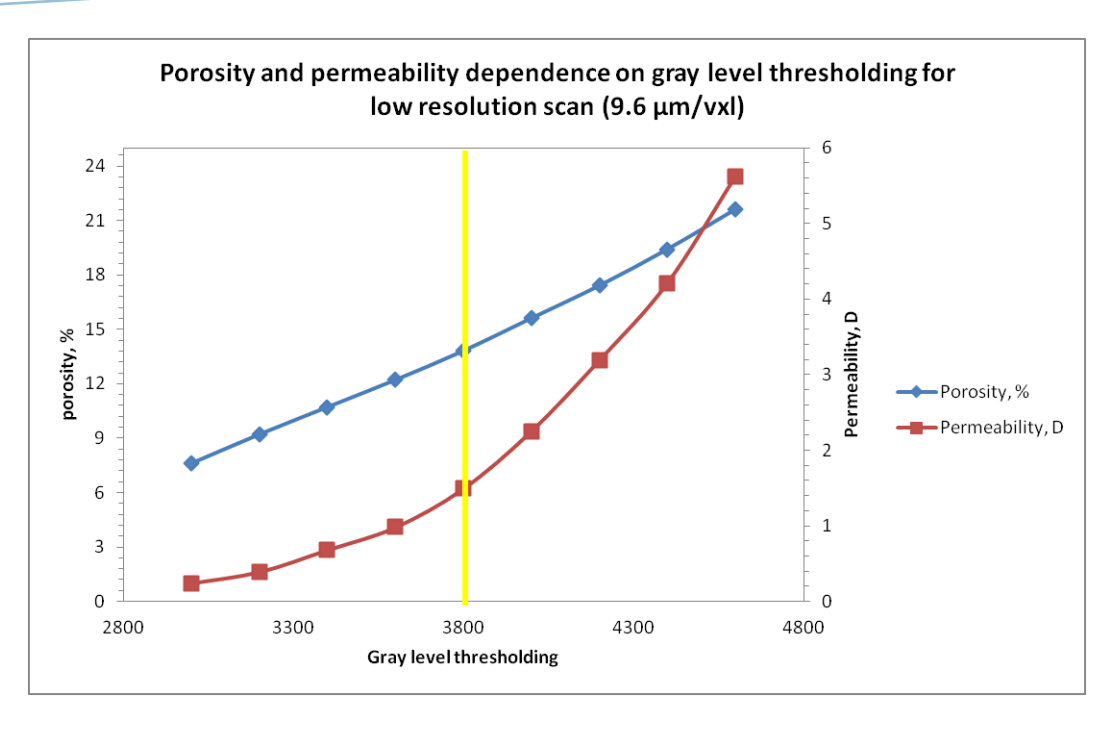


Figure 2.2-26 k-φ evolution as a function of the selected threshold for high (top) medium (middle) and low (bottom) spatial resolutions corresponding to the same sample (Yellow line is the better thresholds)

The figure above shows the permeability might be affected up to 40% of error depending on threshold choice. The porosity variation is about 7 point between the two extreme resolutions with the highest porosity rendered by the highest resolution.

Highest resolutions show higher reliability in petrophysical evaluation due to a relative lower contribution of intermediate gray levels representative of the gradient between void and grains phase in the global volume in spite of additional noise and a reduced contrast coming from local tomography used to zoom in the porous medium.

Classification is favored in the highest resolutions experiments although the contrast is degraded in comparison with the lowest resolutions imaging. The analysis is more secure although noise and local tomographic algorithm contribute to degrade the contrast only benefitting the spatial resolution. The resolution is confirmed to be the main criterion to estimate the pore network porosity and permeability.

In the next chapter we illustrate the limits reached by modern CT-scan concerning the deficiency of actual micro—CT to identify with efficiency a pore network with an appropriate resolution.

### 2.2.5.1.2 Lack of resolution on limestone

To illustrate the criticism and the risk of X-ray microtomography used in Digital Rock Physics we tested an Estaillades Limestone rock sample. This rock sample is characterized by a dual porosity. The macroporosity forms a percolated network through the sample. The microporosities are not in the range of order of the Skyscan microtomograph resolution. This is confirmed by the throat pore distribution

given by Hg-porosimetry curve shown below. Global porosity is 30.7%. The dual distribution of porosimetry is approximately shared in two equal parts (Figure 2.2-27).

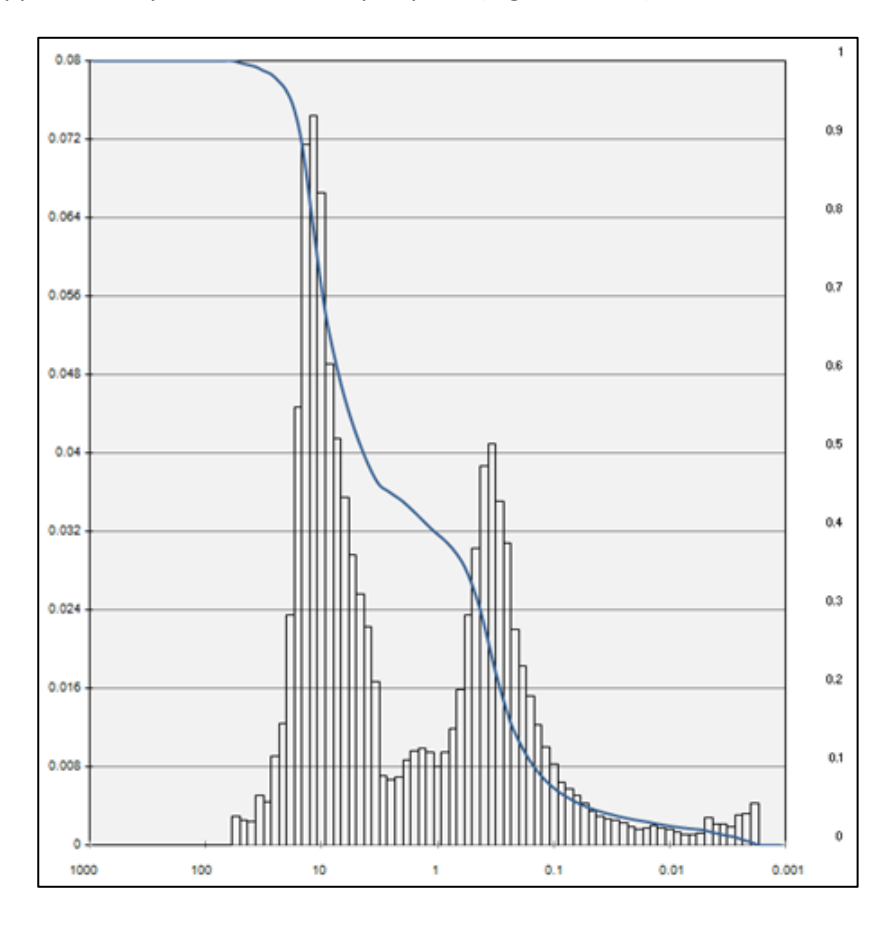
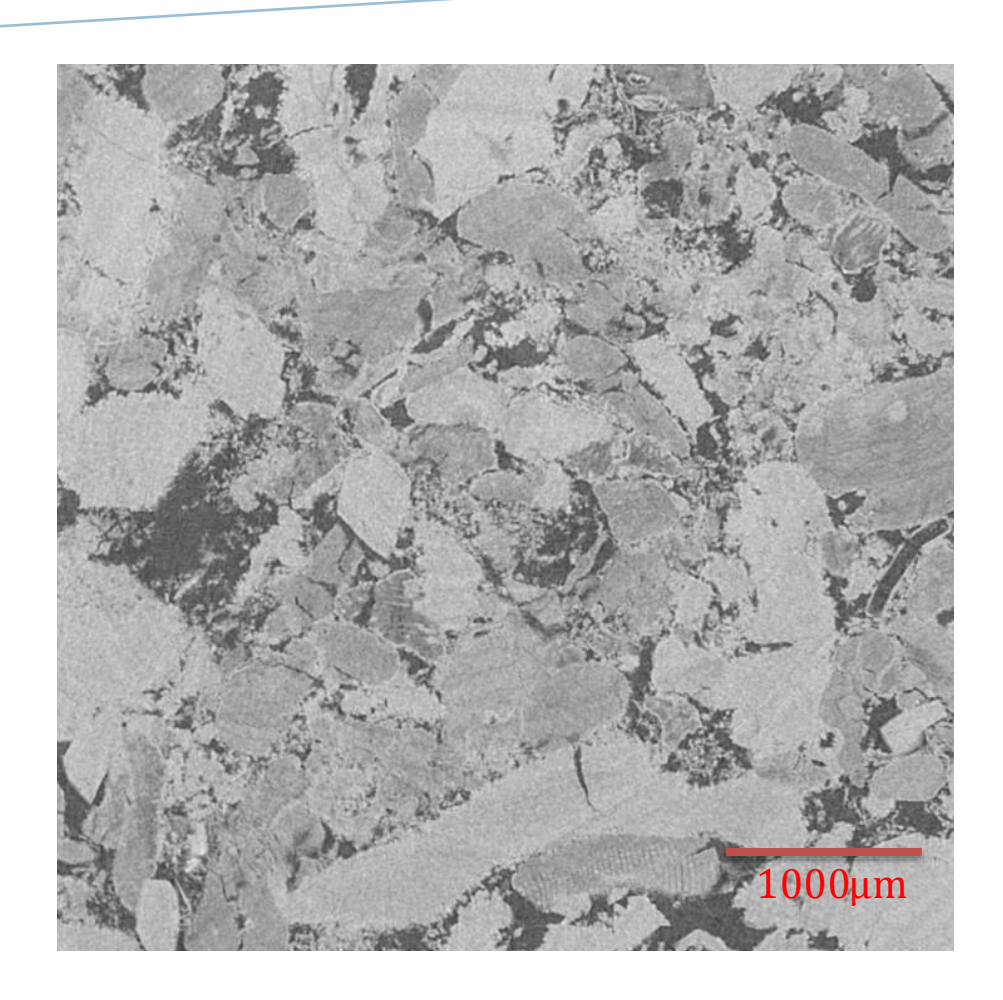


Figure 2.2-27 Hg porosimetry of Estaillades limestone

An 8 mm plug diameter of Estaillades limestone has been scanned and reconstructed thanks to the X-ray Skyscan microtomograph. A slice is shown below (Figure 2.2-28). The gray levels therefore are the X-ray attenuation and finally the variability of grains density is important. From Figure 2.2-28 we may certainly interpret the grain gray levels by CaCO<sub>3</sub> and MgCO<sub>3</sub> presence but also by mesoporosities of grains contributing in the voxels attenuations. The histogram of such porous medium only exhibits two distinct peaks with one of them seeming to be a dual peak in highest densities.



# Estaillades Limestone

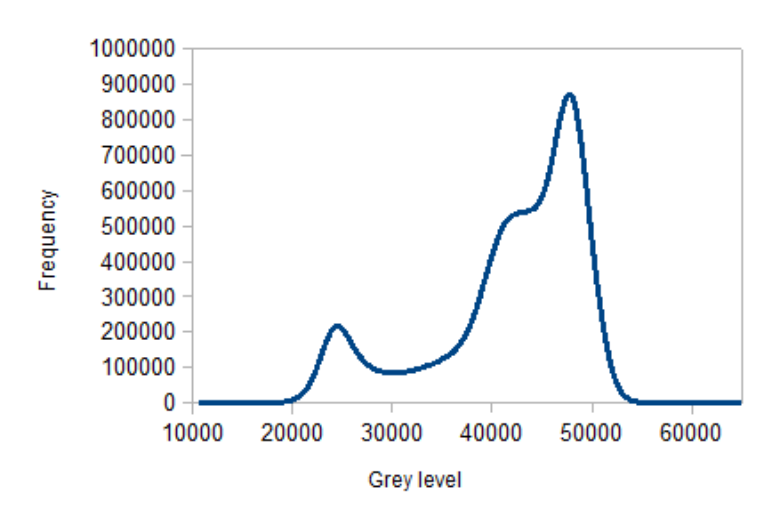


Figure 2.2-28 Estaillades limestone slice observed by X-ray microtomography and the obtained histogram after the Non Local Mean filtering of the image.

The identified from micro-CT image porosity was labeled in the image below. The corresponding macroporosity is about 17 % and only contributes to 50 % of the global porosity. Considering the

exploitation of intermediate gray levels we decided to correlate the images of a Back Scattering Electron Microscopy (BSEM) images with the corresponding micro-CT slice of the porous medium. Imaging correlation of the two images are over imposed and shown in comparison of the raw micro-CT image (Figure 2.2-30).

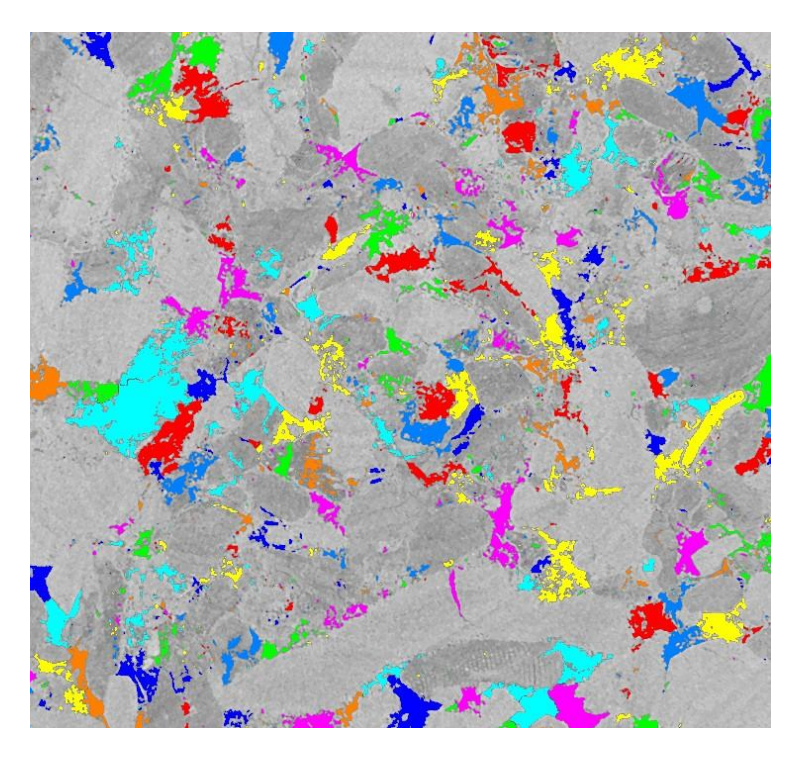


Figure 2.2-29 Macroporosity revealed in the slice and labeled.-

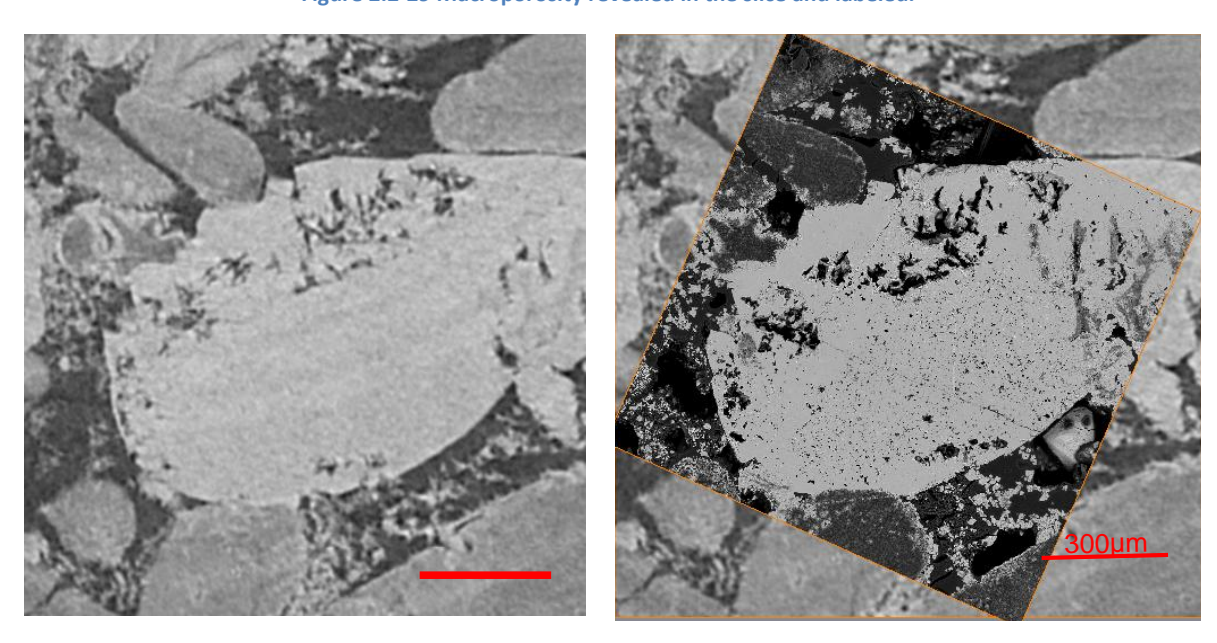


Figure 2.2-30 Left side a grain in its neighborhood obtained by X-ray microtomography (3µm per voxel size), right side the same pore space represented in its center by the corresponding imaging obtained with a Back Scattering Electron Microscopy with a spatial resolution of 500nm

A weak discordance exists in the two images caused by the origin of the compared images. BSEM illuminates only a surface although micro-CT slice has a thickness. The small fluctuations are caused by

differences of subtle textures. A zoomed image of the grain details with the BSEM image over imposed on the micro-CT corresponding slice (Figure 2.2-31 left side) and the micro-CT slice over imposed on the BSEM image clearly exhibit no detail may be deduced form the gray scales issue from the X-ray images. The largest pore diameter observable in BSEM image is undiscerned in micro-CT image. A structured fault we may also observe is no more detectable. The noise level in image only causes the gray level fluctuations of the grain.

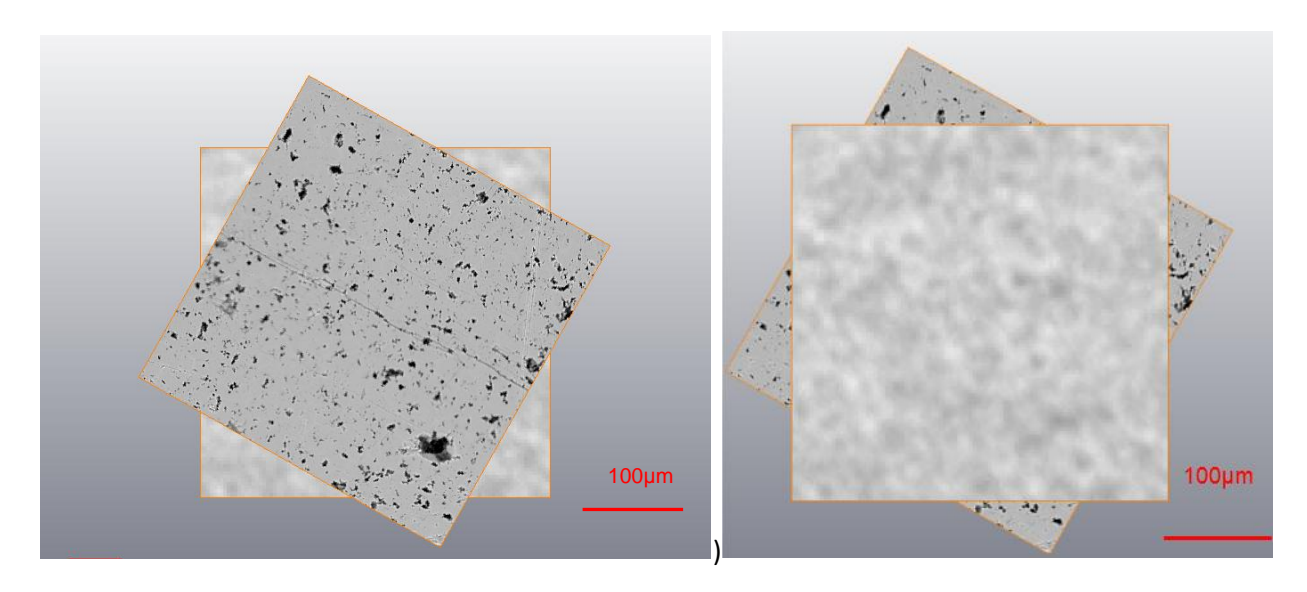


Figure 2.2-31 Superposition of corresponding tomographic slice (3 mm of voxel size) on BSEM image (left) (500 nm of pixel size) and with inversion of the superposition (BSEM image on tomographic slice)

Without any concluding results we decided to proceed to inverse method to observe the pore network which imposes to match the porosity to the experimental value measured with Hg porosimetry device. During the X-ray tomographic segmentation process we have imposed a threshold corresponding to the real porosity of 30%. A slice is shown below (Figure 2.2-32).

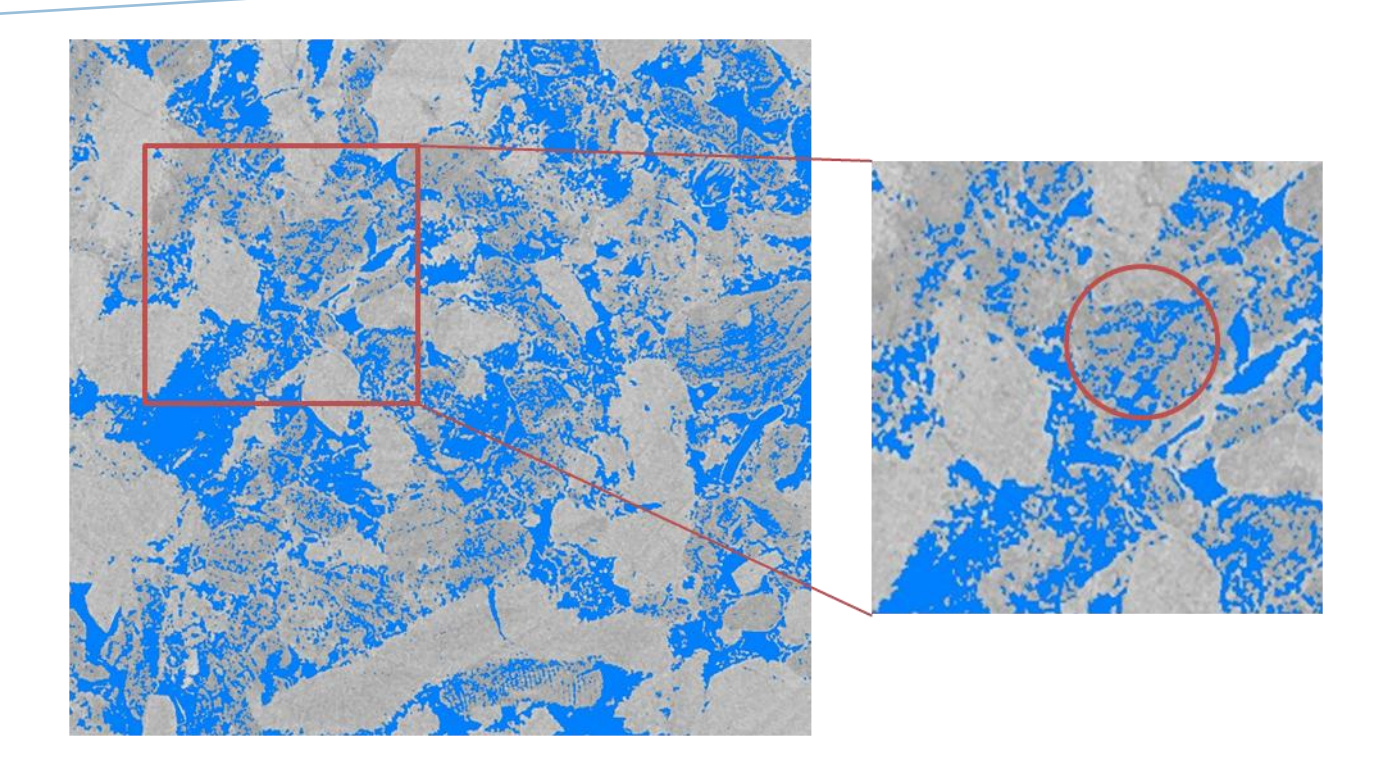


Figure 2.2-32 Slice constrained to 30% porosity by thresholding.

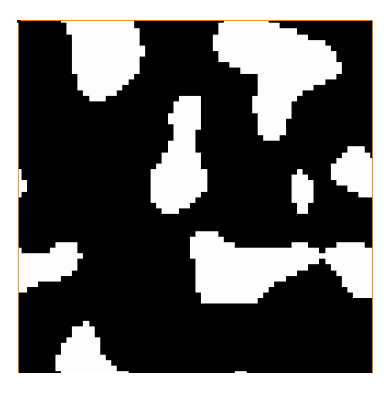
The obtained images clearly propagated by gray level continuity exhibit isolated clusters in images (for example in zoomed circle on figure 2.2-32), which are due to a clear limitation and over interpretation of the images. The spatial resolution is a limiting factor but clearly apparent fluctuations in images are purely issue from the noise. Such inconsistency does not allow properly estimate the porosity of the Estaillades limestone sample. At most the segmentation process may exhibit the resolute porosity and may not be used to reveal the subvoxel contribution. This is very critical to analyze the multiscale objects that are the rocks. The first boundary to express reliability in Digital Rock Physics concerns the ability to image the whole pore network visualization with sufficient details level.

# 2.2.5.1.3 Synthetic sample

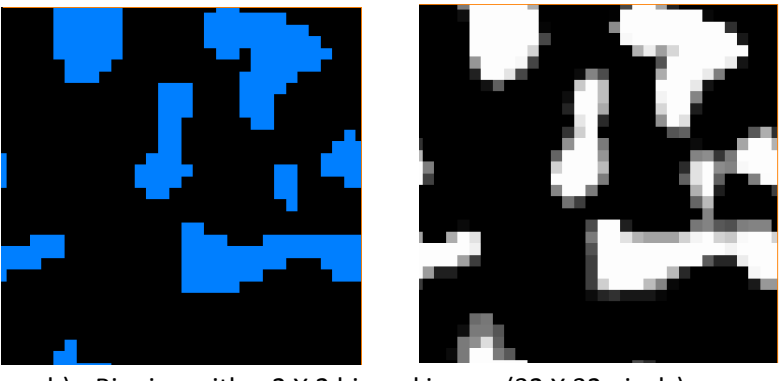
To perform a balance between image resolution and petrophysical properties we propose to eradicate the impact of noise and contrast using a synthetic binary model of periodic pore network. We successively decreased the resolution by a pixel binning process of the initial network. Intermediate gray levels appearing are representative of the averaged gray levels of the binned pixels. The aim of this study is to observe the degradation of porosity and permeability evaluations caused by the resolution decreasing of the image resulting from the binning segmentation process. In terms of detection, binning method simulates the process of combining charge from adjacent pixels in a CCD during readout. The binning is performed prior to digitization in the on-chip circuitry of the CCD by control of the serial and parallel registers. The two main advantages of binning method are to improve signal-to-noise ratio (SNR) and the increase of the frame rate although the spatial resolution is of course degraded proportionally to the used

binning. The occurring binning takes place in post processing therefore lacking of noise almost the image is perfectly representative of the resolution contribution to k- $\phi$  properties.

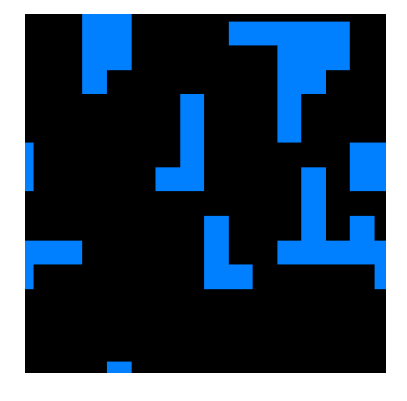
The elementary data set corresponding to the smallest periodic element is a 64 X 64 X 64 voxels (fig. 2.2-33a). Xlab hydro requires defining the voxel size. We arbitrarily select to be one micrometer. The binned images will successively form periodic structure of 32 X 32 X 32 voxels, 16 X 16 X 16 voxels up to 8 X 8 X 8 voxels (Figure 2.2-33 b, c and d). Intermediate gray levels will require a new segmentation process performed from the lowest resolution for an 8 X 8 binning up to the highest resolution. It permits to assume no a priori on the segmentation. The workflow is described below and represented by the same slice to the several step of the process.

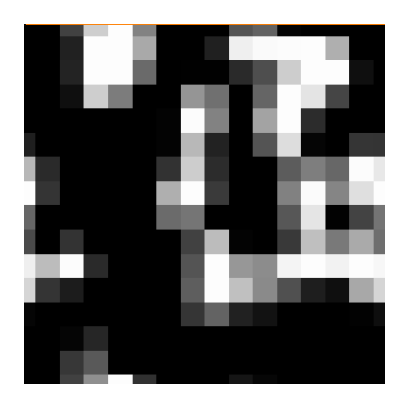


a) Initial image in 64 X 64 pixels

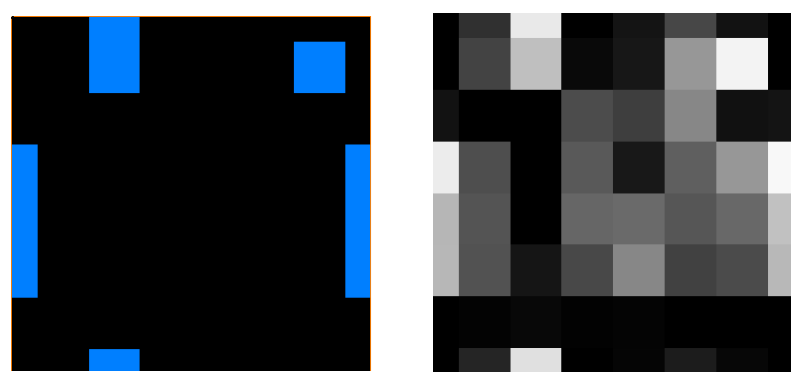


b) Binning with a 2 X 2 binned image (32 X 32 pixels)





### c) Binning with a 4 X 4 binned image (16 X 16 pixels)



d) Binning with a 8 X 8 binned image (8 X 8 pixels)

The exact porosit porosity of 28.62 suppose that the

nducts to a global .44%. One would

The 8-shrink fact. Figure 2.2-33 Workflow of the binning process relative to the sensitivity tes work connectivity dramatically decreases up to reach a no percolating network therefore a null permeability. The loss of resolution is at the origin of changes in porosity and permeability up to alter the pore network connectivity where the permeability suddenly breaks down. The results obtained here clearly show a degradation of the workflow reliability with the loss of resolution of a perfect image due to the binning.

The eigen vectors yielding to the principal directions of flow and the eigen values representing the principal permeabilities evaluate with the binning therefore the reduced resolution. In extreme cases for an 8 X 8 X 8 binning there are no percolating flows between the various inlets and outlets axes of calculated flow. There are no more percolating pathways required for flow.

Table 2.2-2 Calculated eigenvectors and eigenvalues of the permeability as a function of the image binning

Geometry file	kx [μm²]	ky [μm²]	kz [μm²]	Eigen values	Eigen vector x	Eigen vector y	Eigen vector z
Raw 64x64x64	0.2743	-0.0240	0.0014	0.1820	-0.2523	-0.9668	0.0405
	-0.0240	0.1884	0.0032	0.2806	-0.9670	0.2503	-0.0475
	0.0014	0.0032	0.2684	0.2686	-0.0357	0.0512	0.9981
Bin 32x32x32	0.2646	-0.0357	-0.0016	0.1719	-0.3594	-0.9321	-0.0456
	-0.0357	0.1858	-0.0041	0.2784	-0.9331	0.3597	-0.0010
	-0.0016	-0.0041	0.2678	0.2680	-0.0180	-0.0421	0.9990
Bin 16x16x16	0.3085	-0.0434	-0.0248	0.1815	-0.3651	-0.8480	-0.3841
	-0.0433	0.2122	-0.0265	0.3285	-0.9266	0.2910	0.2381
	-0.0250	-0.0265	0.2638	0.2745	0.0880	-0.4415	0.8929
Bin 8x8x8	0.0014	-0.0008	0.0008	0.0029	-0.5767	0.5783	-0.5771
	-0.0014	0.0008	-0.0008	0.0000	0.5140	0.8527	-0.0933
	0.0014	-0.0008	0.0008	0.0000	-0.2195	0.4727	0.8534

The represented absolute permeabilities are determined by the trace of the permeability eigenvalues expresses in eigenvectors base. The results are represented at figures 2.2-34 and 2.2-35.

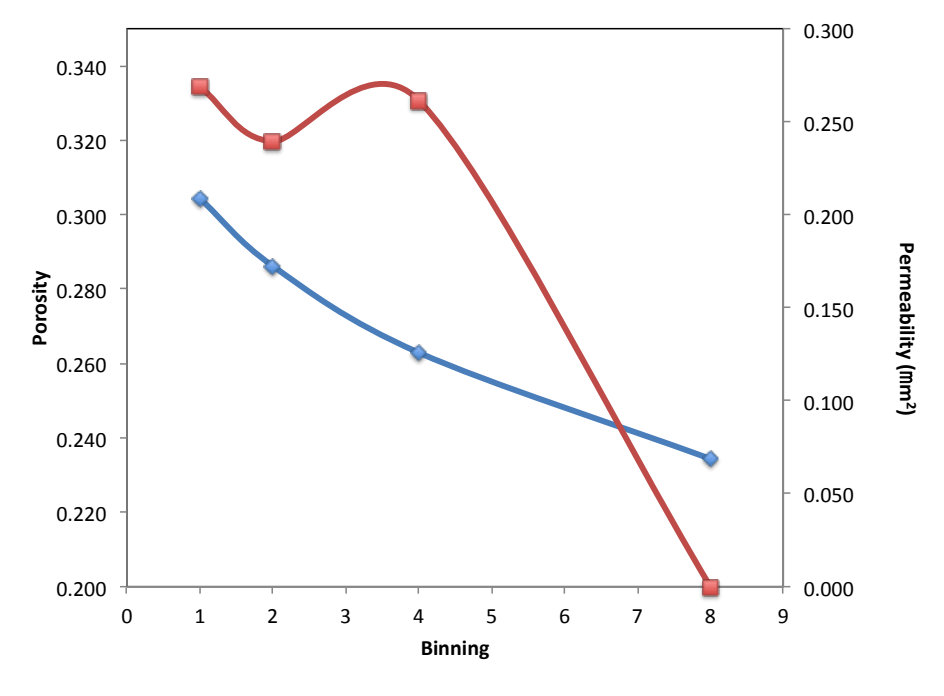


Figure 2.2-34 Porosity (blue diamond) and permeability (red square) evolution as a function of binning shrink factor

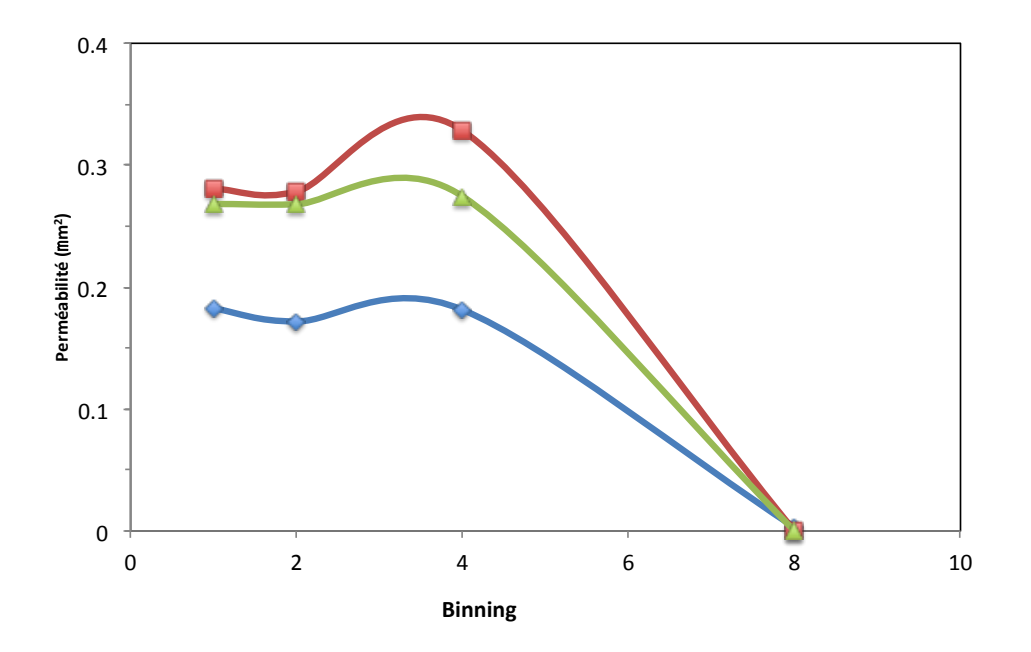


Figure 2.2-35 Eigenvalues kx (blue diamond), ky (blue square) and kz (green triangle) of the permeability tensor.

The permeability has been calculated in a larger data set replicating in the three dimensions the periodic shape. The permeability calculations tensors are the same than for unique periodic pore network.

Streamlines representation of monophasic fluid flow (Figure 2.2-37) shows in red and yellow colors the most impacting topological zone on the permeability flow: the pores throat and constrictions.

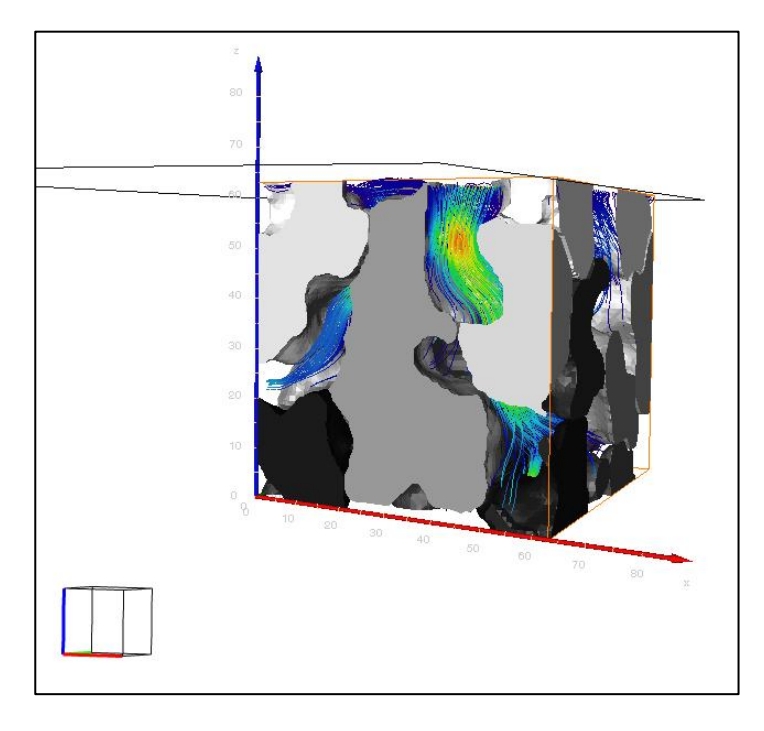


Figure 2.2-36 streamlines of the periodic cell

The throat pores and local constrictions are the most impacting parameter of the flow. These tightest zones especially affect dramatically the permeability when the connectivity is altered. The porosity seems to be less affected in this case by the loss of resolution but the R.M.S. noise usually acquired in the detector and the reconstruction noise may perturb the imaging. These topological loci are the most complex to image due to very low number of voxels describing the topology.

# 2.2.5.2 Computed petrophysics: mesh and method sensitivities (paper form)

To compute permeability in image we preliminarily used Xlab hydro (toolbox in Avizo). This software is based on a finite volume meshing strictly using the voxel. We propagate Stokes equation in a permeameter or periodic configuration with only control on the fluid viscosity and convergence criterion. The preliminaries results clearly exhibited very important changes in the permeabilities with convergence value also we proposed to the IMFT (Institute of Fluids Mechanics of Toulouse) team research to work on the topic in order to be more confident on the parameters permitting to numerically measure the permeabilities. The second objective was to test the scalability with the aim in a near future to test algorithms in images of several natural porous media to validate by experiments the permeameter configuration.

### 2.2.5.2.1 Introduction

Understanding the interactions between the micro-structural geometry and the macroscopic effective properties of porous media is an issue in a wide range of industrial fields as hydrology, petrology, catalysis, filtration and so on. A huge effort has been spent to theoretically estimate or to numerically establish a relation between geometric microstructure and macroscopic physical properties. For porous materials, permeability is the macroscopic parameter of basic practical interest, and its measurement is important to predict macro-scale behavior of flows.

Recently, considerable progresses in pore-space imaging and high performance computing have accelerated the development of a specific domain called Digital Rock Physics (DRP). However, a lot of different works have been previously led for several decades (Anguy et al. 1994; Spanne et al. 1994). This domain aims to complement physical laboratory measurements (Renard et al. 2001) by providing fast and effective access to rock properties from three dimensional images (Andrä et al. 2013a; Andrew et al. 2013; Blunt et al. 2013).

The numerical determination of permeability, and more generally of effective properties, follows a classic upscaling strategy. This strategy is based on two major elements: (i) the knowledge of the local geometry and (ii) the evaluation of the flow inside this local complex structure. The first key point is to ensure that the considered sample is representative of the porous medium, i.e. the effective properties are unchanged for larger volume than the reference used. This minimal required volume is commonly called the representative elementary volume (REV). The upscaling principle is illustrated on figure 2.2-37.

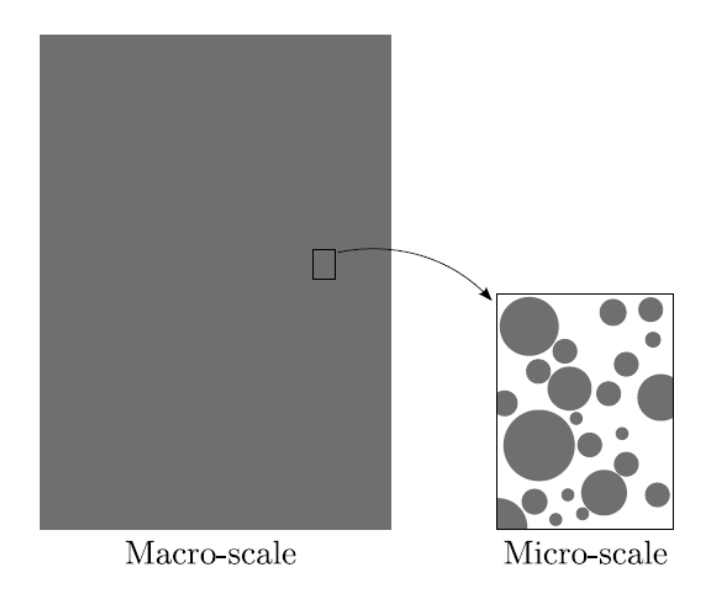


Figure 2.2-37 Sketch of the different scales.

At the pore-scale, as classically admitted (Bear 1972), the single phase flow in porous media is governed by the Stokes equation. The fluid flow on macroscopic level is commonly described by Darcy's law (Whitaker 1986) and characterized by the macroscopic permeability which can be evaluated by integrating the local fields. This upscaling work-flow has several crucial aspects that may affect the resulting computed permeability.

Experimentally, the major source of uncertainty in permeability determination is the statistical error caused by the insufficient resolution. This can lead to a loose of essential local information of the materials (micro and meso-porosities, pore geometry, pore network connectivity or surface roughness of the minerals) (Arns et al. 2005). The image processing, that also includes signal treatments and binarization processes, is known to affect the pore morphology reconstruction and therefore the transport properties (Andrä et al. 2013a).

Numerically, several aspects can influence the computed macroscopic permeability such as the numerical method for example. Finite Volume (Spanne et al. 1994; Bogdanov et al. 2003) and Lattice Boltzmann (Hyväluoma et al. 2012; Khan et al. 2011) are the two most commonly used methods for pore-scale flow evaluation. It has been shown that the used numerical approach has non-negligible influence on the permeability determination (Manwart et al. 2002; Andrä et al. 2013b). Moreover, considering a continuous approach such as the Finite Volume method, the mesh refinement affects also the local flow simulation and consequently macroscopic properties calculations.

Mainly for the large computation time required in DRP, numerical simulations are usually performed on a cartesian grid mesh directly extracted from the initial tomographic image. However, the relative difference in term of intrinsic permeability for different meshes obtained from the same tomographic image has not been explored. Finally, calculated macroscopic properties may depend on the used boundary conditions. The two main conditions are pressure imposed which mimics an experimental

permeameter configuration (Mostaghimi, Blunt, et al. 2012), and the resolution of a closure problem with periodic conditions (Anguy et al. 1994).

The main objective of this work is to evaluate the influence of the several parameters mentioned above (volume of the sample, mesh refinement level and applied boundary conditions) on the permeability computation for a single given sample. Direct numerical simulations are performed using the Finite Volume method implemented in the open-source platform OpenFOAM® (FOAM 2013). This software has efficient parallel capacities required for the following study, particularly for the mesh sensitivity study which leads to large computation time.

We present first the technical aspects of the work-flow (experimental and numerical). Then, numerical results are presented and discussed: sample representativity, mesh sensitivity, configuration comparison and parallel efficiency.

### 2.2.5.2.2 Materials and methods

In this technical section, we firstly describe the experimental imaging and associated post-processing of the considered sandstone sample. Next, we present the different aspects (boundary conditions, meshing, models and methods) used for the numerical evaluation of absolute permeability

### 2.2.5.2.2.1 Experimental imaging and processing

The core-plug we used in this work is an outcrop Dausse sandstone (Permian). The core sample has 2 cm of height and 8mm of diameter. The measured liquid permeability is evaluated to 320mD. The mineral composition of the sample is given in table 2.2-3 and the porosity of the core plug is 12.7%.

We could expect that the initial structure of the matrix was preserved during the sample preparation. The composition mimics fairly well the Berea sandstone composition according to the previous observations of (Khan et al. 2011).

ElementQuartzClaysFeldsparPyritePercentage86.13.110.60.2

Table 2.2-3 Rock sample composition

### 2.2.5.2.2.1.1 Pore-space imaging protocol

The used X-Ray Microscope Computed Tomograph (XRMCT) was the Versa 500 XRM manufactured by XRadia <sup>®</sup>. The resolution is purely determined by the selected objective and the geometrical magnification relative to source/object/detector distances. Although, most of in-lab microtomographs exploit the geometrical magnification limited by the focus spot size. For the used XRMCT the set-up is based on an optical magnification of visible light by a microscope installed behind the scintillator to magnify the

converted visible light. The limiting resolution is here due to Rayleigh's diffraction criterion limiting the reachable detail *d* to

$$d = \frac{1.22\lambda}{N A}$$

where  $\lambda$  is the reemitted wavelength by the scintillator once X-rays converted by the scintillator and N.A. is the numerical aperture of the microscope.

This XRMCT technology, before the only prerogative of synchrotrons, collected 1000 radiographies at 1 second of exposure time were performed at 60 kVp. The reconstructor, developed by XRadia®, has provided to image at 9.6 micrometers per voxel of the core-plug. In a purely absorption mode, the gray values associated with each voxel are theoretically proportional to its X-ray attenuation. The refraction index n in X-ray wavelengths is:

$$n = 1 - \delta + i\beta$$

with  $\delta$  related to the phase-shift and  $\beta$  to the attenuation of X ray wave in a medium. The imaginary term is the absorption term which is purely dependent on the electronic density of the material and the length of the wave vector. The naturally polychromatic X-ray light emitted from electron collisions on a tungsten anode is also to the origin of numerous artifacts linked to the intrinsic of the refraction terms to the wavelength. The occurring summation of the whole energies may also contribute to low contrast level between dissimilar materials. The low flux and low contrast specificities of the visible photons reemitted by the X-ray scintillators are quite limited with the Versa 500 XRM due to the presence of an optimized specific scintillator in thickness and quantum efficiency. The coupled detector is a CCD, manufactured by Andor® technology. It is characterized by a very high detectability and low noise matched to low light fluxes conditions. Nevertheless, a few noisy pixels are produced by the detector. Almost, the Filtered Back Projection algorithm contributes to produce additional noise mainly caused by the conical beam geometry.

However, in a transmitted mode of tomography, the refracted X-rays impact the detector causing a blurring. This defect may alter the reconstructed image causing a phase propagation artifact at the origin of a ghost at the interface levels. It may possible to reduce this structured artifact adjusting the relative positions between source, object and detector but the most common process consists to apply an image treatment to eradicate the defect.

The complete 3D pore space imaging is performed to 9.6  $\mu$ m3 per voxel size with a total size of 4.272 x 4.272 x 3.437 mm3 ( $\approx$  62.7 mm³). To reduce computational effort in the following sensitivity studies, the image is cropped to a sample size of 1.344 x 1.344 x 2.006 mm3 ( $\approx$  3:62 mm³).

#### 2.2.5.2.1.2 Image processing

Image processing is performed with the commercial software Avizo®. It mainly consists to regularize images to avoid potential misclassification of materials during the segmentation phase. By eradicating noise and structured defects such as phase propagation, the voxels intensity values become representative of the refraction index and therefore of the material in the polychromatic X-rays conditions of the experiment. The used numerical filter is the bilateral filter. The dataset was segmented

by choosing an intensity threshold, with values below the threshold assigned to one phase/material, and those above the threshold assigned to the other phase. Histogram thresholding is currently compared to obtained image to enhance the segmentation accuracy. The original and binarized considered volumes are represented on figure 2.2-38.

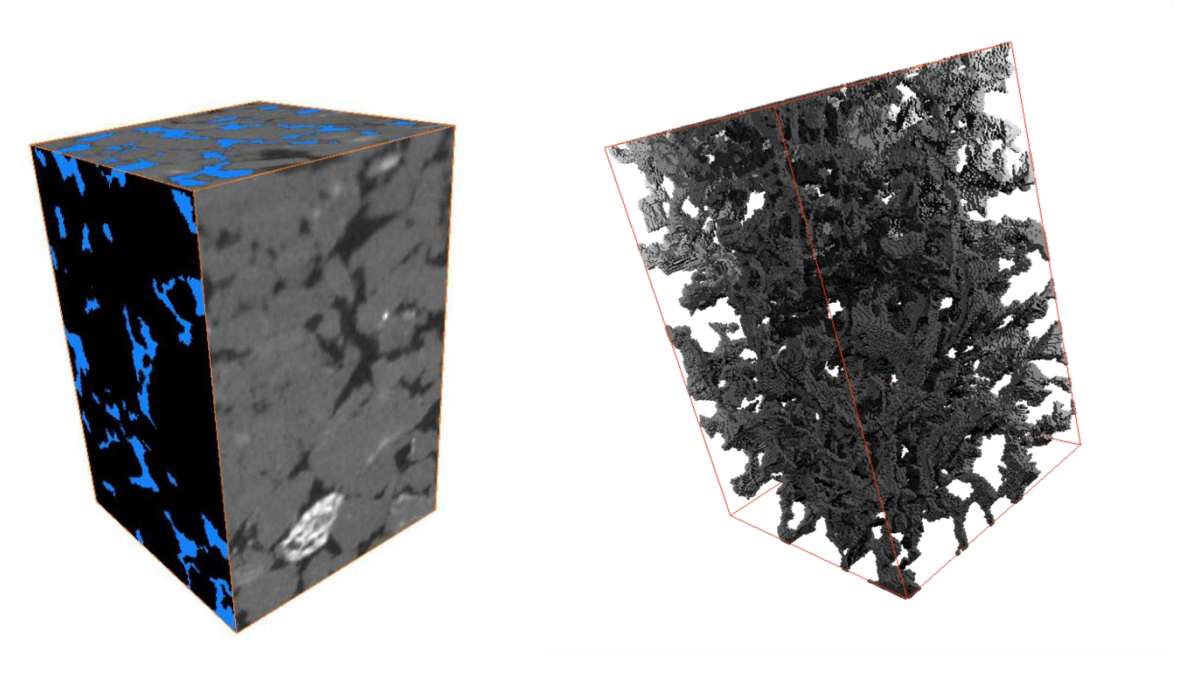


Figure 2.2-38 Visualization of original (a) gray-scale image and extracted void space (b).

From the obtained binarized image, a Representative Elementary Volume (REV) analysis is performed to ensure that the concerned sample is representative of the studied porous medium. The applied REV determination method is the direct application of the Bear definition (Bear 1972), i.e. based on the sample computed porosity. Porosity is calculated from successive sub-volumes, obtained by progressive centered-cropping of the full initial 3D volume, i.e. from  $\approx 62.7~\text{mm}^3$  to  $\approx 0.001~\text{mm}^3$ . This procedure is repeated until microscopic effects dominate the porosity measurement. Figure 2.2-40 reports the computed porosity as a function of the sample volume and exhibits a REV of about 1 mm3. The volume of the core-plug used for numerical computation (3.62 mm³) is larger than obtained REV and can therefore be considered, at least in term of porosity, as representative of the studied porous medium. This result is in good agreement with the observations of Biswal et al. (Biswal et al. 1998) where REV characteristic size of 230 to 700 µm in Berea sandstone has been determined using the same analysis in image processing. Note that the REV definition depends on the studied physical problem and for that reason the representativity of the sample is also explored numerically in terms of permeability in Representativity of the sample section.

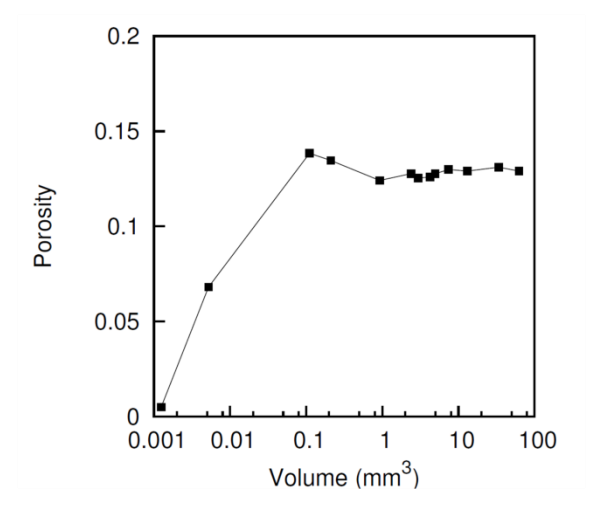


Figure 2.2-39 Sample porosity as a function of considered sub-volume. REV characteristic length size (≈1 mm³) is determined from this pore space characterization (same procedure as Bear (Bear 1972)).

### 2.2.5.2.2 Numerical work-flow

In this subsection, we describe the different steps of the procedure used to evaluate the effective permeability from the digitalized rock surface, evaluating micro-scale flows.

The considered sample is a rectangular parallelepiped whose greatest length is the z-direction. The initial image is composed of 140 x 140 x 209 voxels. The surface describing the fluid space is based on the original image voxels. The choice of keeping a hexahedral description of the surface is done to limit the influence of an additional processing. The sample, imaged with a voxel length size of  $9.6\mu m$ , has a volume of  $3.62 \ mm^3$  and a computed porosity of 12.75%.

### 2.2.5.2.2.1 Configurations

Two different numerical configurations, illustrated on figure 2.2-40, are used to determine the sample permeability. These configurations mainly differ in the boundary conditions used for the evaluation of the flow at the pore scale.

The first one corresponds to the experimental setup of a permeameter (figure 2.2.-40a). A pressure difference is imposed on either side of the sample and a no-slip boundary condition is used on the other faces of the sample.

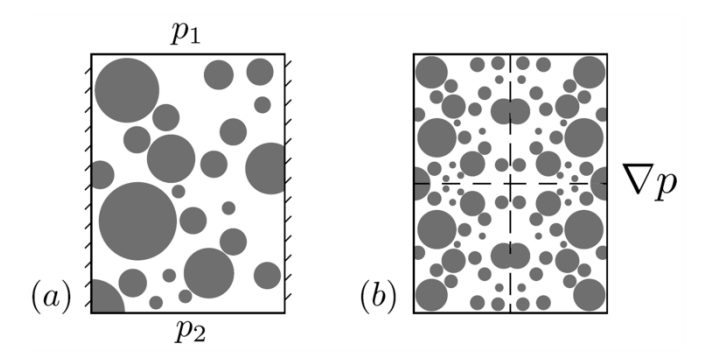


Figure 2.2-40 Description of the two configurations used for the determination of permeability: (a) configuration 1 reproduces the experimental setup of a permeameter and (b) configuration 2 is based on the periodization (by symmetry) of the initial sample which enables the use of a volume averaging approach.

The second method consists in solving a closure problem which has the structure a Stokes problem (see Section "Mathematical models") and implies that the representative elementary volume considered is periodic (Whitaker 1986; Quintard & Whitaker 1987). However, this is obviously not the case of the real sample used in our study and it requires to artificially generate the periodicity by periodizing of the sample as illustrated on figure 2.2-40b. The fields numerically solved are thus periodic in each spatial direction.

In both configurations a no-slip boundary condition is imposed at the solid surface and three calculations (one in each principal direction) are necessary to evaluate the permeability tensor. In the following, these two configurations are respectively referred as configuration 1 for fixed pressures boundary conditions and configuration 2 for periodic boundary conditions.

#### 2.2.5.2.2.2 Meshes

Using the rock surface identified by image processing (see Section "Image processing"), we generate the mesh representing the pore-space of the sample necessary to simulate fluid flow inside the porous medium. For that purpose, we used one of the native meshers of the open-source CFD toolbox OpenFOAM®, snappyHexMesh. A hexahedral mesh perfectly matching the original surface mesh is thus reconstructed as depicted on figure 2.2-41.

The zoom on a part of the mesh (figure 2.2-41) allows illustrating the initial refinement level, corresponding to the native image resolution (refinement level 1 is defined as one computational cell per voxel). In the following, refined meshes are generated from this initial level to verify spatial convergence of computations. To increase refinement level, each cell is equally divided in 8 new cells. The sample porosity and rock surface are unchanged.

Table 2.2-4 Number of mesh elements for the different studied configurations. In the case of configuration 2, the refinement level 3 is not treated because of the too large number of mesh elements ( ≈257 millions)

Refinement	Configuration 1	Configuration 2
Level 1	522 188	4 177 504
Level 2	4 177 504	33 420 032
Level 3	33 420 032	

The different tested levels of refinement in this study are reported in table 2.2-4. Three levels are used in the configuration 1 while solely two levels are used in the configuration 2. For an equivalent refinement level, the configuration 2 needs 8 times more cells because of the periodization (see figure 2.2-40b). Therefore, the third level of refinement in configuration 2 will require too many resources (more than 250 million of cells).

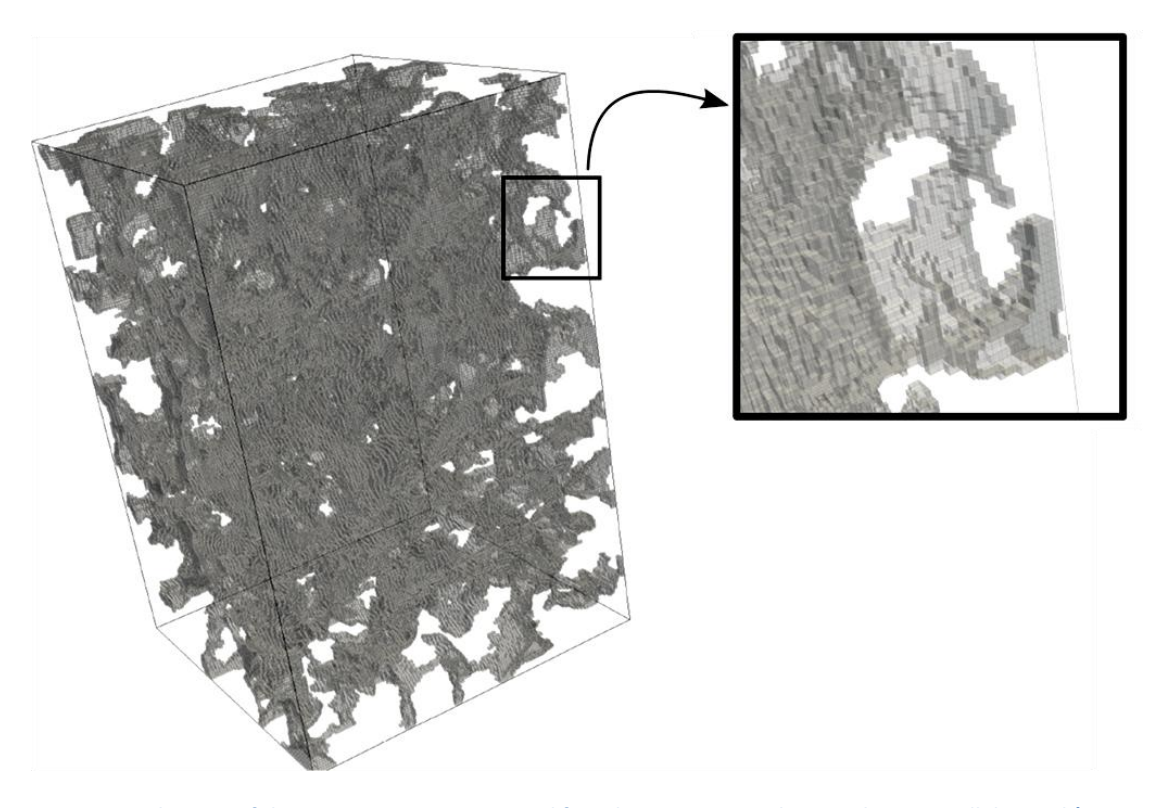


Figure 2.2-41 Visualization of the pore-space reconstructed from binary images. The sample is a parallelepiped ( $1.3 \times 1.3 \times 2$  mm<sup>3</sup>) and the z-direction is the large one. The zoom permits to observe the local refinement of one pore space.

#### 2.2.5.2.2.3 Mathematical models

For mathematical models we consider two scales: the micro-scale, where the pore-space geometry of the sample is explicitly represented (see figure 2.2-38) and the macro-scale, where the sample is considered as a unique computation cell (containing both solid and pore-space) with effective properties. In this study we suggest incompressible non-inertial single phase flows characterized by low Reynolds numbers, involving the resolution of Stokes' equations. Neglecting gravity, the conservation and momentum equations at the pore-scale write

$$\nabla \cdot u = 0$$

$$\mu \Delta u = \nabla p$$

where u(x) is the micro-scale velocity field, p(x) the pressure and  $\mu$  the dynamic viscosity of the fluid. At the macro-scale, the Stokes' momentum equation 2.4 is reformulated as the so called Darcy's law:

$$v = -\frac{K}{\mu} \cdot \nabla p$$

Where  $\mathbf{v}$  is the average fluid velocity and  $\mathbf{K}$  the permeability tensor. Using the Darcy's law, the permeability tensor can be determined from three pore-scale simulations (one for each spatial direction), by averaging the micro-scale velocity field  $\mathbf{u}(\mathbf{x})$  over the sample. To complete this set of equations we need boundary conditions that depend on the different configurations described in section "Configurations". For the configuration 1 (figure 2.2-41a) Dirichlet boundaries conditions are used for the pressure (inlet and outlet boundaries) and the velocity (lateral boundaries). For the configuration 2 (figure 2.2-41b), due to the periodic boundary conditions the pressure gradient in equation is decomposed as:

$$\nabla p = \overline{\nabla p} + \nabla \overline{p}$$

with  $\overline{Vp}$  an average pressure gradient and  $\overline{p}$  the deviation of the pressure gradient. The average pressure gradient is an imposed volumic source term and the computed deviation needs a pressure reference value (fixed at the outlet for example). This configuration is, a priori, more representative of the real permeability because it mimics the encapsulation of the considered sample within a larger porous medium in real reservoir conditions. However, as the periodicity is enforced by mirroring the sample, it could increase significantly computation time.

# 2.2.5.2.2.4 Numerical methods

In previous DRP works, different numerical methods have been used to compute the fluid flow at the micro-scale. For example, Finite Difference (FD) method (Mostaghimi, Bijeljic, et al. 2012) and Finite Volume (FV) method (Petrasch et al. 2008) are classically used. Several works use also particle-based methods such as Lattice Boltzmann methods (see for examples (Keehm 2004; Boek & Venturoli 2010; Ahrenholz et al. 2006; Hyväluoma et al. 2012)). Recently, a study comparing different numerical methods has been proposed (Andrä et al. 2013b).

Simulations within the context of DRP involve a significant number of discretization cells, and therefore require suitable software with parallel computation abilities. The open-source toolbox OpenFOAM® is based on FV method, which seems to be an appropriate platform thanks to its parallel capacities (Bijeljic

et al. 2013). Our two different solvers are based on the classic Semi-Implicit Method for Pressure Linked Equations (SIMPLE) algorithm, and all the discretization schemes are second order. The required precision on the pressure field is of the order of  $10^{-12}$ .

#### 2.2.5.2.3 Results and discussion

In this section we present and discuss the different computations led on the sample. First, the mesh sensitivity of permeability determination is discussed. Next, we compare the measures obtained using different methods of determination. Finally, after a discussion about the non-diagonal terms of the permeability tensor, we present the parallel efficiency of the solvers used in this study.

The figure 3.1 shows an illustration of the computed pressure and velocity fields in the configuration 1 for the mesh corresponding to original image resolution. Its permits to bring out the preferential paths of the fluid flow through the rock in a permeameter configuration.

In this section we present and discuss numerical results obtained on the sample. First the representativity of the sample, initially defined in terms of porosity, is also ensured in terms of permeability. Then, the mesh sensitivity for permeability determination is discussed. Next, we compare the measures obtained using the different configurations. Finally, after a discussion about the non-diagonal terms of the permeability tensor, we present the parallel efficiency of the solvers used in this study.

The figure 2.2-43 shows an illustration of the computed pressure and velocity fields in the configuration 1 for the mesh corresponding to original image resolution. It permits to bring out the preferential paths of the fluid flow through the rock in a permeameter configuration.

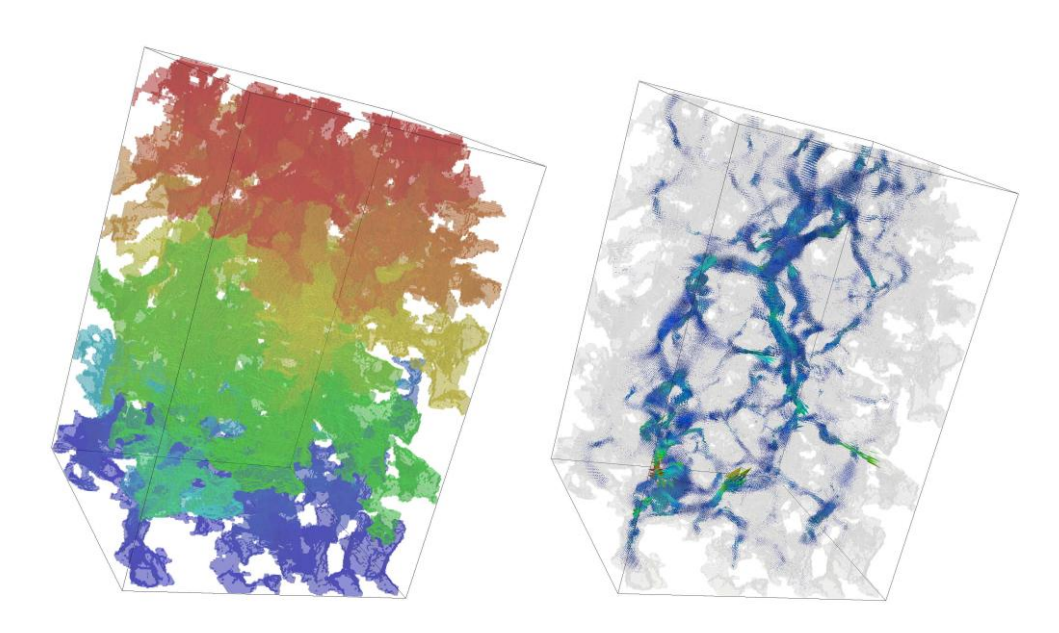


Figure 2.2-42 Illustration of (left) pressure and (right) velocity vector field obtained on the considered sample in the configuration 1 with initial image refinement

# 2.2.5.2.3.1 Representativity of the sample

To test the representativity of the considered sample, we evaluate using configuration 2 and refinement level 1 the equivalent permeability varying the volume of the considered region. Results are reported on figure 2.2-43.

The different considered sub-volumes are constructed from the initial sample mesh, removing computational cells along sample boundaries. To respect the initial sample aspect ratio, note that the number of removed cells depends on the considered direction. For example, the initial sample has a size of  $140 \times 140 \times 209$  voxels and the two first sub-volumes considered have  $136 \times 136 \times 203$  (92% of initial volume) and  $132 \times 132 \times 197$  voxels (84%).

We observe that the relative deviation for computed permeabilities in z-direction is lower than 7% for sufficient large volumes (50% of the initial volume). From this we cannot infer on the representativity in term of permeability of the considered volume but suggests that the permeability REV is approximatively reached. Note that the order of the characteristic length for the computed permeability REV (around 2 mm) is larger than the porosity one (around 1 mm) computed from binarized images.

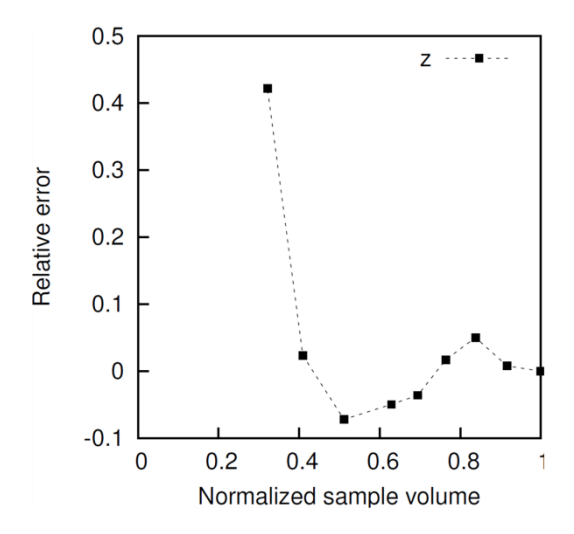


Figure 2.2-43 Relative error of Kzz function of the normalized volume considered (configuration 2, refinement level 1)

#### 2.2.5.2.3.2 Mesh sensitivities

The mesh sensitivity is discussed on the configuration 1 for which we dispose of three refinement levels. The diagonal terms of the obtained permeability tensor are reported in table 2.2-5.

Table 2.2-5 Diagonal permeability tensor terms for the configuration 1 (in darcies) varying the mesh refinement

Refinement	K <sub>xx</sub>	K <sub>yy</sub>	K <sub>zz</sub>
Level 1	0.762676	0.850044	0.576021
Level 2	0.600037	0.659429	0.441091
Level 3	0.521925	0.569730	0.378196

The table 2.2-6 shows the relative error evaluated following

$$\varepsilon_{ii} = \frac{\left|K_{ii}^3 - K_{ii}^j\right|}{K_{ii}^3}$$

With I = x, y, z, and j = 1, 2,

Where the exponent j is related to the refinement level (the maximal refinement, i.e. the level 3 is considered as the reference solution).

Table 2.2-6 Relative errors of the diagonal permeability tensor terms for the configuration 1

Refinement	$\epsilon_{xx}$	$\epsilon_{ m yy}$	$\epsilon_{zz}$
Level 1	0.46	0.49	0.52
Level 2	0.15	0.16	0.17
Level 3	-	-	-

We observe that the permeability values decrease rapidly increasing the refinement level. The first refinement level exhibits a relative error close to 50% while for the second, the relative error is reduced to 15%. This point highlights the fact that the absolute permeability values must be taken with the greatest caution. Moreover, we cannot ensure that the third level is sufficient.

Anisotropic permeability is generally of great importance in reservoir engineering and can be evaluated using the anisotropy ratio R (Clavaud et al. 2008) defined as:

$$R = \frac{K_{min}}{\sqrt{K_{int}K_{max}}}$$

where  $K_{min}$ ,  $K_{max}$  and  $K_{int}$  stand respectively for the minimal, maximal and intermediate value of diagonal permeability tensor. The permeability measurements performed by Clavaud et al. (Clavaud et al. 2008)

over a large set of various sandstones highlight a large range of possible values for anisotropy factor R. It varies from 0.84 for the less anisotropic porous medium to 0.19 for the higher anisotropic sample. Recently (Mostaghimi, Blunt, et al. 2012), numerical determination of permeability values was done using some samples, including sand-packs and carbonates, and gave a ratio R close to 0.78 for sandstone and Berea sandstone. For our sample, the computed ratio varies from 0.715 for the refinement level 1 to 0.693 for the level 3, i.e. of the same order as the study of Mostaghimi et al. (Mostaghimi, Blunt, et al. 2012). We can note that even if the absolute permeability strongly depends on the considered refinement level, the anisotropy is conserved and is therefore well predicted by the coarsest mesh.

## 2.2.5.2.3.3 Comparison between experimental and numerical permeability evaluations

The numerical permeameter configuration (configuration 1) can be compared to experimental values along the z-axis on the complete core plug. The experimental permeability of the sandstone sample is measured using a pressure-decay profile permeameter. The size of the cylindrical core plug tested is 2 cm long and 8 mm diameter and the measured liquid permeability is 320 mD. The relative differences with numerical evaluation of  $K_{zz}$ , are about 80% and 18% respectively for the lower and higher refinement level. This highlights the fact that successive refinements on the same image are necessary and tends to improve the numerical permeability determination. However, the relative difference is not negligible even for the finest mesh and cannot be entirely attributed to numerical errors since numerical and experimental conditions are different. In the experiment, the permeability is measured on a much larger sample (the volume is close to 1000 mm<sup>3</sup> in that case and 3.62 mm<sup>3</sup> for the numerical computation). Other possible physical sources of uncertainties might be caused for example by the presence of clay contents in the rock which can react with the flow during experiment and modify locally fluid properties or pore-space geometry.

# 2.2.5.2.3.4 Comparison of numerical methods

The configuration 1 has a variant consisting in imposing a no-flux condition on the lateral borders instead of the no-slip condition. In practice, this configuration is obtained imposing a symmetry conditions on the lateral faces. We have compared results obtained with the two boundary conditions for the refinement level 1. We observe a difference around 1% for the three spatial directions that permits to conclude about a weak impact of the lateral boundary conditions on the evaluation of the permeability tensor. We assume that the volume of the studied sample is sufficiently large to significantly reduce the boundary conditions effects. Variations of greater amplitude between the two methods can probably be observed when reducing the domain (sample) size.

Permeability determinations are then performed with the configuration 2 and the diagonal terms obtained, for different refinement levels, are reported in table 2.2-7.

Table 2.2-7 Diagonal permeability tensor terms for configuration 2 (in darcies).

Refinement	K <sub>zz</sub>	K <sub>yy</sub>	K <sub>zz</sub>
Level 1	1.027449	1.111863	0.847282
Level 2	0.83	0.89	0.67

For the same refinement level, we observe significantly superior values to those obtained with the configuration 1. Selecting configuration 2 as reference, the relative difference for refinement level 1 is superior to 27% and is close to 7% for refinement level 2. Numerical results highlight that the flow in a constrained environment, i.e. in the permeameter configuration, has a non negligible influence on the computed permeability and potentially underestimates its value. However, this effect seems to decrease when increasing the refinement level.

The method comparison can also be performed in terms of complete permeability tensor. Off-diagonal terms are obtained by the transverse components of the averaged velocity field for a given main direction. We should note that in the configuration 2, the velocity averaging is performed on the initial sample and not on the whole computational domain. The domain mirroring imposes zero transverse components to the averaged velocity field. Note that this has no effects on the main component on the velocity as longitudinal components are the same in both cases. The numerical evaluations of permeability from pore-scale flow resolution do not guarantee the symmetry of the tensor, which depends on the used method. The symmetry of the tensor can be imposed by the used numerical method (periodic boundary conditions on the velocity) or by the reconstruction method used to compute the permeability (Piller et al. 2009). In the case of the direct computation from averaged velocity components (as in this study), the permeability tensor is by default non-symmetrical as reported by several studies (Manwart et al. 2002; Galindo-Torres et al. 2012; Khan et al. 2011).

From our computation at the first refinement, we obtain the following complete tensors (in darcies):

$$K_1 = \begin{pmatrix} 0.762676 & 0.134729 & -0.138165 \\ 0.077101 & 0.850044 & -0.036075 \\ -0.043193 & -0.025040 & 0.576021 \end{pmatrix}$$

For the configuration 1 and

$$K_2 = \begin{pmatrix} 1.027449 & 0.139428 & -0.146501 \\ 0.084241 & 1.111863 & -0.040395 \\ -0.047042 & -0.025816 & 0.847282 \end{pmatrix}$$

for the configuration 2. Note that configuration 2 gives also non-symmetry, even with periodic conditions, because averaging is performed on one eighth of the field, i.e. the initial sample. The off-diagonal terms are, as for the main directions, superior for the configuration 2. However, the maximal absolute difference between the two methods is much lower ( $\approx 0.008$  darcies) than for the diagonal terms ( $\approx 0.264$  darcies). The relative difference between the two methods is inferior for the off-diagonal terms (< 10%) than for the diagonal terms (> 20%).

# 2.2.5.2.3.5 Parallel efficiency

This study is based on the open-source platform OpenFOAM® and the domain decomposition method, available in the toolbox, used for parallel computing is scotch (Chevalier & Pellegrini 2008). The following tests are led on the Hyperion cluster from at CALMIP1 consisting in 368 computation nodes of 2 quadcore Nehalem EX processors at 2.8 GHz with 8 MB of cache per processor. The reference computations are launched on 16 cores which represent an elementary block. We observe first that the parallel computations are really efficient in the studied configuration as reported on figure 3.3. This figure also gives an order of magnitude of the required computational time although this real time strongly depends on several parameters (as the fixed tolerance, the linear solvers, etc.).

This study is based on the open-source platform OpenFOAM® and the domain decomposition method, available in the toolbox, used for parallel computing is scotch (Chevalier & Pellegrini 2008). The following tests are led on the Hyperion cluster 1 consisting in 368 computation nodes of 2 quad-core Nehalem EX processors at 2.8 GHz with 8 MB of cache per processor. The reference computations are launched on 16 cores which represent an elementary block of the cluster. Computation time for 16 to 256 processors and for two refinement levels are reported on figure 2.2-45. This figure gives an order of magnitude of the required computational time (≈ 2200 seconds for the level 1 and ≈184 000 seconds for the level 2) although this real time strongly depends on several parameters, such as the fixed tolerance, the linear solvers, etc.

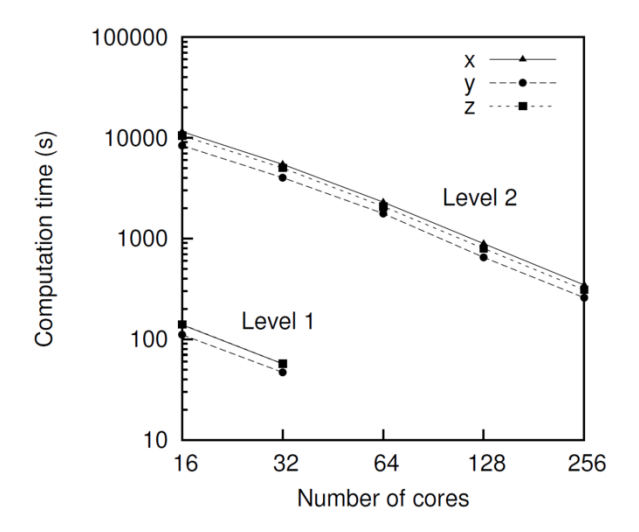


Figure 2.2-44 Evolution of the computational time function of cores number used for the configuration 1 and two refinement levels.

The speed-up *S* for a computation with n processors is computed as follows:

$$S_n = \frac{T_{16}}{T_n}$$

where  $T_n$  is the computation time for n processors and the parallel efficiency  $E_n$  is defined :

$$E_n = \frac{16}{n} S_n$$

We reported the speed-up of the solvers for the configurations 1 and 2, respectively figure 2.2-47a and figure 2.2-47b for the same size of linear systems, i.e. for the same number of cells. It corresponds to the refinement level 2 for the configuration 1 and the level 1 for the configuration 2. The scaling, shown in the z-direction is similar for the other spatial directions.

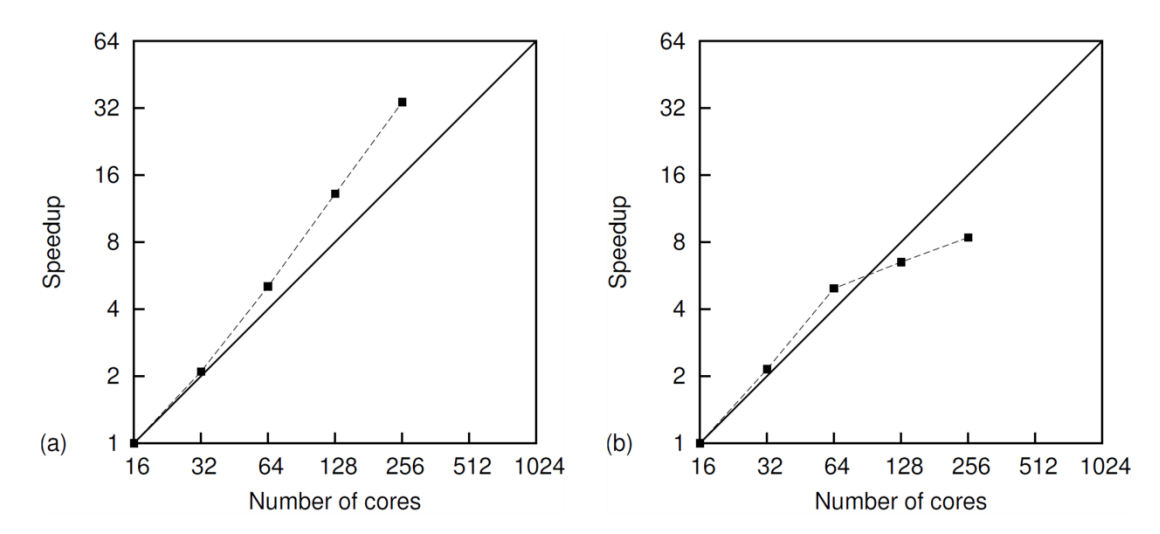


Figure 2.2-45 Strong scaling: (a) for the configuration 1 (refinement level 2, z-direction), this graph shows a super-linear scalability and (b) for the configuration 2 (refinement level 1, z-direction)

For the configuration 1, the observed speed-up is better than the linear speed-up: for 256 processors, the parallel efficiency is even superior to 2 ( $E_{256} \sim 2.12$ ). This super-linear speed-up could be partially explained by a cache memory effect: the high access memory is needed because of the wide amount of meshes which are subdivided when increasing the processors used. This behavior has already been observed with this platform with other solvers. However, for each linear problem, there are a number of processors from which the speed-up should decrease and this limit has not been reached here.

For the configuration 2, the speed-up is super-linear until 64 processors ( $E_{64} = 1.24$ ) but decreases rapidly above 128 processors ( $E_{128} = 0.81$ ). The main difference between the two cases is related to the boundary conditions: using periodic boundary conditions implies more information exchanges between processors than no-slip conditions. This may explains that the speed-up break appears for fewer processors than in configuration 1.

## 2.2.5.2.4 Conclusions

In the study, we describe a complete work-flow from pore-scale imaging to rock effective permeability determination. Due to the large computation time involved in such work, very few studies have explored the work-flow sensitivity, whether in terms of mesh or configuration. Objective of this work was to evaluate these sensitivities using a open-source tool, OpenFOAM®, in constant evolution and presenting interesting parallel abilities.

Preliminarily to this study, the representativity of the considered sandstone sample imaged with a resolution of 9.6  $\mu m^3$ /voxel, has been explored. The representativity of the sample, experimentally assumed in terms of porosity, has been confirmed numerically in terms of permeability. Then, the mesh sensitivity has been tested and the study shows a maximal relative difference which can reach 50% between the original tomographic refinement and the finest tested mesh. The comparison with

experimental results shows that the mesh refinement on a given tomographic image is necessary to improve permeability evaluation. In terms of configurations, the more realistic configuration, i.e. the periodic, exhibits permeability greater than about 20% but also increases substantially the computation time required. However, we note that refining the mesh decreases the difference between the methods. We also noticed that relative difference was inferior for the off-diagonal terms, whose magnitude is lower. Finally, although this study was limited in terms of computing capacities (256 cores), the parallel efficiency study performed shows that the limit was not reached and, therefore, that is possible to perform simulations on finer grids using more intensively the open-source tool proposed.

Insufficiency in discretization process has the consequence to lead not only to an insufficiency in the description of micro and mesoporosities, but also the grain curvatures especially in the narrow pores although permeability is governed by the throat pore sizes and local geometries. The discretization problem is linked to the impossible representation of the continuum mechanics with a low level of gridding. Following the work-flow presented herein, it is necessary to have a better representation of the surface between fluid and solid phases. This is clearly governed by technical constraint and reached resolution. A part of the forthcoming work will be to use volumic mesh conformal to the real non-voxelized surface.

# 2.2.6 Wettability determination

Classical methods of laboratory wettability determination consist to use Amott index (Amott 1959) or USBM method (Donaldson et al. 1969). These are two indirect measurements describing the global average wettability of the sample. We are interested in the direct visualization of local wettability in used core samples.

Wettability of the rock is a key parameter of this work focused on the wettability and its alterations during waterflooding sequences and more precisely on the changes of wettability during LSB flooding. Several authors oriented the wettability of fluids in porous media based on the contact angle theory (Andrew et al. 2014). They used this parameter comfortably because he observed very large ganglions in a very large pore in comparison of the voxel size. We strategically oriented our work towards a system which proved as responsive to LSB injection giving an additional oil recovery when LSB flooded. The rock samples were relatively tight in comparison to Blunt's sample, rendering almost inaccessible to the Skyscan 1172 due to so small voxel size. It was not realistic to determine wettability by the contact angle between solid surface and the fluid of interest. Contact angle measurements can be considered in case of plate solid surface without any roughness or imperfection leading to measurement distortion. In real conditions, reservoir rocks have not a plate surface and nearly always are composed by more than one mineral. Therefore, they are not characterized by a unique contact angle.

To determine the wettability from micro-CT images we have developed a "wettability-index". The method is based on the calculation of the fluid-rock contact; applied to the complete volume of the sample we calculated the global fluid-rock contact area. In detail, from the micro-CT images we define a group of "oil" voxels which borders with "rock" voxels.

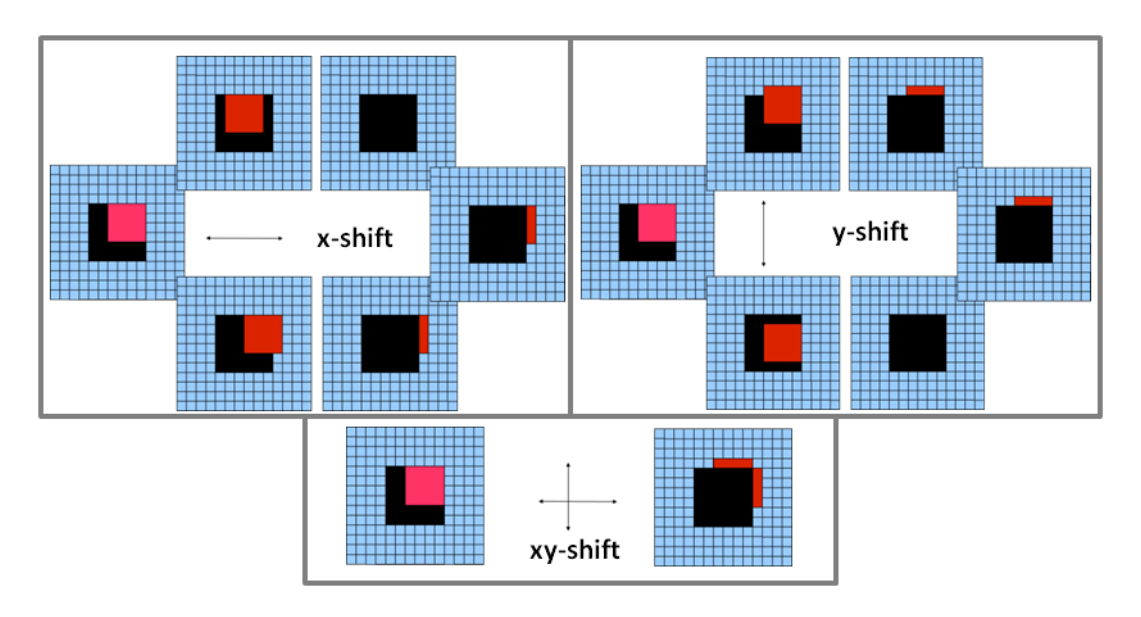


Figure 2.2-46 the principle of oil-solid contact determination with example of 2D shift-method (a – x-shift, b – y-shift, c – the xy-shift result). Solid is blue, pore space is dark, oil phase is rose and solid in contact with oil is red.

We numerically tested several ways. The first attempt was based on the gradient exploitation of the interfaces. We tried to differentiate in the images oil-rock from water-rock contacts by gradient brightness difference but we did not obtained a convincing result.

We developed a "shift-method" permitting to designate the voxels on the rock surface which encounters "oily" voxels. This method was less smart but very efficient and used in the next parts to measure the covered surface with oil or water.

#### 2.2.7 References

- Ahrenholz, B., Tölke, J. & Krafczyk, M., 2006. Lattice-Boltzmann simulations in reconstructed parametrized porous media. *International Journal of Computational Fluid Dynamics*, 20(6), pp.369–377.
- Amott, E., 1959. Observations Relating to the Wettability of Porous Rock.
- Andrä, H. et al., 2013a. Digital rock physics benchmarks—Part I: Imaging and segmentation. *Computers & Geosciences*, 50, pp.25–32.
- Andrä, H. et al., 2013b. Digital rock physics benchmarks—part II: Computing effective properties. *Computers & Geosciences*, 50, pp.33–43.
- Andrew, M., Bijeljic, B. & Blunt, M.J., 2014. Pore-scale contact angle measurements at reservoir conditions using X-ray microtomography. *Advances in Water Resources*, 68, pp.24–31.
- Andrew, M., Bijeljic, B. & Blunt, M.J., 2013. Pore-scale imaging of geological carbon dioxide storage under in situ conditions. *Geophysical Research Letters*, 40(15), pp.3915–3918.
- Anguy, Y., Bernard, D. & Ehrlich, R., 1994. The local change of scale method for modelling flow in natural porous media (I): Numerical tools. *Advances in Water Resources*, 17(6), pp.337–351.
- Arns, C.H. et al., 2005. Pore Scale Characterization of Carbonates Using X-Ray Microtomography. *SPE Journal*, 10(04), pp.475–484.
- Bear, J., 1972. Dynamics of Fluids in Porous Media.
- Beucher, S. & Lantuéjoul, C., 1979. Use of Watersheds in Contour Detection. In *International Workshop on Image Processing: Real-Time and Motion Detection/Estimation, Rennes, France. IRISA Report*.
- Bijeljic, B., Mostaghimi, P. & Blunt, M.J., 2013. Insights into non-Fickian solute transport in carbonates. *Water resources research*, 49(5), pp.2714–2728.
- Biswal, B., Manwart, C. & Hilfer, R., 1998. Three-dimensional local porosity analysis of porous media. *Physica A: Statistical Mechanics and its Applications*, 255(3), pp.221–241.
- Blunt, M.J. et al., 2013. Pore-scale imaging and modelling. Advances in Water Resources, 51, pp.197–216.
- Boek, E.S. & Venturoli, M., 2010. Lattice-Boltzmann studies of fluid flow in porous media with realistic rock geometries. *Computers & Mathematics with Applications*, 59(7), pp.2305–2314.
- Bogdanov, I.I. et al., 2003. Effective permeability of fractured porous media in steady state flow. *Water Resources Research*, 39(1).
- Buades, A. et al., 2005. A non-local algorithm for image denoising., (0), pp.0–5.
- Catté, F. et al., 1992. Image Selective Smoothing and Edge Detection by Nonlinear Diffusion. *SIAM Journal on Numerical Analysis*, 29(1), pp.182–193.
- Chevalier, C. & Pellegrini, F., 2008. PT-Scotch: A tool for efficient parallel graph ordering. *Parallel Computing*, 34(6-8), pp.318–331.

- Clavaud, J.-B. et al., 2008. Permeability anisotropy and its relations with porous medium structure. *Journal of Geophysical Research*, 113(B1), p.B01202.
- Couprie, M. & Bertrand, G., 1997. Topological gray-scale watershed transformation. In R. A. Melter, A. Y. Wu, & L. J. Latecki, eds. *Optical Science, Engineering and Instrumentation '97*. International Society for Optics and Photonics, pp. 136–146.
- Donaldson, E.C., Thomas, R.D. & Lorenz, P.B., 1969. Wettability Determination and Its Effect on Recovery Efficiency. *Society of Petroleum Engineers Journal*, 9(01), pp.13–20.
- FOAM, O. source, 2013. Open source Field Operation And Manipulation. Available at: http://www.openfoam.org.
- Frangakis, a S. & Hegerl, R., 2001. Noise reduction in electron tomographic reconstructions using nonlinear anisotropic diffusion. *Journal of structural biology*, 135(3), pp.239–50.
- Galindo-Torres, S.A., Scheuermann, A. & Li, L., 2012. Numerical study on the permeability in a tensorial form for laminar flow in anisotropic porous media. *Physical Review E*, 86(4), p.046306.
- Haralick, R.M. & Shapiro, L.G., 1985. Image segmentation techniques. *Computer Vision, Graphics, and Image Processing*, 29(1), pp.100–132.
- Hyväluoma, J. et al., 2012. Using microtomography, image analysis and flow simulations to characterize soil surface seals. *Computers & Geosciences*, 48, pp.93–101.
- Kass, M., Witkin, A. & Terzopoulos, D., 1988. Snakes: Active contour models. *International Journal of Computer Vision*, 1(4), pp.321–331.
- Keehm, Y., 2004. Permeability prediction from thin sections: 3D reconstruction and Lattice-Boltzmann flow simulation. *Geophysical Research Letters*, 31(4), p.L04606.
- Khan, F. et al., 2011. 3D simulation of the permeability tensor in a soil aggregate on basis of nanotomographic imaging and LBE solver. *Journal of Soils and Sediments*, 12(1), pp.86–96.
- Manwart, C. et al., 2002. Lattice-Boltzmann and finite-difference simulations for the permeability for three-dimensional porous media. *Physical Review E*, 66(1), p.016702.
- Mostaghimi, P., Bijeljic, B. & Blunt, M., 2012. Simulation of Flow and Dispersion on Pore-Space Images. *SPE Journal*, 17(04), pp.1 131–1 141.
- Mostaghimi, P., Blunt, M.J. & Bijeljic, B., 2012. Computations of Absolute Permeability on Micro-CT Images. *Mathematical Geosciences*, 45(1), pp.103–125.
- Otsu, N., 1979. A Tlreshold Selection Method from Gray-Level Histograms. *IEEE Transactions on Systems, Man, and Cybernetics*, SMC-9(1), pp.62–66.
- Paris, S. et al., 2008. Bilateral Filtering: Theory and Applications. *Foundations and Trends® in Computer Graphics and Vision*, 4(1), pp.1–75.
- Perona, P. & Malik, J., 1990. Scale-Space and Edge Detection Using Anisotropic Diffusion. *IEEE Transactions on Pattern Analysis and Machine Intelligence*, 12(7), pp.629–639.

- Petrasch, J. et al., 2008. Tomography based determination of permeability, Dupuit–Forchheimer coefficient, and interfacial heat transfer coefficient in reticulate porous ceramics. *International Journal of Heat and Fluid Flow*, 29(1), pp.315–326.
- Piller, M. et al., 2009. Analysis of Hydraulic Permeability in Porous Media: From High Resolution X-ray Tomography to Direct Numerical Simulation. *Transport in Porous Media*, 80(1), pp.57–78.
- Quintard, M. & Whitaker, S., 1987. Ecoulement monophasique en milieu poreux: effet des hétérogénéités locales. Journal de mécanique théorique et appliquée, 6(5), pp.691–726.
- Renard, P., Genty, A. & Stauffer, F., 2001. Laboratory determination of the full permeability tensor. *Journal of Geophysical Research*, 106(B11), p.26443.
- Sheppard, A.P., Sok, R.M. & Averdunk, H., 2004. Techniques for image enhancement and segmentation of tomographic images of porous materials. *Physica A: Statistical Mechanics and its Applications*, 339(1-2), pp.145–151.
- Spanne, P. et al., 1994. Synchrotron Computed Microtomography of Porous Media: Topology and Transports. *Physical Review Letters*, 73(14), pp.2001–2004.
- Tomasi, C. & Manduchi, R., 1998. Bilateral filtering for gray and color images. *Sixth International Conference on Computer Vision (IEEE Cat. No.98CH36271)*, pp.839–846.
- Weickert, J., 1998. Anisotropic Diffusion in Image Processing,
- Weickert, J., Romeny, B.H. & Viergever, M. a, 1998. Efficient and reliable schemes for nonlinear diffusion filtering. *IEEE transactions on image processing : a publication of the IEEE Signal Processing Society*, 7(3), pp.398–410.
- Whitaker, S., 1986. Flow in porous media I: A theoretical derivation of Darcy's law. *Transport in Porous Media*, 1(1), pp.3–25.

## 2.3 Experimental protocol

#### 2.3.1 Used materials

The experiments presented here were performed with a micro-Hassler cell permitting to confine multiphase flow in pressure and temperature with a controlled flow rate. The experimental conditions may vary from -80°C to 150° C in a range of pressure between 1 and 120 bars. The scheme of the experimental set up is detailed below (Figure 2.3-1).

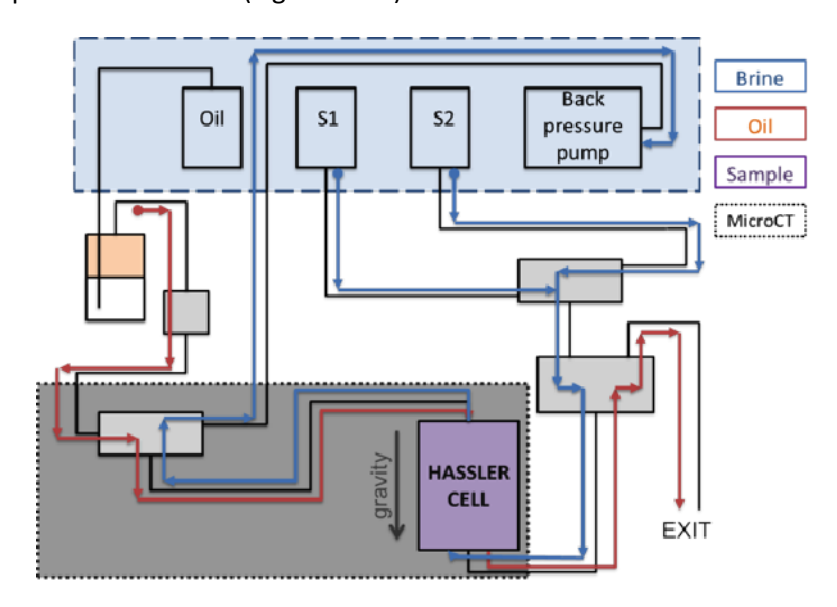


Figure 2.3-1Hassler cell and fluidic system control

Injection flow rates and pressures were controlled by high precision syringe pumps (Teledyne ISCO 100 DM). The back pressure pump maintains a constant pressure equivalent to the wetting phase pressure during primary drainage – it was controlled by a syringe pump operating in constant pressure mode. The dead volumes are consequent one large amount of drop pressure and caused by tubing which is common for this type of experiments.

Hassler cell capacity permits to test flows in 6 cm long core samples and 8 mm of core plug diameter.

#### 2.3.1.1 X-ray microtomograph (summary)

An X-ray microtomograph (Skyscan model 1172) provides the visualization of the inner phases of the rock based on X-ray attenuation. The conical X-ray beam projects the radiography of the sample on a scintillating material, which converts the X-ray photons into optical wavelength photons. The optical image is projected through a fiber optic plate onto the Charge Coupled Diode chip (CCD) manufactured by Hamamatsu. The CCD resolution is 4000 X 2000 pixels. The X-ray lab source is also manufactured by Hamamatsu and emits polychromatic beam light. The applied peak kilovoltage in the X-ray tube is 100 kVp and kept constant for all experiments. All experiments were achieved with a selected exposure time optimized as a function of the X-ray polychromatic material attenuations. Exposure was also selected according to the appropriate physical filtering with the aim to block the emitted low energy spectrum and to enhance the fluid contrast. The 3D reconstructions of the radiographies were performed with Nrecon-GPU software using Nvidia C2070 GPU. The algorithm used for reconstruction is based on the Filtered Back-Projection method.

The raw reconstruction slices are filtered and segmented with Avizo software from FEI. The X-lab hydro package was used for permeability reconstruction.

#### 2.3.1.2 Rock type

The used rock is outcrop Dausse sandstone referred as DU3. The porosity calculated by weighing is about 18% on a large sampling of companion rock plugs. The outcrop cores consist of about 60% of quartz, 30% of feldspar and 9% clays (3% of chlorite, 4% of muscovite, 2% of illite and interstratified clays). There were also variable amounts of dense material like pyrite. Samples have 60mm of height and 8mm of diameter. Pore volume of global sample is estimated to 450mm<sup>3</sup>.

#### 2.3.1.3 Fluid phases

Synthetic high salinity brine was composed of 50g/I, 90% in weight of NaCl and 10% in weight  $CaCl_2$ . Diluted salinity brine is obtained by a 0.1% dilution of initial brine, therefore 0.05 g/I of salts. NaCl and  $CaCl_2$  are manufactured by Sigma Aldrich with a purity grade higher than 99.9%. Water was purified by Elga Purelab classic system to give a resistivity of  $18.2 \text{ M}\Omega$ .cm.

The filtered crude oils are provided from Total Company and used as received. Oil characteristics are presented in the table below.

Table 2.3-1 Summary table of used oil characteristics

		AC-oil	J-oil				
Characteristics	Unit	Dehydrated oil	filtered tank				
BS&W (reception)	%	0.5	0				
TAN	mg/g KOH	n/a	0.31				
TBN	mg/g KOH	1.64	1.85				
Volumic mass @ 35°C	Kg/m3	834.7	854.5				
Cinematic viscosity @ 35°C	cSt	6.46	11.8				
Total Sulfur	%	0.33	1.2				
TCC	°C	32	37				
SARA							
Distillate	% weight	31.5	27.2				
Residual	% weight	68.5	72.8				
ASPHALTENES	1	1	1				
Asphaltenes (residual)	% weight	2.74	5				
IATROSCAN							
Saturated (residual)	% weight	56.8	51				
Aromatics (residual)	% weight	33.6	33.6				
Resin (residual)	% weight	9.6	15.4				

#### 2.3.1.4 Experimental processes

The global workflow is presented on figure below.

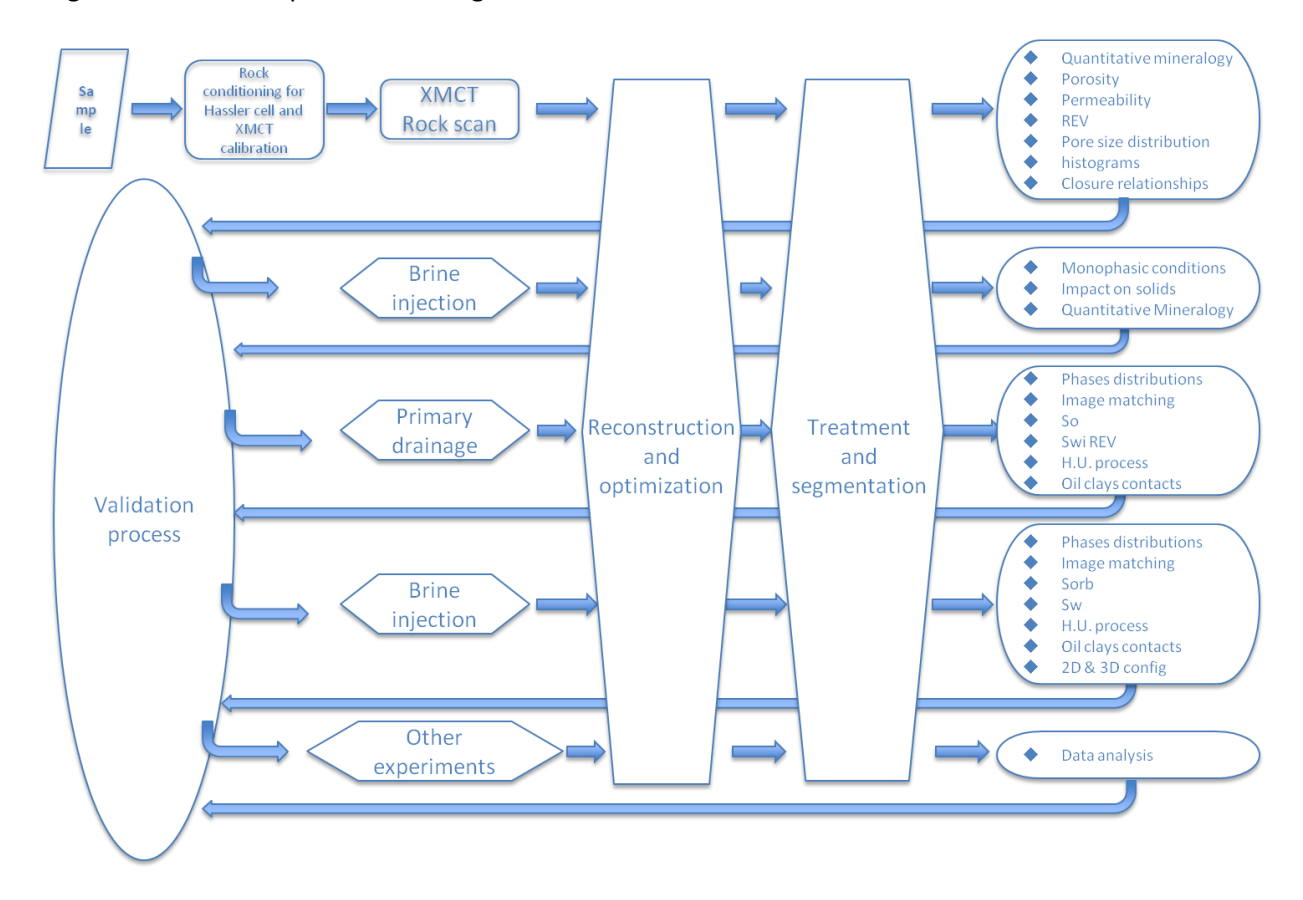


Figure 2.3-2 The global workflow of carried-out experiments

After each fluid displacement preprocessing and post-processing treatments are applied. To achieve the global workflow for one sample at least 3 weeks are required. Such delay is linked to 2 weeks aging step and time-consuming treatments. Our tomograph has not a possibility to exchange samples during aging step, therefore it is impossible to scan others samples during this period.

#### 2.3.1.4.1 Initial water saturation

The test core-plug was saturated with high salinity brine inside the core holder under ambient temperature. The pore space was initially vacuumed for 30 minutes before de-gassed brine was introduced and brought up to experimental pressure. A minimum of 20 pore volumes of brine was injected through the core-plug against back-pressure. The pore volume core-plug is beforehand measured in flow cell without any fluid to dispose of the best imaging of the core-plug in order to calculate static petrophysical properties of the core-plug and to have the reference image of porous medium. The brine flow rate injection is controlled to a constant flow rate of 20 microliters per minute thanks to Isco Pump 500 DM.

#### 2.3.1.4.2 Initial oil saturation

The core was pre-saturated with high salinity brine, and subsequently drained with crude oil (drainage). The crude oil phase was injected into the core-plug against a backpressure at the same constant flow rate of 20 microliters per minute. Here, initial oil saturation (Soi) is considered as reached when brine production ceased. To reach Soi 10 pore volumes of oil are required (Cissokho 2010). For all runs, we decided to inject more of 20 pore volumes by the top of the Hassler cell to gravitationally stabilize the oil injection. For image acquisition phase the fluid flow is stopped and pressure is maintained by a backpressure regulator to avoid bubbles appearing or leakage of fluids in pores.

The primary drainage is performed in ambient thermal conditions (20°C). Once saturated, samples in the Hassler cell were heated at 60°C during 15 days for thermal aging condition experiments

## 2.3.1.4.3 High Salinity Brine Waterflooding

To carry out the waterflooding process, heated core samples were cooled to ambient temperature (20°C) before to start imbibition process. The tested brine has the same composition that used during the initial water saturation of the rock. The brine imbibition phase was performed at a flow rate of 20 microliters per minute. The flooding sequence corresponds to more than 100 PVs. The capillary number was estimated to 10<sup>-5</sup> however a few tested samples reached capillary numbers about 10<sup>-4</sup>. We decided to not present the results obtained concerning these samples.

## 2.3.1.4.4 Low Salinity Brine Injection (Tertiary mode)

The brine imbibition phase was performed in the same experimental conditions than during the brine injection at a flow rate of 20 microliters per minute. The flooding sequence corresponds to more than 100 PVs.

- 2.3.2 Experiment representativity
- 2.3.2.1 Representative Elementary Volume

The very small core plug used for experiments requires much care. To ensure that the sample of interest is homogenous and therefore representative for several petrophysical properties the experiments are required to be comforted by a complete analysis of the core plug especially first is the Representative Elementary Volume (REV). The used method of REV determination is the direct application of the enounced definition by Bear (Bear 1972) extended to porosity. The method on the 3D microtomographic images is obtained by determination of the whole volume specifications of interest. The property is calculated from successive and progressive cropping of the initial whole 3D centered volume. The subvolume is then cropped in all directions a given length and the property is recalculated. This procedure is repeated until domain of microscopic effects dominates on the property measurement. The exposure time was 6 s with an aluminium filtering of 200 microns thick additional to beryllium. The radiography was the averaged image resulting of 9 raw images. One thousand radiographies were collected for the 180° rotation mode.

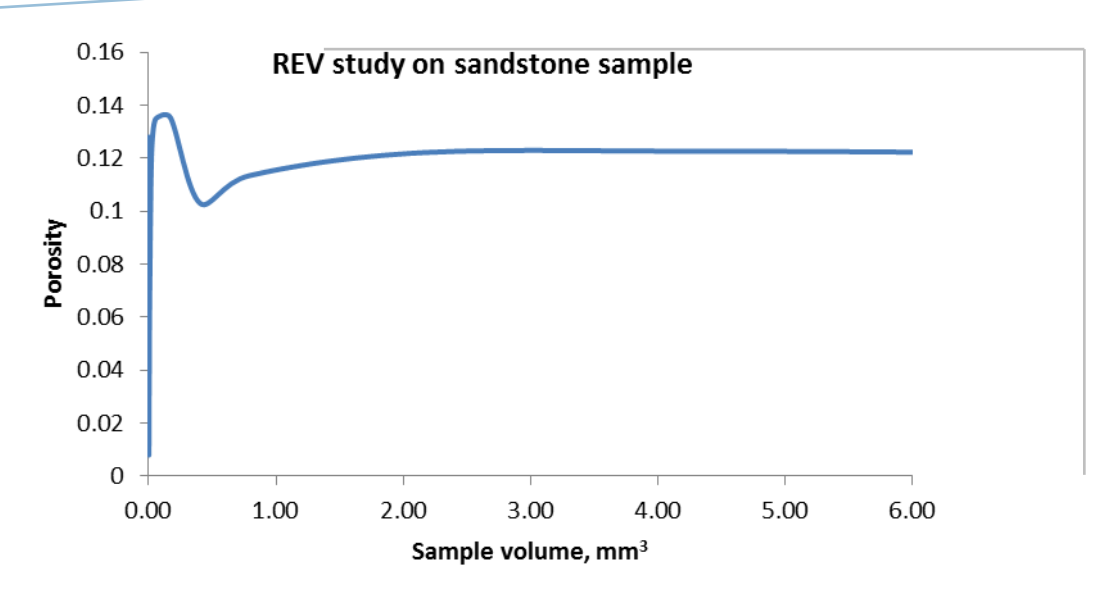


Figure 2.3-3 Study of sandstone sample representativity on porosity

The Representative Elementary Volume (REV) based on the porosity measurement was determined as a function of the sample volume and displayed above (Figure 2.3-3). The constant value of the porosity is reached at averaging window size of 1.5mm<sup>3</sup>. The recorded volume for the study has been more than twice and a half the REV in each direction. We obtain a realistic representative elementary volume size.

## 2.3.2.2 Saturation profiles

We take advantage of the micro-CT permitting to measure the oil, water and matrix fraction along the core sample along the vertical direction (Figure 2.3-4). The fluid distributions are uniform during the different sequences of experiments from the top to the bottom of the sample. Significant water cut or diverted flows are not visible in these saturations profiles representative of the end point.

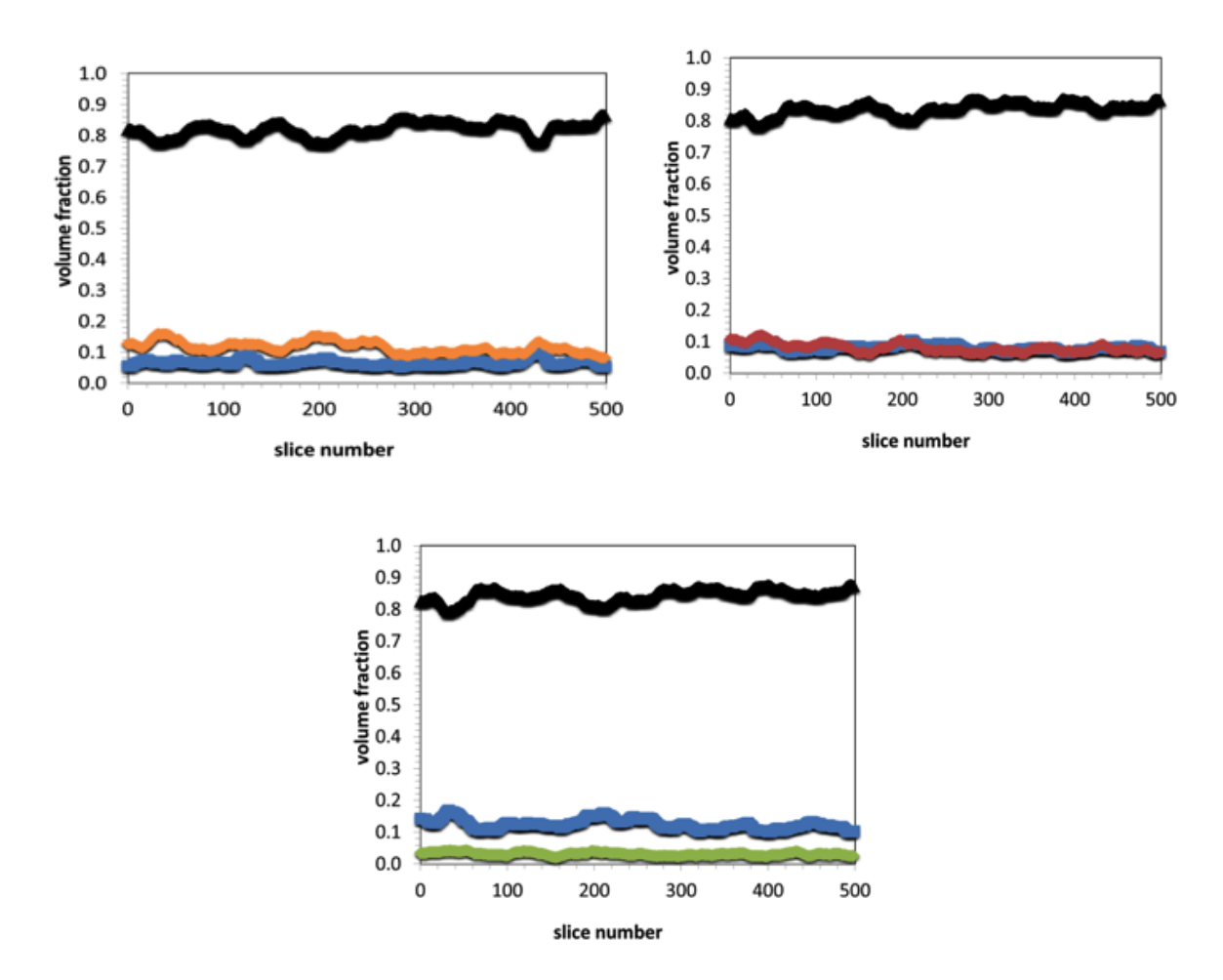


Figure 2.3-4 Volume fraction profiles of samples saturations by fluids from down to top slices of the mineral (black), brine (blue) and oil (orange color) for Initial Saturation (a), in rose color for Residual Saturation (b) and in green color for Residual Saturation after LSB injection (c).

The residual oil saturation evolution versus the porosity curve and expressed slide by slide from the top to the bottom of the reconstructed images shows than the oil saturation evolution fills the whole pore distribution. Oil in place is mobilized uniformly during the waterflood and low salinity brine injection. We may not observe cut off in the mobilization efficiency of the waterflood and the low salinity brine injection. The oil recovery is therefore spatially independent in the core.

### 2.3.3 Wettability

#### 2.3.3.1 Mineral wettability and pore morphology

The wettability can be inferred at the pore scale directly by the micro-CT images with a limitation due to the micro-CT spatial resolution. The wettings of the minerals are characterized using the 3D oil-substrate contact. The outcrop sandstone is rich in feldspars. The feldspars form about 10% of pore surfaces however only 1% of oil is potentially in contact with the feldspar. Concerning observable clays we may visualize with the micro-CT only 3% of the measured 9% of the core sample. No clay aggregate has ever been observed as oil wetted. The pyrite is in inclusion therefore the oil wetting analysis is irrelevant. The oil-quartz contact is the quasi-exclusive contact between the minerals and the crude oil we may observe with a voxel size of 3.7 microns.

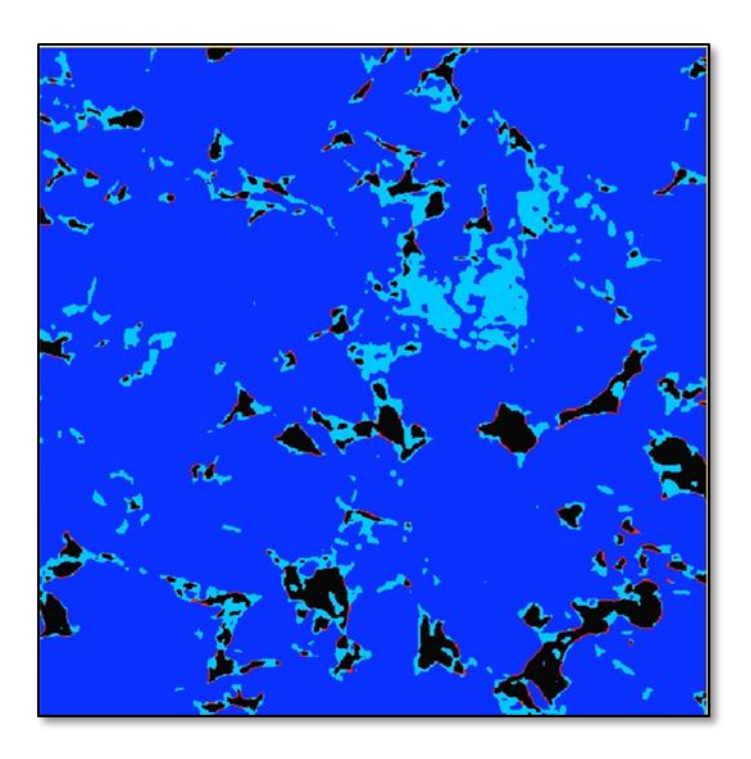


Figure 2.3-5 : Sampling of the wettability 3D map (1850x1850 μm²) representative of the oil-minerals contacts (red color) (oil in black color; dark blue: minerals; light blue: water).

Most of the altered surfaces of the quartz are macroscopically corresponding to flat shapes. The propensity of the oil to alter the mineral wetting is firstly conditioned by the capillary pressure. The macroscopic film thicknesses decrease up to reach tens of nanometers where the capillary pressure is counterbalanced by the disjoining one. The capillary pressure must be sufficiently high to contact a high surface of the minerals. The curved portion of the menisci represents the contribution of capillarity. The wedges and edges of the pore space are therefore less exposed to oil adhesion due to higher level of capillary pressure required to invade these sharp concavities (i.e., the arc menisci are compressed towards the apex of the wedge). Note that because the wettability combines the energy contributions from both capillarity and DLVO forces, the thinner water films may also contribute to less capillary but the interfacial tension effect is probably dominant in permeable porous media. Thus, the angle of the wedge shaped pore affects the degree of saturation, with smaller wedge angles containing substantially more water. This has implications on textural controls; for example, more slit-like or narrow pores will contain

much more capillary water. The quantitative oil-rock contacts permits to define a 3D wettability map (Figure 2.3-5).

The exploitation of the developed algorithm defines a global index linked to the average curvature of the surface. The pore surface shapes are defined from external/internal pore surface ratio, for ideally plate form the ratio will be equal to 1:

$$I_{cc} = \frac{S_{ext}}{S_{int}}$$

Where,  $I_{cc}$  is the convex-concave index,  $S_{ext}$  – external surface (mm²) of studied sample and  $S_{int}$  – internal surface (mm²) of studied sample. If concave forms dominate the ratio will be less than 1 and for convex forms domination the ratio will be more than 1. Defining different surfaces of interest we may calculate the convexity/concavity ratio of the porous medium, the shape of the favorable oil trapping during the primary drainage or dewetting as a function of the brine or low salinity brine injection. We will use the notion of wettability index also wettability geometry in carried-out experiments to determine preferential forms of oil-solid contacts and it dewetting. We note the global form of porous medium of used companion rock samples is more concave.

## 2.3.3.2 Homogeneity of rock wettability at end points

The homogeneity of the wettability in the rock sample is controlled by the projection on two planes (vertical and horizontal) of the whole voxels of the studied volume. With the same concept than defined by Bear (Bear 1972) and used before we defined the representative elementary volume of the wettability by the number of oil contacts per volume.

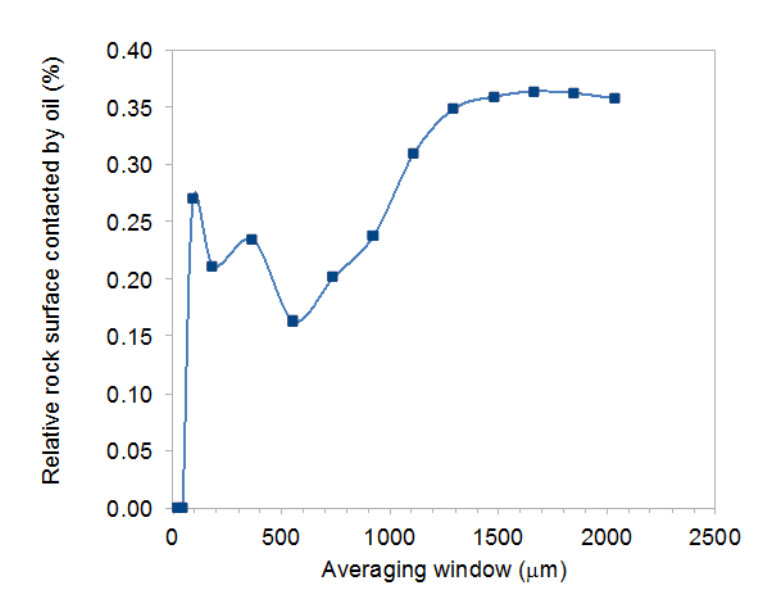


Figure 2.3-6 Wettability Representative Elementary Volume

From the figure 2.3-6 the results show the representative elementary volume is reached for a rock size larger than 1.5 mm. The description and the analysis performed are therefore representative from a

wettability point of view. An in-situ contact angle measurement, such proposed by Andrew & al. (Andrew et al. 2014) is here not realistic due to the low spatial resolution of the available micro-CT.

#### 2.3.4 References

- Andrew, M., Bijeljic, B. & Blunt, M.J., 2014. Pore-scale contact angle measurements at reservoir conditions using X-ray microtomography. *Advances in Water Resources*, 68, pp.24–31.
- Bear, J., 1972. Dynamics of Fluids in Porous Media,
- Borghi, F. et al., 2013. Nanoscale roughness and morphology affect the IsoElectric Point of titania surfaces. *PloS one*, 8(7), p.e68655.
- Bouriat, P. et al., 1999. A Convenient Apparatus to Determine the Zeta Potential of Grains by Electro-Osmosis. Journal of colloid and interface science, 209(2), pp.445–448.
- Boussour, S. et al., 2009. Oil recovery by low salinity brine injection: Laboratory results outcrop and reservoir cores. In *Proceedings SPE Annual Technical Conference and Exhibition*. pp. 1595–1606.
- Buckley, J.S., 2001. Effective wettability of minerals exposed to crude oil. *Current Opinion in Colloid & Interface Science*, 6(3), pp.191–196.
- Cissokho, M., 2010. Etude expérimentale des interactions Huile brute/Saumure/Roche sur la récupération d'hydrocarbures par injection d'eau de faible salinité.
- Cissokho, M. et al., 2010. Low salinity oil recovery on clayey sandstone: Experimental study. *Petrophysics*, 51(5), pp.305–313.
- Creux, P. et al., 2009. Strong specific hydroxide ion binding at the pristine oil/water and air/water interfaces. *The journal of physical chemistry*. *B*, 113(43), pp.14146–50.
- Derjaguin, B. V., Churaev, N. V. & Muller, V.M., 1987. Surface Forces, Boston, MA: Springer US.
- Graciaa, A. et al., 2000. Potential at an Air Water Surface Related to the Critical Micelle Concentration of Aqueous Mixed Surfactant Systems. , pp.2677–2681.
- Hartley, P.G., Larson, I. & Scales, P.J., 1997. Electrokinetic and Direct Force Measurements between Silica and Mica Surfaces in Dilute Electrolyte Solutions. *Langmuir*, 13(8), pp.2207–2214.
- Hunter, R.J., 1981. Zeta Potential in Colloid Science: Principles and Applications, Academic Press.
- I. Bondino, S. Doorwar, R. Ellouz, G.H., 2013. Visual microscopic investigations about the role of pH, salinity and clay on oil adhesion and recovery. In *The Society of Core Analysts*.
- Kosmulski, M., 2010. Surface charging and points of zero charge, CRC Press.
- Kovscek, A.R., Wong, H. & Radke, C.J., 1993. A pore-level scenario for the development of mixed wettability in oil reservoirs. *AIChE Journal*, 39(6), pp.1072–1085.
- Lebedeva, E. V. & Fogden, A., 2011. Micro-CT and wettability analysis of oil recovery from sand packs and the effect of waterflood salinity and kaolinite. *Energy and Fuels*, 25(12), pp.5683–5694.
- Masliyah, J.H. & Bhattacharjee, S., 2006. *Electrokinetic and colloid transport phenomena*, John Wiley & amp; Sons.

- Mohanty, K.K., Scriven, L.E. & Davis, H.T., 1987. Physics of Oil Entrapment. *SPE Reservoir Engineering*, 2(February), pp.113–118.
- Nasralla, R.A., Bataweel, M.A. & Nasr-El-Din, H.A., 2011. Investigation of Wettability Alteration by Low Salinity Water. In *Offshore Europe, 6-8 September, Aberdeen, UK*. Society of Petroleum Engineers.
- Pieterse, S.G.J. et al., 2013. SPE 165180 Experimental Investigation on the Effects of Very Low Salinity on Middle Eastern Sandstone Corefloods.
- Radke, C.J., Kovscek, A.R. & Wong, H., 1992. Pore-level scenario for the development of mixed wettability in oil reservoirs. In *Proceedings SPE Annual Technical Conference and Exhibition*. pp. 163–177.
- RezaeiDoust, a. et al., 2009. Smart Water as Wettability Modifier in Carbonate and Sandstone: A Discussion of Similarities/Differences in the Chemical Mechanisms. *Energy & Fuels*, 23(9), pp.4479–4485.
- Salathiel, R.A.A., 1973. Oil Recovery by Surface Film Drainage In Mixed-Wettability Rocks. *Journal of Petroleum Technology*, 25(10), pp.1216–1224.
- Sanchez-Soto, P.J., Justo, A. & Pérez-Rodriguez, J.L., 1994. Grinding effect on kaolinite-pyrophyllite-illite natural mixtures and its influence on mullite formation. *Journal of Materials Science*, 29(5), pp.1276–1283.
- Schembre, J.M., Tang, G.-Q. & Kovscek, a. R., 2006. Wettability alteration and oil recovery by water imbibition at elevated temperatures. *Journal of Petroleum Science and Engineering*, 52(1-4), pp.131–148.
- Souza, A.E. et al., 2013. Addition of sedimentary rock to kaolinitic clays: influence on sintering process. *Cerâmica*, 59(349), pp.147–155.
- Tang, G. & Morrow, N.R., 1999. Influence of brine composition and fines migration on crude oil r brine r rock interactions and oil recovery.
- Valtiner, M. et al., 2011. Effect of surface roughness and electrostatic surface potentials on forces between dissimilar surfaces in aqueous solution. *Advanced materials (Deerfield Beach, Fla.)*, 23(20), pp.2294–9.
- Valtiner, M. et al., 2012. The electrochemical surface forces apparatus: the effect of surface roughness, electrostatic surface potentials, and anodic oxide growth on interaction forces, and friction between dissimilar surfaces in aqueous solutions. *Langmuir: the ACS journal of surfaces and colloids*, 28(36), pp.13080–93.
- Vledder, P. et al., 2010. Low Salinity Water Flooding: Proof Of Wettability Alteration On A Field Wide Scale. In SPE Improved Oil Recovery Symposium, 24-28 April, Tulsa, Oklahoma, USA. Society of Petroleum Engineers.

#### 3. TWO PHASE DISTRIBUTION IMAGING IN POROUS MEDIUM

#### 3.1 Introduction

The actual understanding of the possible underlying key mechanisms of the additional recovery observed during Low Salinity Brine injection is not really apprehended. Quantitatively, in literature authors assign to the low salinity brine effect an incremental oil recovery of 10 % attributed to micromechanisms (Cissokho 2010).

In this part, we propose to observe and to analyze thanks to the micro computed tomography a low salinity effect obtained in a tertiary recovery process in permeable sandstones. Previously, Cissokho (Cissokho 2010) systematically observed an incremental oil recovery for one of brine-oil-rock triptychs we have used for this work.

To investigate the pore space scale permits to characterize the fluids distributions and interactions with the micro-structural geometry and the nature of minerals. The objectives were to link pore scale mechanisms to macroscopic effective properties of fluids or minerals in porous media to enhance the underlying mechanisms knowledge of subtle mechanisms such low salinity effect process.

The current study investigated crude oil distribution and wettability as a function of the various characteristics saturations of the brine flooding in tertiary recovery mode. Primary drainage, waterflood and low salinity brine injection steps were visualized with an experimental set-up based on X-ray micro-CT visualization at the pore scale. We have imaged the capillary invasion by a non-wetting oil phase at a specific capillary entry pressure during the primary drainage phase. Although the pore body may partially fill with oil, the interstices where grains or non-connected zones meet do not fill, because the capillary pressure is insufficient to force the non-wetting oil phase into those spaces.

Thus, depending on the pore and pore-throat geometry we have analyzed the fluid configuration in the pore space to analyze the oil-brine interactions with a sandstone in two thermal aging conditions (ambient and a temperature of 60°C) and with two types of crude oils. We have used companion rock samples and the same brines for all experiments.

# 3.2 Case of the responsible to LSB injection effect system

3.2.1 Case of the responsible to LSB injection effect system with applied thermal aging conditions

#### 3.2.1.1 Initial Oil Saturation

Due to the importance of initial fluid distribution our particular interest is to study the fluid configuration in the pore network to identify impacting mechanisms on the fluid flow. We proceed to 2D and 3D visualization to illustrate the fluid configuration in pores and we present statistical algorithms to measure on large data sets crucial properties to understand better the low salinity brine injection mechanism. The phase fluid configuration at  $S_{oi}$  conditions after primary drainage is shown on Figure 3.2-1. From this image the presence of thick water films is clearly observed. According to capillary pressure forces concepts, centers of largest pores are filled by oil phase, wedges and edges and smaller pores are generally filled by brine. Thick water films appear between minerals and oil droplets with a characteristic length more than 3 voxels for a great part of the film (a zoomed  $\mu$ -CT image of thick water film is presented on figure 3.2-2). We have a high degree of confidence on such a water films segmentation because several successive voxels to the same gray level may not biased by noise in image or back phase propagation at 3.7 micrometers of voxels size.

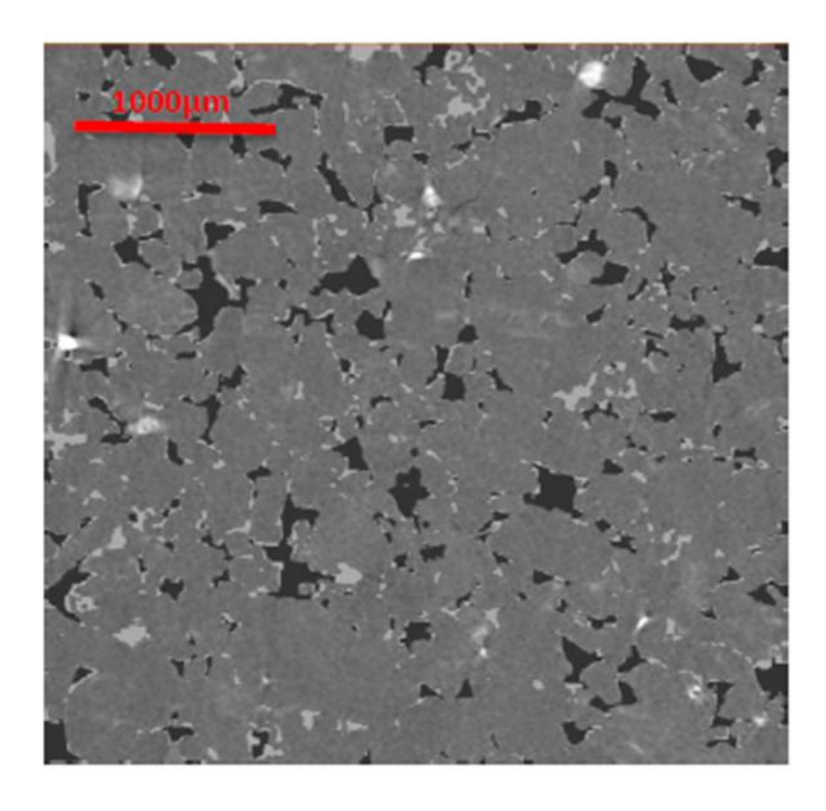
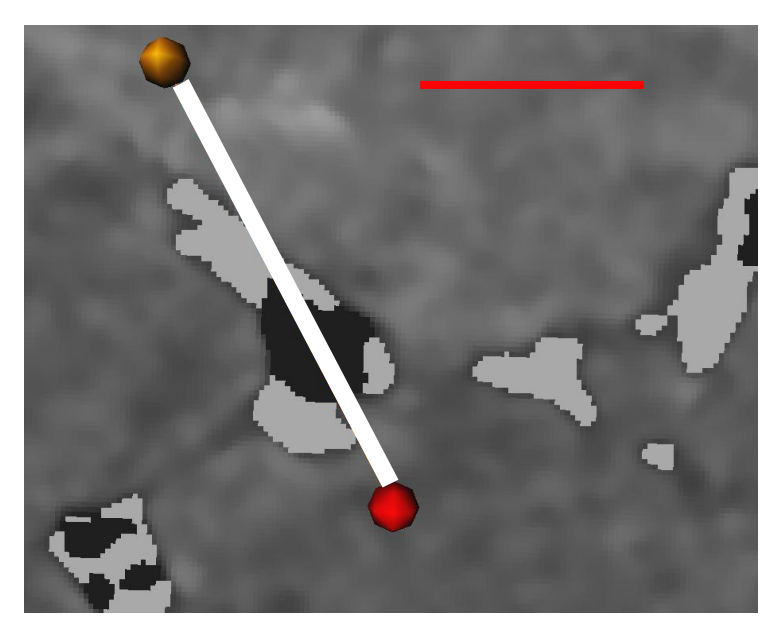


Figure 3.2-1 2D slices of fluid distribution at Initial Oil Saturation state (oily phase is represented in black, water is light gray)



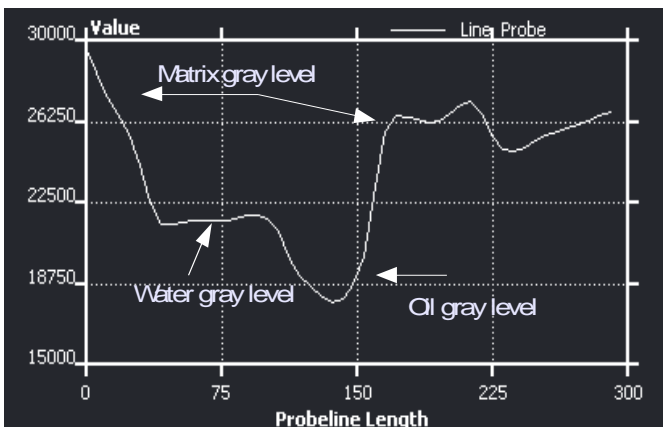


Figure 3.2-2 Zooming on one pore (top) and gray level distribution (bottom) along the white line on μ-CT image confirming water film presence for one pore side and direct oil adhesion on the solid matrix for other pore side. On μ-CT image oil is black, water is clear gray

The initial oil saturation is measured on the representative elementary volume and constitutes 65%. The measurements of the oil-mineral surface contact exhibit 35% of apparent contact onto the mineral surfaces.

For a porous medium filled with brine considered as the wetting fluid, which is drained by a non-wetting fluid, the last will occupy the larger pores and leave wetting fluid to cover large pore walls and to fill smaller pores and wedges. The imbibition of a wetting fluid (brine) into a porous medium previously filled with a non-wetting phase (crude oil), the brine will tend to displace the non-wetting fluid from pore walls and small pores and trap it as snapped-off droplets in larger cavities. The displacements mechanisms in imbibition and drainage are substantially conditioned by capillary mechanisms.

In limited zones, no thick water films appear. This suggests the oil is in contact with matrix or the presence of thin films below the voxel size of the image, which are imperceptible in this study. Thick films

appear in several pore morphologies included far from wedges or edges where the arc meniscus is controlled by the interfacial tension. The apparent water films are thicker than 10  $\mu$ m and may reach 50  $\mu$ m. Tens of micrometers are clearly out of the range of the interfacial forces, usually considered as at the origin of wettability and alteration. At the initial oil saturation and in agreement with the Derjaguin's concepts (Derjaguin et al. 1987) the interfacial tension and the capillary pressure mainly condition the oil distribution. However, the capillary pressure exerts a strong force counterbalanced by the disjoining pressure in the very close neighborhood of the interface (tens to hundred nanometers).

Despite a coarse micro-CT resolution (3.7  $\mu$ m/voxels) out of range of the disjoining forces we may observe the presence of thick water films with a propensity these thick films are favorable to a co-flow between oil and water permitting the fresh water to access to the pore medium.

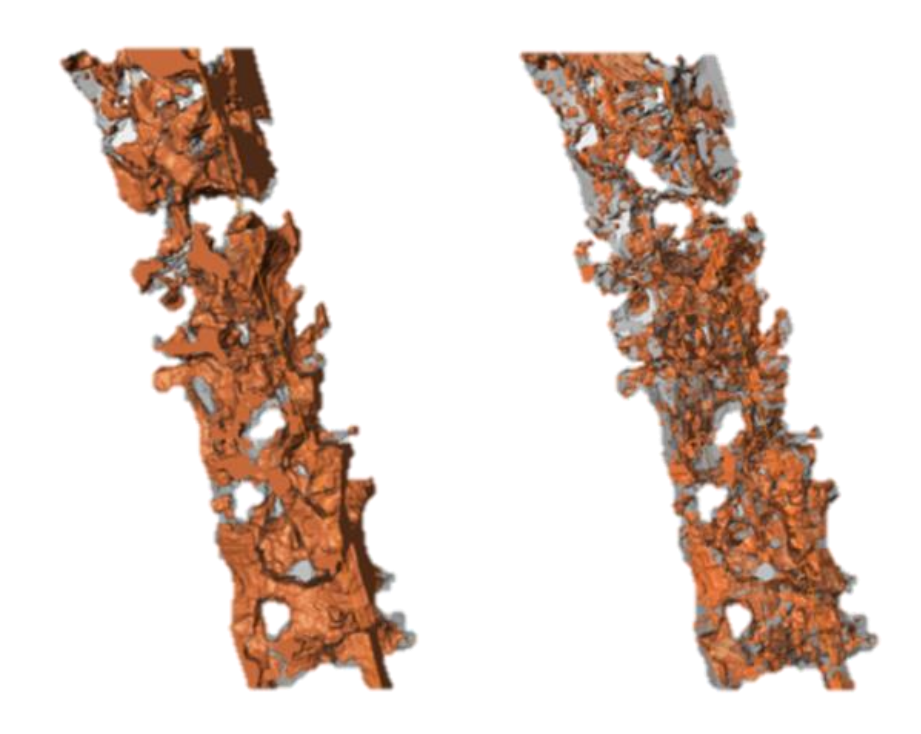


Figure 3.2-3 Subsample with a giant oil droplet percolating through the numerical sample (left sample) and the oil contacts surface on the right side at initial oil saturation state.

As illustrated in a 3D view in figure above, the tightest zones are filled by brine. Although, the most permeable pores are filled by oil. In the field of view the observations take place far from injection zones of the cell, therefore the observations are not due to border effects and are representative of two-phase flow in reservoir condition.

We may note oil blobs may fill several pores and oil is mainly connected through several pore sizes (Figure 3.2-3). This result is therefore quite coherent to usual petrophysical concepts for irreducible water saturation state. However, here for the first time we image very thick water films clearly appearing. Several oil zones are in contact with the porous medium as shown on the figure 3.2-3 on the right side.

# 3.2.1.2 High Salinity Brine Waterflooding

The residual oil saturation was determined from the micro-CT images and shown on Figure 3.2-4. Quantitatively oil saturation is 51%. The corresponding capillary number is estimated to 10<sup>-5</sup>. Oil droplets with surrounding water configuration are quite rare therefore the purely capillary trapping caused by constriction is not observed. We observe oil blobs adhere onto the solid matrix wall (Figure 3.2-5 left side). The imbibition experiment clearly exhibits a global pore voiding and a global increase of the water wet behavior of the rock although residual oil is trapped in contact onto the mineral.

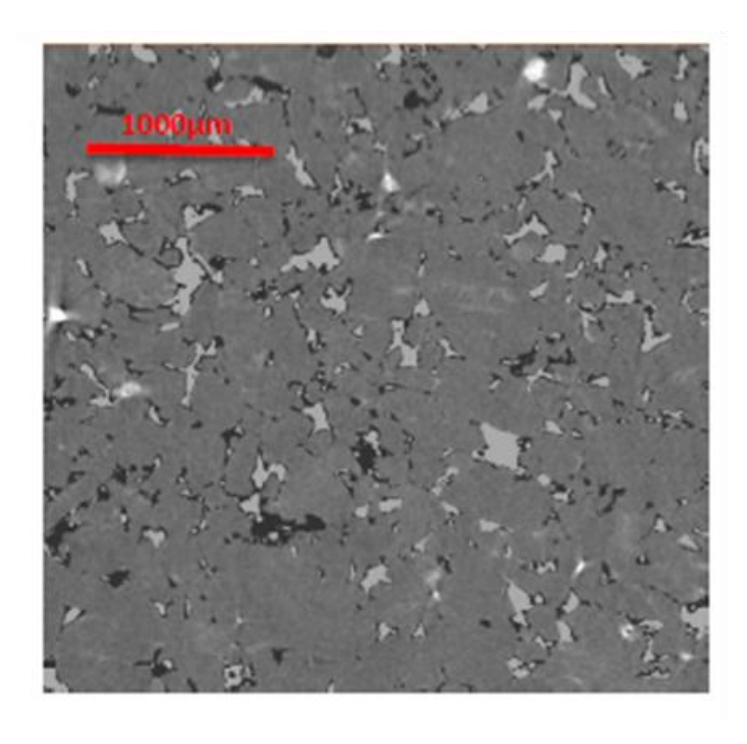


Figure 3.2-4 Residual oil saturation after high salinity waterflooding (oily phase is represented in black, water is light gray).

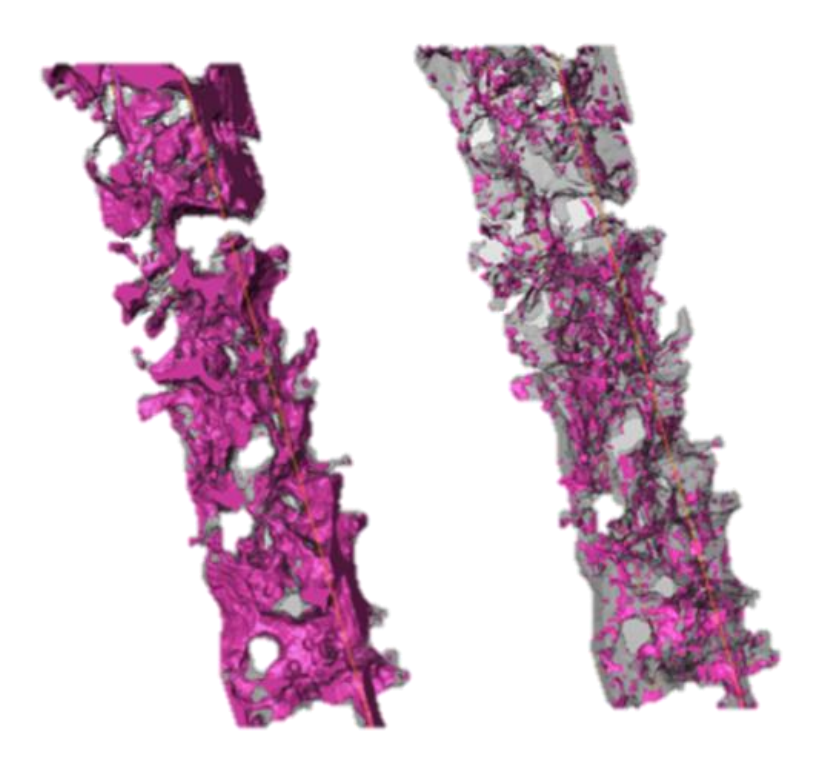


Figure 3.2-5 Subsample with a giant oil droplet percolating through the numerical sample (left) and the oil contacts surface on the right side at residual oil saturation state.

From the figure above, apparent oil-matrix contacts after brine injection show the significant difference in oil distribution on porous medium. The long oil blobs previously observable at Soi step have been fragmented due to water imbibitions and the oil-matrix contacts are reduced in consequence of oil production.

# 3.2.1.3 Low Salinity Brine Injection (Tertiary mode)

The Low Salinity Brine effect is here very important exhibiting a residual oil saturation of 27% (Figure 3.2-6) with a residual oil trapping in at the entrance of throat pores in adhesion conditions as shown by the good correspondence of the oil trapping (Figure 3.2-7 left side) with the adhesion map (Figure 3.2-7 right side) of the residual oil saturation. The very strong increment obtained in oil recovery may not be explained only from these sets of 3D images and a comparative analysis must be led.

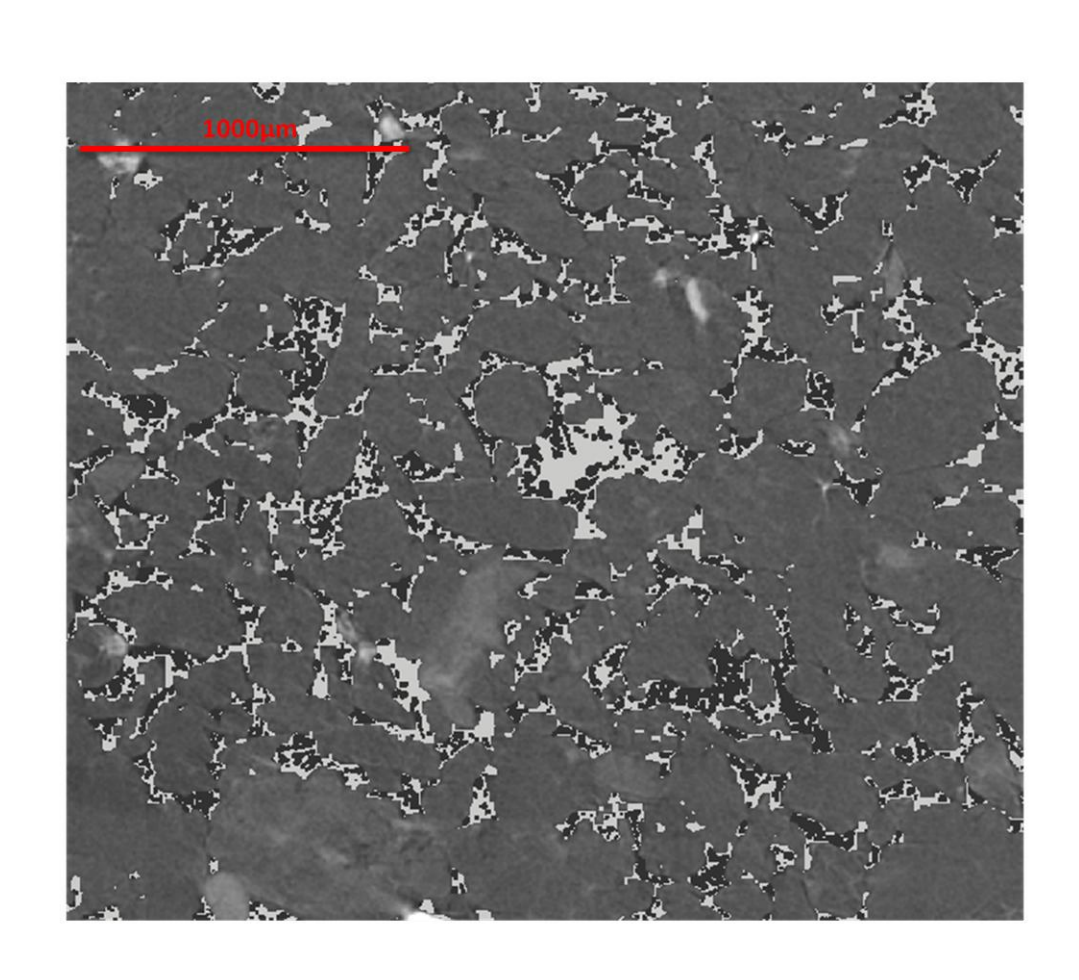


Figure 3.2-6 Residual oil saturation after low salinity waterflooding (oily phase is represented in black, water is light gray).

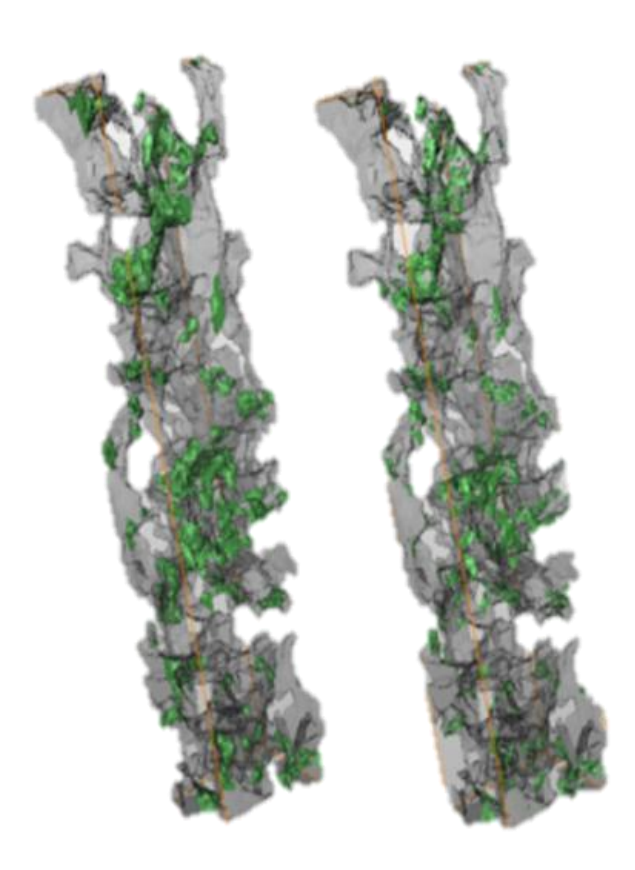


Figure 3.2-7 Subsample with a giant oil droplet percolating through the numerical sample (left sample) and the oil contacts surface on the right side at residual oil saturation state after LSB injection.

## 3.2.1.4 Analysis and discussion

The different oil saturations in this experiment reveal a 65% of initial oil saturation, 37% of recovery after the waterflooding and 60% of recovery after the low salinity brine injection. The very low recovery during the waterflood may be explained by the temperature of the waterflood performed at 20°C. Cissokho (Cissokho 2010) obtained similar results at 35°C for the same system.

These results are quite perturbing because the low salinity effect is very important for the experiment performed here. Considering the fluid uniformly distributed in the core with an effect of the floods similar on the whole pore size without any gravitational effect or breakthrough at the pore size we were interested by the characterization of the wettability.

We may observe the whole oil droplets wet the substrate. This behavior is clearly observed after the waterflood and the low salinity brine injections. More interesting is the covered rock surface by the oil. After the primary drainage, the oil covering the rock surface reaches 30% (at the micro-CT resolution) although the covered surface is reduced after the waterflood down to 22%. The trapped oil droplets are observed in contact with the surface. To reduce the energy trapped oil must be centered in pores in water-wet condition, nevertheless we observe numerous eccentric oil droplets close to rock surface (under  $3.7\mu m$  resolution). From this observation we might conclude on oil adhesion onto mineral surface.

The oil surface measurement is therefore more relevant than after the primary drainage. After the low salinity brine injection the incremental oil recovery is very important (from 37% to 73%) and oil adhesion is reduced of 57%. Such effect may not be due to the water physical properties therefore an interaction favors change in the wettability (Figure 3.2-8).

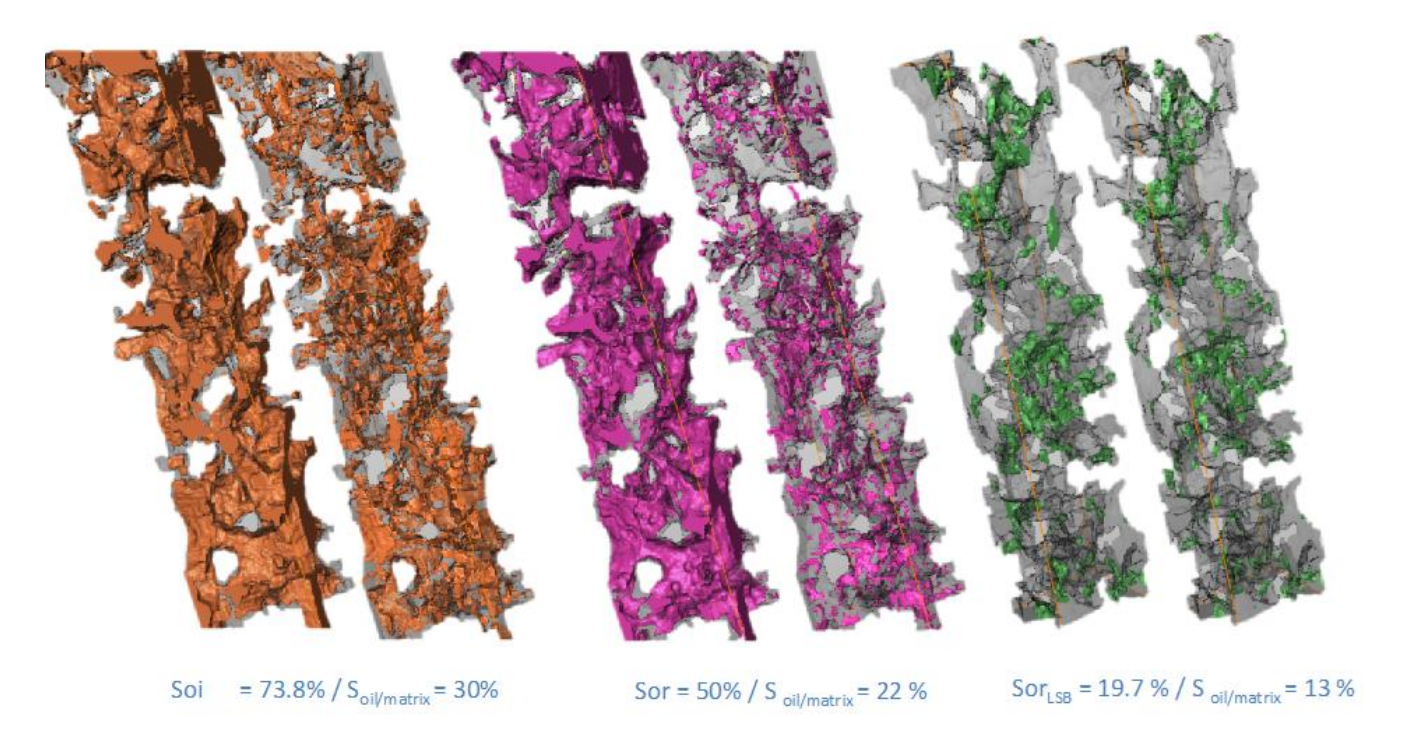


Figure 3.2-8 Visual sub-sampling representative of the pore saturation in oil (left image per color) and the oil- mineral contact (left side for each color).

We analyzed wettability maps at each end point saturation state. The represented rock sample exhibits a more concave surface than convex (table 3.2-1) calculated from external-internal surface ratio. The pore surface shapes are defined from external/internal pore surface ratio: for ideally plate form the ratio will be 1; if concave forms dominate the ratio will be >1.

From the table 3.2-1 we can see the oil contacts are slightly more favorable for convex shapes than concaves at initial oil saturation state. The contacts between the rock and residual oil saturation brine injection are very clearly in concave shapes. The crude oil mobilization is therefore more favorable on convex shapes. A more precise analysis reveals the unchanged surface in contacts between Sor and Soi states of saturations are strongly in favor of a maintain of the oil surface contacts in concavities although

the detached phase is more on convex shapes between the unchanged initial oil saturation and residual oil saturation.

The most troubling result is the low salinity brine injection does not exhibit sensitivity to the pore shapes on oil recovery. The indifference of the pore shape to the incremental oil recovery is caused by global changes of wettability properties in the sample. A strong oil recovery requires activating a mechanism increasing the water-wet properties of the rock.

Table 3.2-1 Statistics of the wettability changes as a function of the pore shape curvature

	Rock sample	Initial oil saturation (S <sub>oi</sub> )	Residual oil saturation (S <sub>or</sub> )	S <sub>oi</sub> and S <sub>or</sub> unchanged contacts	Redistributed oil contacts between S <sub>oi</sub> and S <sub>or</sub>	Residual oil saturation after the low salinity brine injection (S <sub>ortSB</sub> )	S <sub>or</sub> and S <sub>orLSB</sub> unchanged contacts	Redistributed oil contacts between S <sub>or</sub> and S <sub>orLSB</sub>
Convexity/concavity shape factor	0.88	1.01	0.71	0.76	1.1	0.81	0.67	0.71
Evolution between two successive states of saturation		0.13	-0.3	-0.25	0.09	0.1	-0.04	0

# 3.2.2 Case of the responsible to LSB injection effect system without thermal aging conditions

We reiterate the same experiment than with the previous sample (named Du3-ta) excepting the step aging occurring here for another one (named Du3-aa) experiment at 20°C. The rock sister properties concerning representativity of the sample in term of porosity permeability and Soi are measured and does not exhibit significant changes in comparison of DU3-ta.

#### 3.2.2.1 Initial Oil Saturation

The companion rock core of the previously exploited sample DU3-ta is initially fully saturated inside the cell with high salinity brine with the same experimental protocol than described before. In the field of view, the observations take place far from injection zones of the cell therefore the observations are not representative of a border effect.

Drainage occurs at 20 microliter per minute. Oil is injected in downwards direction to stabilize the saturation front. It was injected in abundant quantity to ensure the achievement of initial oil in place that corresponds to irreducible water saturation. Initial oil in place occupies 73% of pore space. Oil injection is stopped once the previously injected brine production is ceased. Cissokho (Cissokho 2010) reported irreducible water saturation is reached for 10 pore volumes. To be more comfortable we injected about 20 pore volumes. Once the oil drained and the Swi reached we proceed to the equilibration of the system. This step is also called "wettability restoration" step and usually done in similar confining conditions to the targeted reservoir.

Once the aging at 20°C completed (about 2 weeks) a microtomography experiment is performed. Of course during the image acquisition all injections are stopped to avoid any fluid displacements during the acquisition that can perturb a better phase identification. Once saturated, image acquisition occurs to visualize the fluid distributions at the several end points.

We also present oil droplets distribution in porous medium to assure a good rock filling. As shown in the Figure 3.2-9 there is not a fractured oil filling, the oily phase is mainly presented by a unique droplet which occupies 80% of the all oil in place. This observation of percolating oil in the porous medium after the primary drainage phase is coherent to usual concepts described in petrophysics.

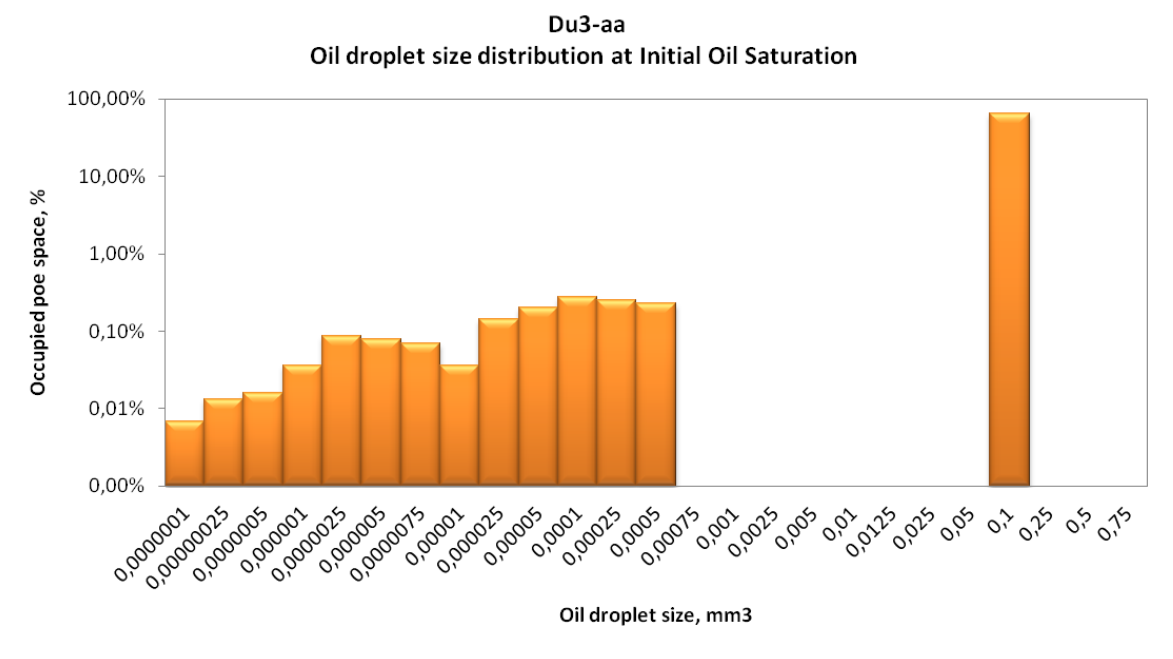


Figure 3.2-9 Oil droplet size distributions at initial oil saturation state

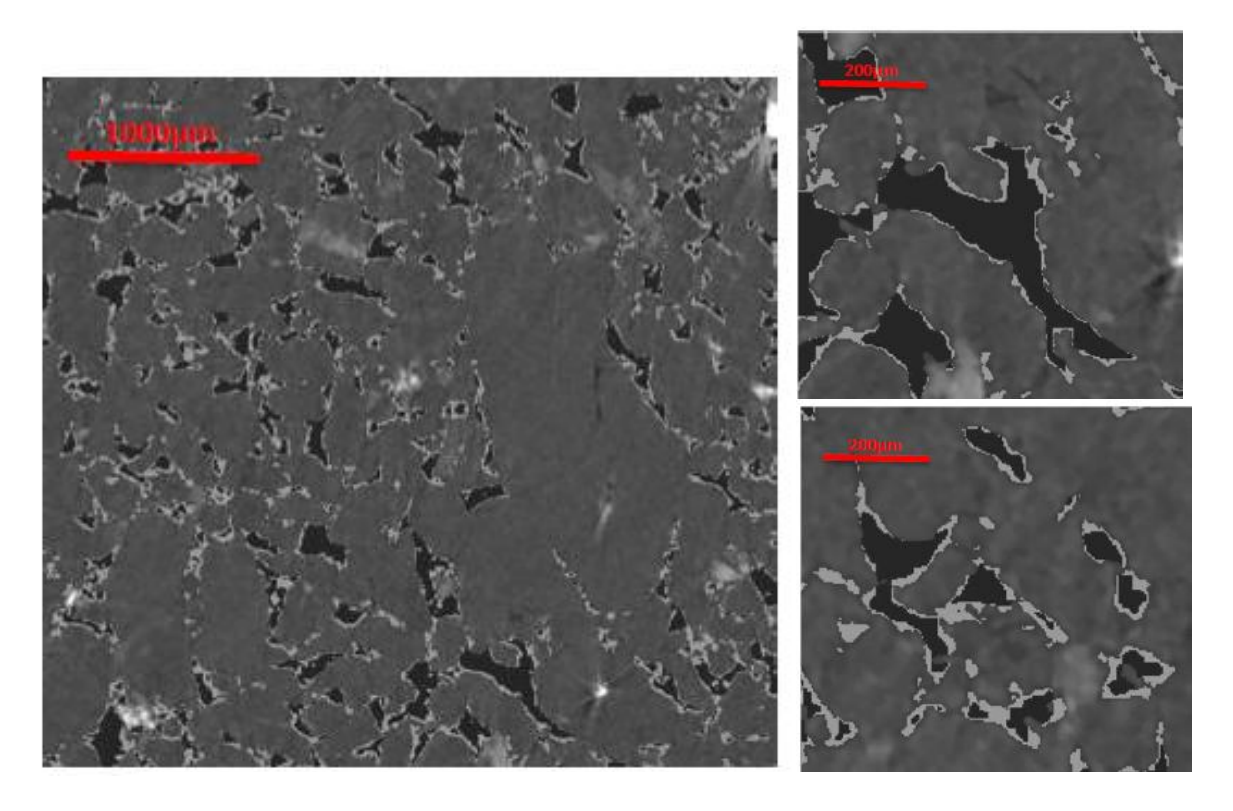


Figure 3.2-10 2D slices of  $\mu$ -CT image at Initial Oil Saturation State (oil is dark gray, water is light gra

The initial oil saturation state exhibits thick water films onto the mineral surface of the rock. The thin film presence is out of range of the micro-CT ability limited in our case to 3.7 micrometers of voxel size. From

imaging, the thin film presence will be quantitatively taken into account with the oil-mineral surface contact part.

The role and the cause of the thick film presence will be discussed later. We supposed in the case of thick water film presence that oil cannot be on mineral matrix. The subsistence of a partial thin water film during the primary drainage caused by the relative insufficiency of capillary pressure in comparison of the disjoining pressure may explain the observations.

Thick water films play a role of lubricating structures on rock surfaces and strongly limit oil-matrix contacts points and maintain a good initial water wettability of the rock. Apparent water films are thicker than 10µm it means they are out of range of the disjoining pressure resulting of the DLVO forces usually considered as at the origin of wettability control (Salathiel 1973; Derjaguin et al. 1987). Nevertheless, in limited zones no thick water films appear. This suggests the presence of oil in contact with matrix or the presence of thin film below the voxel size of the image which are imperceptible in this study. By the algorithm of oil-matrix contact determination we evolve only 13% of pore surface is covered by oil.

As illustrated in the figure before the tightest zones are filled by brine. Although, the most permeable pores are mainly filled by oil.

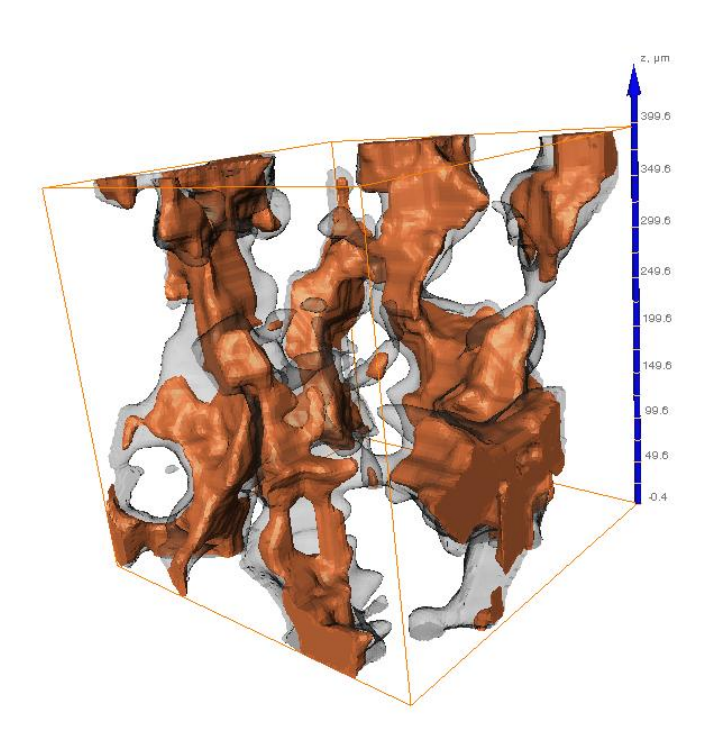


Figure 3.2-11 Initial Oil in place, oily phase is orange; pores filled by brine are gray

3D imaging permits to observe oil and brine distribution through some pores that is more representative than a 2D image. We may observe in our case oil blobs which fill several pores and oil is strongly connected through these pores. Observed water is considered as immobile, trapped and irreducible according to multiphase flow description for initial oil saturation state. Observed result is coherent with

classical petrophysical concepts for Soi state (Figure 3.2-11). As well as we can see water thick films on 2D images, they are presented in 3D image. We observe quasi inexistent contact between oily phase and solid matrix.

We could suppose at this step the preferable water wettability of the rock; however the rock imbibition by the brine will permit to judge the displacement mechanism and observe oil droplet adhesion on the substrate or oil drops in flow to better describe wettability of the rock sample. Brine injection flow rate is controlled to ensure a regime far from capillary desaturation conditions.

#### 3.2.2.2 High Salinity brine injection

Used for the waterflooding brine has the same composition that the brine used for the initial water saturation of rock core. This brine correspond to sea water salinity and describe better the commonly used in fields brines for oil recuperation by waterflooding. For the brine imbibition phase we maintain the flow rate as for initial oil saturation to  $20\mu$ L/min. Capillary number is estimated to  $10^{-5}$ . To ensure the maximum of oil recuperation and irreducible oil saturation we are injected more than 100 pore volumes.

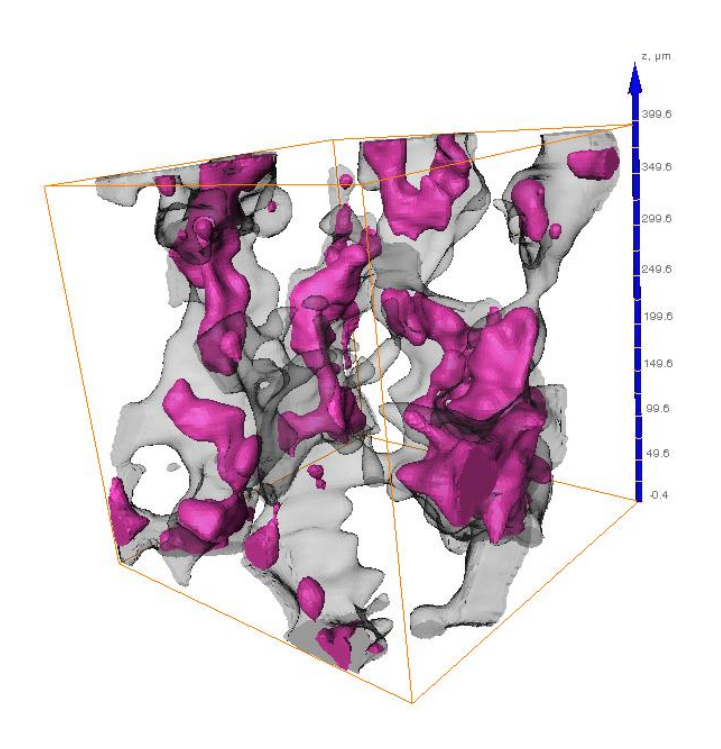


Figure 3.2-12 Residual Oil in flooded pores, oil is rose; pores filled by water are gray

The abundant brine injection clearly increases the film thickness and very thick films appear everywhere in pores (Figure 3.2-12). A very low number of oil droplets are in contact with the porous medium. Oil is fractured by snap-off due to water imbibition. Oil droplets are small and fill no longer one pore. There are

not oil droplet in pore throat, it may be explained by capillary pressure minimizing action which serves to search out the minimal energy for trapping therefore oil preferably occupies the minimal capillary pressure position in the center of pores.

As the result of water injection to recover the oil the oil saturation decreases to 35%. This high recuperation value is probably linked to water wet characteristics of used sample. In this experiment we have not observed any oil-matrix contact indicating any changes in water wet rock behavior. The oil is apparently displaced by snap-off mechanism during waterflooding in this experiment.

#### 3.2.2.3 Low Salinity brine Waterflooding

To study Low Salinity Brine (LSB) effect on the system we performed as a tertiary recuperation mechanism a LSB waterflooding. We would like to observe at micro-scale the changes that LSB injection can introduce in the rock-oil-brine system.

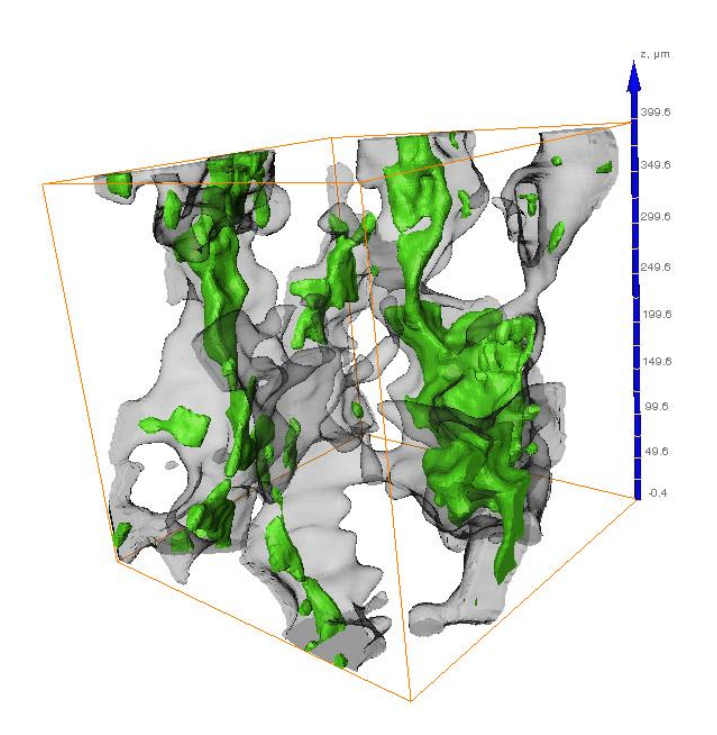


Figure 3.2-13 Residual Oil in flooded pores after low Salinity Brine injection, oil is green; pores filled by water are gray

The experiment of LSB injection was carried out in the same condition than during high salinity brine waterflooding. Flow rate was maintained at  $20\mu L/min$  and the flooding sequence corresponds to more than 100 pore volumes.

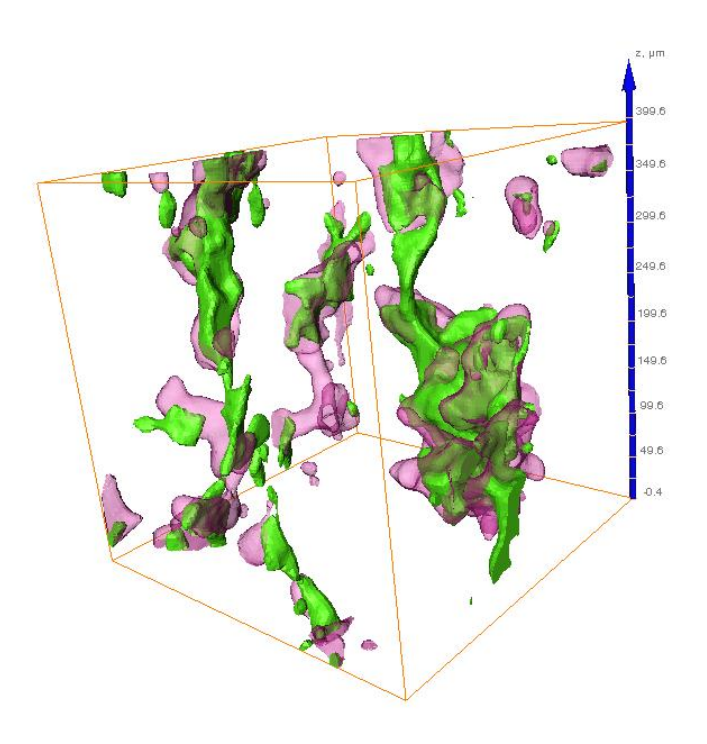


Figure 3.2-14 Two superposed Residual Oil states in the same pore space. Residual Oil after High Salinity Brine injection is rose transparent and Residual Oil after Low Salinity Brine injection is green. Water is neglected

The Low Salinity Effect is not very significant and we have obtained 4% of additional recuperation that is less than expected at this brine-oil-rock system. Despite the change in fluid distribution one to other there are not any contact between porous medium and solid rock matrix. Therefore the LSB injection does not permit to proceed to oil detachment from the substrate and to increase oil recovery.

### 3.2.3 Analysis and comparison

The aim of the experiments is to estimate wettability changes at micro-scale for the given oil-brines-rock system through Low Salinity brine injection and by means of the micro-CT imaging. Here for the first time we image the differences in fluid distributions consequence of two different thermal equilibrium conditions.

Quantitative analysis of oil saturations at the several end points provides to estimate to 73% of the initial oil saturation, 35% of the residual oil saturation after high salinity brine injection and 32% of residual oil saturation after low salinity brine injection. From very similar initial oil saturation we observed here very different fluids distribution in the pore network in comparison of DU3-ta sample although the only parameter of thermal aging is changed.

#### 3.2.3.1 Initial Oil Saturation

The fluid distribution at the micro scale is very different in the two conditions of aging. The moderate thermal aging at 60°C exhibits thinner film creation than film created without thermal conditioning. The cold aging condition develops very numerous thick water films around the non-wetting phase. This difference in fluid distribution might be explained by the insufficiency of capillary pressure forces during the primary drainage phase. Low capillary forces did not permit to create sufficient anchorage points between oily phase and rock matrix to change the wettability of the rock and to switch to another mode of recuperation with low salinity brine injection. The presence of thick water film after initial oil injection indicates the preferable water wettability of the sample and we have not obtained wettability alteration to more oil wet. It was noted in the literature that low salinity brine injection gives good recuperation results when through the wettability alteration the rock becomes more water-wet. The wettability restoration phase is correlated in our case to the additional observed recovery.

In classical conception of wettability alteration, the only DLVO concepts are identified as impacting. In this experiment the water film thicknesses are longer that range of classical DLVO forces and no flow occurs during aging which might favor oil-matrix contacts. These thick films appear when the non-wetting phase has penetrated the central part of a pore and require expelling the residual wetting fluid left in the surface grooves, edges, wedges etc., in the form of "thick" films. If there are sufficient capillary pressure these thick films might decrease the thickness to achieve some nanometers, then the capillary pressure will be counterbalanced by the disjoining pressure on the mineral surface. If the capillary pressure is adequately elevated the non-wetting fluid can adhere on the surface and alter by places the wettability. The geometry of the pore and its roughness play an important role too. The presence of nano-holes on the mineral surface can create a few zones with other micro electrochemical properties compared to its neighbor thereby anchored points between oil and mineral will be created. In this experiments zones of wettability changes are very limited and quasi inexistent thus we note the lack of oil trapping by wettability.

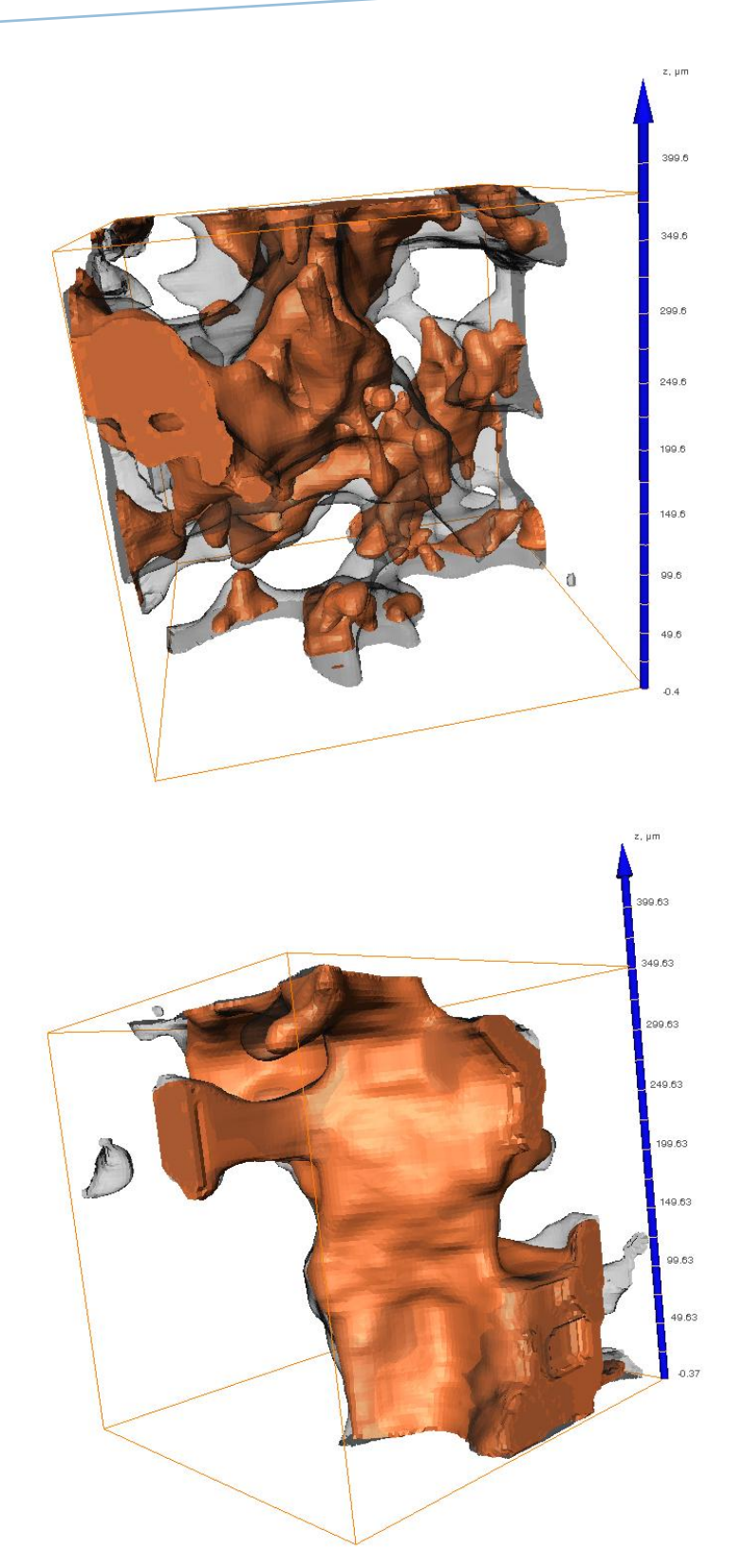


Figure 3.2-15 3D images of Initial Oil Saturation state (At top for du3-aa sample without thermal aging, at bottom for Du3-ta sample with thermal aging; oil is orange, pores filled by water are gray)

The primary drainage experiment on sample with ambient temperature aging (du3-aa) exhibited clear thick water films preventing oil contacts with the matrix. For thermal aging experiment (sample du3-ta), oil-rock contacts appear in the images and water films are thinner or not visible. The very thick water films clearly appear in the sample without thermal aging; very limited oil zones are in contact with the porous medium although very different conditions appear on the du3-ya "aging condition" sample. We conclude on temperature promotion of oil- rock contacts.

#### 3.2.3.2 Residual Oil Saturation

The long oil blobs previously observable at Soi step have been fragmented for both samples by snap-off due to high salinity brine injection. Apparent oil-matrix contacts after thermal aging show the significant difference in oil distribution on porous medium. A very low number of oil droplets are in contact with the porous medium after ambient temperature aging on du3-aa sample. At the opposite, with thermal aging condition sample du3-ta, oil droplet with surrounding water configuration is quite rare; oil blobs seem to adhere onto the solid matrix wall. Oil is located in wedges and edges previously filled by oil at Soi (Figure below).

Oil droplets are fractioned in non-thermal aging conditions and fill no more than one pore; the loci of residual oil saturation are between throat pores in the minimum capillary pressure condition therefore no oil droplet takes place in the throat pores. Capillary pressure is therefore minimized acting on the minimum energy trapping the oil in the pore center (du3-aa, no thermal aging) or in spreading impacting the contact angle (du3-ta, thermal aging).

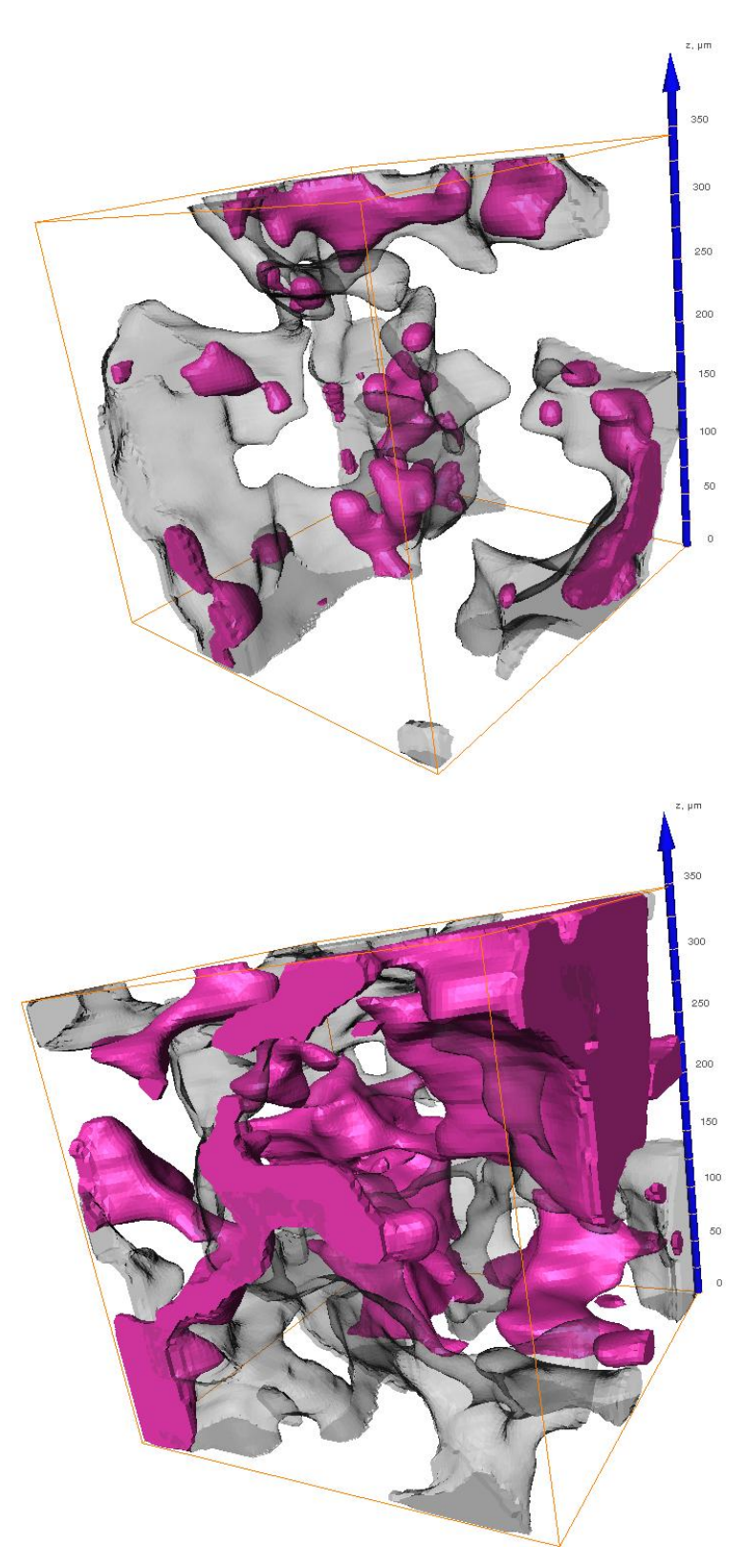


Figure 3.2-16 3D images of Residual Oil Saturation state (at top for du3-aa sample without thermal aging, at bottom for Du3-ta sample with thermal aging; oil is pink, pores filled by water are gray)

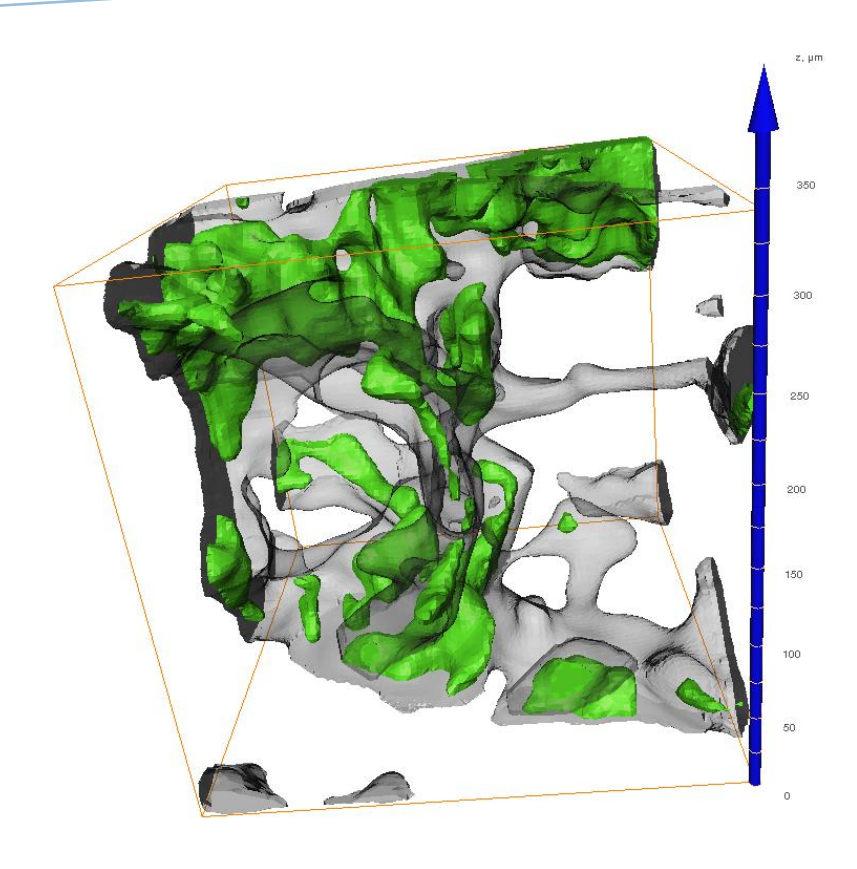
On the representative volume in sample du3-aa, only 35% of pore volume is oil filled whilst in experiment du3-ta 50.9% of pore volume is oil filled. The water wet porous medium favors higher recovery in this case.

The thermal aging experiment shows oil to be a more wetting fluid than in sample du3-aa without thermal aging. The residual oil saturation tends to be located in long thin oil drops, which partially coat the pore network. In sample du3-ta with thermal aging, the oil-trapping configuration is mainly caused by wettability changes on rock surfaces. Sample du3-ta became more oil-wet than sample du3-aa and the trapping seems now to be caused by the changes in rock (Schembre et al. 2006). We may not conclude to anchorage points due to the very limited spatial resolution we reach (3.7 microns per pixel) but brine injection clearly shows that residual trapped oil in thermal aging experiment is situated on pore walls due to wettability changes therefore the minimum energy of a non-altered system should exhibit centered oil droplets.

We recall the two systems are initially the same in the two experiments up to thermal conditioning.

## 3.2.3.3 Low Salinity Brine Injection (Tertiary mode)

Two recuperation ratios are strongly different after Low Salinity Brine injection. By the reason of oil-matrix contact absence after high salinity brine flooding in ambient temperature aging sample we note the absence of oil detachment from rock surface. In opposite, considering numerous oil-rock contacts for thermal aging condition sample we expected to proceed to significant LSB injection response. The oil droplets emplacement after HSB injection is eccentric for the thermal aging sample; therefore we state oil adhesion on rock surface. LSB injection reduces doubly this adhesion and permits to recover ¾ of residual oil after HSB injection in thermal aging sample.



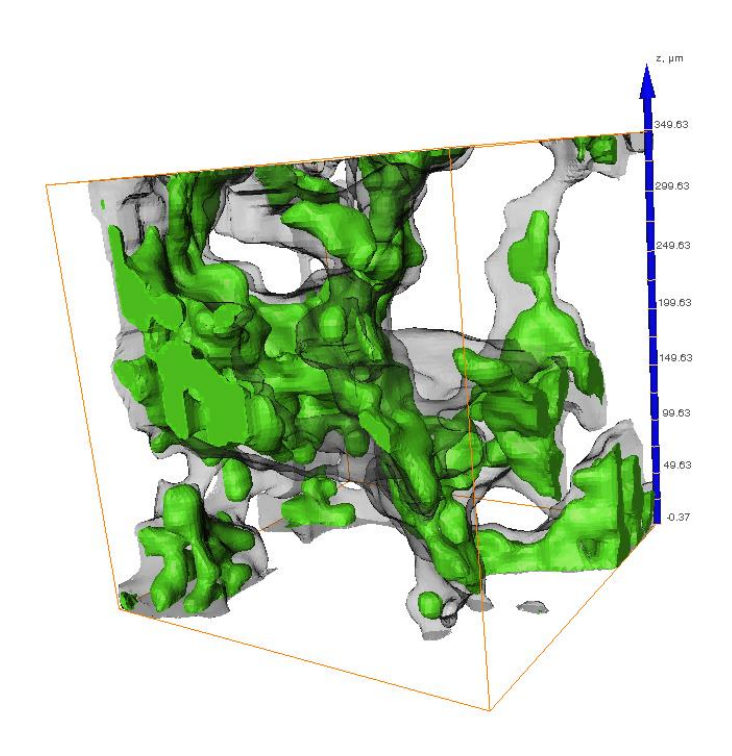


Figure 3.2-17 Oil in pores after Low Salinity Brine injection for two samples (after ambient temperature aging (a) and after thermal aging (b), oil is green, filled by brine pores are gray)

The very important incremental oil recovery is not really representative of oil field conditions especially because the waterfloods occur at 20°C although the sequences were preceded of a thermal aging.

#### 3.2.4 Conclusions

We may clearly admit the fluids in place are inserted at the same controlled flow rates although drop pressure is not measured and really controlled however we never have found public documents where the drop pressure is taken into account in the various experiments during the filling phase.

Usual concepts in petrophysics consider wettability must be restored by a long period of thermal aging to be representative of the reservoir conditions. This concept is comforted here by experimental results obtained with an innovative system based on micro-CT experiments which have exhibited a change of wettability when a sample is exposed to heating in comparison of a reference obtained during an isothermal experiment.

The change of wettability caused by the thermal aging process has clearly exhibited a transition from a capillary trapping of the non-wetting phase to an adsorbed trapping probably activated by the sample heating.

The pore shape seems not decisive in this last step of Low Salinity Brine injection indicating the whole rock surface becomes more water-wet for thermal aging sample (du3-ta). The observed images and quantifications assigned to the low salinity a dewetting role of the oil adhering on the surface. This conclusion is not negligible because considering the dewetting of the surface at the origin of the low salinity it may occur only for surface rocks wetted by the oil. A necessary high level of capillary pressure is required to contact the oil onto the mineral. To the usual capillary pressure used in petrophysics and based on a contact angle we prefer to follow a more subtle way. Kovscek and Radke (Kovscek et al. 1993) have shown the impact of the disjoining pressure onto the wettability. The net interfacial forces balance conditions the state of wettability of the mineral surface. Oil trapping onto the mineral may be caused by a primary direct oil adhesion considering the capillary pressure exceeds the disjoining pressure term of contact. It may be also evocated the presence of a stable thin brine film.

## 3.3 Effect of crude oil on LSB injection effect

#### 3.3.1 Representative Elementary Volume

Before all calculations on the sample we estimated the representativity of treated volume. To estimate the rock sample representativity we used bear's method (Bear 1972) that consists to study the stability of the measured property decreasing the volume of the sample. The study on porosity stability of the sample is represented in the figure below.

#### REV study on sandstone sample 0.18 0.16 0.14 0.12 0.10 0.08 0.06 0.04 0.02 0.00 0.00 1.00 2.00 3.00 4.00 5.00 6.00 Sample volume, mm<sup>3</sup>

Figure 3.3-1 Study of the sample representativity on porosity

From this figure we conclude the transient between the domain impacted by the microscopic effect and porous medium is close to 0.5 mm<sup>3</sup>. We work with volumes about 5mm<sup>3</sup> that is significantly superior to required volume.

For these two samples we used the Ja-oil which is a little more viscous then Ac-oil. Oil characteristics are presented in the table below.

Table 3.3-1 Comparison table of Ac-oil and J-oil. Oils are used as received

	ĺ				
		AC-oil	Ja-oil		
		Dehydrated	filtered tank		
Characteristics	Unit	·	il		
BS&W (reception)	%	0.5	0		
TAN	mg/g KOH	n/a	0.31		
TBN	mg/g KOH	1.64	1.85		
Volumic mass @ 35°C	Kg/m³	834.7	854.5		
Cinematic viscosity @ 35°C	cSt	6.46	11.8		
Total Sulfur	%	0.33	1.2		
TCC	°C	32	37		
SARA					
Distillate	% weight	31.5	27.2		
Residual	% weight	68.5	72.8		
,	ASPHALTENES				
Asphaltenes (residual)	% weight	2.74	5		
IATROSCAN					
Saturated (residual)	% weight	56.8	51		
Aromatics (residual)	% weight	33.6	33.6		
Resin (residual)	% weight	9.6	15.4		

## 3.3.1 Initial Oil Saturation

As for all experiments the rock sample was initially saturated by the bottom of the cell with high salinity brine (45g/L of NaCl and 5g/L of CaCl<sub>2</sub>) to reproduce the history of classical reservoir formation. After brine saturated core was exposed to non-wetting phase injection in the opposite direction to limit the instabilities when primary drainage occurs.

For the first experiment we have heated the sample saturated with oil to water irreducible saturation that signs the non-displacement one phase by other. To restore the wettability of the sample and to equilibrate the compounds of the two liquids with mineral phase we proceed to aging state. The saturated core was aged during 2 weeks and heated at 60°C during this time to stimulate ionic and material exchange between phases. For image acquisition the core was cooled to ambient temperature.

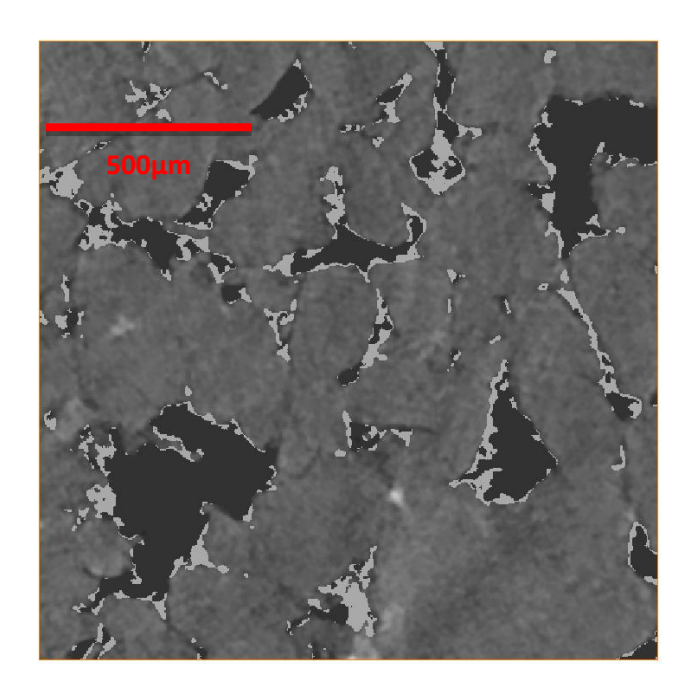


Figure 3.3-2 2D slice of  $\mu$ -CT image at Initial Oil Saturation State (oil is dark gray, water is light gray)

Even on 2D reconstructed image we can state the development of thick water films. Water films are larger in pore corners and their thickness decrease on wedges. Small pores are filled by brine showing preferential water wet behavior of the rock sample.

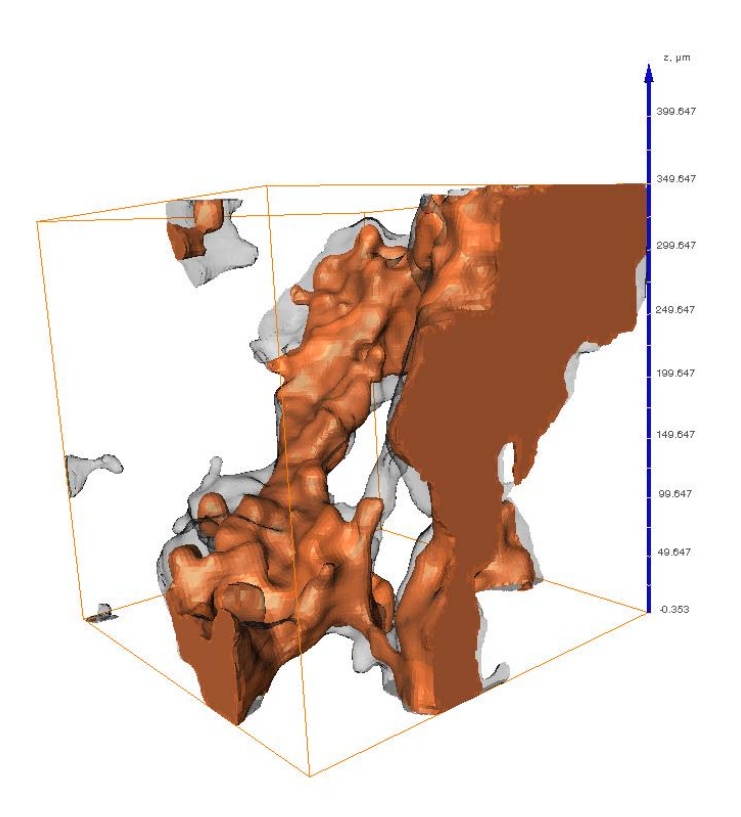


Figure 3.3-3 Initial Oil in place, oily phase is orange; pores filled by brine are gray

The 3D image exhibits a percolating oil blobs through a few pores. Oily phases fill preferentially the center of pores. It confirmed on the 2D images of the sample. There are not a lot of differences in fluid distribution in comparison with Ac-oil in sandstone without thermal aging (du3-aa). In the oil saturated core oil represents 62% of pore space globally and 79% on the local image (Figure 3.3-3).

In the case of J-oil with thermal aging we might supposed the oil spreading on solid surface, for this we have analyzed the neighborhood of pore surfaces voxel, if they are bordered by oil or water in preference. It is important to note that we analyze the neighborhood at the  $\mu$ -CT scanner resolution, it means we might identify closed voxels as contact between oil and solid matrix but in reality the presence of water thin film between oil and rock surface might be neglected caused the scanner resolution. To better describe surface states and relative contacts we proceed to high salinity brine injection. In the classical concepts of oil recovery we suppose that in the case of thin water film absence the recovery process cannot be performed by film flow. Thereby, if there is not film flow most of previously labeled voxel as oil on solid surface will stay in the same emplacement.

#### 3.3.2 High Salinity Brine Waterflooding

For all experimental samples we injected more than 100 pore volumes to ensure achievement of the residual oil saturation in core plugs.

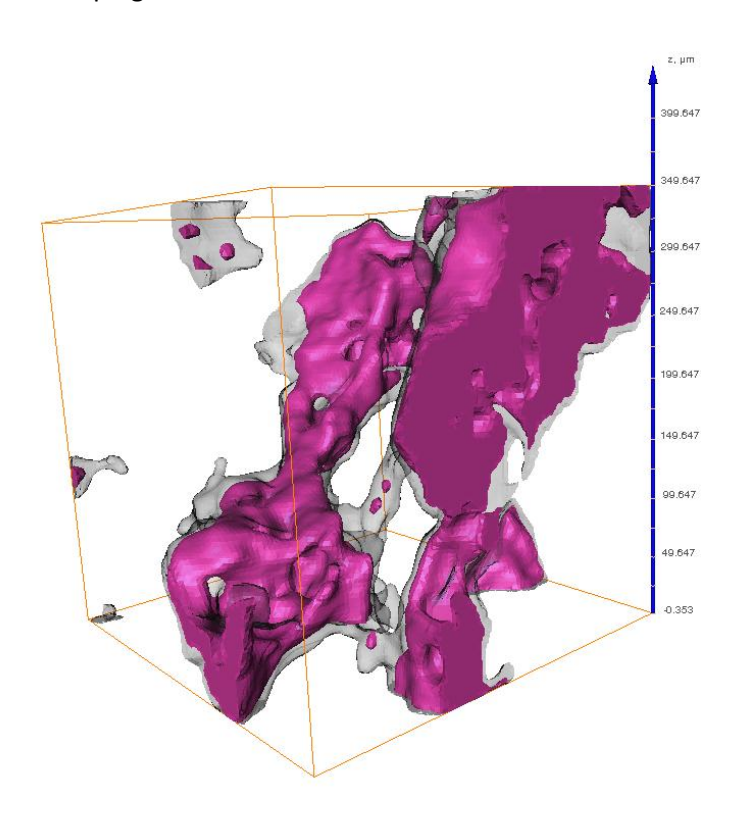


Figure 3.3-4 Residual Oil in flooded pores, oil is rose; pores filled by water are gray

The abundant brine injection does not permit to recover large amount of oil despite 100 pore volumes brine injection. The residual oil saturation after high salinity injection for the sample is 51% globally and 56% in the field of view. Considering the obtained saturation we might suppose oil spreading on the rock surface, thereby not accessible for recovery by high salinity waterflooding. Nevertheless oil distribution at

residual oil saturation shows trapped oil preferably in the center of pores. Statistical study on oil - solid matrix contact reveals the quasi total inexistence of spreaded oil on rock surface; there are less than 1% of contacts. We obtained similar results with Ac-oil and the companion rock sample.

## 3.3.3 Low Salinity Brine Injection (Tertiary mode)

Low salinity brine injection is referred to improve oil recovery by the oil detachment previously spreaded on the rock surface. In the way that we did not note the presence of oil-matrix contact after high salinity waterflooding, we did not expect to recover a lot with low salinity brine injection.

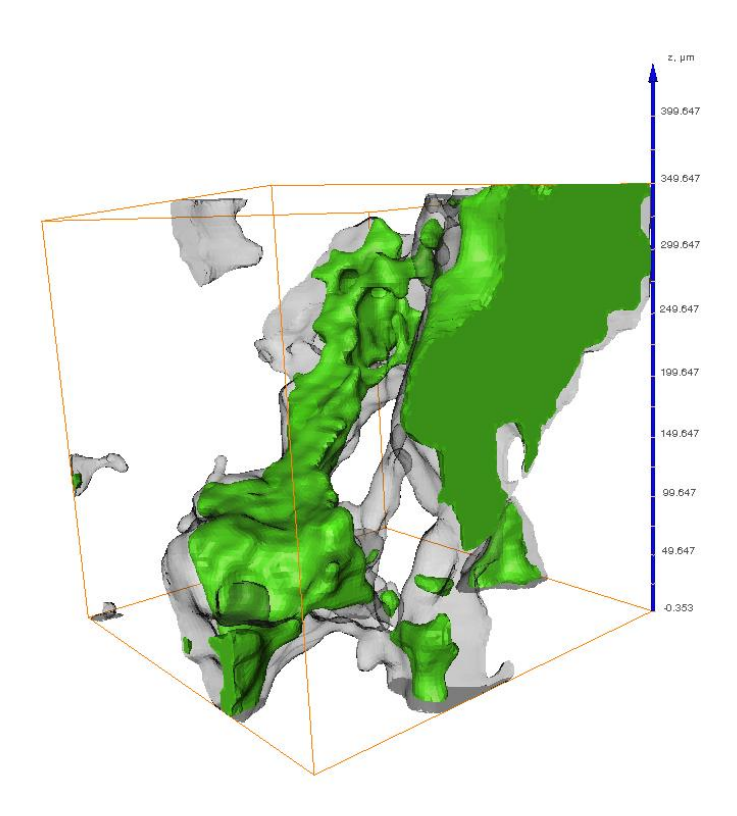


Figure 3.3-5 Residual Oil in flooded pores after low Salinity Brine injection, oil is green; pores filled by water are gray

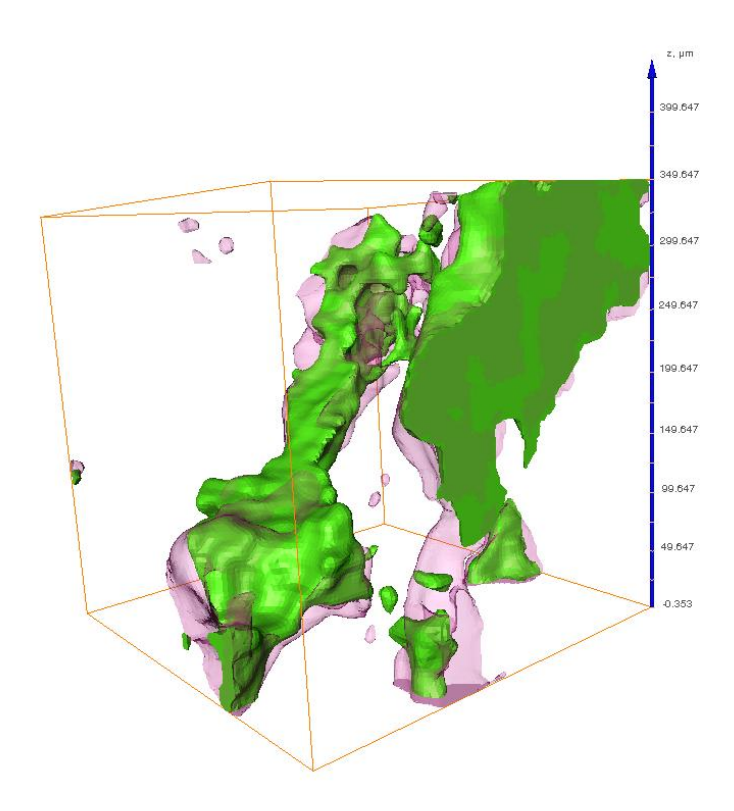


Figure 3.3-6 Two superposed Residual Oil states in the same pore space. Residual Oil after High Salinity Brine injection is rose transparent and Residual Oil after Low Salinity Brine injection is green. Water is neglected

After low salinity brine injection the oil saturation in the rock sample was not changed a lot, for global analyzed volume it decreases to 48% against to 51% of residual oil saturation after high salinity brine injection. Low salinity brine injection allowed insignificant oil redistribution in pore space and did not lead to important recovery. This result is not surprising considering the absence of oil-matrix contact after high salinity brine injection. Therefore, LSB waterflooding is unable to detach oil from rock matrix meaning the low level of adhered oil on rock surface.

#### 3.3.4 Analysis and conclusions

Obtained results with Ja-oil and Du3 sandstone at thermal aging condition are similar to obtained results with Du3 sandstone and Ac-oil without thermal aging conditions. There are not a lot of oil-matrix contacts after the aging step, therefore Low Salinity Brine injection did not permit to detach adhered oil due to absence of such adhesion. The similitude might be explained by similar oil properties at two used temperature regimes. Nevertheless, we will not really conclude concerning the comparison between the two samples considering the presence of non-controlled parameters. Here, we note the absence of significant additional oil recovery after LSB flooding for two samples.

## 3.4 Conclusions

We showed the consequence of the choice of oil-rock-brine system to Low Salinity brine injection effect observation. Scattered results indicate the importance of total parameters control in the carried out experiments. The presence of significant dead-volume in the observation installation impede the accurate control of several parameters such the pressure drop in the samples during imbibition-drainage phases.

Observed results under different thermal conditions and for two different oils are presented in table below. We show only described experiments because of the majority of samples have helped to improve the experimental setup and get rid of problems during fluids injection steps.

Table 3.4-1 Summary table of described experiments

Brine H: 50g/l : 45g/l NaCl + 5g/l CaCl2			
	Du3-aa	Du3-ta	Du3-ja-ta
Porosity	19%	17%	16%
	Du3-aa	Du3-ta	Du3-ja-ta
Brine HS	Н	Н	Н
Injected VP	20	20	20
T° of injection, °C	20	20	20
T° of scan, °C	20	20	20
	1		
	Du3-aa	Du3-ta	Du3-ja-ta
Oil	Ac	Ac	Ja
Injected VP	20	20	20
T° of injection, °C	20	20	20
T° of scan, °C	20	20	20

Aging	15 days	15 days	15 days
T° of aging, °C	20	60	60
T° of scan, °C	20	20	20
	Du3-aa	Du3-ta	Du3-ja-ta
LSB injection	tertiary	tertiary	tertiary
	Du3-aa	Du3-ta	Du3-ja-ta
Brine LS	0.1H	0.1H	0.1H
Injected VP	20	20	20
T° of injection, °C	20	20	20
T° of scan, °C	20	20	20
	1	1	
	Du3-aa	Du3-ta	Du3-ja-ta
Swi, %	28,3	35	26
Pore surface in contact with oil, %	13	45	44
Sor, %	35	51	42
Pore surface in contact with oil, %	7	30	5
Sor_lsb, %	32	13	38
Pore surface in contact with oil, %	0	12	12

We showed than the classical concepts of wettability controlled by interfacial forces (DLVO theory) are not sufficient to detail the observed wettability alteration mechanism. This evidence was possible due to the X-ray microtomograph technique that has brought very precious information. The low speed registration of radiographies and relatively low resolution are the main difficulties to progress in order to analyze the very complex mechanisms encountered during a multi-phase flow in porous media.

To improve our understanding of the underlying mechanism of Low Salinity Brine injection at other scale and to verify some proposed in literature mechanisms we decides to use other techniques to study Low Salinity Brine effect.

#### 3.5 References

- Andrew, M., Bijeljic, B. & Blunt, M.J., 2014. Pore-scale contact angle measurements at reservoir conditions using X-ray microtomography. *Advances in Water Resources*, 68, pp.24–31..
- Bear, J., 1972. Dynamics of Fluids in Porous Media.
- Borghi, F. et al., 2013. Nanoscale roughness and morphology affect the IsoElectric Point of titania surfaces. *PloS one*, 8(7), p.e68655.
- Bouriat, P. et al., 1999. A Convenient Apparatus to Determine the Zeta Potential of Grains by Electro-Osmosis. *Journal of colloid and interface science*, 209(2), pp.445–448.
- Boussour, S. et al., 2009. Oil recovery by low salinity brine injection: Laboratory results outcrop and reservoir cores. In *Proceedings SPE Annual Technical Conference and Exhibition*. pp. 1595–1606.
- Buckley, J.S., 2001. Effective wettability of minerals exposed to crude oil. *Current Opinion in Colloid & Interface Science*, 6(3), pp.191–196.
- Cissokho, M., 2010. Etude expérimentale des interactions Huile brute/Saumure/Roche sur la récupération d'hydrocarbures par injection d'eau de faible salinité.
- Cissokho, M. et al., 2010. Low salinity oil recovery on clayey sandstone: Experimental study. *Petrophysics*, 51(5), pp.305–313.
- Creux, P. et al., 2009. Strong specific hydroxide ion binding at the pristine oil/water and air/water interfaces. *The journal of physical chemistry*. *B*, 113(43), pp.14146–50.
- Derjaguin, B. V., Churaev, N. V. & Muller, V.M., 1987. Surface Forces, Boston, MA: Springer US.
- Graciaa, A. et al., 2000. Potential at an Air Water Surface Related to the Critical Micelle Concentration of Aqueous Mixed Surfactant Systems., pp.2677–2681.
- Hartley, P.G., Larson, I. & Scales, P.J., 1997. Electrokinetic and Direct Force Measurements between Silica and Mica Surfaces in Dilute Electrolyte Solutions. *Langmuir*, 13(8), pp.2207–2214.
- Hunter, R.J., 1981. Zeta Potential in Colloid Science: Principles and Applications, Academic Press.
- I. Bondino, S. Doorwar, R. Ellouz, G.H., 2013. Visual microscopic investigations about the role of pH, salinity and clay on oil adhesion and recovery. In *The Society of Core Analysts*.
- Kosmulski, M., 2010. Surface charging and points of zero charge, CRC Press.
- Kovscek, A.R., Wong, H. & Radke, C.J., 1993. A pore-level scenario for the development of mixed wettability in oil reservoirs. *AIChE Journal*, 39(6), pp.1072–1085.
- Lebedeva, E. V. & Fogden, A., 2011. Micro-CT and wettability analysis of oil recovery from sand packs and the effect of waterflood salinity and kaolinite. *Energy and Fuels*, 25(12), pp.5683–5694.
- Masliyah, J.H. & Bhattacharjee, S., 2006. Electrokinetic and colloid transport phenomena, John Wiley & D. Samp; Sons.

- Mohanty, K.K., Scriven, L.E. & Davis, H.T., 1987. Physics of Oil Entrapment. *SPE Reservoir Engineering*, 2(February), pp.113–118.
- Nasralla, R.A., Bataweel, M.A. & Nasr-El-Din, H.A., 2011. Investigation of Wettability Alteration by Low Salinity Water. In *Offshore Europe, 6-8 September, Aberdeen, UK*. Society of Petroleum Engineers.
- Pieterse, S.G.J. et al., 2013. SPE 165180 Experimental Investigation on the Effects of Very Low Salinity on Middle Eastern Sandstone Corefloods.
- Radke, C.J., Kovscek, A.R. & Wong, H., 1992. Pore-level scenario for the development of mixed wettability in oil reservoirs. In *Proceedings SPE Annual Technical Conference and Exhibition*. pp. 163–177.
- RezaeiDoust, a. et al., 2009. Smart Water as Wettability Modifier in Carbonate and Sandstone: A Discussion of Similarities/Differences in the Chemical Mechanisms. *Energy & Fuels*, 23(9), pp.4479–4485.
- Salathiel, R.A.A., 1973. Oil Recovery by Surface Film Drainage In Mixed-Wettability Rocks. *Journal of Petroleum Technology*, 25(10), pp.1216–1224. A
- Sanchez-Soto, P.J., Justo, A. & Pérez-Rodriguez, J.L., 1994. Grinding effect on kaolinite-pyrophyllite-illite natural mixtures and its influence on mullite formation. *Journal of Materials Science*, 29(5), pp.1276–1283.
- Schembre, J.M., Tang, G.-Q. & Kovscek, a. R., 2006. Wettability alteration and oil recovery by water imbibition at elevated temperatures. *Journal of Petroleum Science and Engineering*, 52(1-4), pp.131–148.
- Souza, A.E. et al., 2013. Addition of sedimentary rock to kaolinitic clays: influence on sintering process. *Cerâmica*, 59(349), pp.147–155.
- Tang, G. & Morrow, N.R., 1999. Influence of brine composition and fines migration on crude oil r brine r rock interactions and oil recovery.
- Valtiner, M. et al., 2011. Effect of surface roughness and electrostatic surface potentials on forces between dissimilar surfaces in aqueous solution. *Advanced materials (Deerfield Beach, Fla.)*, 23(20), pp.2294–9.
- Valtiner, M. et al., 2012. The electrochemical surface forces apparatus: the effect of surface roughness, electrostatic surface potentials, and anodic oxide growth on interaction forces, and friction between dissimilar surfaces in aqueous solutions. *Langmuir: the ACS journal of surfaces and colloids*, 28(36), pp.13080–93.
- Vledder, P. et al., 2010. Low Salinity Water Flooding: Proof Of Wettability Alteration On A Field Wide Scale. In SPE Improved Oil Recovery Symposium, 24-28 April, Tulsa, Oklahoma, USA. Society of Petroleum Engineers.

#### 4. NON-TOMOGRAPHIC METHODS TO STUDY OIL-ROCK-BRINE SYSTEM

# 4.1 Electric double layer expansion impact on the oil-quartz adhesion for high and low salinity brine solutions (paper form)

#### 4.1.1 Introduction

Various industrial processes are concerned by fluid flows in porous media as well as in natural rocks for i.e. petroleum industry, hydrology, geothermal, carbon dioxide or methane underground storage, as synthetic ones for i.e. catalysis, separators, microfluidics, ... The liquid behavior in porous media is conditioned by the physical chemistry of fluids and also by the interactions with the solid substrate. The electrical force is one of the intermolecular forces which influence the fluid distribution in the pore structure. This property is of interest for public and industrial research teams and especially for oil companies. Indeed there could be a link between electrical forces and the "smart water" effect observed in laboratory or fields to boost oil production. Among numerous intermolecular forces influencing fluid distributions in natural pore structures, the electrical force is the center of interest for numerous public and industrial research teams all over the world. This interest is due to a possible link existence between electrical forces and the "smart water" (Tang & Morrow 1999) effect observed in lab or fields to boost oil production.

Smart water is an EOR technique (Enhanced Oil Recovery). It corresponds to a design water formulation with a specific ionic composition and salinity adapted to targeted reservoirs, which could change oil/rock interaction and enhance oil recovery. This technique has been highlighted by Tang and Morrow (Tang & Morrow 1999). After low salinity injection, they observed an incremental oil recovery in sandstone.

After this remarkable observation numerous scientists attempted to reproduce observed effect and to identify its origin. During the low salinity brine injection in secondary or tertiary recovery modes numerous authors have reported an incremental oil recovery in lab or field conditions. Most troubling observation concerning this recovery technique is the experimental incoherent behavior met by numerous authors. Several authors considered that the origin of such effects was linked to the electrical double layer expansion when dilution occurs. Other numerous hypothesis have been suggested such fines particles mobilizations (Tang & Morrow 1999)-(Lebedeva & Fogden 2011), electrochemical reactivity (RezaeiDoust et al. 2009) -(Pieterse et al. 2013) or the wettability alteration (Buckley 2001)-(Vledder et al. 2010).

Recently, proposed by Nasralla et al. the double layer expansion in low salinity brine condition as one of responsible mechanisms to explain the additional oil recuperation with LSB injection (Nasralla et al. 2011). Authors have conducted experiments measuring zeta potential at rock-brine and oil-brine interfaces. They observed that interfaces were highly charged with low salinity brine, that is not in contradiction with commonly accepted phenomenon of surface screening by electrolytes in high salinity (Hunter 1981).

Silica particles interactions immersed in brines have been already investigated by Hartley et al. (Hartley et al. 1997) using atomic force microscopy (AFM) by measuring the forces as a function of the separation distance. They showed a very good agreement between experimental measurements performed with

electrokinetics methods and the direct measurement obtained by AFM at low ionic strength. At high ionic strength, more than 0.1 M interfacial saturation introduces complex steric mechanisms at the origin of a progressive divergence between AFM and electrokinetical measurements. Moreover Israelachvili et al. (Valtiner et al. 2011; Valtiner et al. 2012) have modeled semi empirically the measured force profiles between rough and smooth surfaces on solid substrates and theoretically with an extended DLVO model on the characteristic roughness of the studied materials. The model is in agreement with AFM experiments and allows to exhibit repulsive contributions due to steric and hydration forces between rough and smooth surfaces.

The pore level scenario, proposed by Radke et al. (Radke et al. 1992), described the crucial role of wetting thin film layers between the non-wetting phase usually oil and the minerals for oil-wet or mixed-wet reservoirs. These thin films are the consequences of molecular interaction forces. Consequently a new parameter: the disjoining pressure is added in the classical Young-Laplace equation. The disjoining pressure term expresses the net force balance of the intersurfacial forces acting at both sides of the wetting film. This film stability depends mainly on three major forces: van der Waals interactions, hydration forces and electrostatic forces.

The current work investigated the electrical double layer effect of a low salinity brine on an oil-brine-mineral system previously referenced as respondent to a Low Salinity Brine injection effect (Boussour et al. 2009, Cissokho et al. 2010). The electrical double layer expansion hypothesis was tested as a function of pH and salinity for the system rock-brine-crude oil used by Cissokho et al. (Boussour et al. 2009, Cissokho et al. 2010) and those obtained by flotation-like experiments performed by Bondino et al. (I. Bondino, S. Doorwar, R. Ellouz 2013).

#### 4.1.2 Experimental section

In the current work global interactions between oil, mineral and brine were studied with in-home zeta-potential measurement techniques. The experiments were carried out with zeta potential measurement of pair interaction oil-brine and rock-brine. To ensure the ionic exchange in the solution, all the elements of each system (oil/brine and rock/brine) were put in contact to equilibrate the system before the measurement.

#### 4.1.2.1 Fluid phases

Synthetic high salinity brine with TDS = 50 g/L (Total Dissolved salts) was prepared with 90 wt% of NaCl and 10 wt% of CaCl2. Diluted salinity brine is obtained with a 0.1% dilution of initial high salinity brine, therefore 0.05 g/l of salts. NaCl(s) and CaCl<sub>2</sub>(s) are manufactured by Sigma Aldrich® with a purity grade higher than 99.9%. Water was purified by Elga Purelab® classic system to give a resistivity of 18.2 M $\Omega$ .cm.

The crude oil was provided by TOTAL and used as received. The crude oil is characterized by a cinematic viscosity of 5.82 cP @ 40°C and a density of 830.7 kg/m3. The natural surfactants in oils, characterized by the Total Acid Number (TAN) and Total Base Number (TBN), were 0.17 and 0.95 mg KOH/g respectively. Using standard extraction process asphaltene content was found to be 2.3 wt% whilst SARA analysis exhibited fractions of 58.2 wt% of saturated, 31.4 wt% of aromatic and 10.4 wt% of polar compounds.

#### 4.1.2.2 Minerals

The minerals used for this study are sands and sandstones. Fontainebleau sand provides from VWR, Ottawa sand from Fischer Scientific, Landes sand and Dausse sandstone (referenced as DU3) from TOTAL Company. The chemical analyses of the samples are displayed in the Table 4.1-2. Sandstone has been used as received. One sample of DU3 sandstone was pyrolysed at 650°C during 4 h.

Mineral	Quartz	Clays	Feldspar	Pyrite
Landes Sand	99.11	0	0	0
Ottawa sand	99.90	0	0	0
Fontainebleau Sand	99.91	0	0	0
DU3	86.1	3.1	10.6	0.2

Table 4.1-1 Mineralogy of rock samples (wt%)

#### 4.1.2.3 Methods

For the single drop measurements, we developed an in-house spinning cell for electrophoresis measurements. It was made with an uncharged special coating to prevent electro-osmotic flow when voltage is applied. The drop remains suspended on the rotation axis thanks to the centrifugal gravity effect like for the spinning drop tensiometer and the mobility of the dispersed particle is measured by voltage applying. The zeta potential is measured via the drop mobility. The complete set-up is described by Graciaa et al. (Graciaa et al. 2000).

Concerning the brine-mineral zeta-potential, a simple experimental setup by direct weighing (Bouriat et al. 1999) was used for measuring the electro-osmotic flow through a porous media. The objective was to increase the range of zeta potential measurement application for solid particles and to measure zeta potential regardless of the particle size. Instead of current measurement, potential allows the determination of electrokinetic mobility, even with a significant surface conduction. This set-up is validated for flow equations for porous medium made of monodispersed and randomly shaped and sized packs of fiber grains. The measured electrokinetic mobility is in agreement with those deduced from electrophoresis measurements and referenced materials (Hunter 1981, Bouriat et al. 1999).

Methods and set-ups developed in our laboratory for both oil-brine and brine-rock zeta-potential measurements offer a very easy and swift technique. The technical advantage of the electro-osmotic device upon the electrophoresis is that it is not necessary to crush the material in order to obtain very small particles required for electrophoresis. Sandstones might contain some mineral inclusions which do not come out on pore surfaces and therefore not in contact with fluids in reservoir. Material crushing

might perturb mineral distribution and bring to the surface these inclusions giving erroneous measurement results. Some of the samples used in this study contain pyrite. Electrokinetically, we may attempt a release of multivalent iron ions solubilized in contact with the brine which extremely impact the zeta potential (Hunter 1981). This remark was supported by the micro-CT image of the DU3 sandstone (Figure 4.1-1) used in the experiments. We clearly observed very attenuating material (brightest elements) inclusions corresponding to pyrite inclusions. However we have not observed macroscopic inclusions in possible contact with the brine.

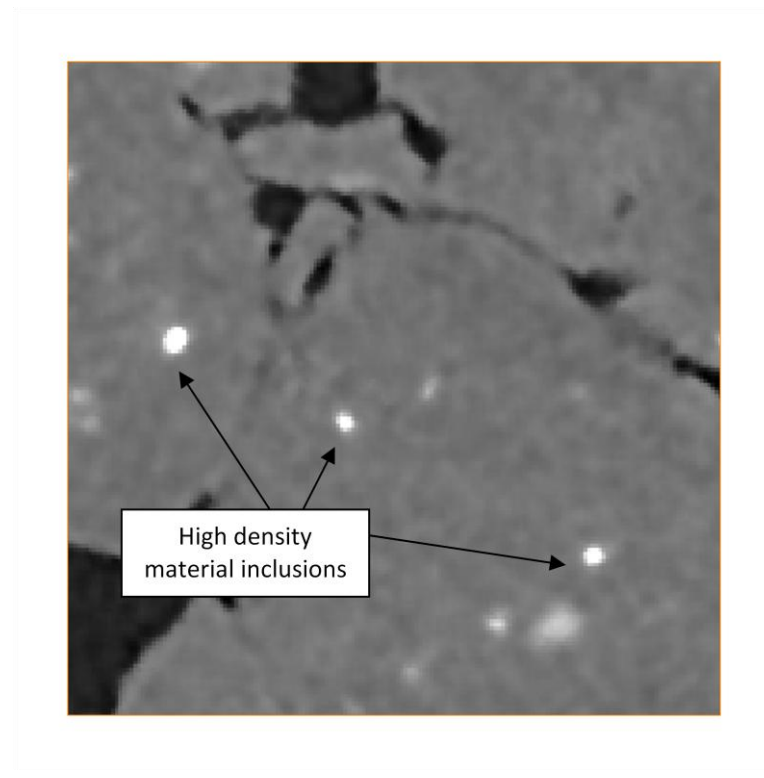


Figure 4.1-1 Inclusion on 350 x 350 μm image of the sandstone obtained by X-ray micro-CT at 2 μm

#### 4.1.2.4 Set-ups

The samples are unconsolidated (sands) except the sandstone DU3. This one is very permeable (about 0.8D) and porous (17% in consolidated state and 39% once broken) and the cementation very friable. It was manually crushed without any crusher to avoid grains destruction with consequent mineral inclusion apparition on surface and inserted into the electro-osmometer.

The crude oil has indigenous surfactants content. The effect of these surfactants on zeta potential is considered as non-negligible and especially the ionic ones. The used procedure was to take into account the exchanges between oily and mineral phases which are stimulated by brine pH and salinity. The minerals are equilibrated in ratio of 1 for mineral to 10 for brine with specific pH and salinity for each measurement during 12h. 5 volumes of crude oil are added and the solution was stirred with a magnetic stirrer and heated at 60°C during 24h to favor the crude oil partitioning and surfactant migration.

The oily supernatant was removed with a syringe from the system and the resulted brine and sand solution was centrifuged at 4000 rpm (rotation per minute) during 2 minutes to get rid of small oil droplets. The oil droplet from the centrifugation was measured with the spinning zeta-meter in the brine previously equilibrated with the rock and the oil. The droplet was maintained at the center of the capillary by spinning of the tube at 800 rpm during the measurement with equilibrated brine.

## 4.1.3 Results 4.1.3.1 Minerals

Zeta potentials of charged materials such minerals is quasi inexistent in brine solution with a salinity 0.1 M and always null for a salinity above 1 M. For high salinity brines, the surface charge of the rock sample is saturated by ions close to the interface. The electrical double layer thickness is 1 nm at 0.1 M and 0.3 nm at 1 M. This could explain why no zeta potential was observed with the electro-osmometer whatever the mineral and the used aqueous solution (1 M NaCl or 0.95 M NaCl and 0.05 M CaCl<sub>2</sub>). This range of salinity was studied to reproduce classical brines of natural reservoir and geological system as sea water and formation water. The low salinity effect studied in enhanced oil recovery processes corresponds for example to similar brine diluted to 0.1% in ultra pure water. The 1 mM solution has been tested on the whole minerals of interest.

Zeta potentials of DU3 and pyrolysed DU3 samples are shown in Figure 4.1-2. The DU3 equilibrated with the crude oil exhibits a higher magnitude of zeta potential than the non-equilibrated one for alkaline pH (7-9). This is certainly due to crude oil indigenous surfactants in acidic form. Consequently, the whole systems were equilibrated in order to be representative of realistic systems.

The isoelectric points (IEP) seem to converge for the three non pyrolysed samples although the magnitude of the zeta potential is lower for pyrolysed sample (Figure 4.1-2). The electrokinetical features of the minerals are not only similar between themselves but also with the quartz (Masliyah & Bhattacharjee 2006). These curves clearly show the very low impact of impurities in quartz.

The difference of magnitude is about 10 mV as for the fact that the chemistry of the surfaces is not equivalent. The pyrolysis at 650°C showed a loss of adsorbed water as reported in numerous thermogravimetric analyses (Sanchez-Soto et al. 1994; Souza et al. 2013). The heating led to structural modifications in quartz, but the rapid variation of temperature is at the origin of clay cracks. This modification favored clay releasing in the solid matrix which once immersed in brine solution formed gellike structure. The clay content was also reduced by the thermal pre-treatment that could explain the low zeta potential changes (Figure 4.1-2).

As an indicator of the ionic exchanges, the graph of final pH in function of initial pH for DU3 sample was drawn (Figure 4.1-3), like for electrochemistry with the brine mineral system. Compared to the pyrolysed DU3 sample, the pHi – pHf curve of DU3 sample highlights a broad buffer effect between pH 5-9. The heat treatment could reduce this effect due certainly to clay particles which are released in the solution during the imbibition which followed the pyrolysis. This treatment is however not very decisive concerning the zeta potential magnitude and the IEP pH. Nevertheless both systems have quite the same behavior despite all the performed treatments (brine interaction and heating).

In Figure 4.1-4 zeta potential of three used sands are displayed. The curves correspond to classical curve of pure quartz (Masliyah & Bhattacharjee 2006),(Kosmulski 2010); the differences are due to surface charge densities and potentially impurities on the surfaces. Ottawa sand is characterized with the highest purity grade. The zeta potential curve follows a very classical shape with a sigmoidal pH dependence characterized by an isoelectric point at about pH=2 and a half adsorption point at about pH=5.5 (Figure 4.1-4). Landes sand exhibits the largest range of magnitude on the tested pH range compared to Ottawa sand especially in the pH below pH4 and above pH8. The electrical double layer of Ottawa sand is very similar to the Fontainebleau one. The zeta potential magnitude in the pH range of experiments is comprised between -30 mV and -50 mV. These strong zeta potential are conform to bibliography data of quartz grains (Masliyah & Bhattacharjee 2006; Kosmulski 2010).

The pHi-pHf curves of the three sands show similar behavior with very low ionic exchanges during the equilibrium phase (Figure 4.1-5).

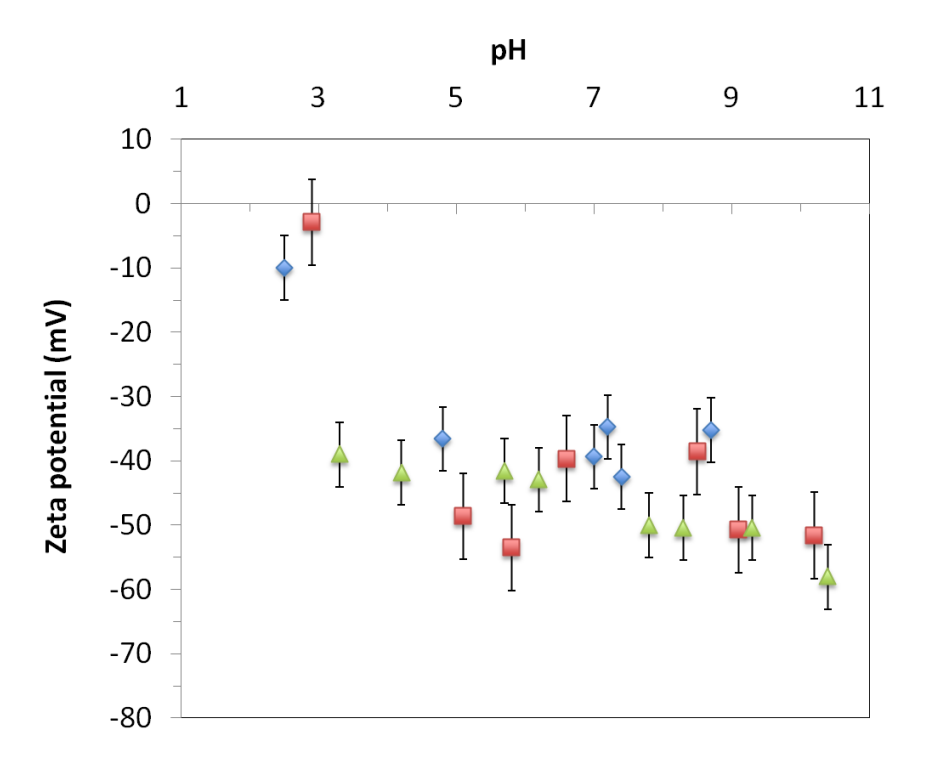


Figure 4.1-2 Zeta potential of the DU3 sandstone for equilibrated pH (blue diamond: DU3 sandstone; red square: Pyrolysed and equilibrated DU3 sandstone; green triangle: DU3 sandstone equilibrated).

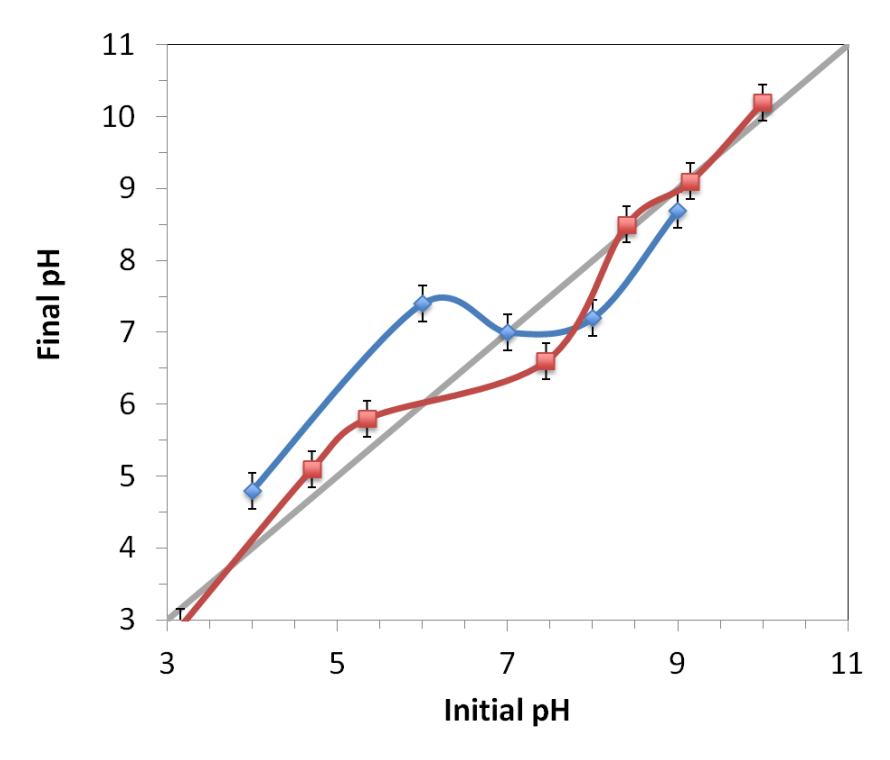


Figure 4.1-3 Final pH versus Initial pH of crushed (blue diamond) and pyrolysed DU3 sandstone (red square)

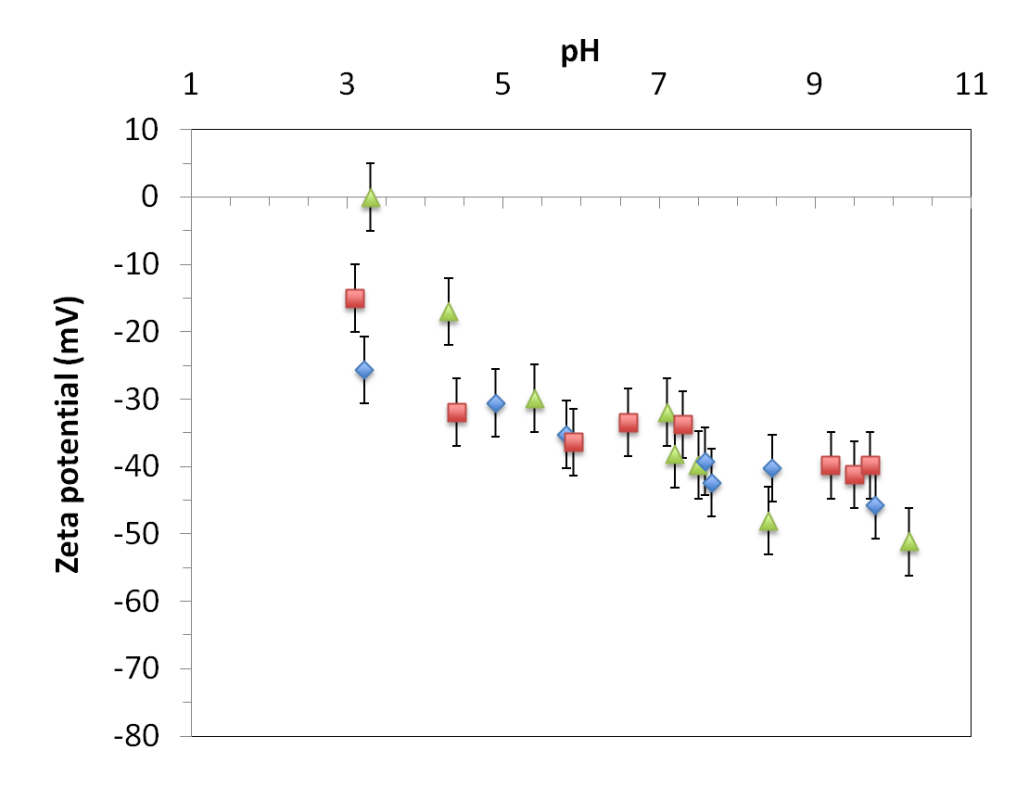


Figure 4.1-4 Zeta potential of the various studied sands for equilibrated pH (green triangle: Landes sand; blue diamond: Fontainebleau sand; red square: Ottawa sand).

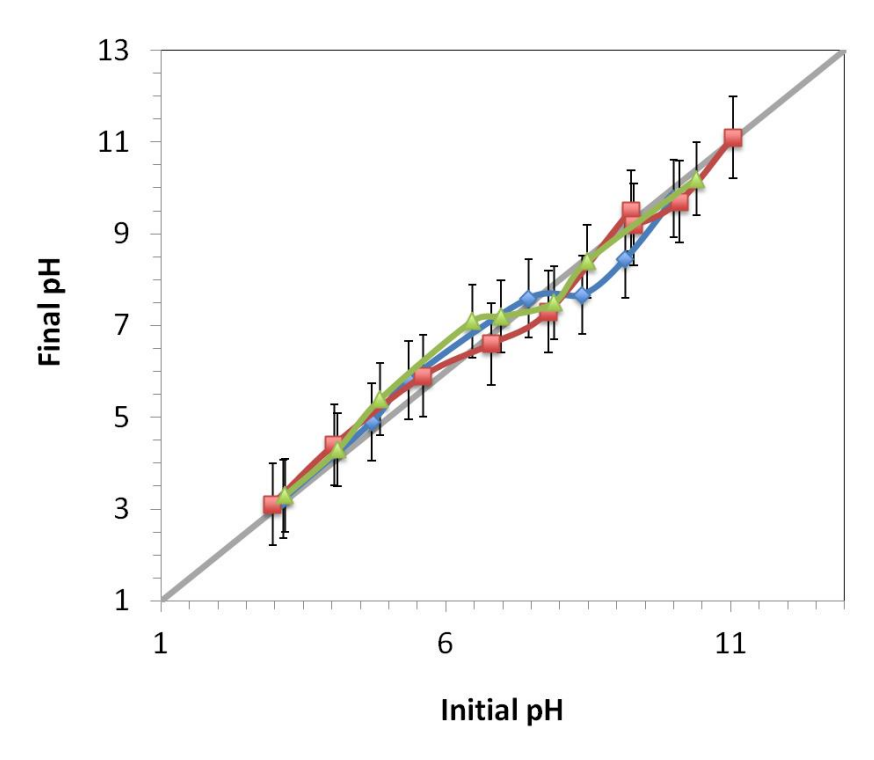


Figure 4.1-5 Final pH versus Initial pH of Fontainebleau sand (blue diamond), Ottawa sand (red square) and Landes sand (green triangle).

## 4.1.3.2 Oil

The experimental evidence of a negative zeta potential even in weakly acidic solutions for the crude oil is quite similar to previously works led on pristine oils in term of magnitude (about -50mV for neutral pH) (Creux et al. 2009). An isoelectric point of pH 2-3 indicates a preference for hydroxide or anionic indigenous surfactants over protons of the crude oil brine interface. The zeta potential above pH 5 corresponding to the range of pH in petrophysical experiments is strongly negative and over – 50 mV (Figure 4.1-6). The Iso Electric Point measured is below pH 3, which is strongly acidic.

The origin of the surface charge will not be discussed in this work although its spontaneous origin is relatively unknown. A crude oil is a more complex system and is not so studied than pristine oils or gas bubbles. We only may observe in spite of the presence of cationic surfactants or macromolecules in the crude oil the acidic chemical groups are dominant.

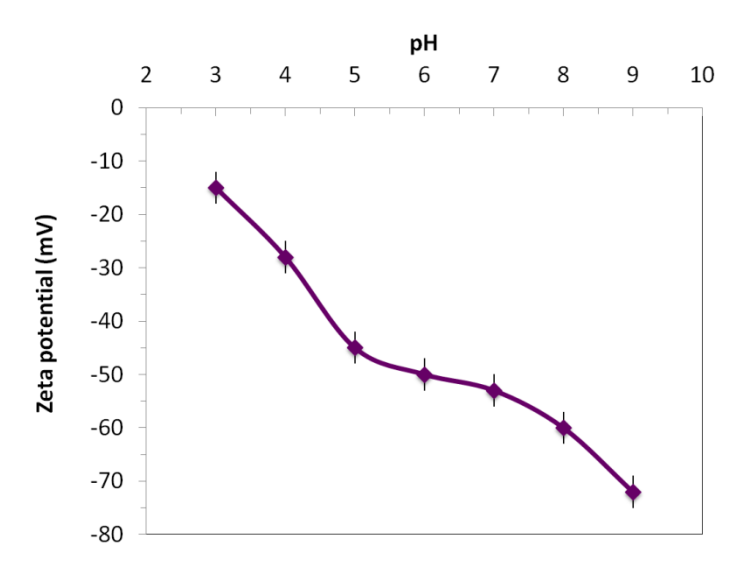


Figure 4.1-6 Zeta potential of Ac oil droplet immersed in 1 mM of aqueous solutions in function of pH

#### 4.1.4 Discussion

It is often reported than divalent ions in brines play an important role in oil-rock-brine interaction for "smart-water" phenomenon. Two aqueous solutions were compared: NaCl at 1mM and NaCl (95wt%) and CaCl<sub>2</sub> (5 wt%) at 1mM (Figure 4.1-7). In Figure 4.1-7 we can observe that the divalent ions tend to increase the electronegativity of the surface. This quite troubling result has been verified by additional experiments on commercial zeta-meter from Malvern for dispersed particles but also by measurements of the zeta potential of the supernatant (Figure 4.1-7). The surface became more electronegative and this could be explained by the fact that divalent ions are more active on the surface compared to monovalent ones. This result could be explained by species transfer from oil onto the mineral.

The increase in the number of negative surface functional groups from 0.3 acid sites to 0.5 acid sites per nm<sup>2</sup> when CaCl<sub>2</sub> is used in isoconcentration, suggests a complex electrochemical mechanism. Zeta potential measurements were able to confirm a more negative surface charge in the presence of organic matter than the only material immersed in brine. We might attribute a specific interaction of the Ca<sup>2+</sup> with acidic indigenous surfactants or ions screening mechanism in clays structures or a co surfactant role played by the cations favoring the sorption of organic acids on the clay surface as a function of increasing pH.

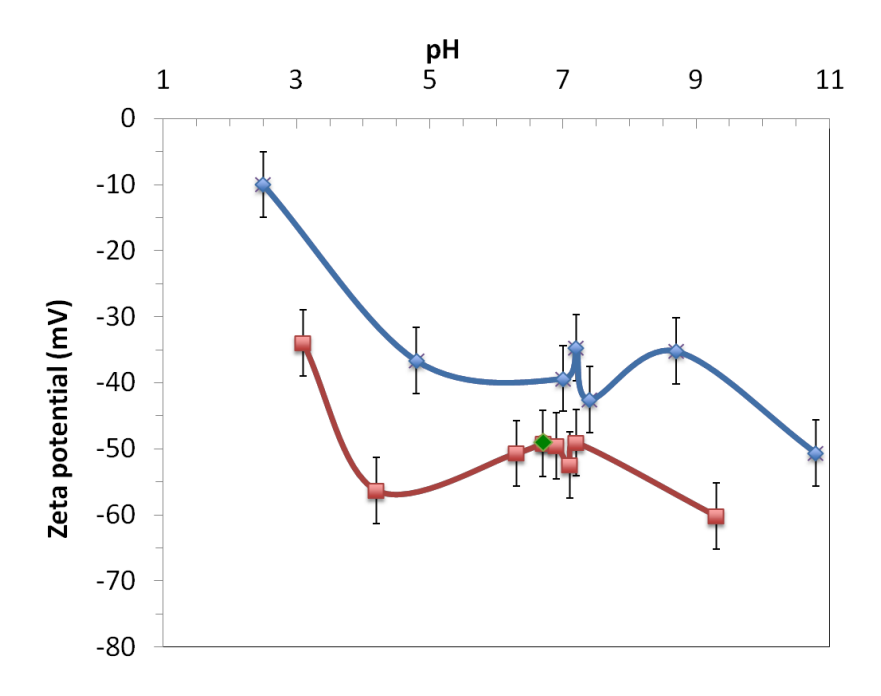


Figure 4.1-7 Zeta potential of DU3 immersed in aqueous solutions at 1 mM of NaCl brine (blue diamond), 0.95 mM NaCl and 0.05 mM CaCl2 measured with electro-osmometer (red square). The green diamond corresponds to the zeta potential of recovered supernatants relative

The sands used in comparison to DU3 clearly exhibit similar electrokinetics fingerprint behaviors. Nevertheless only two of the studied sands (Ottawa and Landes) adhere at the classical optimum of coagulation corresponding to the brine (pH and saline concentration) permitting to obtain a concordance in the IEP between oil and mineral. The Fontainebleau sand adheres at the oil interfaces on the whole range of tested pH as well as for DU3 sandstone. The three tested sands have been compared in an adhesion experiment based on a flotation-like protocol (I. Bondino, S. Doorwar, R. Ellouz 2013). These adhesion experiments highlight that there is an oil adhesion on Fontainebleau sand in a large range of pH compared to Landes sand and Ottawa sand, for which no oil adhesion occurred for pH higher than 3. The zeta potentials are similar and the ionic exchanges are low for the two systems therefore the electrical double layer expansion is similar for the two experiments and only one mineral associated to the brine and the crude oil is adhering to the oil. The origin of these behaviors could be explained by many parameters as mineralogy, roughness, size particles etc.

Lebedeva and Fogden(Lebedeva & Fogden 2011) have shown that organic deposition of crude oils might occur in various conditions of pH and salinity. The results we obtained in this work and the zeta-potential measurement do not clearly highlight evidence of coagulation in brine as well as a redispersion to the brine dilution. We obtained in the various experiments similar electrokinetical behavior of the whole tested samples with or without equilibration of the brine with the crude oil. Low Salinity Brine injection

may cause the electrical double layer expanding and this could be a favorable mechanism to increase the water-wetness of core samples. Nevertheless the variety of obtained results on various samples and oil in terms of oil adhesion cannot be entirely explained by the effect of electrical double layer expanding.

A classical approach linked to these results is not electrically favorable in adhesion, considering a pure DLVO approach for moderated pH although experimental evidences clearly show. If we consider a pure DLVO approach, the obtained results are not electrically favorable for an oil adhesion at neutral pH despite the fact that we observed a good adhesion of fines particles at the brine- crude oil interface (Figure 4.1-8).

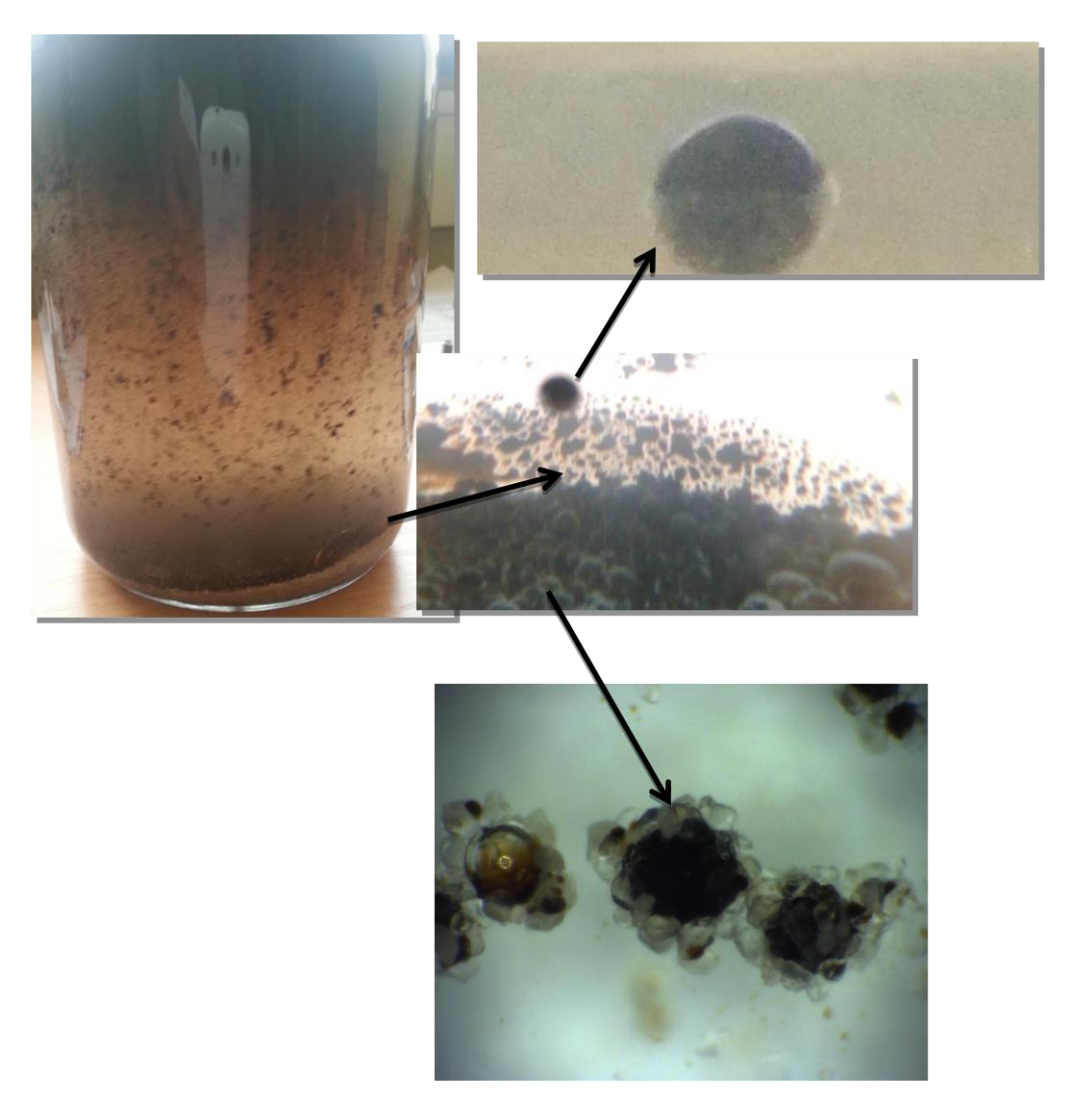


Figure 4.1-8 Coagulation experiment when adhesion occurs (illustration with Fontainebleau sand and Ac crude oil, T°C = 60°C, 24 hours), pH 7.

Experimental investigations of the coagulation properties on a wide range of electrolytes solutions suggest that not all systems can be described using a classical DLVO theory (Hunter 1981) based on the calculation of interaction energy between two flat plates because similar materials characteristics are at the origin of very singular results (Table 4.1-2).

Other involved forces at the interface have to be taking into account to achieve the first net balance forces minimum. Israelachvili et al. (Valtiner et al. 2012) exhibited experimental evidences of the hydration forces impact one of the two main non-DLVO forces with surface force apparatus. The hydration force is a very short range repulsive force which is complex to take into account and most of the time is neglected. They showed that in concentrated aqueous solutions with multivalent ions, particles remain stable, even at the isoelectric point due to the hydration forces which arise for the more hydrated ions. At low pH, protons replace bound hydrated ions and this replacement eliminates the hydration forces which favor adhesion. Note, Hunter (Hunter 1981) observed silica particles do not coagulate even at high electrolyte concentrations, when the double layer is expected to collapse.

Considering oil adhesion on minerals means the achievement of the primary minimum of net forces balance on oil – mineral interface (Figure 4.1-9) the energy map in the neighborhood of the interface may be drastically modified by crevices and roughnesses. The mineral roughness is known to affect the van der Waals forces and the electrical properties as shown by Israelachvili et al. (Valtiner et al. 2012). The spatial forces distribution is more diffuse considering a rough material therefore which reduce the magnitude of the interfacial forces. The addition of the non-DLVO forces and the mineral roughness might be taken into account in further works in order to characterize the reversibility of the oil-wet to water-wet properties of the rock during a brine dilution (Borghi et al. 2013; Valtiner et al. 2011)

Table 4.1-2 Coagulation results of the tested systems for several pH (D: for dispersed, C for coagulated).

Rock sample	pH 2	pH 3	pH 4	pH 5	рН 6	pH 7	pH 8
DU3	С	С	С	С	С	С	С
Ottawa sand	С	D	D	D	D	D	D
Fontainebleau sand	С	С	С	С	С	С	С
Landes sand	С	C/D	D	D	D	D	D

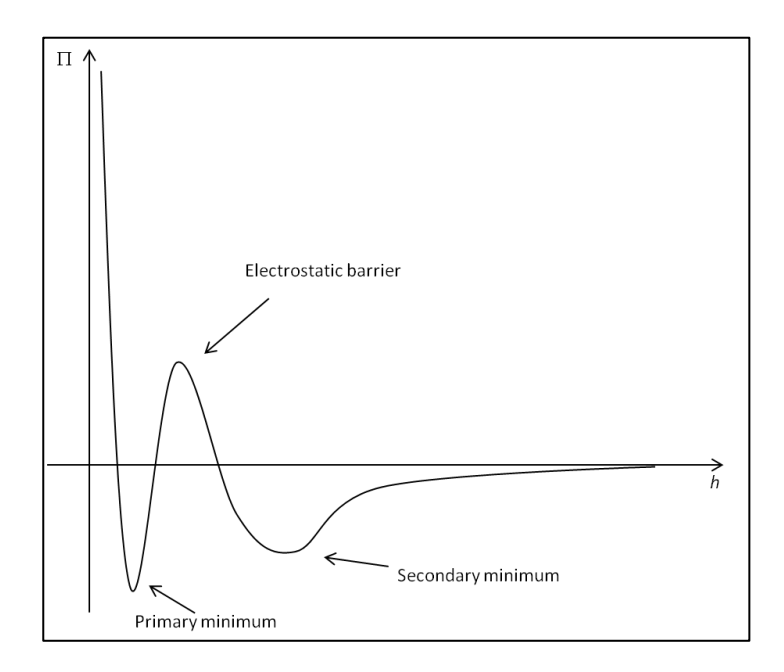


Figure 4.1-9 Disjoining pressure versus distance of the interfaces based on DLVO theory

#### 4.1.5 Conclusions

Among the various systems studied in this paper, DU3 associated with the Ac crude oil was revealed as a petrophysical system leading to systematic incremental oil recovery in case of LSB injection. In this work we have shown than pre-equilibrated DU3 with brine and oil was did not exhibit a different electrokinetical fingerprint from clean sands whatever in high or low salinity brine.

Electrical interactions representative of a rock – brine – oil electrokinetical interaction were quantified and we showed that the zeta potentials are very close for all studied samples. We tried to correlate these results to coagulation experiments considering the electrical double layers similarities for tested minerals.

We observed for Landes sand and Ottawa sand zeta potential curves in agreement with coagulation tests with adhesion around the Iso Electric Point although we observed Fontainebleau sand and DU3 exhibited coagulation on the whole range of pH and salinities. We also observed Ca2+ contributes more than Na+ to the electronegativity of the material. This result is in apparent contradiction with classical results.

It seems reasonable to confer that the net force balance issue from the DLVO theory is not correct and it appears as reasonable to take into account the surface roughness and non-DLVO forces which seem to play a key role in the coagulation process.

Considering these results, we are not able at this time to explain the variability in all results of Smart Water scientific paper. This work shows that the low salinity brine effect has to be explained not only by the double layer expansion but requires new solutions of characterizations of the wettability in reservoir formations than used today.

#### 4.1.6 References

- Andrew, M., Bijeljic, B. & Blunt, M.J., 2014. Pore-scale contact angle measurements at reservoir conditions using X-ray microtomography. *Advances in Water Resources*, 68, pp.24–31.
- Bear, J., 1972. Dynamics of Fluids in Porous Media.
- Borghi, F. et al., 2013. Nanoscale roughness and morphology affect the IsoElectric Point of titania surfaces. *PloS one*, 8(7), p.e68655.
- Bouriat, P. et al., 1999. A Convenient Apparatus to Determine the Zeta Potential of Grains by Electro-Osmosis. Journal of colloid and interface science, 209(2), pp.445–448.
- Boussour, S. et al., 2009. Oil recovery by low salinity brine injection: Laboratory results outcrop and reservoir cores. In *Proceedings SPE Annual Technical Conference and Exhibition*. pp. 1595–1606.
- Buckley, J.S., 2001. Effective wettability of minerals exposed to crude oil. *Current Opinion in Colloid & Interface Science*, 6(3), pp.191–196.
- Cissokho, M., 2010. Etude expérimentale des interactions Huile brute/Saumure/Roche sur la récupération d'hydrocarbures par injection d'eau de faible salinité.
- Cissokho, M. et al., 2010. Low salinity oil recovery on clayey sandstone: Experimental study. *Petrophysics*, 51(5), pp.305–313.
- Creux, P. et al., 2009. Strong specific hydroxide ion binding at the pristine oil/water and air/water interfaces. *The journal of physical chemistry*. *B*, 113(43), pp.14146–50.
- Derjaguin, B. V., Churaev, N. V. & Muller, V.M., 1987. Surface Forces, Boston, MA: Springer US.
- Graciaa, A. et al., 2000. Potential at an Air Water Surface Related to the Critical Micelle Concentration of Aqueous Mixed Surfactant Systems., pp.2677–2681.
- Hartley, P.G., Larson, I. & Scales, P.J., 1997. Electrokinetic and Direct Force Measurements between Silica and Mica Surfaces in Dilute Electrolyte Solutions. *Langmuir*, 13(8), pp.2207–2214.
- Hunter, R.J., 1981. Zeta Potential in Colloid Science: Principles and Applications, Academic Press.
- I. Bondino, S. Doorwar, R. Ellouz, G.H., 2013. Visual microscopic investigations about the role of pH, salinity and clay on oil adhesion and recovery. In *The Society of Core Analysts*.
- Kosmulski, M., 2010. Surface charging and points of zero charge, CRC Press.
- Kovscek, A.R., Wong, H. & Radke, C.J., 1993. A pore-level scenario for the development of mixed wettability in oil reservoirs. *AIChE Journal*, 39(6), pp.1072–1085.
- Lebedeva, E. V. & Fogden, A., 2011. Micro-CT and wettability analysis of oil recovery from sand packs and the effect of waterflood salinity and kaolinite. *Energy and Fuels*, 25(12), pp.5683–5694.
- Masliyah, J.H. & Bhattacharjee, S., 2006. *Electrokinetic and colloid transport phenomena*, John Wiley & amp; Sons.

- Mohanty, K.K., Scriven, L.E. & Davis, H.T., 1987. Physics of Oil Entrapment. *SPE Reservoir Engineering*, 2(February), pp.113–118.
- Nasralla, R.A., Bataweel, M.A. & Nasr-El-Din, H.A., 2011. Investigation of Wettability Alteration by Low Salinity Water. In *Offshore Europe, 6-8 September, Aberdeen, UK*. Society of Petroleum Engineers.
- Pieterse, S.G.J. et al., 2013. SPE 165180 Experimental Investigation on the Effects of Very Low Salinity on Middle Eastern Sandstone Corefloods.
- Radke, C.J., Kovscek, A.R. & Wong, H., 1992. Pore-level scenario for the development of mixed wettability in oil reservoirs. In *Proceedings SPE Annual Technical Conference and Exhibition*. pp. 163–177.
- RezaeiDoust, a. et al., 2009. Smart Water as Wettability Modifier in Carbonate and Sandstone: A Discussion of Similarities/Differences in the Chemical Mechanisms. *Energy & Fuels*, 23(9), pp.4479–4485.
- Salathiel, R.A.A., 1973. Oil Recovery by Surface Film Drainage In Mixed-Wettability Rocks. *Journal of Petroleum Technology*, 25(10), pp.1216–1224.
- Sanchez-Soto, P.J., Justo, A. & Pérez-Rodriguez, J.L., 1994. Grinding effect on kaolinite-pyrophyllite-illite natural mixtures and its influence on mullite formation. *Journal of Materials Science*, 29(5), pp.1276–1283.
- Schembre, J.M., Tang, G.-Q. & Kovscek, a. R., 2006. Wettability alteration and oil recovery by water imbibition at elevated temperatures. *Journal of Petroleum Science and Engineering*, 52(1-4), pp.131–148.
- Souza, A.E. et al., 2013. Addition of sedimentary rock to kaolinitic clays: influence on sintering process. *Cerâmica*, 59(349), pp.147–155.
- Tang, G. & Morrow, N.R., 1999. Influence of brine composition and fines migration on crude oil r brine r rock interactions and oil recovery.
- Valtiner, M. et al., 2011. Effect of surface roughness and electrostatic surface potentials on forces between dissimilar surfaces in aqueous solution. *Advanced materials (Deerfield Beach, Fla.)*, 23(20), pp.2294–9.
- Valtiner, M. et al., 2012. The electrochemical surface forces apparatus: the effect of surface roughness, electrostatic surface potentials, and anodic oxide growth on interaction forces, and friction between dissimilar surfaces in aqueous solutions. *Langmuir: the ACS journal of surfaces and colloids*, 28(36), pp.13080–93.
- Vledder, P. et al., 2010. Low Salinity Water Flooding: Proof Of Wettability Alteration On A Field Wide Scale. In SPE Improved Oil Recovery Symposium, 24-28 April, Tulsa, Oklahoma, USA. Society of Petroleum Engineers.

## 4.2 Evidence of Temperature Transition of Crude Oils Spreading

4.2.1 Evidence of Temperature Transition of Crude Oils Spread on Brines (paper form)

#### 4.2.1.1 Introduction

The oil spreading on brine in the presence of gas is thermodynamically described by the spreading coefficient S. The spreading coefficient is defined as the difference between the surface tension of the brine  $\gamma_B$  and the film tension  $\gamma_F$ . The film tension  $\gamma_F$  is given by the sum of surface tension of the oil  $\gamma_O$  and the interfacial tension between oil and brine  $\gamma_{O/B}$ , therefore the spreading coefficient S is determined as:  $S = \gamma_B - (\gamma_O + \gamma_{O/B})$ . Here the three tensions are known, the wetting state of the fluid follows directly. If  $\gamma_B < (\gamma_O + \gamma_{O/B})$ , therefore S < 0 and the droplet is characterized by a finite contact angle minimizing the free energy of the oil droplet exposed to the brine and the gas interfaces. In this case we speak about partial wetting (figure 4.2-1b). If  $\gamma_B = (\gamma_O + \gamma_{O/B})$ , therefore S = 0 and the contact angle is zero, therefore the system will consequently be in equilibrium when a uniform liquid layer covering the surface. This state called complete wetting (Figure 4.2-1a). Beyond these two regimes a mixed case where a thin oil film coexists with oil lenses can occurs and we talk about the pseudo partial wetting regime (Figure 4.2-1c) with a positive spreading coefficient S. In this case an additional term in the oil thin film tension appears:  $\gamma_F = \gamma_O + \gamma_{O/B} + e\Pi(e) + W(e)$ , where  $\Pi(e)$  is the disjoining pressure in the thin film

of thickness e and W(e) is the potential energy related to the disjoining pressure by  $\Pi(e) = -\frac{dW(e)}{de}$ .

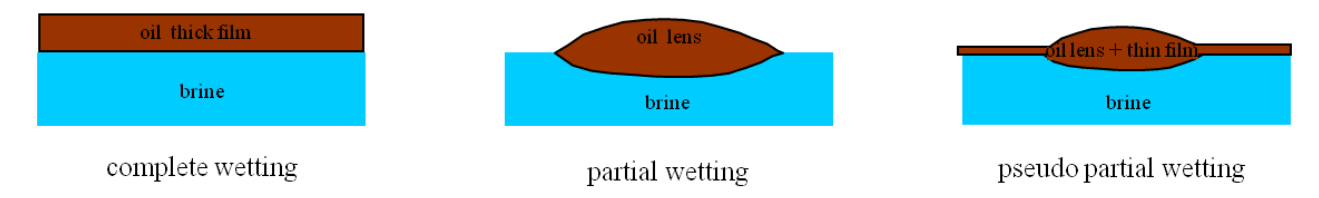


Figure 4.2-1 Different wetting regimes occurring when oil contacts brine

Such wetting transition induced by temperature/salinity conditions between these different states were showed on alkanes ((Bertrand et al. 2001)

The objective of this work is to show that more complex oil phases such crude oils are also able to exhibit wetting transitions induced by temperature. For this two different oils are observed with an imaging ellipsometer in order to evidence the presence or the absence of thin films surrounding the oil lenses deposited on an aqueous substrate. Experiments were carried out in a closed cell in order to avoid any substrate or oil evaporation.

#### 4.2.1.2 Materials

Crude oils have been provided by TOTAL E&P and preserved from any contaminations, which might occur in oil field processes (surfactants, polymers or solvents). The main crude oil characteristics are mass fractions of Saturates, Aromatics, Resins, and Asphaltenes (SARA) as determined by ASTM D2007 methods were reported table 4.2-1a: below for the various crude oils and API, viscosity and TAN and TBN of the various crude oils are reported table 4.2-1b:

Table 4.2-1: Fluid properties of Ac, and Ja oils

Oil type	Saturated (%)	Aromatics (%)	Resins (%)	Asphaltenes (%)
AC	58.2	31.4	8.1	2.3
JA	51	33.6	10.4	5

Oil type	Density (kg/m³)	Viscosity (cP)	TAN (mg KOH / gram)	TBN (mg KOH / gram)
AC	835.4 @ 35°C	5.4 @ 35°C	0.17	0.95
JA	858@30°C	14@30°C	0.31	1.85

Water was purified by an Elga Pure lab classic system to give a resistivity of 18.2 M $\Omega$  cm. Salts were from Aldrich with purity grades better than 99.9 % for sodium chloride and Calcium chloride. The main brine is prepared with 45g NaCl and 5g CaCl<sub>2</sub> per liter. The other ones are obtained by dilution in ultra-pure water to keep the same NaCl - CaCl<sub>2</sub> ratio in the experiments.

#### 4.2.1.3 Methods

Imaging ellipsometer combining a nulling ellipsometry with microscopy was used to determine film thicknesses based on its optical properties. Interferograms were recorded with a microscope ellipsometer Accurion nanofilm EP3 with unique 532 nm wavelength light source. The lateral resolution is 2 micrometers per pixel. Polariser, analyser and compensator were set to 0° in order to perform reflectometry imaging with light polarisation in the incident plane.

The phase difference  $\varphi$  between consecutive rays reflected by the oil layer of thickness e is given by:  $\varphi = \frac{4\pi}{\lambda} n \, e \cos r$ , where  $\lambda$  is the wavelength and r the refracted angle in the oil layer of refractive index n. Constructive interferences will occur when  $\varphi = (2k-1)\pi$ , with k = 1, 2, 3, ... because of the presence of an additional phase shift of  $\pi$  corresponding to the reflections at the oil water interface due to the fact

that refractive index of oil is higher than those of water. Then destructive interferences will occur when  $\varphi=2\pi k$ . When the oil layer thickness tends to zero a minimal intensity will be reflected. As the refractive index of air is about unity, Snell's law which relates the incident angle i to the refracted angle gives  $\sin i=n\sin r$ , so that  $\cos r=\sqrt{1-\frac{\sin^2 i}{n^2}}$  Then the first maximum in reflected intensity will be obtained when the thickness is:

$$e^* = \frac{\lambda}{4\sqrt{n^2 - \sin^2 i}}$$

In case of variable film thickness,  $e^*$  is then the thickness difference that separates a reflected intensity minima to its consecutive maxima and vice versa. A film of variable thickness will exhibit an alternation of bright and dark fringes which number will easily permit to determine film thickness. For an incidence angle  $i = 45^\circ$  and a laser wavelength  $\lambda = 532$ nm one finds, for a crude of refractive index of about 1.47, we have interference length  $e^* = 103$ nm.

Oil drops were deposited in the center of water or brine surface contained in a cylindrical (r = 10 mm) hydrophobic cell. The hydrophobic cell was enclosed in a prismatic transparent isosceles cell. To eradicate beam deviation water surface was enlighten with an incident angle of 45° and the microscope positioned at a reflection angle of 45° too. The cell is thermostated and the temperature inside the cell is recorded with a thermocouple. The prism is sealed on the thermostatic cell in order to maintain saturating vapor pressures of both water and oil in the cell, this way thin film evaporation is avoided and it permits to assume a thermodynamic equilibrium during observations at the various tested temperatures.

The same thermal constraints were imposed during all experiments to similarly impact the various samples. Steady states are considered to characterize the oil configuration onto aqueous solution but the dynamics of spreading is also recorded.

## 4.2.1.4 Experimental Results

The crude oils samples are used in the specific cell we developed to visualize the film spreading in controlled thermodynamical conditions.

Considering usual concepts of films physics interfacial tensions (IFT) have been measured using a tracker tensiometer manufactured by Teclis to determine hypothetic anomalous behavior of fluids with the temperature changes.

Table 4.2-2 is shown below and exhibit crude oil behavior of the IFT with temperature. For the first oil the IFT decreases and the relative IFT decrease may be estimated to 20% for a temperature variation of 35°C.

Table 4.2-3 shows IFT of oils. From these two tables we conclude on positive spreading coefficient *S* for the whole, therefore the oil should spread completely in order to lower its surface energy.

Table 4.2-2 IFT measurements of AC and JA crude oils for various temperatures in aqueous solutions (50g/I)

Oil type	IFT <sub>wo</sub> @ 25°C	IFT <sub>wo</sub> @ 35°C	IFT <sub>wo</sub> @ 50°C	IFT <sub>wo</sub> @ 60°C
Ac	22 mN/m	21.77 mN/m	19.36 mN/m	18.44 mN/m
Ja	15 mN/m	13.98 mN/m	13.29 mN/m	12.88 mN/m

Table 4.2-3 IFT measurements of AC and JA crude oils in aqueous and saturated vapor phase and corresponding spreading coefficients at 25°C

Oil type	IFT <sub>wo</sub> @ 25°C	IFT <sub>GO</sub> @ 25°C	S@25°C
Ac	27 mN/m	22 mN/m	23
Ja	28 mN/m	15 mN/m	29

For all samples the spreading coefficient S is positive, therefore the oil should spread completely in order to lower its surface energy.

#### 4.2.1.5 Ellipsometry experiments

## 4.2.1.5.1 Ac crude oil behavior on high salinity brine

In figure below the interference replicates the interface shape and thickness of oil spreading shows a precursor film coexists with the drop (lens) onto brine at 40°C. Caused by a weak field of view in this range of resolution of 2 micrometers by pixels, the sample positioner allows displacements to visualize around the oil droplet revealing the thin film borders the whole lens.

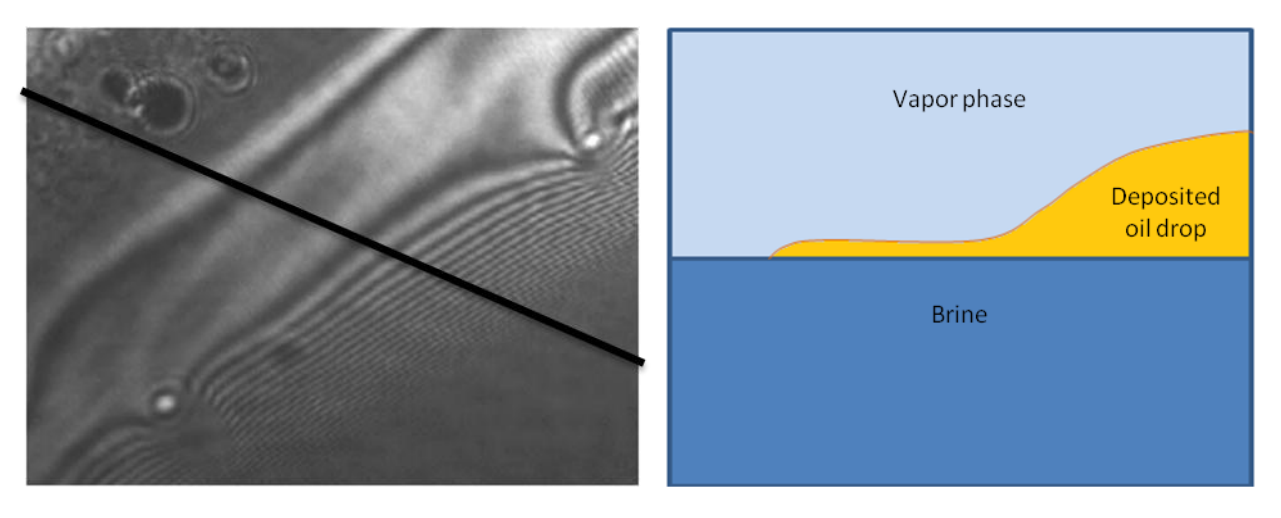


Figure 4.2-2 Interferogram - Partial wetting of crude oil AC on brine at 40°C and its simplified profile

At 60°C (figure 4.2- 4) the AC oil droplet is spread in a regime where oil lenses coexist with uniform mesoscopic film of 80 nm thickness. At this temperature the AC oil droplet exhibits two thicknesses of equilibrium representative at primary and secondary minimum of a force-distance profile (figure 4.2-3).

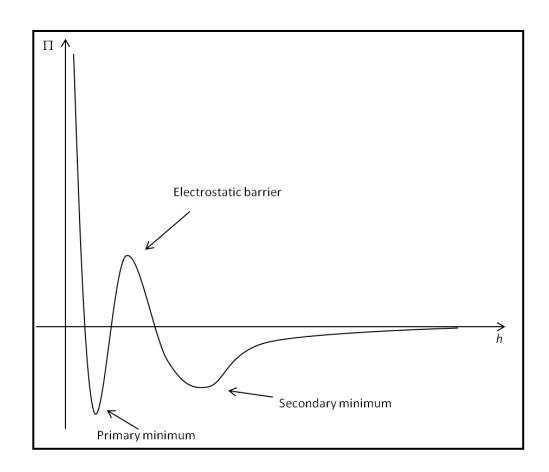


Figure 4.2-3 Disjoining pressure profile versus distance of the interfaces based on DLVO theory

Simultaneously, this spreading state of equilibrium coexists with thin film and oil lens. Based on classical wetting transitions theory, the observed behavior looks like a complete wetting state where the short-range forces favor complete wetting although van der Waals forces maintain the film thickness at a finite value.



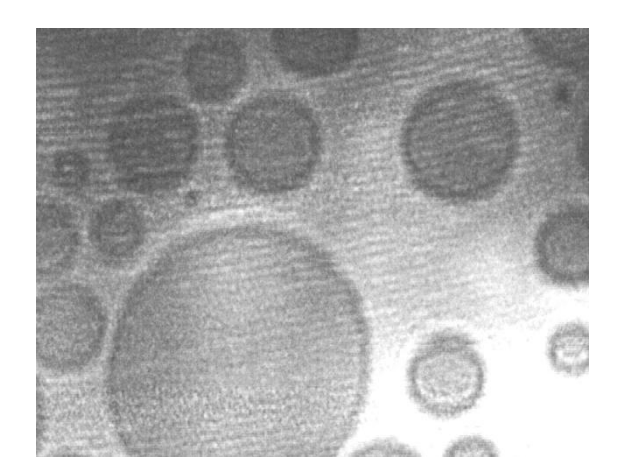


Figure 4.2-4 Interferogram - concomitant images at 60°C exhibiting oil spreading of AC oil in complete wetting on brine.

Thermal cooling of the system causes a film retraction and oil lens filling with coalescence events exhibiting a relative reversibility (figure 4.2-5).

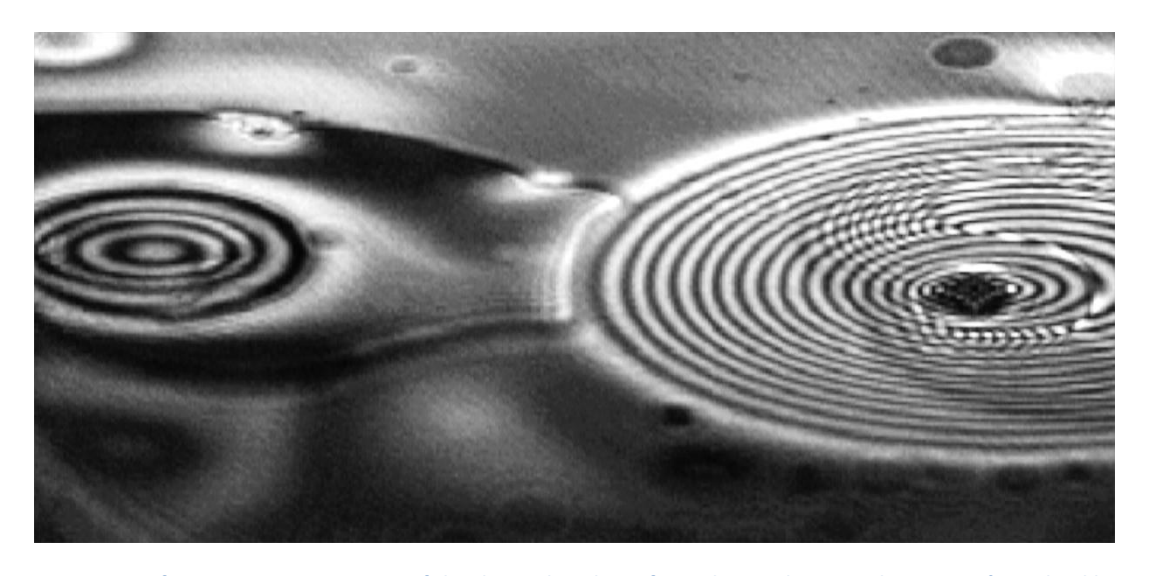


Figure 4.2-5 Interferogram representative of the thermal cooling of AC oil spreading onto brine at 40°C with oil lenses reappearing and coalescence

The results found here are perturbing because of positive spreading coefficient although we have never observed a complete wetting at low temperature. A negative disjoining force is therefore required to explain the several results obtained here. This pressure term is a long range attractive force which is also saline and thermal sensitive.

The wetting transitions such described by Bertrand (Bertrand 2000) clearly demonstrate the saline impact on the wetting transitions; high salts concentration favoring the transition in lower temperatures. However, (Bertrand et al. 2001) observed a first transition order obtained by the disjoining pressure sign changes. To relate the observed experimental results to the previous works led on wetting transition we

tested the salt effect for the same crude oil. The results of spreading in low salinity brine (1mM) are represented in the figure 4.2-6.

On the whole range of tested temperatures, heating does not alter the oil spreading onto the low salinity brine for similar temperatures than used before. On the range of tested temperatures the oil droplet remains in a lens shape without any growth of the plateau border. This is purely representative of the pseudo partial wetting as met in the lowest temperature in presence of brine. This second result continues to be coherent to the previous experiment and seems to indicate that the oil droplet does not meet any wetting transition in the range of tested temperatures for low salinity brine. We observed with low salinity brine microscopic contact angles are very similar than observed in low temperature with high salinity brine. The microscopic contact angle is about 0.4°.

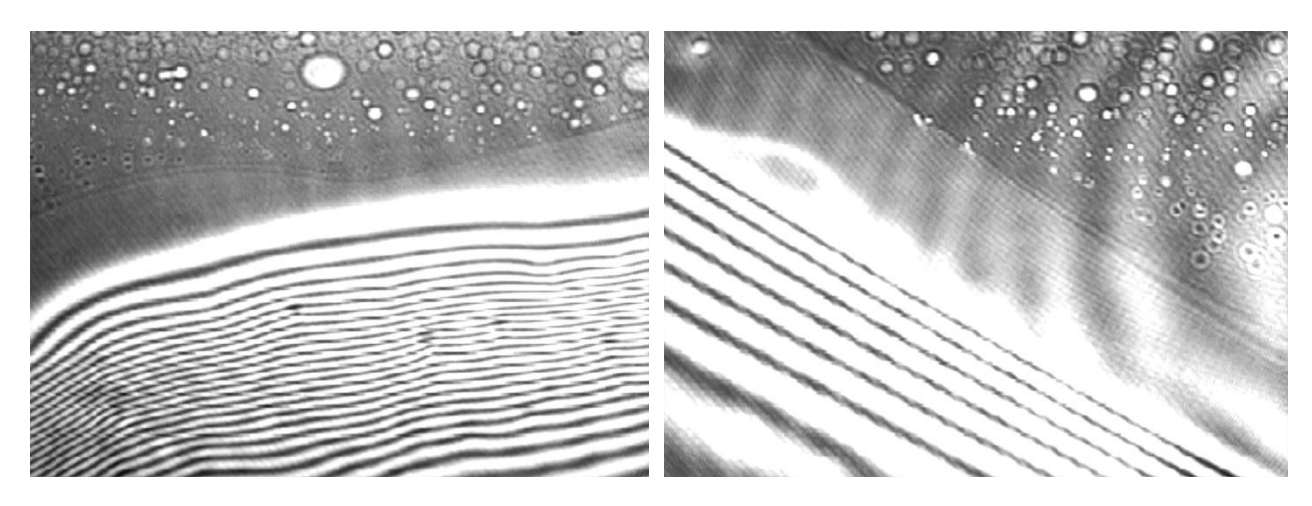


Figure 4.2-6 Interferogram - Partial wetting of crude oil AC on low salinity brine at 40°C and 60°C

Wishing to extend this kind of experiment to the second crude oil tested in micro-CT experiments we performed in similar conditions than for Ac test with another crude oil called Ja. In the experimental micro-CT part we had never observed wettability changes with Ja oil in the range of tested temperatures and salinities.

## 4.2.1.5.2 Ja crude oil behavior on high salinity brine

The Ja oil is then tested and images are shown figure 4.2-7. The Ja oil did never meet any evolution in term of wetting transition with temperature evolution. The oil lenses shape is very weakly changing and due to the simultaneity of refraction index changes and spreading due to viscosity and interfacial tension changes with temperature we may not conclude on significant changes on the contact angle representative of the oil wetting on brine. We might oppose the spreading is governed by a very slow dynamics delayed by higher viscosity and interfacial tension. Despite elapsed time of several hours made it possible by the confinement cell we have never observed changes of the oil lens shape. An 80nm prefilm thickness is observable but this mesoscopic film does not swell due to oil lenses voiding. The oil droplet seems to be in pseudo partial wetting.

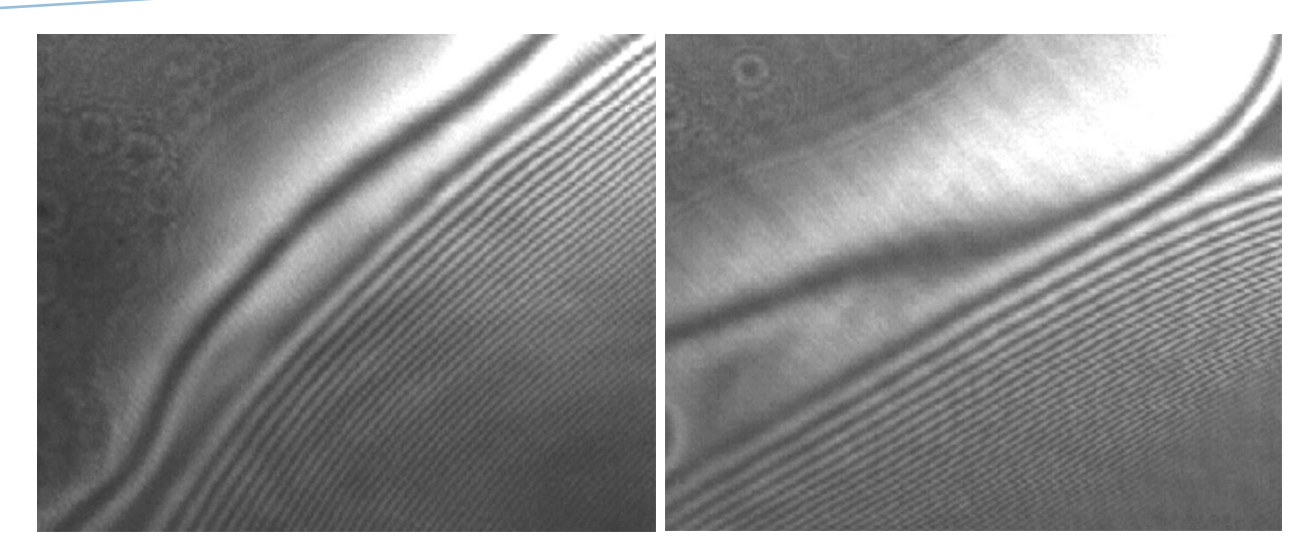


Figure 4.2-7 Interferogram of Ja oil film spreading in pseudo partial wetting conditions and film nucleation at 40°C and 50°C.

## 4.2.2 Evidence of Temperature Transition of Crude Oil Spreading on substrate

The clear observed wetting transition of oil on brine was completed by experiments on glass. We used here the Ac crude oil with 1M salinity brine and a thin glass. We controlled with ellipsometer the complete wetting of glass by water to avoid perturbing micro-bubbles. A micro oil droplet was deposited down onto the glass substrate with a curved syringe. The system was heated stepwise to 60°C.



Figure 4.2-8 Schematic representation on ellipsometry experiments on plate substrate

We represent on figure 4.2-9 the triple line oil-brine-glass by the red line and the blue one represents the triple line of the previous image. Considering the images obtained by ellipsometry and for a spatial resolution of 2 micrometers per pixel the triple line advance reaches more than 300 micrometers of distance from 20°C up to 60°C although approximate volume expansion should contribute to about 40 micrometers maximum.

The advancing angle progress seems to be with a quasi-constant microscopic contact angle of 0.5°.

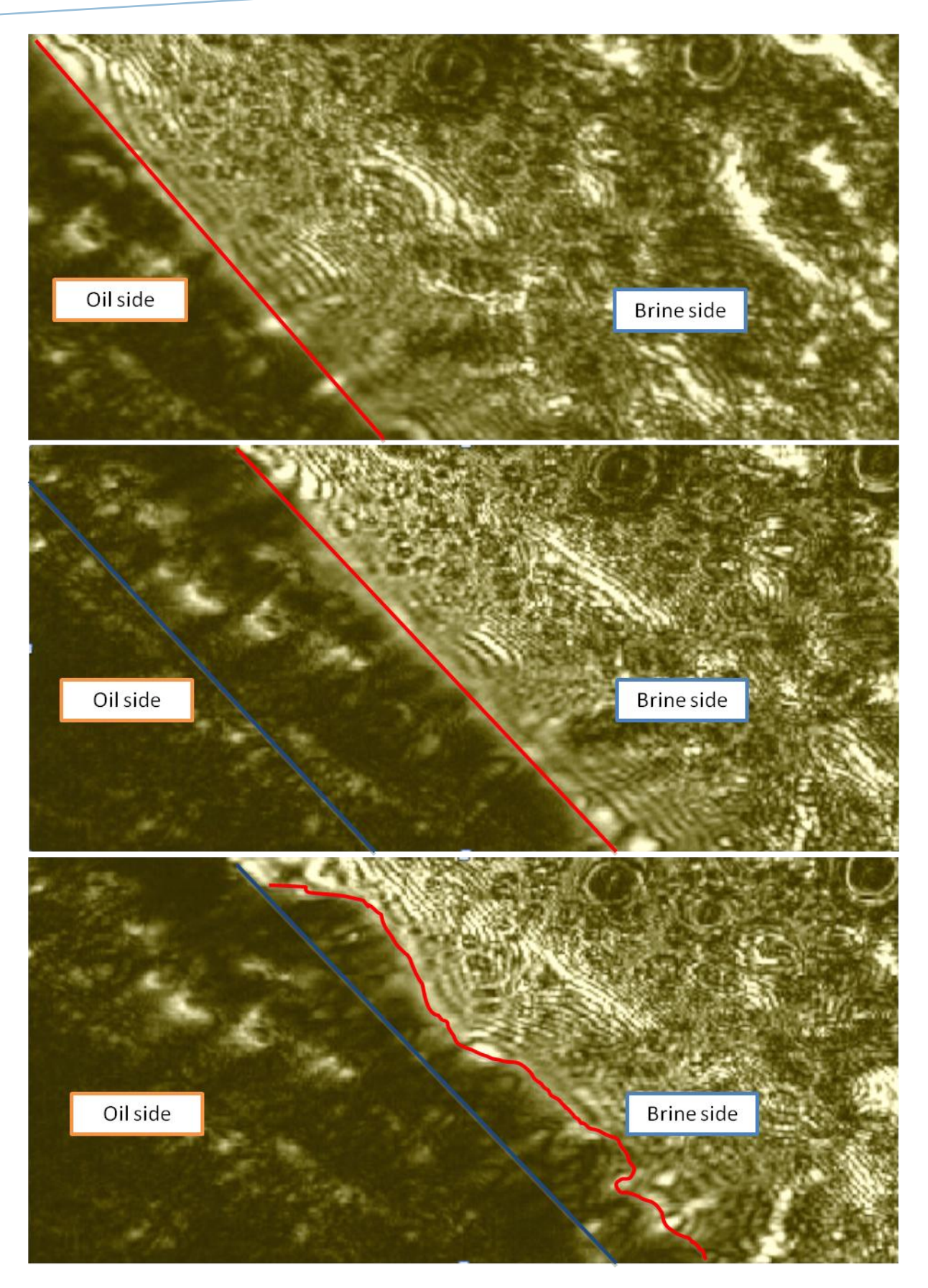


Figure 4.2-9 Dynamics of spontaneous drainage of Ac oil on high salinity brine (1 M) between 20°C and 60°C.

At 60°C in the same field of view we initiate a cooling from 60°C to 20°C and we extract from the movie the images below. Here we observe the retreat of the triple line caused by the spontaneous imbibition assisted by the volumic expansion mechanism. The bright zones illuminated by the interferometry give information about the receding angle and the triple contact line evolution. However here during the receding of oil from substrate several lenses are trapped on the glass and crude oil residues do not permit to follow with accuracy the contact angle.

The microscopic contact angles are here very distributed but clear brine imbibitions in very thin films appear onto the substrate at the origin of the partial oil dewetting.

The microscopic angle of 0.5° shows a very good affinity of the oil for the glass included at the lowest temperature. It shows a very good affinity for the surface although macroscopic angle measured in drop down has exhibited a contact angle of 42°. The good oil wetting at the microscopic scale on hundreds micrometers reveal a similar behavior than observed during the oil-brine spreading experiment for the same oil.

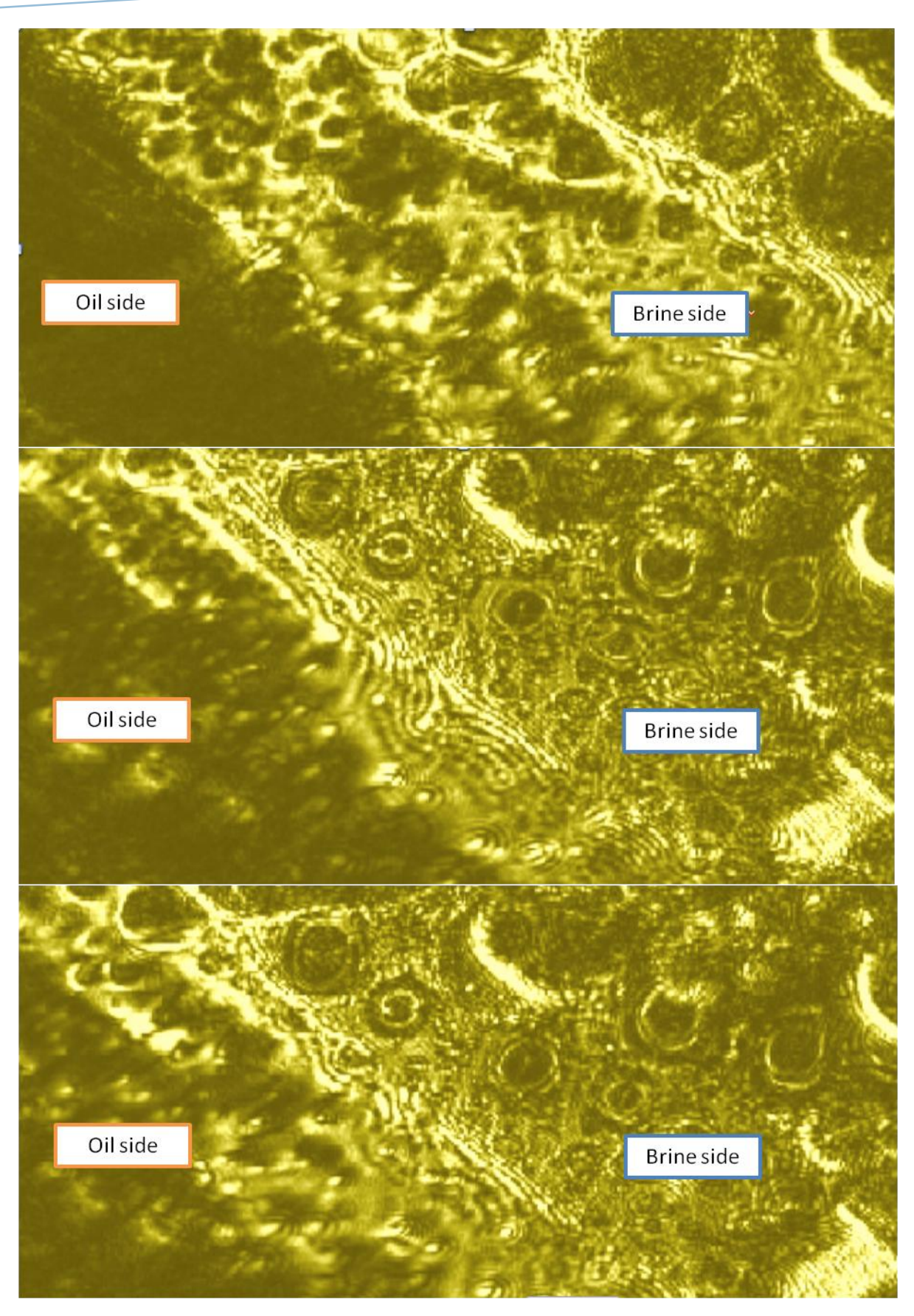


Figure 4.2-10 Dynamics of spontaneous imbibition of Ac oil on high salinity brine (1 M) between 60°C and 20°C.

The experiments are also performed with low salinity brine (1mM) but we did not observe changes in term of oil spreading on the substrate. With temperature changes oil behavior on substrate stay stable at low salinity brine condition.

Here again we observe the high salinity favors oil spreading propagation in thin films onto the substrate. The depth of field of view is very weak here and we may not observe deeper than 1 micrometer below the substrate. The contact point is the only observable element we access therefore we may not define the order of the observed transition. The imaging system may not permit to visualize the complete drop due to a limited field of view. The experimental set up permits to follow the oil droplet thanks to a multi axis stage installed. The experiments exhibited the same zone but we verified the oil wetting and dewetting was similar around the oil droplet.

Of course, these results were obtained in very different experimental conditions however we have observed similar changes of wetting at the origin of a fluid redistribution during the aging phase. This redistribution is counterbalanced by saline dilution at the origin of a spontaneous imbibition in thin aqueous films.

#### 4.2.3 Conclusions

The wetting transition was observed for a crude oil (Ac) and is representative of a second order wetting transition such described by de Gennes (de Gennes 1985). This wetting transition observed at temperature about 50°C for Ac oil, although the other oil (Ja) does not exhibit such property at equilibrium. The wetting transition was the first observed on crude oils. The observations seem to be less spatially uniform than observed on pure paraffinic components. This might be explained by the extreme heterogeneity of the crude oil composition and it may intuitive to observe a relative inhomogeneity of shapes due to surface reactivity, adsorption, ... causing more or less local mechanisms.

The global behavior of the different forces evolves independently with temperature up to invert the net force balance of dispersive and cohesive forces. The salinity plays a similar role: with low salinity brine no wetting transition has been observed with the two used oils the only 1M brine permitted to observe wetting transition. In term of net force balance and considering the thickness of such films the experiments reveal the evidence of a long range repulsive force which is ion sensitive.

The wetting transition on brine is quite decisive because it demonstrates crude oils ability to spread on brine in thin films at very specific conditions. The wetting transition temperature  $T_w$  is therefore supposed to be an intrinsic property of oil-brine-gas and relevant to describe oil spreading corresponding to wettability change. In this way it should be considered as a very important petrophysical property.

Concerning the origin of such wetting changes we must be precautionous due to the extremely large number of chemical components in crude oil able to affect the wettability: indigenous surfactants, waxes, asphaltenes and other macromolecules which may affect IFT alone or in self association.

Geometrically, a drop partially wetting a substrate is characterized by a microscopic angle of inclination, approaching zero degree as the fluid approaches zero thickness. The microscopic foot protrudes from the end of the capillary body of any partial wetting system.

A drop pseudo partially wetting a substrate has a film of finite length, protruding from its tip. It seems arbitrary whether the structure protruding from the end of a drop is a foot or a film and there have no

quantitative criteria for distinguishing partial wetting from pseudopartial wetting although the complete wetting is assumed to be reached for a macroscopic contact angle is zero.

Note these subtles geometrical considerations have a deep impact on the oil – brine contact and therefore on the wetting properties of the rock so decisive in term of capillary pressure. Note these performed experiments are demonstrative of the similar tendencies obtained with cooling or with low salinity brine injection. Note the micro-CT experiments with a wettability restoration were performed at 20°C for fluid injection because we could not thermoregulate the sample in the Skyscan 1172 due to the very high compactness of the set up and to avoid degradation of the detector (scintillator and camera). Consequently, we superimposed two changes of wettability in our experiments not relevant of in situ oil recovery process. To be more realistic of reservoir conditions it should be important to inject fluids in the core with a constraint of temperature corresponding to the targeted temperature especially for crude oil in order to restore more efficiently the wettability.

The physical chemistry may not give very decisive information in such complex systems. Based on a first order DLVO approach, the oil redistribution observed might be caused by changes of the long-range forces of van der Waals as agonist (de Gennes 1985) because they usually tend to thicken the films at long range. At short range van der Waals forces may be agonist or antagonist. These changes are described and modeled by E. Bertrand (Bertrand 2000) on very pure alkanes. Such approach would require being able to collect more information on the oil and on the film properties than we can today.

For these reasons an interpretation based on DLVO net force balance is not clear to explain the observed wetting transition. Indeed, DLVO approach to quantify forces is not relevant due to the incapacity we have to identify and quantify most of the intersurfaces forces. Without any possibility of qualitative and quantitative analysis of the relevant surface forces, the very singular observed behaviors and reversibility of the oil spreading with thermal cooling argues the observed mechanisms are second order transition like and exclude the hypothesis of the only interfacial tension impact.

### 4.2.4 References

Bertrand, E. et al., 2001. Wetting of Alkanes on Water. *Physical Review Letters*, 86(14), pp.3208–3208.

Bertrand, E., 2000. WETTING TRANSITIONS OF ALKANES ON WATER: Influence of interfacial interactions. Université de Paris 06, Paris, FRANCE.

Cahn, J.W., 1977. Critical point wetting. The Journal of Chemical Physics, 66(8), p.3667.

Derjaguin, B. V., Churaev, N. V. & Muller, V.M., 1987. Surface Forces, Boston, MA: Springer US.

De Gennes, P.G., 1985. Wetting: statics and dynamics. Reviews of Modern Physics, 57(3), pp.827–863.

## 5. CONCLUSIONS and PERSPECTIVES

To study the rock wettability we used X-ray micro-tomograph in this thesis. The quantitative and qualitative analysis of fluids distributions in the pore space from obtained images are used to progress in the rock wettability mechanisms understanding.

The decisive role of workflow has been evidenced including the crucial role of images treatments. Thereby, hardware and software experimental optimizations permitted to minimize several errors linked to image processing on the SkyScan 1172 micro-CT available in the UPPA.

Regarding the image exploitation, we were particularly interested in errors, which are linked to image segmentation and resolution. They play a decisive role in static petrophysical properties calculations, here the porosity and absolute permeability. This work was performed on geological samples of different natures, but also on a numerical rock sample where we exhibited that the resolution insufficiency modifies drastically the pore space connectivity, therefore the numerical result of permeability calculation, although the sample porosity degradation of the measurement seemed to be less affected. We have also shown that a forced thresholding to the sample porosity leads to clear aberrations for a multi-material dual porosity. Contrarily to medical CT scans, the exploiting of subvoxels was therefore not possible with such micro-CT than used here.

Beyond the limiting parameter of resolution, to access to a good contrast between oil and brines with the available micro-CT it required an adaptation of the initial experimental protocol. In order to increase natural contrast and limit X-ray scattering to reduce the saturations measurements errors thanks to a special physical filtering and parameters.

Once the experimental protocol fixed, we developed several scripts on Avizo® to perform pertinent analysis of indicators which are relative to the rock wettability of fluids. The highest resolution of the micro-CT is about 3.5 micrometers per voxel therefore the low number of voxels recorded in the throat pores of a sub darcean rock did not permit to analyze accurately the whole shape of the trapped drops in the pores. Nevertheless, to access to wettability criteria in porous medium, we defined indicators based on the numerical calculations of the contacts between surfaces, the contacts by curvatures types ... whereby we were able to qualify the wettability degree of the rocks.

We confirmed the decisive role played by the physical resolution of the micro-CT. To test the numerical calculation accuracy we tested in collaboration with the IMF of Toulouse the effect of the meshing in a fixed pore space. We observed a convergence of the permeability over the Representative Elementary Volume and a good accuracy of the calculated values with the measured one. Based on Stokes equation in periodic and permeameter conditions we observed this effect of mesh sensitivity leading to a prohibiting computing time especially for the periodic configuration. Nevertheless, the scalability of the code led to reasonable calculation times.

With the help of these numerical tools useful in the global analysis of the rock samples we proceeded to the establishment of a new microfluidic system permitting to access to petrophysical experiments of multi-phase flow inside the micro-CT in representative conditions. However, such installation requires an immobilization of the micro-CT during the wettability restoration during 2 weeks that corresponds to the oil-brine-rock system equilibrium time.

During the three years of the PhD micro-CT has been available for this work up to 18 months, the other 18 months the machine was unusable due to breakdowns and maintenance phases including changing a tube and a RX detector. The experimental protocols have evolved during these three years (thermal aging, water bottom injection and oil from the top to minimize breakthroughs, flexible compatibility with oils used ...). There are more than 15 sequences of experiments carried out on saturated with oil and brine rocks that we have conducted in porous media. Here we have chosen to present the experiments with a

petrophysical interest and we chose to not present the experiments of installation amelioration or experimental having several experimental problems.

Through these experiments, the treatments and calculations process we have accessed to the information about the contact surface between the oil and the substrate but also to quantify the geometrical preferences of oil wetting in porous media (i.e. concavities and convexities). We showed the trapped after waterflooding oil is located more in concavities. Low Salinity Brine injection permitted to liberate trapped in concavities oil. This experiment permitted us to observe the wettability changes in porous media. The porous medium response to the low salinity brine injection confirms an idea largely represented in the literature, considering the wettability changes in a more water wet conditions are the cause of the additional recovery in case of low salinity brine injection.

We led experiments to demonstrate the feasibility of such type experiments with micro-CT. Following the same protocol with companion rocks and the same crude oil, we changed the aging temperature to show the importance of the wettability restoration phase. Thanks to this very important experiment we have shown that the increase in the aging temperature permitted to reach hightly contrasted conditions in term of wettability although the difference in term of initial oil saturation was less of 3%. From here we concluded on the existence of one or more physicochemical characteristics responsible for such fluid behavior.

Despite the Micro-CT is a direct observation method for content analyzing of the pore space, it is an extremely complex system to understand in-situ, so we decided to complete micro-CT experiments by physico-chemical experiments ex-situ to better describe our observations.

The wettability testing permitting to study oil spreading we selected to use is an ellipsometer to access to thin films and therefore the disjoining pressure range of forces.

We first observed wetting transitions of a crude oil on high salinity brine although we did not obtained similar results with low salinity brine. In LSB oil lenses are not spreading. The non-spreading of another tested crude oil revealed the wetting transition is observable with a specific crude oil. We exhibited this behavior with a crude oil for the first time to our knowledge. We observed here a wetting transition of second-order for the first oil responding to thermal aging and nothing for the second one in used temperature range. These transitions were also observed on plate glass previously wetted by water. Observed transitions for the first oil appear at temperature about 50°C. This experiment permitted to confirm the obtained with micro-CT wetting changes. We evidenced the importance of such petrophysical oil property until that time only showed on pure alkanes.

The petrophysical bibliography attributes a double layer expansion as at the origin of the oil dewetting of the rock. In term of physical chemistry, the consequence is a zeta potential increase with the brine dilution or system cooling. We measured zeta potential of the various components (oil and sandstone equilibrated with the brine). We also measured zeta potential of several sands previously used by TOTAL adhesion tests to be able to compare zeta potential results to these adhesion tests. From these experiments we could note that all tested media (sandstone, pyrolyzed sandstone, Fontainebleau sand, sand of Landes, Ottawa sand, all equilibrated with oil and brine et 60°C) exhibit very close zeta potentials. These curves are very similar to quartz. Zeta potential of the oil in the whole pH range (from 2 to 9) is electronegative and strongly electronegative for pH > 4. These conditions are usually considered as repulsive although the oil droplets adhere on the solid particles for low salinity brine and for the whole range of tested pH.

We showed the electrical double layer of the tested minerals are similar and meet similar electrical double layer expansion with the salinity dilution. The similarity of ions-ions interactions of all tested rocks is not related to the adhesion behavior. Dausse sandstone with Fontainebleau sand exhibit oil adhesion,

although Landes sand and Ottawa sand did not adhere with oil. More complex mechanisms were evoked to explain such strong differences as mineral roughness for example or more subtle mechanisms based on the precise definitions of the electrical term of the disjoining pressure.

We are convinced that to progress in wettability study the experimental access to the quantification of forces between crude oil-brine and substrate is required. It would require the development of a special surface force apparatus optically conceived for crude oil experiments. Based on a Scheludko or Mysels set up we could measure the wetting disjoining film thickness and the corresponding pressures. It could be an interesting extension of this job. It might permit also to take into account another characteristic of the formation rock: the roughness and the confinement therefore the capillary pressure for petrophysicists.

We have shown the possible existence of wettability transition in oil-brine system under saline and temperature conditions and relative reversibility for temperature or salinity decreasing. The very high additional oil recovery obtained after a thermal aging with Ac oil is explained by the concomitance of the two mechanisms. To be more realistic of reservoir conditions it should be important to inject fluids in the core to the targeted reservoir temperature especially for crude oil in order to restore more efficiently the wettability.

After all carried out experiments, we think oil and brine conditioning plays the most important role in experiments and measurements to explain the dispersion of the results obtained concerning low salinity brine injection in oil recovery. The disjoining pressure term has to be taken into account in characterization works, which are linked to the wettability studies. In this way, wettability tests and capillary pressure might be investigated more precisely.

Our study shows the low salinity brine injection in porous medium saturated in both fluids seems to increase water wetness of the rock.

New technical solutions should be found to reduce as far as possible the dead volumes to facilitate the access to physical quantifications of the core by a direct measurement at the inlet and outlet of the core plug.

Another experimental study on low salinity brine injection has to be carried out to ameliorate the comprehension of the underlying mechanism and proposed in the literature theories to explain it. Low salinity brine injection in secondary mode under micro-CT visualization might give new results of surface state changes. We propose to carry out a new set of experiments on micro-CT to better show the Low Salinity Brine effect on oil recover. Firstly, we would like to follow the pore surfaces changes caused by LSB injection in secondary recovery mode. Secondary, LSB injection as formation water might introduce new elements in "smart water" effect comprehension. This type of experiments must be traced for ionic exchange between oil and water phase.

Moreover the very limited information is also linked to the lack of performances of micro-CT in term of dynamics. This is today only possible in a few international synchrotrons such Swiss Light Source or ESRF. Almost, due to the inner configuration of the micro CT the dead volumes represent two times the pore volumes of the core sample. The end points are the only measured states but intermediate states are not visualized.

An important awaited advance of the next years is linked to the access to a 4D micro-tomography. A visualized full field Hassler type microcell should be great to visualize the inlet and outlet in order to perform a mass balance during the experiment. In this way image treatment will need to evaluate to faster treat images. In the case of 4D micro-tomography the image normalization will be required. Image

normalization will permit to access to automatic image treatment which is a necessary condition in rapid data acquisition conditions.

# ECOLE DOCTORALE : SCIENCES EXACTES ET LEURS APPLICATIONS - ED 211

# LABORATOIRE:

LFC-R de Fluides Complexes et leurs Réservoirs

# CONTACT

Marfa NAZAROVA CHERRIERE marfa-nazarova@yandex.ru